Imperial College London

Synthesis of Novel Indacenodithiophene Derivatives and their Application in Organic Solar Cells

Petr Ufimkin

Supervisor – Prof. Martin Heeney

Submitted in partial fulfilment of the requirements for the degree of

Doctor of Philosophy in Chemistry

Imperial College London

Department of Chemistry

March 2022

Abstract

Organic semiconductors have risen as a promising replacement for silicon in electronic applications. They benefit from increased flexibility, transparency, and the potential for cheaper device production. Particularly, the field of organic photovoltaics (OPV) has seen tremendous progress, with power conversion efficiencies (PCEs) over 19% being reported for single junction devices. Much of their performance growth has been driven by the synthetic modification of non-fullerene acceptors (NFAs). 3,9-Bis(2-methylene-(3-(1,1-dicyanomethylene)-indanone))-5,5,11,11-tetrakis(4-hexylphenyl)-dithieno[2,3-d:2',3'-d']-s-indaceno[1,2-b:5,6-b']dithiophene (**ITIC**) is a high-performing example of these and the development of novel electron donating cores and NFAs based on its structure is the focus of this work.

In Chapter 2, a series of indacenodithiophene (**IDT**) derivative cores were synthesised via a novel route utilising a triflic acid ring-closing reaction. This is more direct than earlier reported synthetic pathways, with synthesis of indacenodithienothiophene (**IDTT**) taking two steps fewer and proceeding in 66.8% overall yield instead of 9.4%. Three main synthetic strategies were applied in the design of novel cores: ring-extension, fluorination, and isomerisation. Overall, six cores were synthesised, with four entirely novel and two having their synthesis optimised. In addition, a route to asymmetric alkyl-chain **IDT** was developed.

NFAs with the **ITIC** structure were then synthesised in Chapter 3 with modification by side-chain engineering, end-group fluorination, core fluorination, and end-group replacement. The NFAs were taken to our sponsor's site and screened in large-area devices. Because of observed poor acceptor solubilities, derivatives were then produced with longer sidechains. Further testing and optimisation were performed on small-area devices. The novel **C8-2FITIC** acceptor performed at a respectable 8.3% PCE but trailed the performance of NFAs previously prepared in our group.

Finally, in Chapter 4, the fluorinated p-type polymer **P2FIDTT-BT** was synthesised from the novel **2FIDTT** core and tested in OFET devices. The polymer had a saturated mobility (μ_{sat}) of 0.29 cm^2/Vs in devices and a threshold voltage (V_T) of -29 V.

Declaration

The work described in this thesis was carried out in the Department of Chemistry at Imperial College London unless stated otherwise. The work was performed between October 2017 and June 2021 under the supervision of Prof. Martin Heeney. The content herein is my own work unless stated otherwise.

Petr Ufimkin, March 2022

Acknowledgements

I would first like to thank Prof. Martin Heeney for his constant help throughout my PhD. I couldn't wish for a kinder and more knowledgeable supervisor and am very thankful that you have given me the opportunity to do research in your welcoming and supportive group. I would also like to thank my industrial supervisors Dr. Agnieszka Pron and Dr. Kane Heard for their sage advice and support.

Thank you to Merck Chemicals for providing me with funding for this project and thank you to my loving mother for her financial and emotional support throughout this work.

I would like to extend my thanks to all the members of the Heeney and McCulloch groups that I have worked with. This includes Alex, Andy, Ben, Bowen, Brett, Byron, Charlie, Charlotte, Eddie, Fei, Filip, Flo, Florian, Haojie, Helen, Iain, Ilknur, James, Luxi, Mark, Martina, Matthias, Max, Maxime, Notina, Petruta, Qiao, Shengyu, Simon, Sophie, Tao, Tingmang, Tom, Weimin, Zeinab. You have all made my PhD much more enjoyable and have provided me with endless encouragement in my work. I am sorry for surely missing some people off this list.

Special thanks to Dr. Matt Bidwell for his constant advice and friendship during my PhD and to Dr. Adam Marsh for teaching me how to do lab work properly. Further thanks to Charlotte Rapley for running my MALDI measurements on short notice and helping me to order chemicals.

Contributions

This work would not have been possible without the help of others, and I would like to particularly thank the following people for their contributions:

Merck Chemicals kindly provided funding for this work and gave me the opportunity to make devices at their site (Chapter 3.3.1). The original syntheses of **IDTBt** and **2FIDTBt** were performed by an MSci student under my direct supervision, Jiaye Rong (Chapters 2.2.4 and 2.2.5). The final small area OPV devices were fabricated and tested by Dr. Flurin Eisner (Chapter 3.3.3). OFET devices were fabricated and tested by Dr. Aniruddha Basu (Chapter 4.2.3). Dr. Qiao Hei synthesised **PFBDB-T** and **PIDT-BT** polymers for device testing (Chapters 3.3 and 4.2.3). Dr. Fei Zhuping synthesised the **4F-C8-ITIC** acceptor (Chapter 3.3.3). Special thanks to Filip Anies for his erudite DFT assistance and Bowen Ding for his cyclic voltammetry consultation.

Copyright

The copyright of this thesis rests with the author. Unless otherwise indicated, its contents are licensed under a Commons Attribution Non-Commercial No Derivatives 4.0 International Licence (CC BY-NC-ND). Under this licence, you may copy and redistribute the material in any medium or format. You may also create and distribute modified versions of the work. This is on the condition that: you credit the author and do not use it, or any derivative works, for a commercial purpose. When reusing or sharing this work, ensure you make the licence terms clear to others by naming the licence and linking to the licence text. Where a work has been adapted, you should indicate that the work has been changed and describe those changes. Please seek permission from the copyright holder for uses of this work that are not included in this licence or permitted under UK Copyright Law.

Abbreviations

μ_{lin}	Linear mobility
μ_{sat}	Saturated mobility
A-D-A	Acceptor-donor-acceptor
BHJ	Bulk heterojunction
BT	Benzo[c][1,2,5]thiadiazole
Bt	Benzothiophene
CB	Chlorobenzene
CIGS	Copper indium gallium diselenide
CV	Cyclic voltammetry
d_2-TCE	Deuterated tetrachloroethane
D-A	Donor-acceptor
DCI	Dicyanovinylindanone
DCM	Dichloromethane
DFT	Density functional theory
DIBAL-H	Diisobutylaluminium hydride
DMC	Dimethyl carbonate
DMF	Dimethylformamide
DMP	Dess–martin periodinane
DMSO	Dimethyl sulfoxide
DPP	Diketopyrrolopyrrole
EA	Electron affinity
EQE	External quantum efficiency
ETL	Electron transport layer
Fc/Fc^+	Ferrocene/ferrocenium redox couple
FF	Fill factor
FL	Fluorescent lamp
FMO	Frontier molecular orbital
FTIR	Fourier-transform infrared spectroscopy
GIWAXS	Grazing-incidence wide-angle X-ray scattering
GPC	Gel permeation chromatography
HOMO	Highest occupied molecular orbital
HTL	Hole transport layer
I_{DS}	Source/drain current
IDT	Indaceno[1,2-b:5,6-b']dithiophene
IDTT	Indacenodithieno[3,2-b]thiophene

I_{OFF}	Off current
I_{ON}	On current
IP	Ionisation potential
IPA	Isopropanol
IR	Infrared
ITO	Indium tin oxide
J_{SC}	Short-circuit current
JV	Current-voltage
LDA	Lithium diisopropylamide
LED	Light emitting diode
LUMO	Lowest unoccupied molecular orbital
M.P.	Melting point
Mn	Number average molecular weight
MO	Molecular orbital
MS	Mass spectrometry
Mw	Weight average molecular weight
NBS	N-bromosuccinimide
NFA	Non-fullerene acceptor
NMP	N-methyl-2-pyrrolidone
NMR	Nuclear magnetic resonance
oDCB	1,2-Dichlorobenzene
OFET	Organic field-effect transistor
OPV	Organic photovoltaic
P3HT	Poly(3-hexylthiophene-2,5-diyl)
PBTTT	Poly(2,5-bis(3-alkylthiophen-2-yl)thieno(3,2-b)thiophene)
PCE	Power conversion efficiency
PDI	Perylene diimide
PEDOT:PSS	Poly(3,4-ethylenedioxythiophene) polystyrene sulfonate
P_m	Maximum power
PQT	Poly(3,3'-dialkylquaterthiophene)
PQT	Poly(3,3'-dialkylquaterthiophene)
R_F	Retardation factor
TBAF	Tetra-*n*-butylammonium fluoride
TG-BC	Top-gate bottom-contact
THF	Tetrahydrofuran
TIPS	Triisopropylsilyl
TIPSCl	Triisopropylsilyl chloride
TLC	Thin-layer chromatography

TMS	Trimethylsilyl
TMSCl	Trimethylsilyl chloride
UV-Vis	Ultraviolet-visible
V_D	Drain bias
V_G	Gate bias
V_{OC}	Open-circuit voltage
V_T	Threshold voltage
XPhos	2-Dicyclohexylphosphino-2’,4’,6’-triisopropylbiphenyl

Table of Contents

Abstract 2
Declaration 3
Acknowledgements 4
Contributions 5
Copyright 6
Abbreviations 7
Table of Contents 10
Chapter 1 – Introduction 13
1.1 - Energy Generation Today 13
1.2 - Solar Cell Variety Overview 13
1.3 - Organic Semiconductor Theory 15
1.4 - OPV Devices 17
1.5 - Donor Polymer Structure 23
1.6 - Fullerene Acceptor Structure 26
1.7 - Early Non-Fullerene Acceptors 27
1.8 - A-D-A Non-Fullerene Acceptors 28
1.9 - Wide Bandgap NFAs 34
1.10 - OFET Device Theory 36
1.11 - OFET Semiconductor Selection 39
1.12 - Coating Methods 41
Chapter 2 - Synthesis of **IDT** Derivative Cores for Organic Electronics 43
2.1 – Introduction 43
2.1.1 – Development of the **IDT** core 43
2.1.2 – Synthetic Strategies 49
2.1.3 – Ring-Closing Reaction Background 51
2.2 - Results and Discussion 55
2.2.1 – **IDTT** 55
2.2.2 – **2FIDT** 57
2.2.3 – **2FIDTT** 59
2.2.4 – **IDTBt** 60
2.2.5 – **2FIDTBT** 65
2.2.6 – **meta-IDTT** 69
2.2.7 – Optoelectronic and Electrochemical Properties of Cores 75

2.2.8 – Asymmetric Sidechain **IDT** via Double Suzuki Coupling 78
2.2.9 – Asymmetric Sidechain **IDT** via the Wittig Reaction 81
2.3 – Conclusions 84
2.4 – Experimental 87
Chapter 3 – **IDT** Derivative Acceptors and their use in OPV 114
3.1 – Introduction 114
3.1.1 – **ITIC** Derivatives in the Literature 114
3.1.2 – Target **ITIC** Derivatives 118
3.2 – NFA Synthesis and Properties 121
3.2.1 – Synthesis of **C6-ITIC** 121
3.2.2 – Synthesis of End-Group Halogenated **C6-ITIC** 124
3.2.3 – Synthesis of Core Fluorinated **C6-ITIC** 125
3.2.4 – Synthesis of Rhodanine End-Group **C8-ITIC** 127
3.2.5 – Optoelectronic and Electrochemical Properties of NFAs 128
3.3 – Device Performance of Novel NFAs 131
3.3.1 – Initial Screening on Large Area Devices 131
3.3.2 – Small Area Devices – Influence of Fabrication Facility 142
3.3.3 – Devices Made by Collaborator 151
3.4 – Conclusions 155
3.5 – Experimental 157
3.5.1 – Material Sources 157
3.5.2 – Synthetic Procedures 157
3.5.3 – Merck Site Device Fabrication Procedure 174
3.5.4 – Clean Room Device Fabrication Procedure 174
3.5.5 – Physics Department Device Fabrication Procedure 175
Chapter 4 – Polymers for OFET 176
4.1 – Introduction 176
4.1.1 – **IDT** Derivative OFET Polymers 176
4.1.2 – Target OFET Polymer 177
4.2 – Results and Discussion 179
4.2.1 – Polymer Synthesis 179
4.2.2 – Optoelectronic and Electrochemical Properties of **2FIDTT-BT** 183
4.2.3 – **2FIDTT-BT** Device Performance 184
4.3 – Conclusions 187
4.4 – Experimental 188
4.4.1 – Material Sources 188

4.4.1 – Synthetic Procedures 188
5 – General Experimental 192
5.1 – Materials and Reaction Conditions 192
5.2 – Characterisation 192
6 – References 194
7 – Appendices 207
7.1 - Chapter 2 207
7.1.1 - CV traces 207
7.1.2 - NMR Spectra 209
7.2 - Chapter 3 226
7.2.1 -CV traces 226
7.2.2 - NMR Spectra 231
7.2.3 – DFT results 250
7.3 - Chapter 4 252
7.3.1 - CV Traces 252
7.3.2 - NMR Spectra 253
7.3.3 – OFET Data 260
8 – Permissions 265

Chapter 1 – Introduction

1.1 - Energy Generation Today

Humanity has required ever increasing amounts of energy to maintain its exponential population growth. Historically, most of this growth has been enabled by the combustion of fossil fuels and in 2021, 61% of global electricity generation was produced by fossil fuels.[1] However, whilst burning fossil fuels is a cheap and facile energy source, they release a series of gases that cause damage to the environment.[2–4] The released gases are the main contributors to the greenhouse effect, with CO_2 being most notable due to its high atmospheric concentration. Fossil fuels are estimated to account for a startling 70% of total global CO_2 emissions.[5] Additionally, fossil fuels are finite, albeit their depletion date has been adjusted constantly as new sources are found and it is likely that severe climate change will occur long before they run out.[6,7] To counteract this climate change, there has been a major societal push for cleaner renewable forms of energy generation. To this end, the proportion of the worlds electricity generated by fossil fuels has fallen 4.7% from 2015 to 2021.[1] Solar, wind, biomass, geothermal and hydropower are the most common renewable energy sources.[8] However, all of these energy sources besides solar and biomass are heavily location dependent, whilst power generation from biomass can be limited by availability of bio-waste. Solar power generates electricity from light, which is abundant across the world making it a reliable energy source for the world's transition from fossil fuels.

1.2 - Solar Cell Variety Overview

To date most solar cells have been produced from crystalline silicon, these are known as "first-generation solar cells". Single-junction crystalline silicon solar cells have achieved impressive PCEs of over 26%, however due to crystalline silicon having an indirect bandgap they suffer from poor light absorption and therefore require thick layers on the scale of hundreds of micrometers.[9–11] This thickness coupled with the high temperatures required to produce silicon wafers makes production of these cells expensive, although industrial costs have to date reduced due to the wide adoption of the cells.[12]

To overcome crystalline silicon's weaknesses, second-generation solar cells have been developed from direct bandgap materials such as amorphous silicon, CdTe and CIGS (copper indium gallium diselenide) allowing growth of thin films of sufficient absorption on a substrate rather than cutting larger crystals, thus lowering manufacturing costs.[13,14] Second-generation cells have PCEs of over 22% and unlike crystalline silicon, can be made flexible if the correct substrate-absorber combination is used.[15] Unfortunately, these thin film cells suffer from a number of drawbacks that make them impractical for wide-scale adoption. CdTe cells use toxic cadmium and rare tellurium whilst CIGS cells utilise a quaternary structure making synthesis challenging whilst also using the rare element Indium. Other types of second-generation cell using Cu_2ZnSnS_4 or amorphous silicon don't have problems with sourcing material or toxicity, but suffer from low PCEs of 14% or under.[16,17]

More recently, a further third generation of solar cells has been developed. Third-generation solar cells include emerging photovoltaic technologies that are often at an early research stage or not yet commercially applied. These include dye sensitised solar cells, Organic photovoltaic (OPV) cells, quantum dot cells, and perovskite cells.[18–21] Generally, third generation cells are amenable to printing from solution rather than the vacuum deposition necessitated for inorganic thin film cells, resulting in improved throughput, scalability, and therefore reduced costs. Moreover, the organic materials commonly used for these cells seldom contain rare metals and besides lead-containing perovskite cells do not have the issues with toxicity often observed for second generation cells. The PCEs of third-generation cells vary by type with perovskite cells the highest at 25.5% to date, followed by OPV cells with 18.2%, quantum-dot cells at 18.1% and finally dye-sensitised solar cells at 13.0%.[22] Although lower in record PCEs than perovskite cells, OPV cells do not use toxic lead that is present in the most efficient perovskite solar cells. While attempts have been made to improve the performance of lead-free perovskite cells, they maintain record PCEs of only around 10%.[23] Therefore, OPV cells are one of the most promising third-generation solar cell types and warrant further research.

1.3 - Organic Semiconductor Theory

The organic materials used in OPV cells behave differently from inorganic semiconductors such as silicon used in earlier solar cell types. The transport of charge within OPV is performed by conjugated molecules. These form a single electron cloud from the combination of neighbouring p-orbitals on sp^2 hybridized carbons down the molecule allowing higher energy charge carriers to freely move around. As more p-orbitals are added to the conjugated system, they extend it and contribute to the overall molecular orbital (MO). By the linear combination of atomic orbitals, the energy levels of the MO can be predicted. The effect of increased conjugation on energy levels is depicted for a series of molecules in **Figure 1.1(a)**.

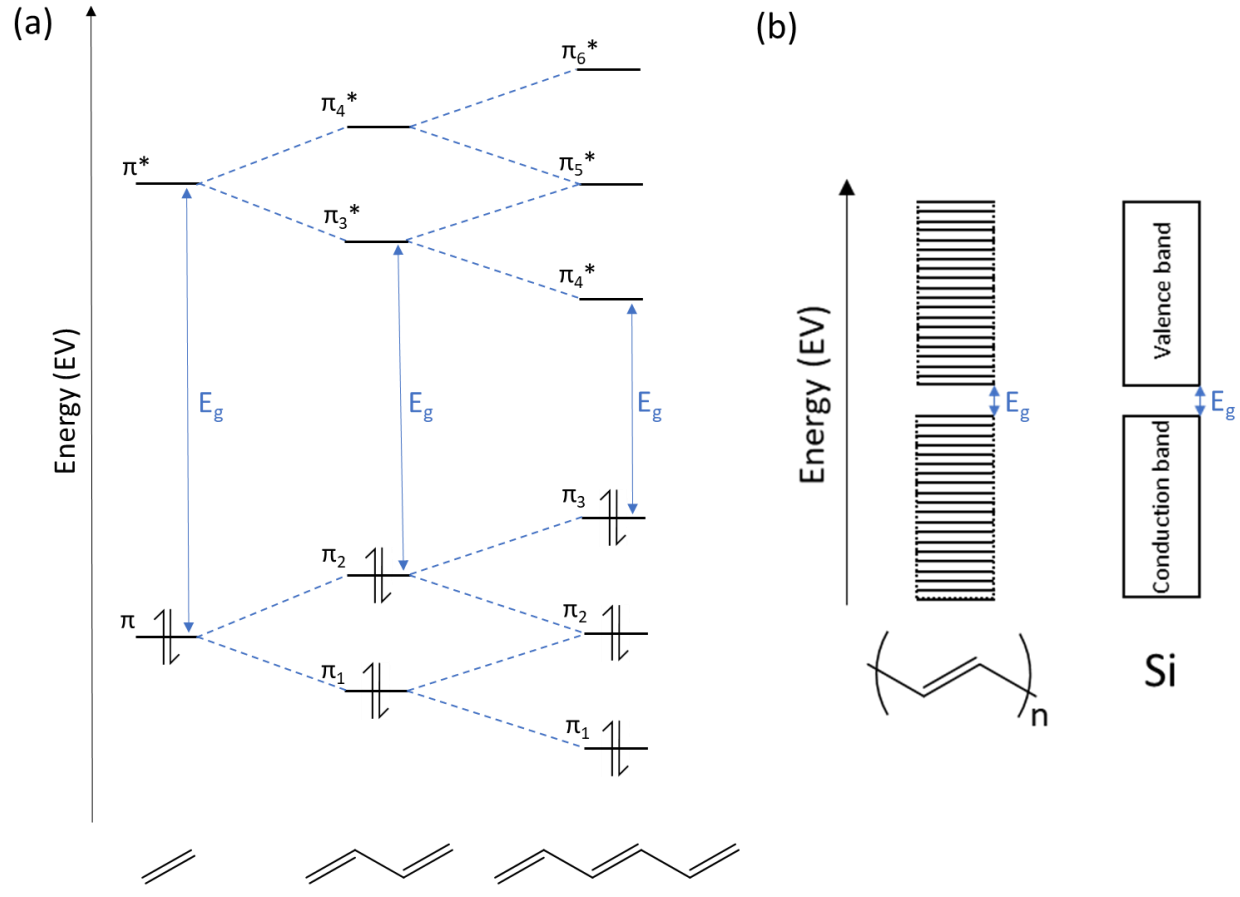


Figure 1.1: *(a) Hückel Molecular Orbital Theory approximation of energy levels of ethylene and the effects of increased conjugation (not to scale). (b) Visualisation of the similarities between the hybridised energy levels of polyethylene and the band structure in silicon.*

Notably, increased conjugation leads to a reduction in the bandgap (E_g) of conjugated molecules. This bandgap between the highest occupied molecular orbital (HOMO) and lowest unoccupied molecular orbital (LUMO) energy levels of molecules can be viewed as analogous to the bandgap between the valence band and conduction band in an inorganic semiconductor such as silicon (**Figure 1.1(b)**). As the degree of conjugation is increased, the gaps between energy levels become smaller with polymeric materials approaching the continuous energy levels found in the bands of inorganic materials. The effect of increased conjugation is however, limited. Perpetually elongated conjugated systems suffer from Peierl's theorem that states that a one-dimensional equally spaced chain with one electron per ion is unstable.[24] For polymers, this results in alternations in bond lengths that cause irregularities in the polymer and disallow conjugation to an infinitely small bandgap as in a metal.[25,26]

When multiple conjugated molecules are in contact, high energy charge carriers can hop between them and allow conductivity in the bulk. This charge hopping can be problematic and reduce current due to the presence of trap states in areas of irregularity in the bulk. Therefore, to maximise charge carrier mobility highly ordered crystalline compounds should be used as a more-narrow density of states reduces the probability of a charge carrier hopping to a trap. Besides minimising trapping, charge carrier mobility can be improved by minimising reorganisation energy in the material and by maximising the charge transfer integral.[27] The reorganisation energy of a molecule reflects the geometry relaxation when the electronic state changes and is maximised in rigid fused systems. The charge transfer integral on the other hand relates to the electronic splitting of a given energy level of a molecule when it interacts with other molecules, this is improved by highly ordered morphologies in the bulk.[27]

Another consequence of using organic semiconductors is the high binding energy of excitons formed upon photoexcitation of electrons. The coulombic attraction between the electron and hole pair in an exciton is screened less and is therefore higher for excitons in organic systems than for those in inorganic ones. This effect is due to the low dielectric constant (ε_r) of organic materials and can be quantified through **Equation 1.1**.

$$V = \frac{q_1 q_2}{4\pi r \varepsilon_r \varepsilon_0}$$

Equation 1.1: *Coulombic attraction between two charges (V), where q_1 and q_2 are the charges of particles, r is the distance between the charges, ε_0 is the electric constant, and ε_r the dielectric constant.*

Because of their high binding energy, excitons formed in organic systems recombine if unassisted, therefore it is essential to split the excitons prior to this occurring if charge is to be extracted.

1.4 - OPV Devices

OPV devices utilise both a donor and an acceptor material of varying energy levels to provide a step change that helps to split excitons. When a photon hits the donor, an electron is excited, and a hole is formed creating an exciton (**Figure 1.2**). The exciton then diffuses to the interface between the donor and acceptor material, where it is split apart by the local difference in frontier orbital energy level. The free charge carriers then move to their respective electrodes, thus generating current from the device. It must be noted that the same process can occur in the acceptor, with the free hole moving to the donor instead when the exciton is split.

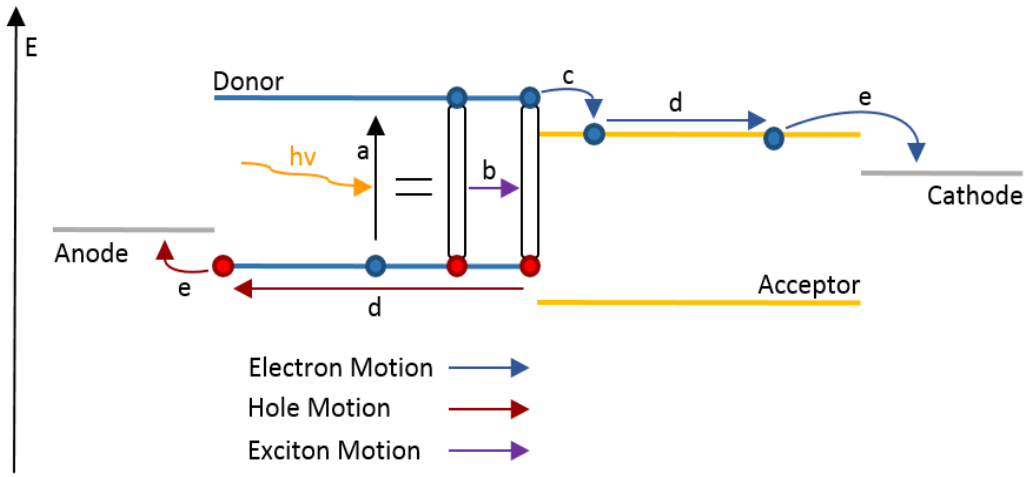


Figure 1.2: *The operation of an OPV device: (a) electron excitation, (b) exciton diffusion, (c) exciton splitting, (d) free carrier transport, (e) charge extraction.*

The excitons formed in organic devices can only diffuse a short distance prior to recombining, this is known as geminate recombination (non-geminate recombination involves free charge carriers released from separate excitons). Most organic semiconductor films have exciton diffusion lengths below 20 nm, for example the common OPV donor polymer poly(3-hexylthiophene-2,5-diyl) (**P3HT**) reportedly has an exciton diffusion length of only 3.5-5 nm.[28–30] Early OPV devices utilised a thin bilayer of donor and acceptor material to ensure that excitons can reach the donor-acceptor interface and split prior to recombining. However, minimising exciton recombination by lowering bilayer thickness inevitably causes loss in charge generation in thin film devices as the optical absorption pass length for organic materials is around 100-200 nm.[30] Bilayer devices additionally either require costly vacuum deposition or for the donor and acceptor to be processed from orthogonal solvents so that they don't disturb the lower layer onto which they are deposited, limiting material choice. To overcome these problems bulk heterojunction (BHJ) active layers were developed for OPV. These involve blending the acceptor and donor materials in a single solvent and depositing them together resulting in many interfaces being formed between the materials. In an ideal world, this would result in interdigitated domains of donor and acceptor, wherein each formed exciton can reach an interface before recombining and the free charge carriers have a path to their respective electrodes (**Figure 1.3(a)**).

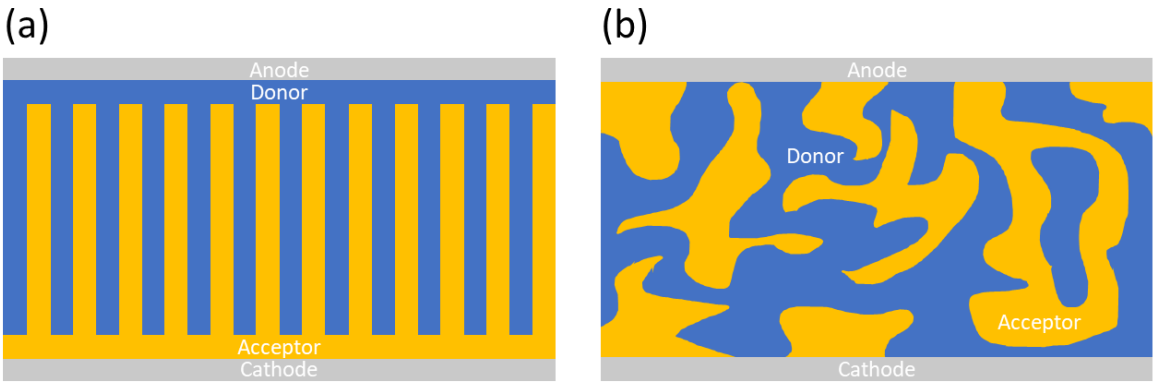


Figure 1.3: *Morphology in a BHJ: (a) Ideal morphology. (b) Optimised morphology.*

However, in practice there is more disorder in the BHJ such as in **Figure 1.3(b)** where there are irregularly mixed domains of the materials. This disorder causes loss in current generation as excitons may form too far from an interface and recombine or free charge

carriers may be left in “islands” of one material wherein they cannot reach their electrodes. To minimise these losses, control of intermolecular interactions between the donor and acceptor materials, and their interaction with other layers in the device and the deposition solvent are important considerations in the design of OPV materials.

Besides the active layer and electrodes in OPV devices interlayers are also used, namely the hole transport layer (HTL) at the anode and the electron transport layer (ETL) at the cathode (**Figure 1.4**).[31] These help to align the work function of the electrodes to that of the active layer, ensuring Ohmic contact and more efficient electron extraction. Additionally interlayers are used to help tune active layer morphology and carrier recombination dynamics.[32] The bottom of an OPV device is made up of a transparent substrate such as glass or plastic with a transparent layer of electrode on it, commonly made of indium tin oxide (ITO). Two configurations have been used in OPV devices, the conventional stack and inverted stack. In conventional stack devices the HTL is found near the bottom transparent electrode, that acts as an anode. In inverted stack devices the ETL is found at the bottom and the bottom electrode acts as a cathode thus inverting the direction of current flow. Between the ETL and HTL there is the active layer of the device, and the top of the device is completed with a metal electrode.

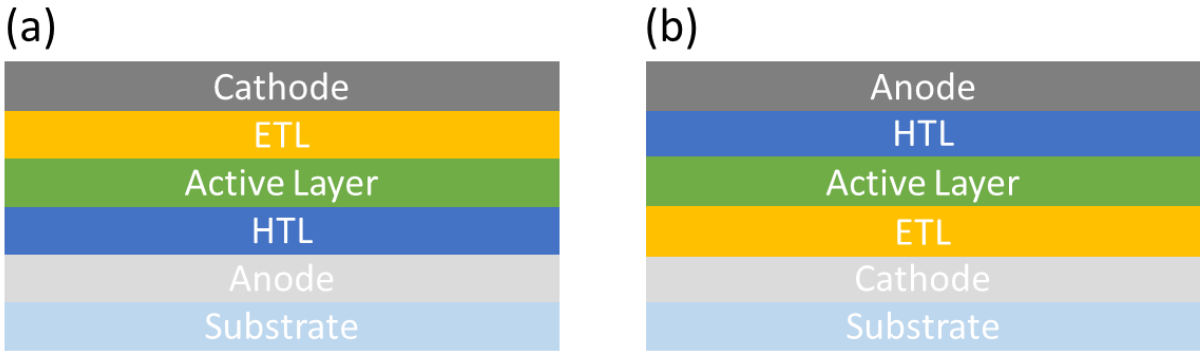


Figure 1.4: *(a) Conventional stack device. (b) Inverted stack device.*

The top electrode used in conventional stack devices is usually aluminium, and an inorganic ETL such as Ca or LiF is commonly used.[32] Due to the facile oxidation of these materials and formation of pinholes that allow water and oxygen to pass through and degrade the active layer, their use decreases overall device stability and requires fabrication under inert atmosphere.[33] The most common HTL used in a conventional stack is poly(3,4-

ethylenedioxythiophene) polystyrene sulfonate (PEDOT:PSS), this can however lead to stability issues due to its acidity.[34] Inverted devices can avoid the use of PEDOT:PSS (although it is still common) by use of MoO_3 or other inorganic oxides as the HTL. Similarly, being able to use a high work function metal such as silver as the top electrode improves the stability of inverted stack devices. Whilst this improvement in stability generally makes the inverted stack more favourable, different active layer materials can affect which stack performs better due to each component of the active layer having a different propensity to sink to the bottom during solution processing. This results in some active layers having either more donor or acceptor towards the bottom, meaning that performance can be improved by positioning the cathode towards the side with more acceptor and the anode towards the donor. Thermal or solvent vapour annealing are used for OPV devices to allow the used materials to reorganise into a more favourable morphology. Annealing is commonly performed on the ETL in inverted stack devices, and under inert atmosphere after active layer deposition or on completed devices.

A current-voltage (JV) curve can visualise the performance of an OPV device and values concerning its performance can be extracted from it (**Figure 1.5**).

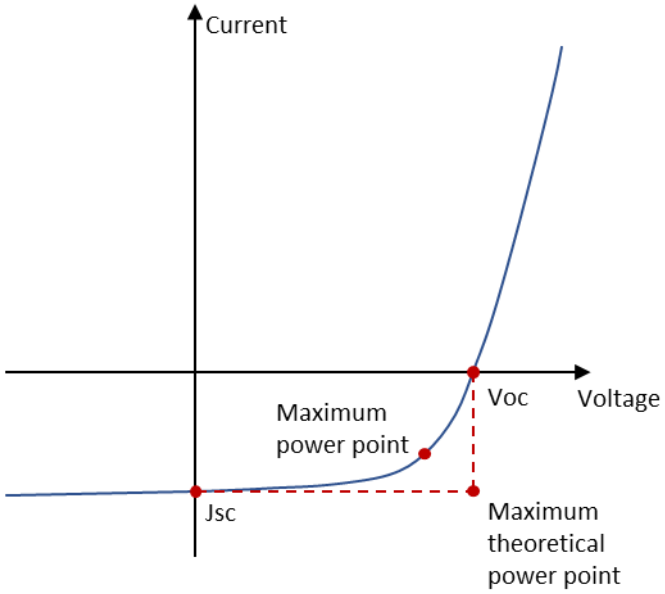


Figure 1.5: *J-V curve for an OPV device under illumination, with measured parameters labelled.*

The main parameter used to classify the performance of OPV devices is power conversion efficiency (PCE). This is the percentage of the input power from light photons that is extracted from the cell and is given by **Equation 1.2**.

$$PCE = \frac{P_m}{P_{in}} = \frac{J_{SC} V_{OC} FF}{P_{in}}$$

Equation 1.2: *Power conversion efficiency.*

Open-circuit voltage (V_{OC}) is the potential across the device when no current flows and short-circuit current (J_{SC}) is the current of the device when the potential difference is set to zero. These values can be multiplied together to find the maximum theoretical power of the cell. In practice OPV devices do not perform as an ideal diode and lower maximum power (P_m) is obtained due to recombination and other losses. The fill factor (FF) of a device can describe how close a cell is to being an ideal diode and can be visualised as a measure of the "squareness" of the J-V curve. A further measured parameter is the external quantum efficiency (EQE) of the device, this represents the percentage of charge carriers extracted as current per incident photon on the device and is given by **Equation 1.3**.

$$EQE = \frac{hcJ_{sc}}{q\lambda I_0(\lambda)}$$

Equation 1.3: *EQE of a cell, h is Planck's constant, q is the charge of an electron, c is the speed of light, J_{SC} is the short-circuit current, λ is the wavelength of incident light and $\lambda I_o(\lambda)$ is the current due to the photoelectric effect.*[35]

An ideal solar cell would have 100% EQE at every wavelength of sunlight, however real values are lower and can be optimised by appropriate material choice and device engineering. J_{SC} can be increased by improving the overlap of the overall absorption spectrum of the active layer with that of the incident light by choosing a donor and acceptor material that complement each other's absorption. Additionally, the materials themselves can be improved by using dye-based chromophores with high molar attenuation coefficients, and in theory by improving HOMO-LUMO overlap in the materials and therefore oscillator strength.[36,37] Other parameters can similarly be improved: V_{OC} can be improved by increasing the gap between the HOMO of the donor and the LUMO of the acceptor, whilst FF can be increased through control of morphology to minimise recombination. Moreover, FF can be improved by ensuring mobilities of charge carriers are balanced in the BHJ, so that there isn't a surplus of one of the carriers and non-geminate recombination is minimised. It must be noted that care must be taken when trying to optimise HOMO and LUMO energy levels as a sufficient gap between the frontier orbitals of the donor and acceptor is required to split formed excitons. Values of around 0.3 eV for the LUMO-LUMO or HOMO-HOMO gap between donor and acceptor have been required for this, with variation depending on material. If possible, smaller gaps should be used leading to lower energy loss.[38,39]

1.5 - Donor Polymer Structure

The classic OPV device active layer contains a donor polymer and a fullerene acceptor.[40] Donor polymers are used due to having readily tuneable properties, good rheology and potential for cheap production. Early successful donor-polymers had alkyl side chains and a single repeating unit such as in **MDMO-PPV** and **P3HT** (**Figure 1.4**).[40,41] These sidechains both allowed higher molecular weight polymers to be solution processed and allowed for the morphology of the active layer to be controlled, whilst the single repeating unit allowed for facile synthesis. Side chain engineering has since emerged as a common tool for tuning the properties of polymers.[42]

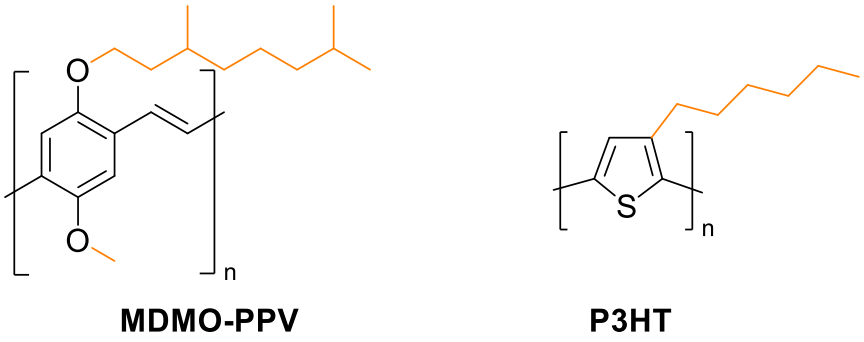


***Figure 1.4: MDMO-PPV** polymer and **P3HT**, sidechains in orange.*

A plethora of new donor polymers have been developed since, with more recent polymers utilising copolymerisation of alternating electron donating components and electron accepting components. These are known as donor-acceptor (D-A) or push-pull polymers.[43] The combination of these two (or more) components results in reduced band gap for the polymer due to hybridisation and allows facile tuning of the HOMO and LUMO of the polymer by modifying these components. Because solar irradiation releases a large proportion of its photons in the infra-red region, reduction in polymer bandgap is generally favourable as it helps match the polymer to absorb these photons and maximise charge generation in devices.[44] The HOMO and LUMO (the frontier molecular orbitals) of the overall polymer are localised on the more electron rich and the more electron poor component respectively. Therefore, strategies such as selective halogenation can be used to lower the HOMO or LUMO of the overall polymer with little effect on the other orbital. Alternatively, substituting electron rich functional groups can be used to raise either the

HOMO or LUMO of the overall polymer. Example successful D-A type polymers are shown in **Figure 1.5**.

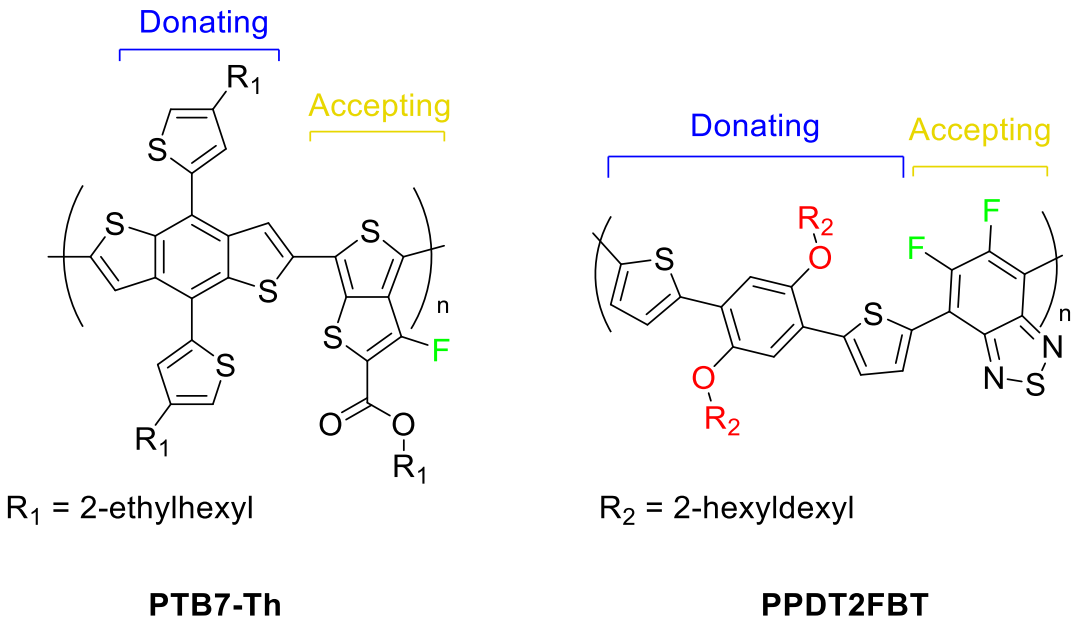


Figure 1.5: *Structures of* ***PTB7-TH*** *and* ***PPDT2FBT*** *with electron donating and electron accepting components labelled and additional frontier orbital raising substitutions in red and lowering in green.*[45,46]

Besides benefiting form a D-A structure, the donor polymer **PPDT2FBT** also demonstrates how substituting functional groups onto the backbone can help control crystallinity via intramolecular interactions between the components (**Figure 1.6**).

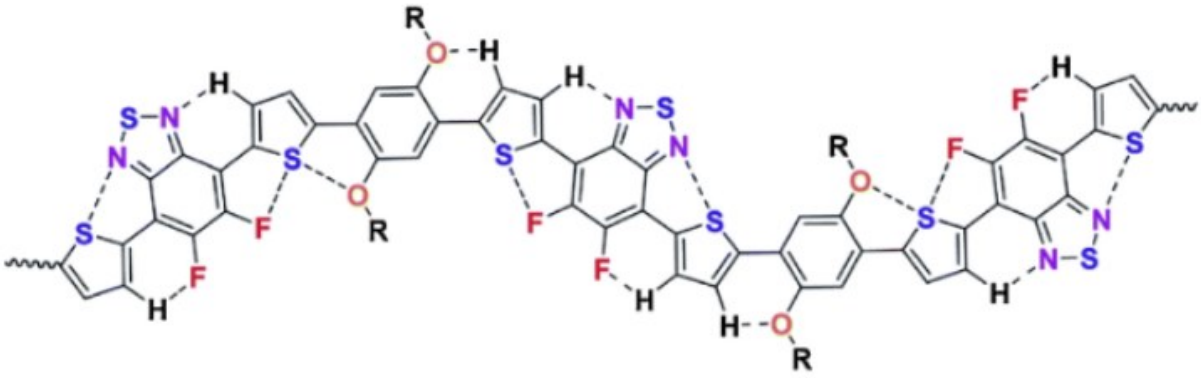


Figure 1.6: *Intramolecular interactions in* ***PPDT2FBT****. Reproduced from reference with permission from the Royal Society of Chemistry.*[45]

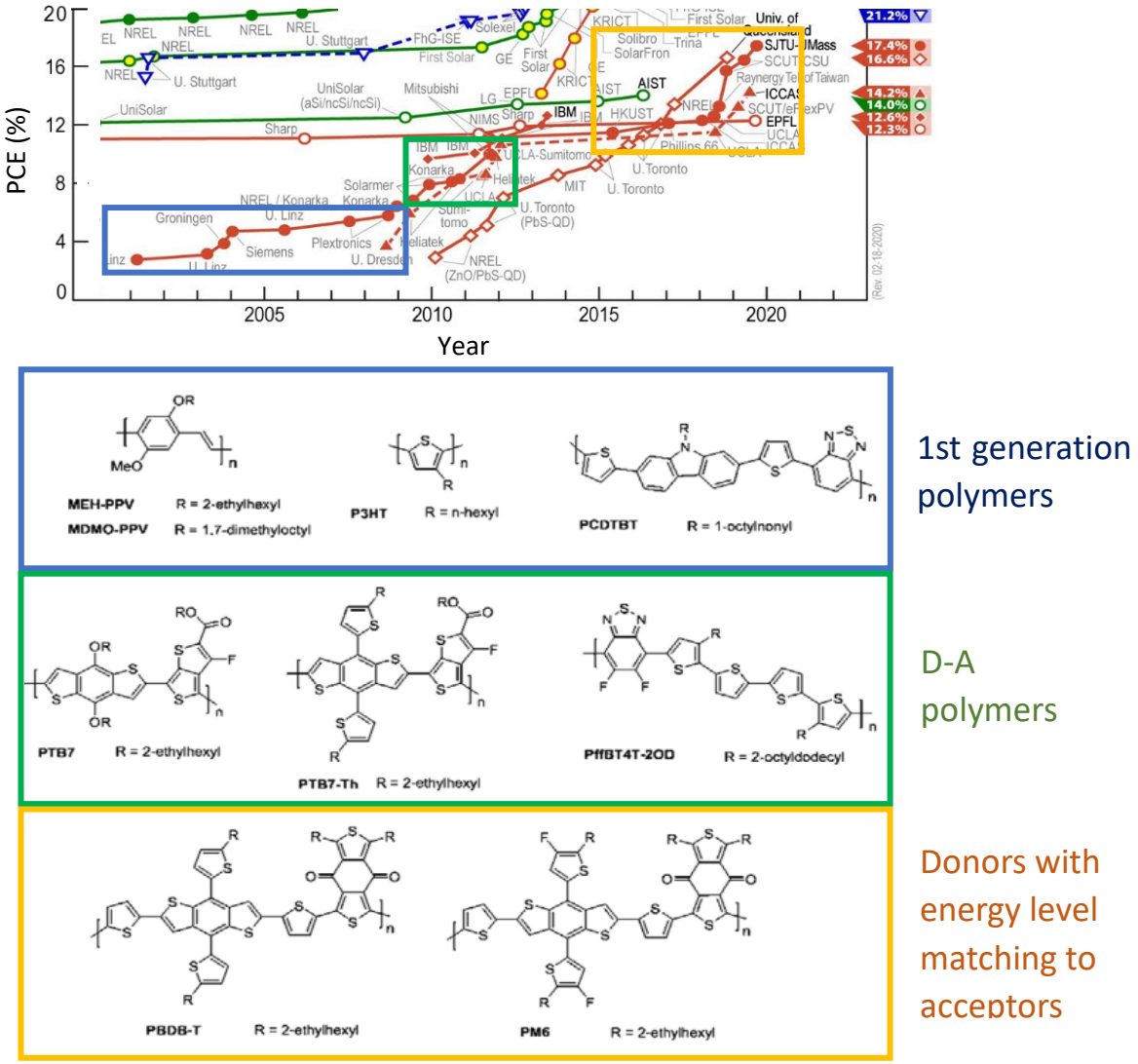


Figure 1.7: *Segment of the 2020 NREL "Best Research-Cell Efficiency" chart with the growth in OPV PCE depicted by filled red circles and developments in donor polymers shown. Polymer types and example polymers contributing to PCE growth during various time periods are depicted below the chart.*[47,48]

In recent years polymer development has focused on energy level matching to new acceptor types, producing polymers such as **PBDB-T** and **PM6**.[47,49] These novel polymers have supplemented new acceptor materials that have driven growth in OPV PCEs since 2015 (**Figure 1.7**).

1.6 - Fullerene Acceptor Structure

Fullerene acceptors have been successful because: they have a LUMO delocalised across the fullerene core allowing for isotropic charge transport, many reversible reduced states that increase stability, good orbital overlap and therefore high electron mobilities through their fused ring systems, and appropriate aggregation for use in BHJs. These acceptors are made up of a fullerene core substituted with a solubilising group to allow processing from organic solvent and to improve morphology in the BHJ (**Figure 1.8**).

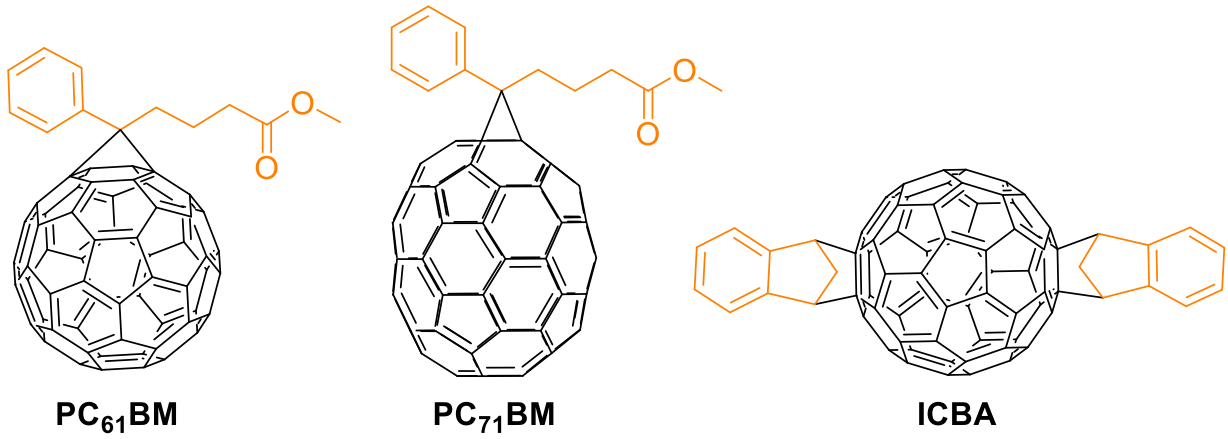


Figure 1.8: *Fullerene derivative acceptor materials, solubilising group in orange.*

Through these favourable properties, fullerene OPV cells have achieved impressive PCEs of over 10%.[50] However, fullerene acceptors suffer from a series of weaknesses. Fullerene acceptors have rigid symmetrical structures that result in forbidden optical transitions and limit their absorption of light in the visible and infra-red (IR) regions. This limited absorption requires the donor polymer to function as the primary site of photon absorption, limiting donor polymer choice and overall light absorption. The broken symmetry in the C_{70} core of **$PC_{71}BM$** helps to alleviate this issue relative to **$PC_{61}BM$**.[51] However, this improvement is limited due to the poor synthetic tenability of fullerenes and **$PC_{71}BM$** still has much lower intensity absorption than donor polymers. The addition reactions used to attach solubilising groups to fullerenes further limit synthetic flexibility as they disallow conjugation between the solubilising group and the fullerene, restricting modification of optoelectronic properties to weak induction effects.[52] The V_{OC} of fullerene cells is limited by the deep electron affinities of fullerene acceptors. The use of two indene solubilising groups on the C_{60}

acceptor **ICBA** improves V_{OC} by raising its LUMO by 0.17 eV relative to **$PC_{61}BM$**.[53] However, this core especially suffers from another limitation of fullerene cells, their expensive syntheses.[54] Finally, fullerene acceptors introduce stability problems to OPV devices as they are known to diffuse through the BHJ under device operation and thus cause excessive aggregation.[55]

1.7 - Early Non-Fullerene Acceptors

The restrictive structures of fullerene acceptors have caused most OPV research to originally focus on improvements to the donor polymer.[40] More recently non-fullerene acceptors (NFAs) have been developed to overcome the limitations of fullerene acceptors.[54,56–58] A number of design strategies have been used for NFAs, two are shown in **Figure 1.9**.

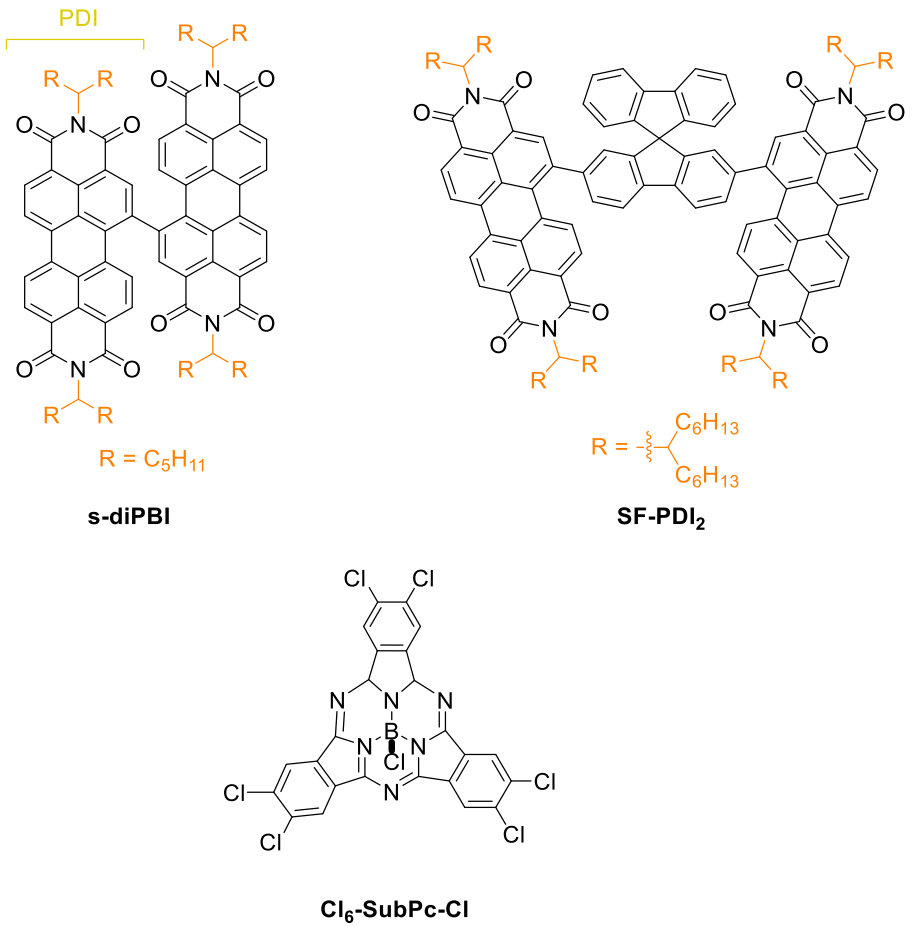


Figure 1.9: *Structures of perylene diimide (PDI) acceptors* ***s-diPBI*** *and* ***SF-PDI_2*** *including a label depicting the PDI monomer, and the structure of rotationally symmetrical acceptor* ***Cl_6-SubPc-Cl****. Solubilising groups in orange.* [54,59–61]

Acceptors made from derivatives of the PDI monomer were some of the earliest to show success. The planar large fused-ring conjugated systems used in these acceptors have good orbital overlap throughout the molecule and therefore give high electron mobilities. Moreover, the electron poor PDI unit gave these acceptors energy levels complimentary to donor polymers. The high crystallinity afforded due to the high π-π stacking between these fused ring systems is both a blessing and a curse for PDI acceptors. The crystallinity yielded high electron mobilities, however it also interfered with the morphology of the BHJ in devices and caused excessively large domains of acceptor that introduced trap states. Therefore, common design strategies for PDI acceptors are oligomerisation, introduction of spacers, or modification of solubilising groups. These are used to limit PDI acceptor's packing but still ensure high charge mobility. To this end acceptors such as **s-diPBI** and **SF-PDI$_2$** have been produced, with **SF-PDI$_2$** performing at an impressive PCE of 9.5%.[54,59,60] NFAs using rotationally symmetric molecules derived from the structure of fullerenes such as **Cl$_6$-SubPc-Cl** have also seen success. These attempt to leverage the beneficial qualities of fullerenes whilst allowing for more synthetic tuneability. However, they have performed worse than fullerene acceptors, with high-performing examples like **Cl$_6$-SubPc-Cl** reporting PCEs of 6.86%.[61]

1.8 - A-D-A Non-Fullerene Acceptors

Currently the most successful NFA structure is the acceptor-donor-acceptor structure (A-D-A) (**Figure 1.10**). This mimics the push-pull hybridisation in successful donor polymers, giving reduced bandgap and better matching to solar radiance. These small molecules can be assembled from pre-made monomers, simplifying syntheses and lowering costs. Common electron donating groups include carbazole, fluorene, indaceno[1,2-b:5,6-b']dithiophene (**IDT**), indacenodithieno[3,2-b]thiophene (**IDTT**), and thiophene; these are depicted in **Figure 1.10**.[58] Electron accepting groups include dicyanovinylindanone (**DCI**) and rhodanine derivatives, diketopyrrolopyrrole (**DPP**), benzo[c][1,2,5]thiadiazole (**BT**) derivatives, and the malonitrile group. The modular nature of the NFAs means that the frontier orbitals on each component can be tuned allowing for fine control of HOMO-LUMO energy levels. Further control of energy levels is enabled by use of either electron donating spacers such as thiophene, or electron accepting spacers like **BT** or **DPP**. The thiophene

spacer is particularly common due to its low cost and propensity to block phenyl-phenyl linkages that introduce backbone twisting to avoid steric clash between their ortho hydrogens. As with earlier NFAs and donor polymers, solubilising chain optimisation can also improve morphology.

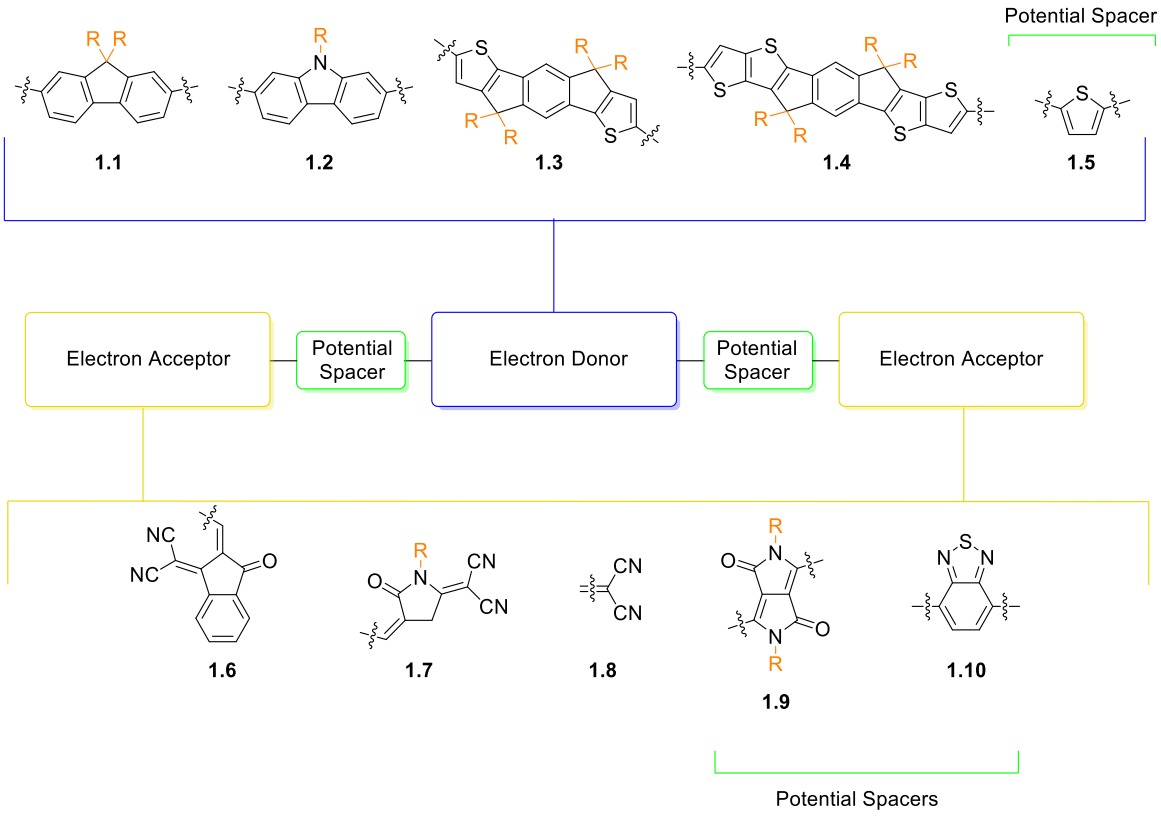


Figure 1.10: *General structure of an A-D-A type acceptor with example structures of electron accepting and electron donating components and potential spacers labelled, solubilising chains are shown in orange. Standard structures for derivatives of fluorene* ***(1.1)****, carbazole* ***(1.2)****,* ***IDT (1.3)****,* ***IDTT (1.4)****, thiophene* ***(1.5)****,* ***DCI (1.6),*** *rhodanine* ***(1.7)****,* ***DPP (1.8)****,* ***BT (1.9)****, and the malonitrile unit* ***(1.10)****.*

Flu-RH was one of the first A-D-A acceptors and made use of a fluorene core, thiophene spacers, and rhodanine-based electron acceptor groups (**Figure 1.11**). Blends of this acceptor with **P3HT** yielded devices with 3.08% PCE due to their impressive V_{OC} of 1.03 V.[62] The high V_{OC} of **Flu-RH** can be attributed to the electron rich fluorene and thiophene units raising its LUMO. Low J_{SC} was the greatest issue with PCE and was likely lowered by the high spectral overlap between **Flu-RH** and **P3HT** narrowing EQE, this was caused by the similar bandgap of **Flu-RH** (2.05 eV) to that of P3HT (2.10 eV). Modification of the spacer groups

from thiophene to **BT** produced the acceptor **FBR**.[63] Devices containing **FBR** and **P3HT** had high PCEs of 4.11%, however this improvement from **Flu-RH** may be partially due to the use of a more favourable inverted stack architecture as opposed to a standard stack. The approximately 35° phenyl-phenyl twist in **FBR** calculated from density functional theory (DFT) calculations raised its bandgap to 2.14 eV, overshadowing potential bandgap reduction due to greater electron acceptance at the flanks of the molecule. This bandgap was again very similar to that of **P3HT** and therefore the devices suffered from low overall spectral coverage and had a low optimised J_{SC} of 7.95 mA/cm^2. Backbone twisting additionally limited the crystallinity of **FBR** and caused it to mix too thoroughly with **P3HT**, increasing non-geminate recombination losses and lowering **FF**. When devices were made with **FBR** and the low bandgap polymer **PffBT4T-2DT** a high PCE of 8.00% was obtained.[64] This high PCE can be attributed to the high J_{SC} of 11.7 mA/cm^2 offered by improved spectral overlap between the donor and acceptor and impressive V_{OC} of 1.13 V enabled by the lower HOMO energy level of **PffBT4T-2DT.**

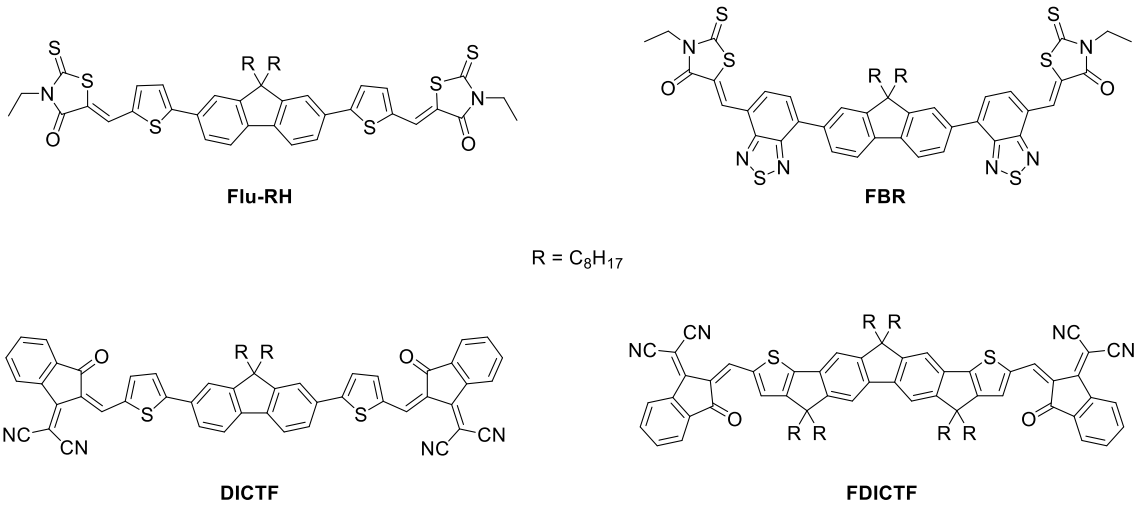


Figure 1.11: *Structures of* ***Flu-RH, FBR, DICTF,*** *and* ***FDICTF*** *A-D-A type NFAs.*[58]

A different modification to **Flu-RH** changed the end group from a rhodanine to **DCI**, forming **DICTF.**[65] This design did not suffer from backbone twisting as in **FBR** and the more strongly electron accepting **DCI** lowered bandgap further. These changes led to a highly impressive J_{SC} of 16.6 mA/cm^2 in devices containing blends of **DICTF** with the complimentary polymer **PTBT-7-Th**. Although V_{OC} was lowered to 0.86 V due to the shallow LUMO of **DICTF**, a good PCE of 7.93% was still obtained. To improve performance further, **FDICTF** was synthesised.[66]

FDICTF was essentially **DICTF** with the thiophene spacers fused onto the central fluorene core. This modification greatly increased the planarity of the NFA, therefore improving orbital overlap, and increasing conjugation. Resultantly, **DFICTF** had a very low band gap of 1.62 eV. Due to good spectral overlap and favourable stacking, when **FDICTF** was matched with the medium-bandgap **PBDB-T** polymer devices with a good J_{SC} of 16.09 mA/cm^2 were produced. Moreover, a high V_{OC} of 0.95 V was achieved due to appropriate energy level matching between donor and acceptor. A high FF of 0.67 was obtained because the increased π- π stacking in **FDICTF** caused it to aggregate more relative to **DICTF** and form clear domains that were missing from **DICTF** active layers. These improvements to optoelectronic properties and morphology through lengthening of the fused ring system gave the devices an impressive PCE of 10.06%, making **FDICTF** one of the first NFAs to yield PCEs higher than 10%.

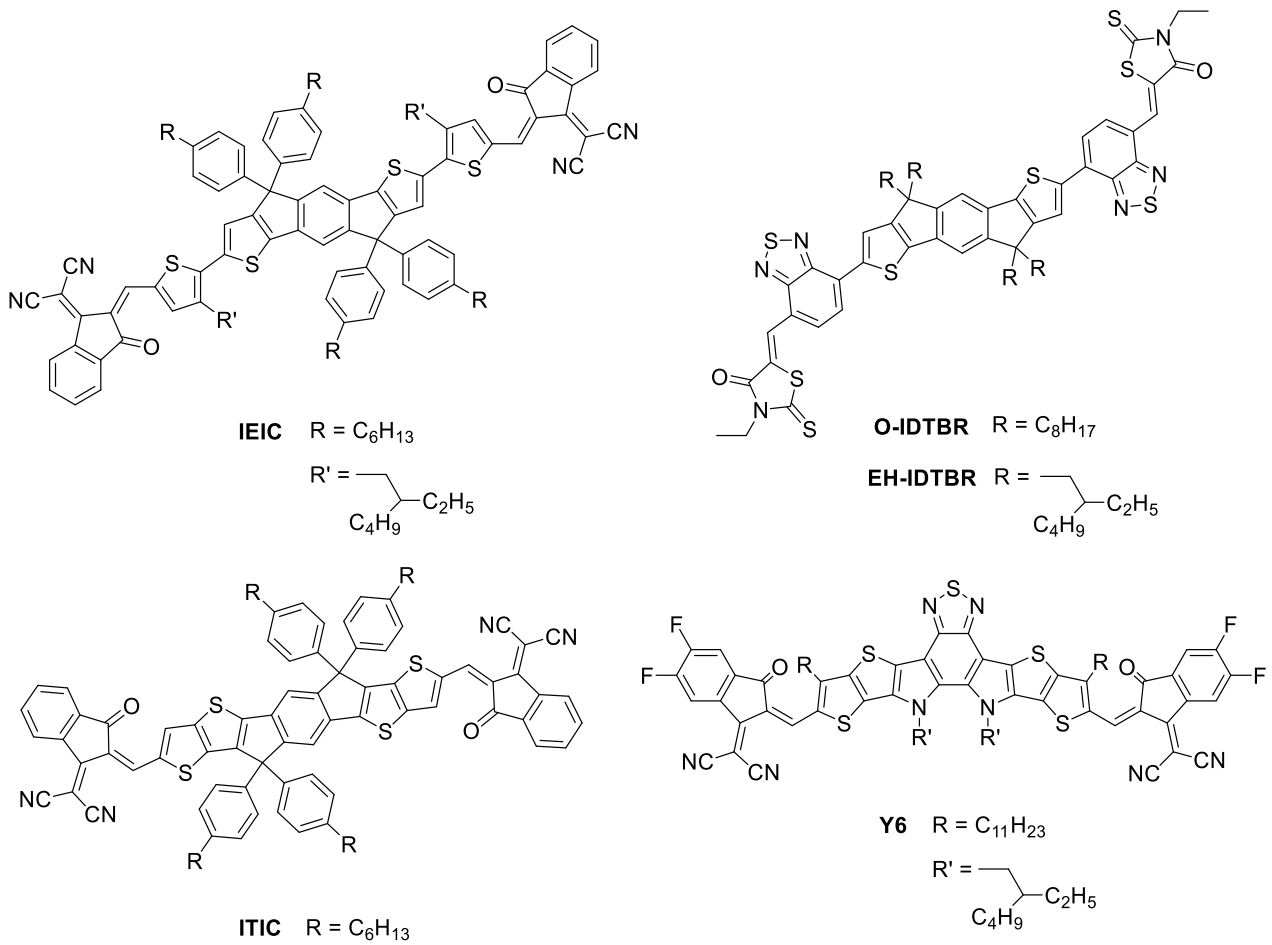


Figure 1.12: *Structures of* ***IEIC***, ***IDTBR***, *and* ***ITIC*** *A-D-A type NFAs.*[67–69]

The **IDT** core was used as an improvement on the fluorene core due to its packing characteristics and ability to form lower bandgap acceptors because of its more electron donating nature. **IEIC** can be seen as **DICTF** with the fluorene core replaced with **IDT** and solubilising chains modified, including the addition of alkyl chains onto the thiophene spacers (**Figure 1.12**). Notably, the optical bandgap of **IEIC** is 1.57 eV compared to 1.82 eV for **DICTF** due to the more electron rich **IDT** deepening the localised LUMO more than the HUMO.[67] **IEIC** performed at a PCE of 6.31% with the **PTB7-Th** polymer, lower than **DICTF** in the same device make-up. This reduction is mostly due to a greater spectral overlap between **IEIC** and **PTB7** causing a loss in J_{SC} (16.61 and 13.55 mA/cm^2 for **DICTF** and **IEIC** respectively). The **IEIC** devices also suffered from a loss in FF because of active layers having hole mobilities 4.5 times greater than electron mobilities and overlarge acceptor domains of 30 nm encouraging non-geminate recombination. The performance of **IEIC** devices was improved to 7.30% by use of the wider bandgap polymer **PffT2-FTAZ-2DT**, albeit with a change to an inverted architecture that reduces comparability**.** Improved spectral overlap increased J_{SC} for these devices. Furthermore, an improvement to FF was observed because the more favourable intermolecular interactions between the polymer and NFA reduced acceptor domains to 20 nm, encouraging more exciton splitting.

The acceptors **O-IDTBR** and **EH-IDTBR** also used the **IDT** core but instead took the structure of **FBR.**[68] Use of **IDT** blocked the twisting phenyl-phenyl interactions observed in **FBR** and therefore planarized the acceptor. This in turn lowered bandgap, increased oscillator strength and therefore extinction coefficient, and counteracted the excessive mixing observed in active layers containing **FBR**. As **P3HT** is cheap to make and is truly scalable, the **IDTBR** acceptor devices were optimised with this polymer resulting in **O-IDTBR** solar cells of impressive 6.38% maximum PCE. While these devices have lower PCE than others in the literature, in practice their use of relatively cheap and scalable materials makes them more suited for real world use. On the other hand, with view to maximise PCE devices of **PffBT4T-2DT:EH-IDTBR** were produced and had 11.09% PCE.[70] The lower HOMO of **PffBT4T** greatly improved the V_{OC} of the devices to 1.02 V. Interestingly, the J_{SC} of **PffBT4T:EH-IDTBR** devices was an impressive 17.20 mA/cm^2 although the NFA and donor polymer had a lot of spectral overlap. This was attributed to a high photon absorption in the 500-700 nm region and good active layer morphology. A major benefit of the **PffBT4T:EH-IDTBR** system is that the BHJ in

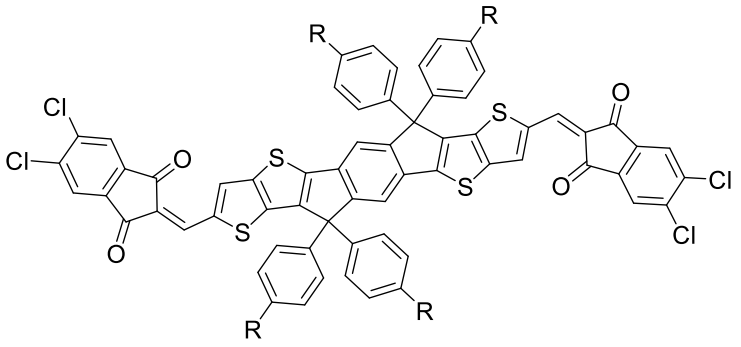
its champion devices is processed from mesitylene solvent rather than the chlorinated solvents used commonly for OPV active layers. It's important to reduce the use of toxic chlorinated solvents for the commercialisation of OPV as many are banned from use in industrial printing due to their hazards.

A third successful structure for **IDT** acceptors is that of **ITIC** (**Figure 1.12**).[69] The relationship between **ITIC** and **IEIC** is akin to that between **FDICTF** and **DICTF**, with a fusing of the thiophene spacers to the central core. Both frontier orbitals were raised in energy for ITIC, causing **ITIC:PTBT7-Th** to have a low V_{OC} of 0.81V. However, FF was improved to 0.59 by superior electron-hole mobility alignment in the blend relative to **IEIC:PTBT7-Th** devices resulting in a PCE of 6.80%. Past these initial measurements, **ITIC** has been often studied in other polymer systems. Notably, in optimised **ITIC:PBQ-4F** devices high PCEs of 11.34% were obtained, highlighting the importance of choosing optimal donor-acceptor combinations.[71] These devices had a high J_{SC} of 17.87 mA/cm^2 due to the high overall spectral coverage of the blend and improved carrier mobility in the planar donor polymer. Additionally, the devices had an impressive FF of 0.67 because both electron and hole mobilities were 1.00 x 10^{-3} cm^2/Vs in the active layer, reducing non-geminate recombination.[71] Similarly to the **PffBT4T:EH-IDTBR** system, **ITIC:PBQ-4F** is best processed from the non-chlorinated solvent tetrahydrofuran (THF) with 5% isopropanol additive making it scalable. Besides **ITIC** itself multiple successful derivatives have been produced based on its structure, these derivatives and their performance will be introduced in Chapter 3 of this thesis.

Whilst not the focus of this thesis, the acceptor **Y6** has been synthesised recently and shown to perform at a very impressive PCE of 18.22% with the **D18** polymer.[72,73] Other derivatives of the acceptor have shown exceptional performance as well.[74] The high performance of devices containing these acceptors is largely due to a high J_{SC} and low voltage loss. Unlike the A-D-A structure taken in **ITIC** derivative NFAs **Y6** derivatives contain an electron accepting unit fused within their core (A') and take the structure A-D-A'-D-A. This allows a smaller bandgap of 1.2 – 1.4 eV and improves J_{SC} by harvesting more of the solar spectrum. Moreover, the **Y6** structure is curved rather than linear increasing dipole moment.[75] Studies have suggested that large dipole moments aid charge separation in donor:acceptor blends. Investigations into the high performance of **Y6** derivatives are ongoing and have also included explanations based on their improved packing characteristics.[76,77]

1.9 - Wide Bandgap NFAs

Although the above examples of NFAs all focused on lowering bandgap to improve performance, this isn't the only design strategy used for NFAs. Lower bandgaps tend to improve the performance of OPV devices because more of the infra-red spectrum can be harvested, it's easier to align the energy levels of the donor and acceptor and therefore minimise energy loss during exciton splitting, and because the structures that lead to reduced bandgaps commonly increase crystallinity and therefore charge transport.[78] However, as OPV devices themselves are more suited for niche applications that make use of their transparency or flexibility than higher PCE silicon devices, wider bandgap NFAs have their own set of niche applications that they are more suited for than narrow bandgap NFAs. Namely, wide bandgap NFAs are suited for indoor applications, tandem solar cells, and tertiary cells.



IO-4Cl R = C_6H_{13}

Figure 1.13: *Structure of the wide bandgap NFA* ***IO-4Cl****.*[79]

With the advent of the Internet of Things, indoor spaces have been filled with smart devices that communicate with each other and each require their own power source.[80] These devices have applications for consumers such as in smart homes, but are in fact finding use in all sectors of society. OPV cells are highly suitable to power these off-grid devices due to their potential for alignment with the indoor light spectrum. In outdoor settings, at a solar illumination of AM 1.5 (standard light illumination used to test OPV devices) single material cells with a bandgap of 1.3 – 1.4 eV have the highest potential PCE based on the Shockley-Queisser limit.[81] However, most indoor lights are either light emitting diodes (LEDs) or fluorescent lamps (FLs) and have blue shifted spectra relative to outdoor light. As

such wider bandgap materials with bandgaps of 1.8 – 2.0 eV are optimal to maximise PCE.[82] Unfortunately there has been a shortage of suitable acceptors at these wavelengths, and as such wider bandgap NFAs must be developed to complement further research into indoor OPV.[83] **ITIC** has been the most studied NFA design for indoor light applications, with optimised **CD1**:**ITIC** devices themselves giving high indoor light PCE of 17.9%.[83] One of the highest performing **ITIC** derivatives for indoor applications is **IO-4Cl** (**Figure 1.13**).[79] Through use of more electron rich accepting groups, **IO-4Cl** has a wide bandgap of 1.80 eV that's blueshifted 90 nm relative to **ITIC**. The resulting alignment to the spectrum of LED light has given **PBDB-TF:IO-4Cl** devices a very impressive PCE of 26.1 % under indoor conditions.

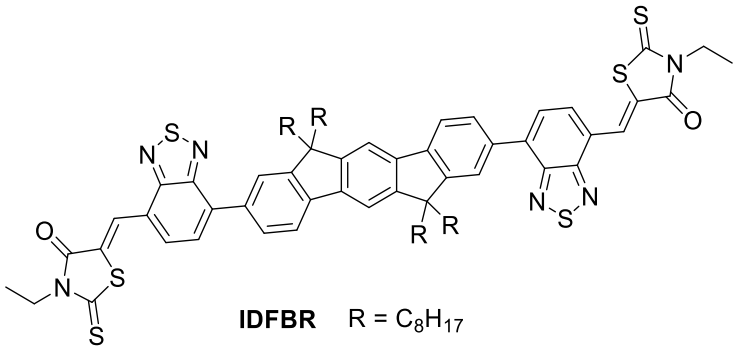


Figure 1.14: *Structure of the wide bandgap NFA* ***IDFBR****.*[84]

A further use of wide bandgap NFAs is in either tandem or ternary cells. Tandem cells stack two OPV cells on top of each other (with only one set of electrodes) whilst ternary cells use three components in the active later, with either two donor polymers or two acceptors.[85–87] Both architectures increase PCE by use of an improved energetic cascade to lower recombination losses and benefit from an increased spectral coverage through use of extra absorbing components. As most research into NFAs has been on lowering bandgaps, there is a shortage of wider bandgap NFAs in the literature for use in widening the absorption of tandem or ternary devices. A successful example system that uses a wide bandgap NFA to complement the absorption of a low bandgap NFA is the ternary **P3HT:O-IDTBR:IDFBR** system.[84] The novel NFA **IDFBR** is twisted due to phenyl-phenyl links and is therefore a wider bandgap analogue of the aforementioned **O-IDTBR** (**Figures 1.12** and **1.14**). **IDFBR** has a bandgap of 2.05 eV compared to 1.55 eV for **O-IDTBR**. Besides a slight improvement in J_{SC} of 0.5 mA/cm^2 over **P3HT:O-IDTBR** devices due to improved absorption, the ternary devices had a 0.1V improvement in V_{OC} due to the higher lying LUMO of IDFBR and a small 0.04 FF

improvement because of the superior energy cascade. These improvements gave **P3HT:O-IDTBR:IDFBR** and **P3HT:O-IDTBR** devices PCEs of 6.3% and 7.3% respectively, record breaking for single junction **P3HT** devices. In addition, the ternary device had very impressive photo-stability to light in air. After 90 hours of illumination, the **P3HT:O-IDTBR:IDFBR** retained 85% of its original PCE, in comparison **P3HT:O-IDTBR** retained 70% and **P3HT:PC_{71}BM** devices stopped producing power after only 50 hours. This high stability together with the scalability of **P3HT** make devices with **O-IDTBR** suitable for practical use. To achieve maximum PCE McCulloch *et al* also made ternary devices of **PCE10:O-IDTBR:IDFBR** with higher performing polymer, yielding 11.0% PCE.

1.10 - OFET Device Theory

Besides in OPV, organic semiconductors find use in organic field effect transistors (OFET). Transistors are found throughout the world of electronics and are most used as simple switches that store information. As for solar cells, currently the most common transistor semiconductor material is amorphous silicon. However, due to their potential for low cost and large area processing organic semiconductors are increasingly used.[88]

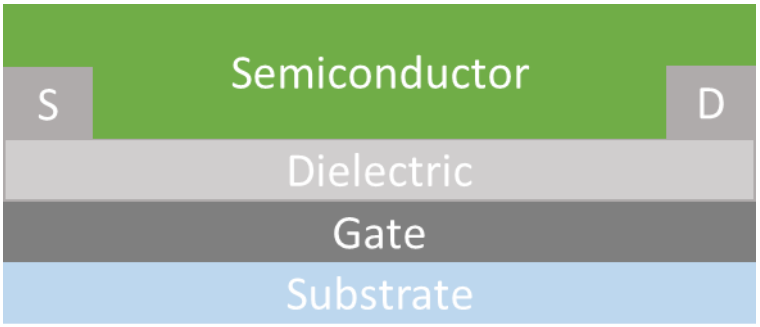


Figure 1.15: *General OFET structure. S and D are source and drain electrodes respectively.*

An OFET device can have multiple architectures but always consists of a semiconductor, an insulating dielectric, a gate electrode, source and drain electrodes, and a substrate (**Figure 1.15**). In the off position, when no bias is applied at the gate, no current flows through the semiconductor between the source and drain electrodes. However, if a positive bias is applied at the gate an electric field induced through the dielectric will cause electrons to accumulate at the semiconductor - dielectric boundary. Once a positive potential difference is applied between the source and drain electrodes, the build-up of charge allows current to

pass between them turning the transistor on. Once the bias at the gate or source-drain electrodes is stopped, the transistor will return to the off position and no more current will pass between the source and drain electrodes. The aforementioned mode of operation pertains to OFET devices fabricated with an n-type semiconductor. Conversely if a p-type semiconductor is used and negative bias is applied at the gate, and source and drain electrodes, an accumulation of holes rather than electrons at the dielectric-semiconductor interface will turn the transistor on.

Three main parameters are considered in the performance of an OFET device, the semiconductor's charge carrier mobility, the threshold gate voltage necessary to induce mobile charges (V_T), and the on/off ratio of the device. As for OPV devices, a graphical representation of the devices' performance is used to find the necessary performance values. Output curves plot drain bias (V_D) against the source/drain current (I_{DS}) (**Figure 1.16**), whilst transfer curves plot the gate bias (V_G) against I_{DS} (**Figure 1.17**).

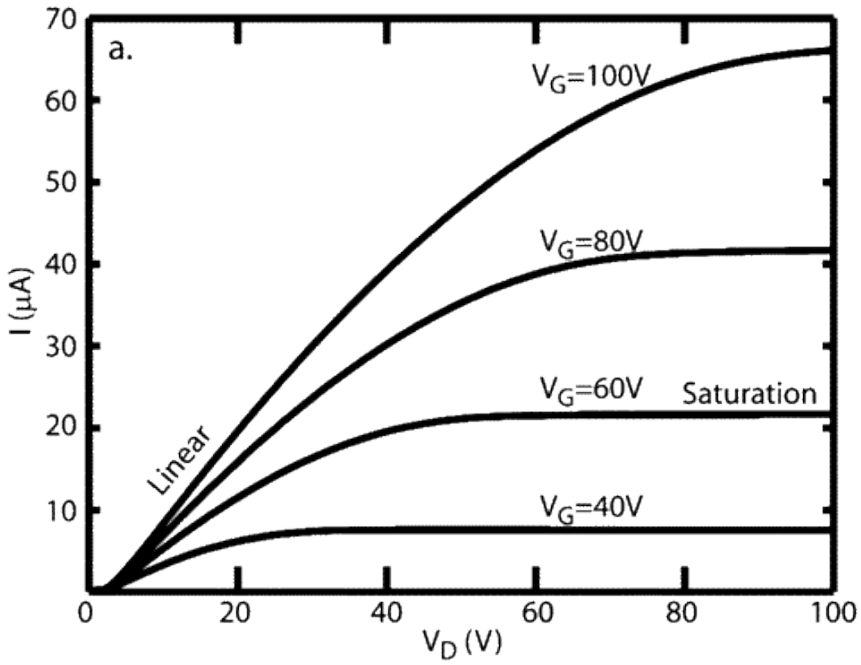


Figure 1.16: *Example OFET output curve for an n-type semiconductor. Reprinted (adapted) with permission from reference.*[89] *Copyright 2004 American Chemical Society.*

As can be seen from **Figure 1.16**, at $V_D << V_G$ the device performs in the linear regime where current simply increases with voltage according to Ohm's Law. However, at $V_D \geq V_G - V_T$ current levels off as the maximum (saturation) current is reached. The output curve can be used to find where the linear and saturation regimes begin.

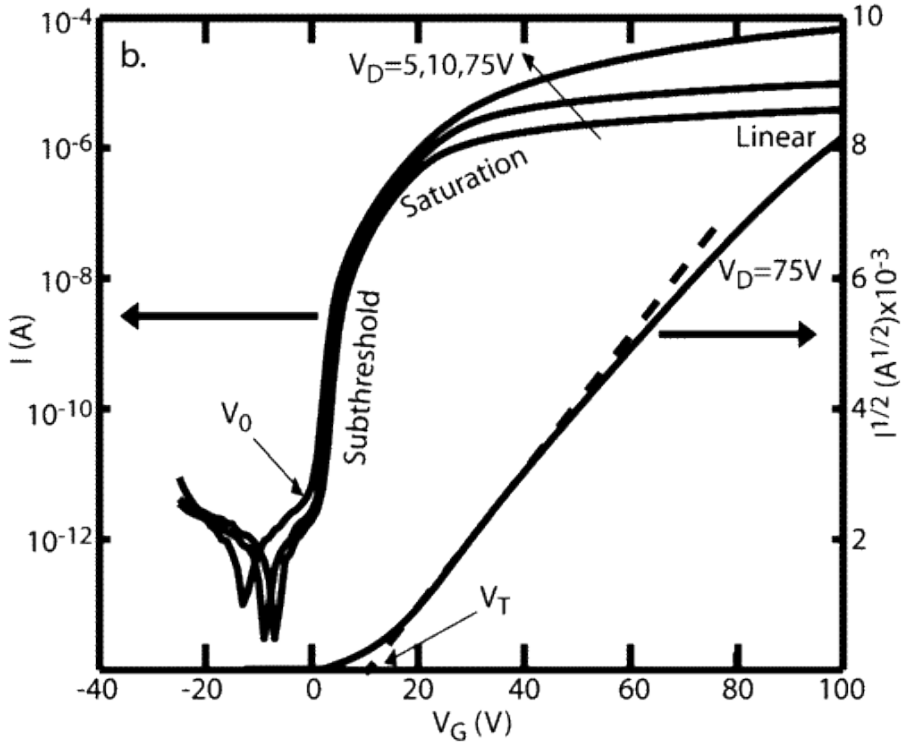


Figure 1.17: *Example OFET transfer curve for an n-type semiconductor at multiple V_D. Reprinted (adapted) with permission from reference.*[89] *Copyright 2004 American Chemical Society.*

In **Figure 1.17**, the transfer curve shows us the subthreshold regime wherein the device is turning from the OFF mode to the ON mode as sufficient current begins to pass between the drain and source electrodes. The saturation and linear regimes are shown as in the output curve. To find V_T a graph of $I^{1/2}$ against V_G can be plotted on the transfer curve, if a straight line from the gradient is drawn in the saturation region and extrapolated to I_{DS} = 0 (as in **Figure 1.17**), V_T will be given by the point of intersection with the V_G axis. To find the linear mobility (μ_{lin}), the derivative of the transfer curve in the linear mode and Equation 1.4 can be used.

$$\mu_{lin} = \frac{L}{W C_G V_D} \frac{\partial I_{DS}}{\partial V_G}$$

Equation 1.4: *Equation for the linear mobility of an OFET device, derivation available in reference.*[90]

To find saturated mobility (μ_{sat}) on the other hand, **Equation 1.5** and the derivative of $I^{1/2}$ vs V_G in the saturated mode can be used.

$$\mu_{sat} = \frac{2L}{WC_G} \frac{\partial \sqrt{I_{DS}}}{\partial V_G}$$

Equation 1.5: *Equation for the saturated mobility of an OFET device, derivation available in reference.*[90]

The on/off ratio of a transistor can be found from the ratio of the saturation current (I_{ON}) to current at $V_G = 0$ (I_{OFF}). When looking for the point of current saturation it must be noted that I_{DS} commonly continues to increase beyond the saturation current in the saturated region. This can be attributed to energetic/conformational disorder causing deep-lying trap states to be filled at high voltages.[88] To maximise the on/off ratio I_{OFF} can be increased by limiting current leakage whilst I_{ON} can be increased by improving the mobility of the semiconductor.

1.11 - OFET Semiconductor Selection

The selection of a semiconductor for OFET applications can be seen as simplified in relation to OPV devices. Unlike in OPV devices, the light harvesting properties of an OFET semiconductor are not considered as charge is injected into the device. Moreover, since only one semiconductor is commonly required the morphological considerations within the OFET device are greatly reduced. The main consideration towards improving the performance of an OFET semiconductor is maximising its charge mobility. This mobility relates to the structure that the semiconductor takes at the dielectric-semiconductor interface where charge transport occurs, rather than in the bulk as in OPV. As in OPV the HOMO-LUMO energy levels of the semiconductor must be appropriate for the used electrodes to limit contact resistance and improve charge injection.

The most common semiconductors for OFET are p-type small molecules and polymers due to their improved operational and environmental stability over n-type species. These materials have shallow HOMO energy levels for hole transport. The focus of this thesis is specifically on p-type polymers. The same considerations for improving charge carrier mobility are applied in OFET as in OPV, with more rigid crystalline molecules being favoured. Early successful OFET polymers include **P3HT** and poly(3,3'-dialkylquaterthiophene) (**PQT**). These were both simple homopolymers that take on semicrystalline lamellar

microstructures with edge-on polymer orientation.[91,92] Alternating layers of conjugated backbones are formed in these polymers along the plain of the device that are separated by flexible insulating side chains, yielding high conductivity between the source and drain electrodes. An example of a particularly highly performing homopolymer that takes on this morphology is poly(2,5-bis(3-alkylthiophen-2-yl)thieno(3,2-b)thiophene) (**PBTTT**), that has given OFET devices with an impressive 1 cm^2/Vs.[93]

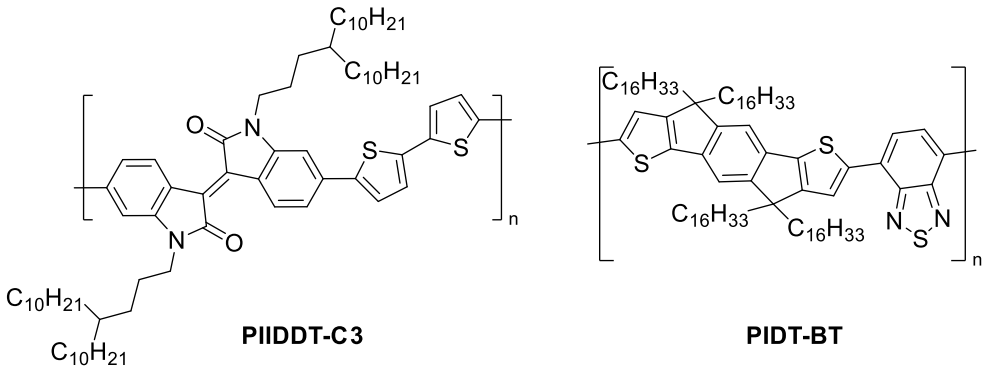


Figure 1.18: *Structures of the* ***PIIDDT-C3*** *and* ***PIDT-BT*** *p-type OFET polymers.*[94,95]

The D-A polymers used as donor polymers in OPV have also seen use as OFET p-type polymers. Whilst lowering bandgap doesn't necessarily directly improve charge carrier mobility in polymers, it can make choosing appropriate contacts for charge injection easier. Moreover, it is theorised that intermolecular interactions between stacked donor and acceptor units can help reduce π-π stacking distance in certain systems, improving charge transport.[88] Two examples of high-mobility D-A polymers are the isoindigo-based **PIIDDT-C3** and **IDT** containing **PIDT-BT**, these polymers both have high optimised hole mobilities of 3.6 cm^2/VS in OFET devices (**Figure 1.18**).[94,95] Peculiarly, these polymers have less long-range order than earlier homopolymers and don't necessarily take on an edge-on lamellar orientation but still perform well with high charge carrier mobilities. The investigation of the cause of high mobilities in D-A copolymers is ongoing, but a series of favourable properties can be inferred. These favourable properties include a coplanar backbone conformation with minimum backbone torsion that improves intramolecular charge transport, potentially reduced π–π stacking through intermolecular interactions between donor and acceptor groups, high in plane alignment that allows increased molecular weight to improve hole mobilities while avoiding polymer chain entanglement, and an edge-on or face-on orientation on the dielectric.[88,96]

1.12 - Coating Methods

Whilst a plethora of coating methods are now available for coating organic semiconductors from solution, the most commonly used methods in research labs are spin coating and blade coating.[97–99] Whilst it can be difficult to predict which coating method produces optimal morphology for a system, there are general considerations for choosing an appropriate coating method.[97]

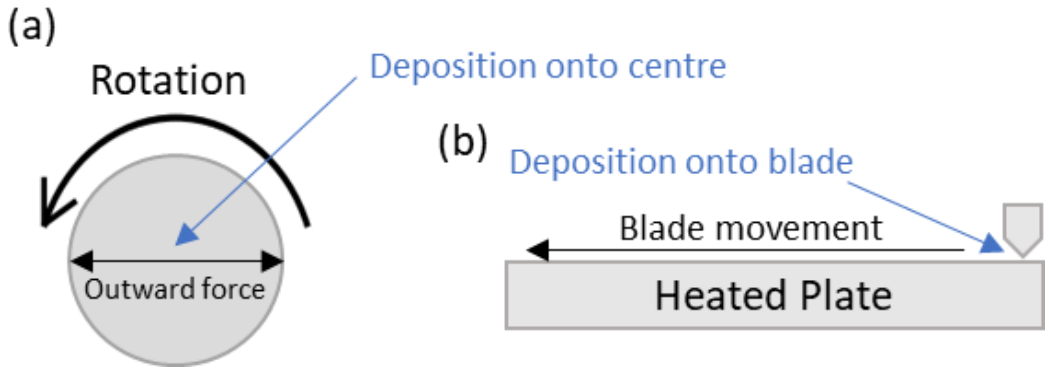


Figure 1.19: *Mode of operation for (a) spin-coating, (b) blade-coating.*

Spin-coating is arguably the simpler method of coating of the two. Solution is simply deposited onto the centre of a substrate on a rotating disk, and an outward centrifugal force pulls the solution across the substrate as it deposits material because of fluid spin-off and evaporation (**Figure 1.19 (a)**).[100] Besides formulation make-up, only four parameters are typically controlled for spin coating: spin speed, volume of solution, and temperature of solution upon deposition. Therefore, it's easier to optimise spin coating conditions as often the spin-speed is simply tuned to control layer thickness. Additionally, films coated by spin-coating become progressively more uniform as the spinning continues and remain thus for the remainder of the process. Together with the cheap cost of spin-coaters and the rapid nature of the coatings, spin-coating is currently the most common method of coating in lab. Unfortunately spin-coating suffers from two significant problems that affect its scalability to real world applications. Namely, spin coating requires great amounts of material and only around 2-5% of material is coated into a thin film whilst the rest is ejected from the substrate.[100] Moreover, large substrates can't be spun at a sufficient speed for thin film deposition.

Blade-coating on the other hand is compatible to a roll-to-roll fabrication wherein a continuous flow of substrate can be coated and is used by research groups focusing on device scalability. The standard process of blade coating in a lab environment involves deposition of a formulation onto a doctor blade, which then rapidly moves across a substrate placed on a heated plate, depositing a thin film (**Figure 1.19 (b)**). The absence of centrifugal force results in a formation of different morphologies than by spin-coating. This is beneficial as the morphologies formed are more comparable to those that would be produced by large scale roll-to-roll processes such as gravure printing and slot-die coating, giving an indication of how formulations would behave with these processes.[101,102] Additional benefits of blade-coating are that it produces relatively uniform films and uses much less material than spin coating. A weakness of blade-coating is the many variables that must be controlled to ensure a good coating. Namely, formulation temperature, formulation volume, surface temperature, blade speed, and blade height (or screw gap).

Chapter 2 - Synthesis of IDT Derivative Cores for Organic Electronics

2.1 – Introduction

2.1.1 – Development of the IDT core

The popular fused-ring heterocycle core **IDT** was first synthesised in 2006 with alkylated phenyl sidechains (**phenyl-IDT)** at the bridgehead carbons (**Figure 2.1**).[103] The core has favourable properties and is often used in organic electronics: it's rigid and fused resulting in improved charge conductivity, it's amenable to synthetic modification at the bridging carbons giving control of processability and performance via alkylation, and the core can be extended via the terminal thiophenes allowing further control of optoelectronic properties such as bandgap and charge carrier mobility.

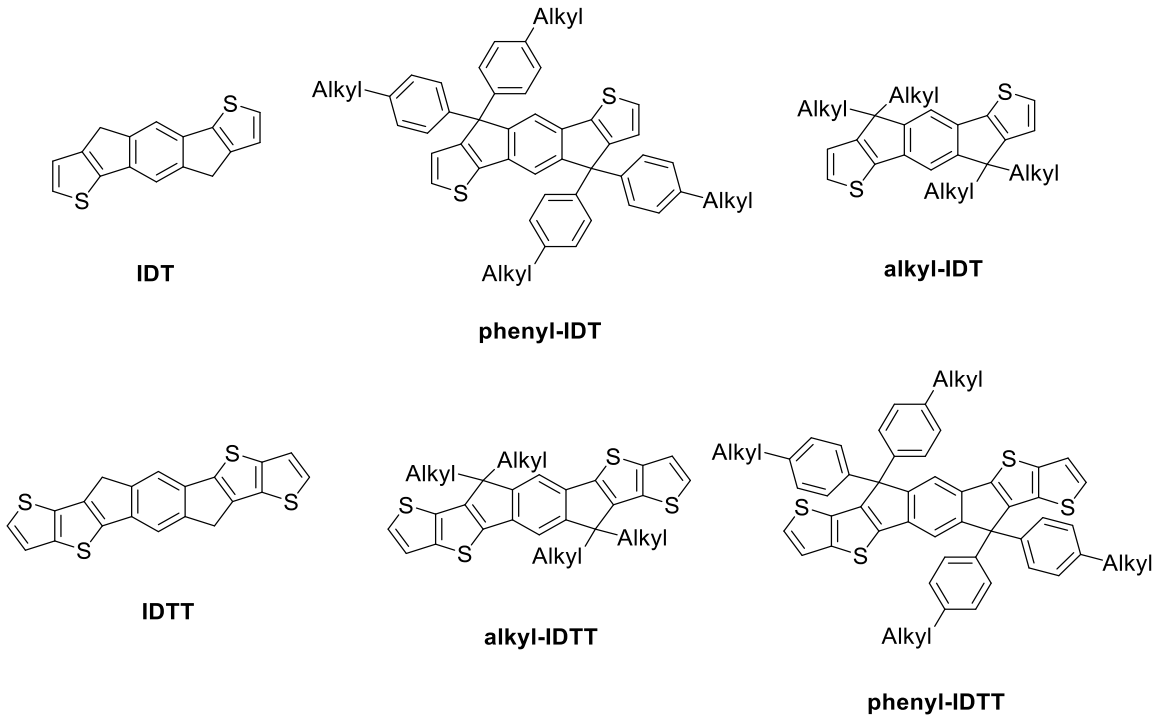
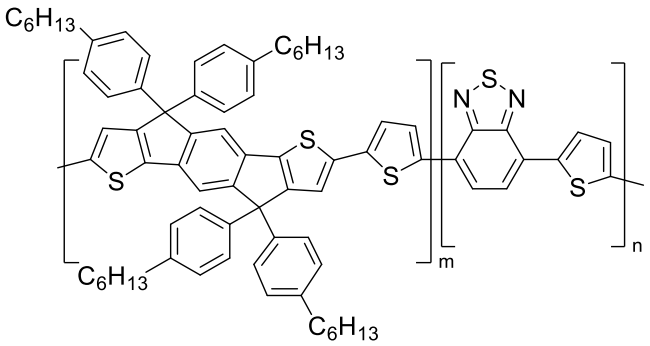
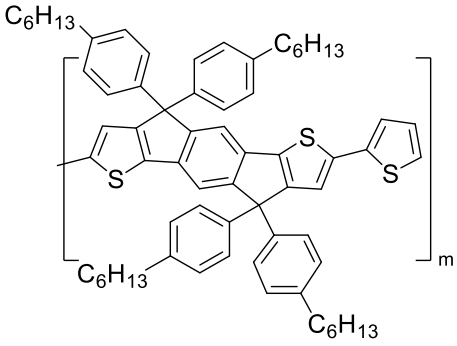


Figure 2.1: *General structures of derivatives of* ***IDT*** *used as building blocks for organic electronics.*

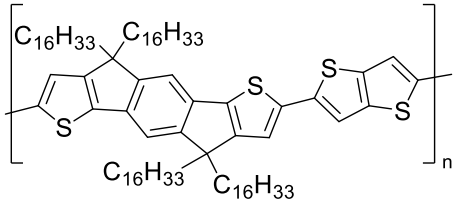
To make use of its aforementioned beneficial properties, **IDT** was first used in organic electronic devices as the **phenyl-IDT** monomer within donor-polymers for OPV.[104,105] The polymers were produced by Ko *et al* with either a solely donor structure or using a donor-acceptor structure wherein **IDT** was the electron donating component and **BT** electron accepting (**Figure 1.9** and **Figure 2.2**). The electron rich nature of **IDT** made it suitable for use in donor-acceptor polymers and **2.1** performed at a PCE of 4.3% with **$PC_{71}BM$** whilst the leading polymer made of solely electron donating components **2.2** performed at a PCE of 3.3%, largely due to its wider bandgap and less complimentary absorption spectrum to $PC_{71}BM$. The **BT** unit used has additionally been noted to reduce energetic disorder by stiffening polymer backbones and promoting close π-π stacking, therefore improving molecular ordering and yielding higher charge carrier mobilities.[106]



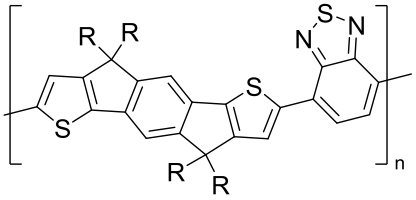
2.1



2.2

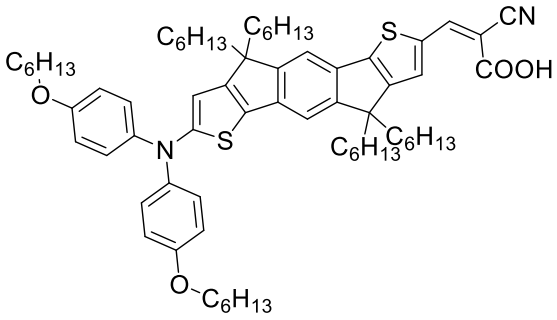


PIDT-TT



PIDT-BT, R = Hexadecyl

EH-PIDT-BT , R = 2-Ethylhexyl



LC-5

Figure 2.2: *Example* ***IDT*** *derivatives used in plastic electronics:* ***2.1*** *and* ***2.2*** *are early donor polymers for OPV,* ***PIDT-TT*** *is a p-type polymer for OFET,* ***PIDT-BT*** *is a p-type polymer for OFET and a donor polymer for OPV,* ***LC-5*** *is a sensitiser for dye-sensitised solar cells*.[105,107,108]

After some synthetic modification, the alkylated side chain form of **IDT (alkyl-IDT)** was produced and used in donor polymers for OPV as well as polymers for OFET.[108,109] This modification gave the polymers one of the highest charge carrier mobilities at the time as alkyl chains have less steric bulk and allow closer packing of polymer strands. The use of the **BT** unit further improved charge carrier mobility, this is highlighted by **PIDT-BT** transistors having a semi-crystalline polymer structure and a hole mobility of 1.00 ± 0.25 cm^2/Vs as

opposed to **PIDT-TT** transistors that had amorphous active layers and hole mobilities of only 0.15 ± 0.02 cm^2/Vs.[110] Any phenyl-phenyl links that could introduce twisting and lower hole mobility in **PIDT-BT** were blocked by the terminal thiophenes on **IDT**. **PIDT-BT** was more crystalline and gave higher charge carrier mobility than branched alkyl chain **EH-PIDT-BT** in transistors. However, **EH-PIDT-BT** cells with **$PC_{71}BM$** performed at a highest average PCE of 4.46% as opposed to only 0.66% PCE for **PIDT-BT**, demonstrating the increased morphological considerations required for OPV devices. Both the alkyl and phenyl forms of **IDT** have also been used in dye sensitised solar cell applications, highlighting its suitability for use throughout organic electronics.[107,111]

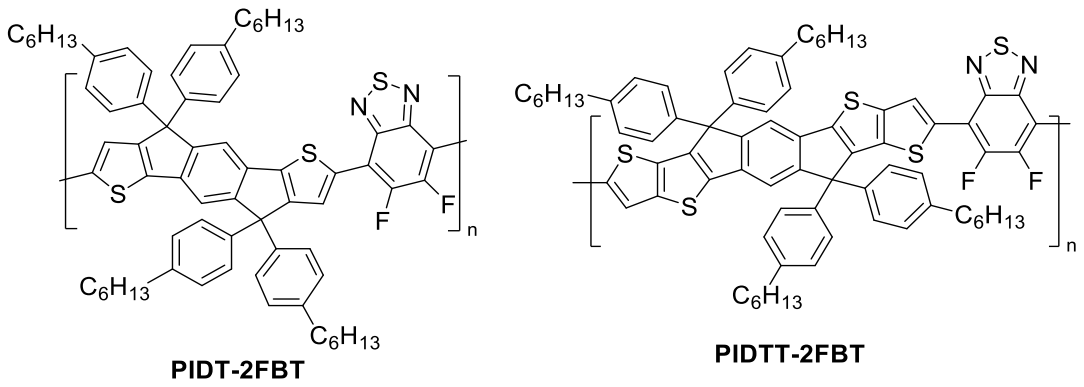
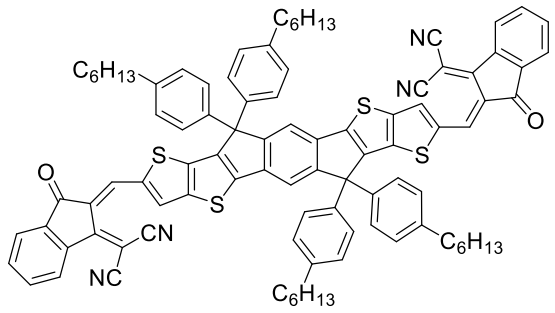
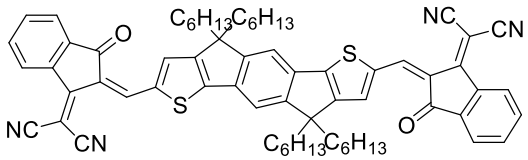


***Figure 2.3**: Structure of **PIDT-2FBT** and **PIDTT-2FBT** polymers.*[36,112]

To lower bandgap further, and to improve charge transport through greater coplanarity and conjugation polymers containing the ring extended form of **phenyl-IDT**, **phenyl-IDTT** were synthesised for OPV applications (**Figure 2.1**).[36,112] This modification improved J_{SC} for **PIDTT-2FBT** cells by 1.01 mA/cm^2 compared to analogous **PIDT-2FBT** cells and gave the cells PCEs of 7.03% and 5.97% respectively (**Figure 2.3**).[36] Whilst suitably crystalline for OPV, **PIDTT-2FBT** only gave low hole mobilities of 0.01 cm^2/Vs in OFET devices, stressing the importance of using low-bulk linear side-chains to achieve greater crystallinity for OFET applications.[10]



ITIC



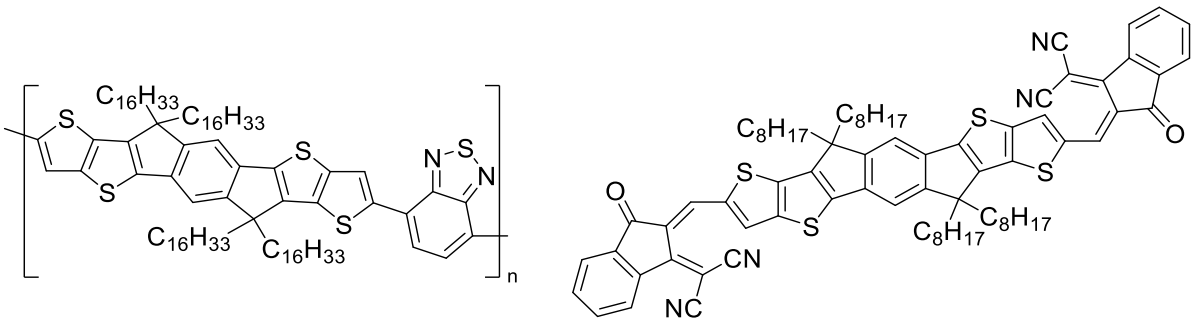
IDIC

Figure 2.4: *Structure of **ITIC** and **IDIC** NFAs for OPV*.[113,114]

As discussed in Chapter 1, in 2014 the first examples of **IDT** based NFAs were reported in literature.[115,116] However, it wasn't until 2015 that the highest performing structural motif for **IDT** derivative NFAs, **ITIC**, was synthesised (**Figure 2.4**). Initial devices using the acceptor gave good PCEs of 6.5%, but with side chain engineering and selective halogenation PCEs of over 12% have since been obtained consistently.[113,117–119] **ITIC** used the extended indacenodithiophene with aryl side chains (**phenyl-IDTT)**, making use of an extended conjugation to improve intramolecular charge transport and light absorption over **phenyl-IDT** (**Figure 2.1**).

The A-D-A structure of **ITIC** gave it a low bandgap, and rigid out of plane sidechains allowed it to overcome the common failure of non A-D-A NFA architectures, excessive aggregation that led to overlarge crystalline domains.[120] Similarly, in 2016 a shorter form of **ITIC**, **IDIC** was synthesised.[114] Although this acceptor did not benefit from the increased conjugation of **IDTT**, it still performed at a high PCE of 8.71% in initial devices. As in earlier mentioned polymers, **IDIC** benefitted from the increased crystallinity bought by using alkyl chains on the **IDT** bridgehead relative to acceptors with phenyl side chains, as can be seen from the high J_{SC} of 15.05 mA/cm^2 for **IDIC** devices with appropriate polymer. For comparison, the original published **ITIC** devices only had 14.31 mA/cm^2 J_{SC}. It must be noted however, that whilst this difference shows **IDIC** devices to be capable of high J_{SC}, the measurements were performed in different research groups and used different device architectures. The many factors to consider in OPV device fabrication make comparing the performance of NFAs difficult. To minimise this issue certified values for performance can be obtained, but these are not available for most of the devices produced in literature. Generally, the most reliable

comparisons of NFA performance in devices are between those made in the same conditions, by the same researchers, and with similar architectures.



PIDTT-BT **C8-ITIC**

***Figure 2.5**: Structure of **IDTT-BT** p-type OFET polymer and **C8-ITIC** NFA developed in our group.*[121,122]

Building on this previous work on **IDT** derivatives, our group developed the NFA **C8-ITIC** and OFET polymer **PIDTT-BT**, these materials utilised alkyl substituted **IDTT** (**alkyl-IDTT) (Figure 2.5)**.[121,122] The materials had increased crystallinity and this improved charge transport relative to **phenyl-IDTT.** Whilst **ITIC** benefited from reduced crystallinity compared to earlier types of NFA such as **PDI** NFAs, it was found that the reduction was excessive and more crystalline **C8-ITIC** had better morphology in the **BHJ**. **C8-ITIC** had a high average J_{SC} of 19.3 ± 0.7 mA/cm^2 as opposed to 17.9 ± 0.4 mA/cm^2 for analogous **ITIC** devices, leading to **C8-ITIC** and **ITIC** devices having PCEs of 12.4 ± 0.4 % and 11.5 ± 0.4 % respectively. Similarly, **PIDTTBT** had a very high optimised hole mobility of 8.7 cm^2/Vs due to its high rigidity that was aided by the presence of less-bulky sidechains. The high rigidity allowed rapid transport between crystalline domains in the semi-crystalline polymer. The performance and characteristics of **C8-ITIC** and **PIDTT-BT** will be further elaborated on in chapters 3 and 4 respectively. This chapter will focus on building analogues of **IDT** for use in plastic electronics.

2.1.2 – Synthetic Strategies

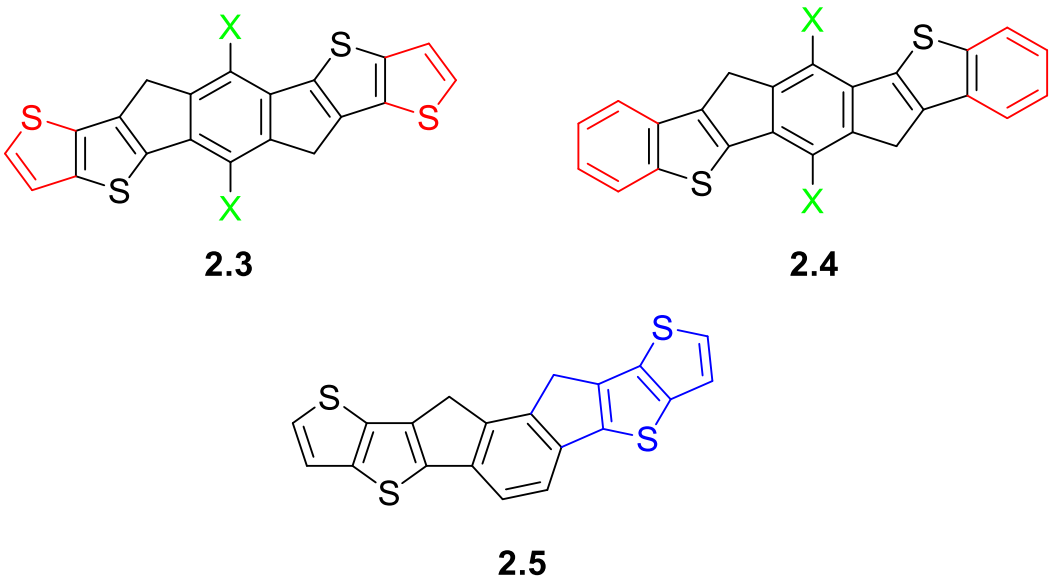
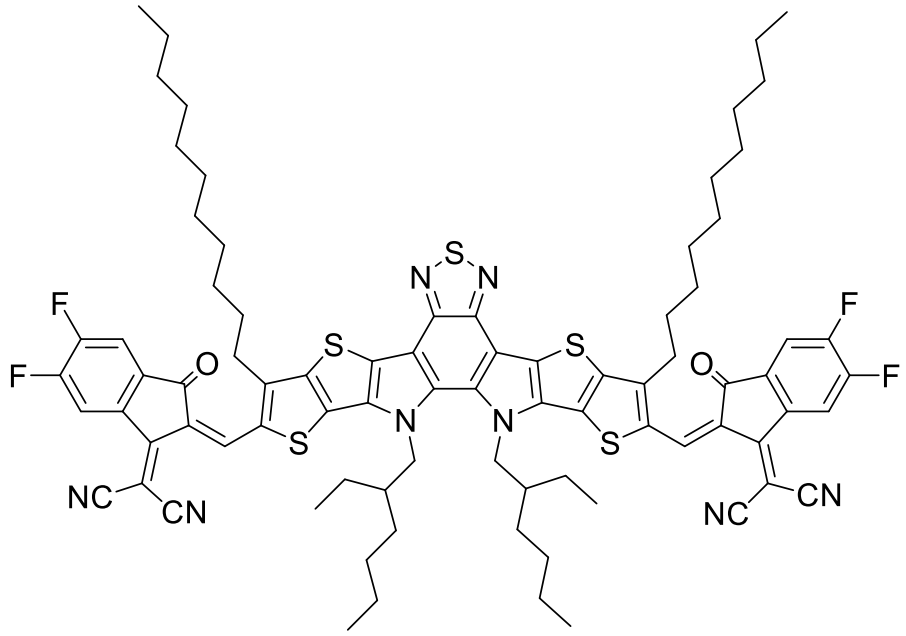


Figure 2.6: *Areas of the* ***IDT*** *core chosen for modification.*

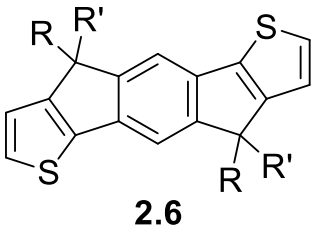
Three main synthetic strategies were employed to modify the **IDT** core and are shown in **Figure 2.6**: ring extension (red, **2.3**), halogenation (green, **2.4**), and isomerisation (blue, **2.5**). Ring extension was performed in order to increase the π conjugation in the cores. Since charge transport relies on intermolecular interaction and orbital overlap, extending the conjugated core can potentially improve charge transport for OPV and OFET applications. The use of fused, conjugated rings potentially minimises reorganisation energy in such systems, compared to the addition of non-fused aromatic rings, thereby further helping to facilitate charge transport. The ring extension can be performed either with an extra thiophene or alternatively by adding a phenyl ring (**2.4**). In the latter case, the reduced electron density of phenyl over thiophene is expected to reduce bandgap to a lesser degree such that the core is suitable for use in wide-bandgap NFAs.



Y6

Figure 2.7: *Structure of* ***Y6*** *NFA.*[72]

Halogenation was performed on the central phenyl ring to improve processability in organic solvents, tune morphology in films, and to widen band gap for A-D-A wide-bandgap NFA applications (**2.3**, **2.4**). Additionally, it was hoped that non-covalent F-S or F-H interactions may improve intra or inter molecular interactions for molecules produced from the core as is commonly observed.[123] Finally, isomerisation of the core was planned in order to ascertain if an increase in dipole moment would improve the performance of NFAs (**2.5**). This change was made due to the success of the recent acceptor **Y6** that achieved a PCE of over 15% with a unique core structure (**Figure 2.7**).[72] One of the notable changes in **Y6** from previous acceptors is its bent core, this has been theorised to improve OPV performance through increased dipole moment.



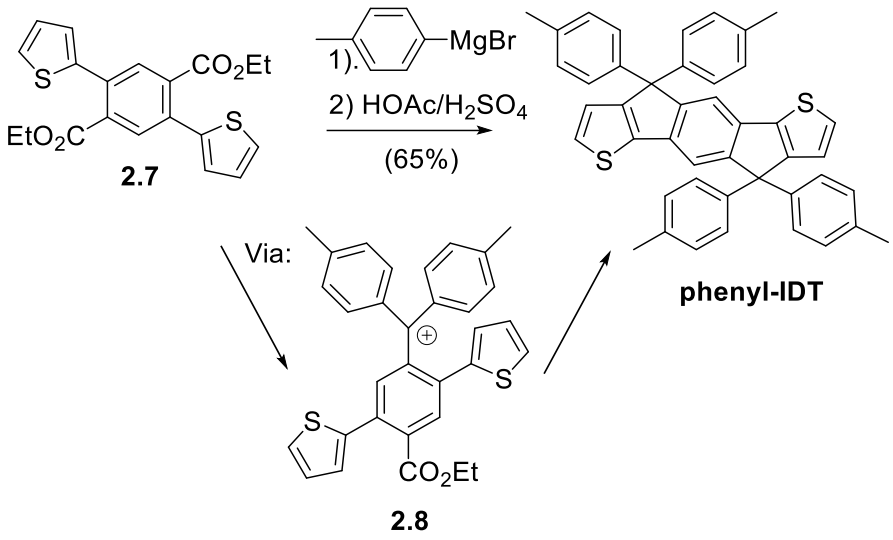
2.6

Figure 2.8: *General form of the structure of asymmetric alkyl chain* ***IDT****. R and R' are different alkyl groups.*

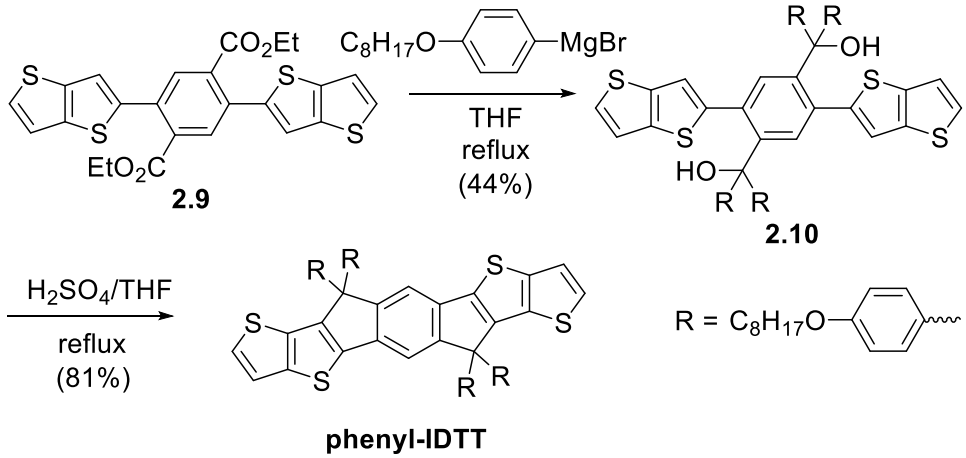
In addition to the unsubstituted **IDT** derivatives, an analogue of **alkyl-IDT** with asymmetric sidechains was designed (**Figure 2.8**). This modification would allow more careful tuning of active layer morphology in organic electronics as each chain could be altered separately. It's likely that asymmetric side chains would inhibit the crystallinity of functionalised derivatives of **2.6**. Therefore, they would be most appropriate for use in OPV where excessive crystallinity is unfavourable due to the necessary sufficient mixing of the active layer components in the BHJ for efficient exciton splitting.

2.1.3 – Ring-Closing Reaction Background

At first glance the **IDT** core may appear synthetically complex, as it comprises five fused aromatic rings. However, the synthesis of **phenyl-IDT** has been reported in relatively good yield by Friedel-Crafts acid catalysed ring closure. Thus, treatment of a diester precursor with excess aryl-Grignard reagent leads to a tertiary alcohol, which in the presence of strong acid undergoes dehydration to a cationic species (**Scheme 2.1**). This undergoes subsequent ring closure, likely in a two-step process through the formation of cations as shown in **Scheme 1.1** with varying degrees of arylation on the ester positions. Key to the success of the reaction is the high stability of the tertiary cation due to the presence of the electron donating aryl substituents. Attempts to prepare **alkyl-IDT** under analogous Friedel-Crafts conditions are complicated by the tendency of non-stabilised dialkyl-cations to rearrange or eliminate, rather than ring close.[103,124] An analogous route has been used in literature to prepare **phenyl-IDTT** (**Scheme 2.2**).[112]

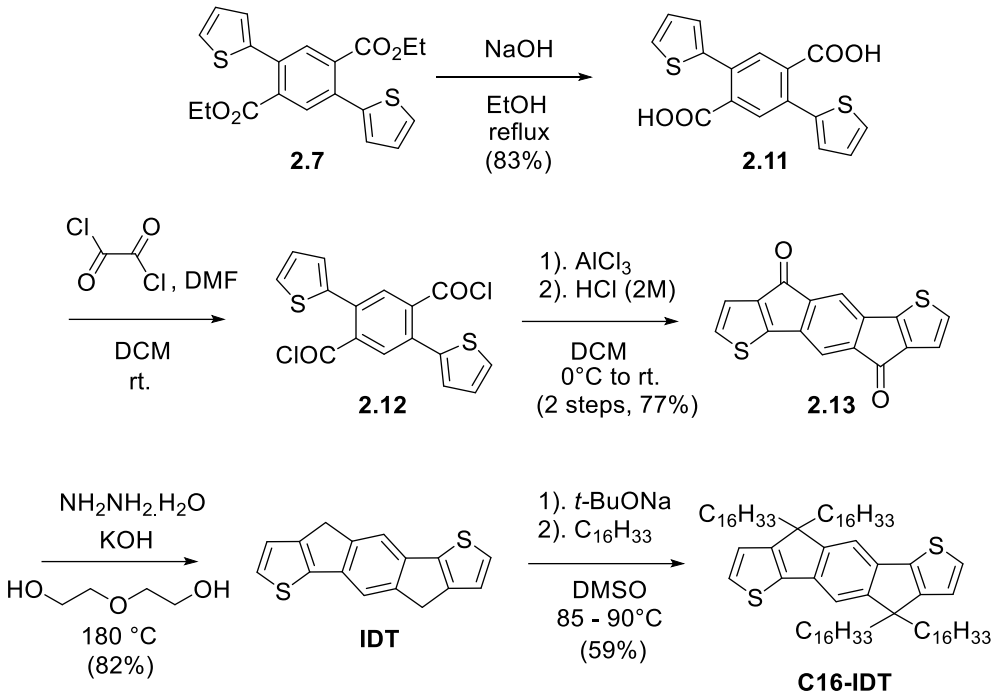


Scheme 2.1: *Synthesis of* ***phenyl-IDT***.[1]

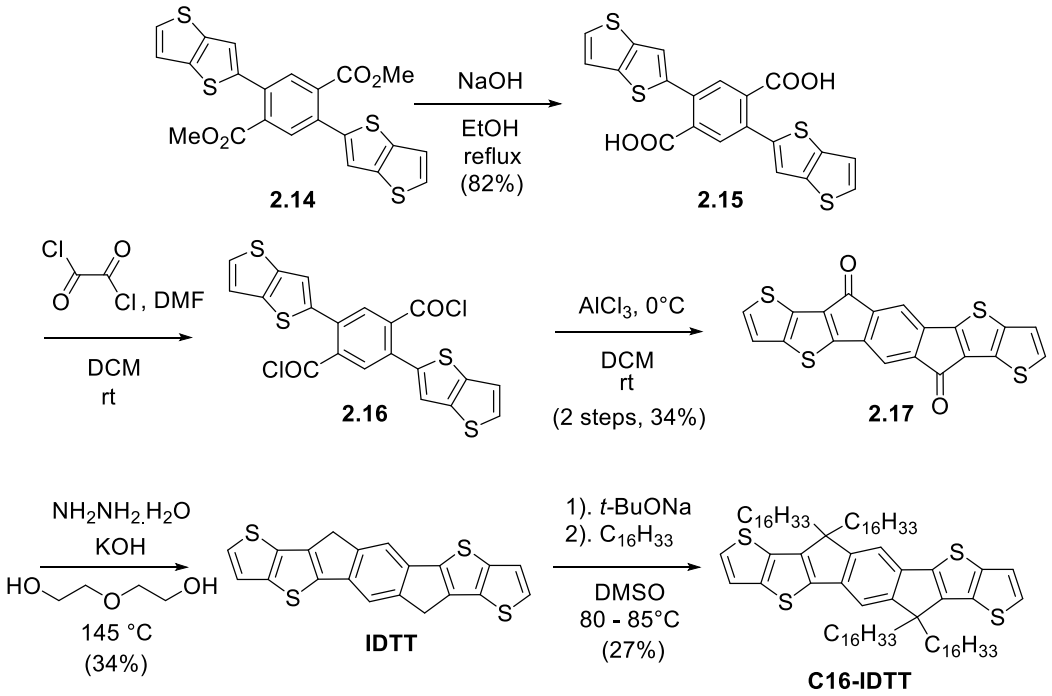


Scheme 2.2: *Synthesis of* ***phenyl-IDTT***.[112]

The first synthesis of **alkyl-IDT** involved an indirect route wherein the diketone form of **IDT** (**2.13**) was produced first, via a Friedel-Crafts acylation of an acid chloride precursor (**Scheme 2.3**). Subsequent reduction gave **IDT**, which was alkylated at the bridgehead positions by treatment with a base and an alkylating agent.[108] This synthesis takes five steps to reach **alkyl-IDT** from **2.7** as opposed to one step for the earlier route to **phenyl-IDT**. A similar synthetic route proceeding via the diketone (**2.17**) is used in the synthesis of **alkyl-IDTT** (**Scheme 2.4**).[121] Handling of the ketone is troublesome in both routes as it is very insoluble in organic solvents which makes the synthesis difficult.



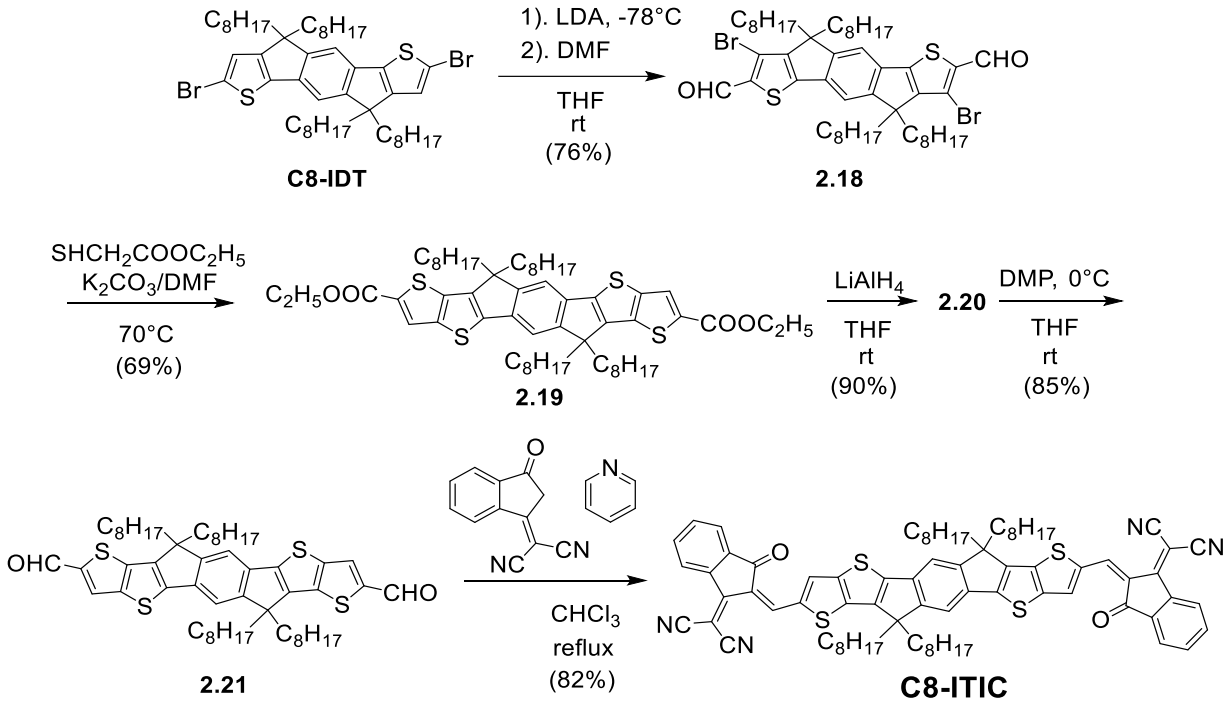
Scheme 2.3: *Synthesis of* ***alkyl-IDT***.[108]



Scheme 2.4: *Synthesis of* ***alkyl-IDTT*****.**[121]

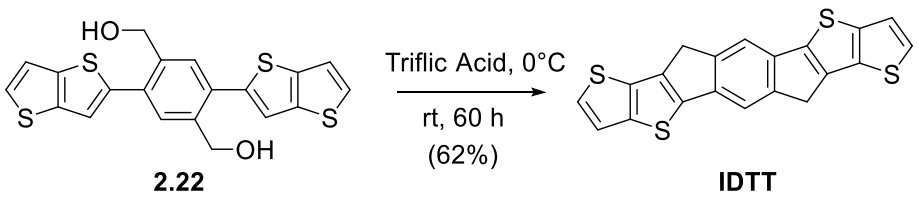
The problems and difficulty in the upscaling of the ketone route towards **alkyl-IDTT** has prompted some investigation of alternative routes. One alternative is via a ring extension of **C8-IDT**, as performed in our group towards **C8-ITIC** (**Scheme 2.5**)**.**[122] In this example the

additional ring is formed via a ring closure condensation between a bromo-aldehyde precursor, itself prepared via a halogen dance reaction, and ethyl mercaptoacetate. An additional bonus of this approach was the inclusion of an ester group in the alpha position, which could be readily converted into an aldehyde for subsequent formation of the electron accepting end group.



Scheme 2.5: *Synthesis of* ***C8-ITIC*****.**[122]

Today, **C8-IDT** is commercially available on the research scale. However, for real world applications the high cost of **C8-IDT** and the complexity of its synthesis would result in an excessively long and expensive pathway towards **alkyl-IDTT** NFAs. Moreover, the above methodology doesn't allow for modification beyond **IDTT**. To develop more derivatives of **IDTT** to search for a more practical methodology, a new pathway is required. At the outset of this work, our sponsors at Merck had found a novel ring-closing utilising triflic acid (**Scheme 2.6**), which was later patented and in this work we further improved and investigated the versatility of this method to unlock more complex and desired aromatic cores.[125]

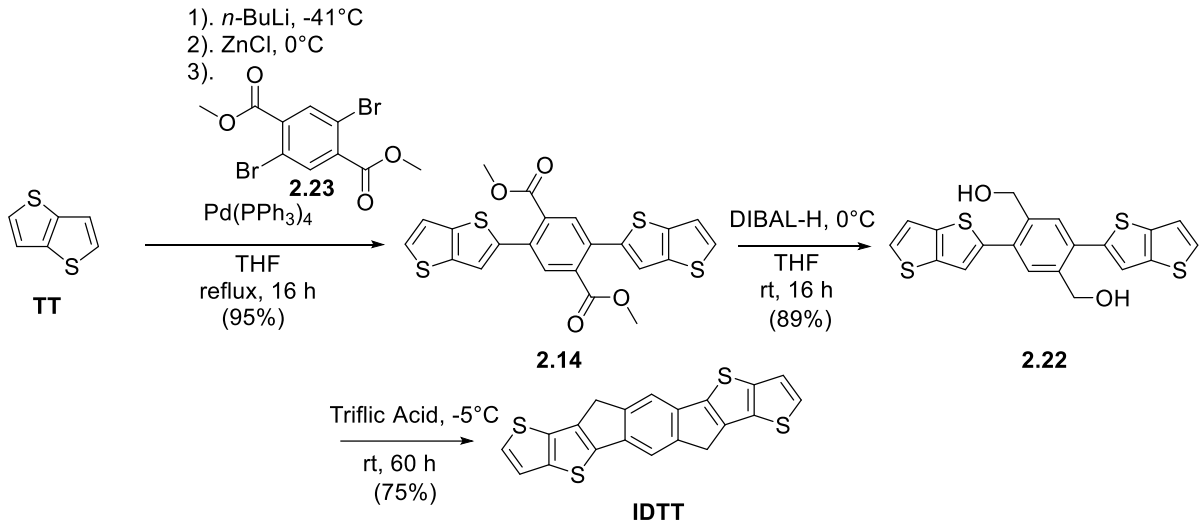


Scheme 2.6: *Patented triflic acid catalysed ring-closing reaction*.[125]

2.2 - Results and Discussion

2.2.1 – IDTT

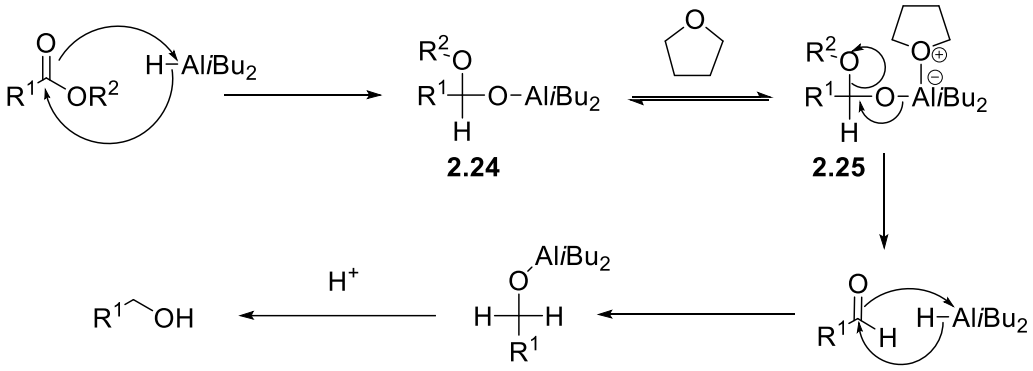
To confirm the effectiveness of the triflic acid reaction, the first core synthesised was **IDTT**, directly repeating the ring-closing conditions previously utilised.[125] The route taken to this core started with a Negishi coupling of thienothiophene (**TT**) with commercially available **2.23** (**Scheme 2.7**). Whilst a number of cross-coupling chemistries can potentially be utilised, previous routes had utilised Stille coupling. We instead performed a Negishi coupling due to its use of less toxic reagents than the Stille coupling and its suitability to a one-pot single step procedure, reducing the overall number of steps.



Scheme 2.7: *Synthesis of* ***IDTT***.[125]

The coupling proceeded in an excellent 95% yield but the required purification was difficult. Washes of the crude product with water and methanol did not provide sufficient purity for the product and therefore column chromatography was employed. This often-required

multiple columns due to the insolubility of the product and close Retardation Factor (Rf) values to impurities. The resulting ester was reduced using diisobutylaluminium hydride (DIBAL-H) to the alcohol. This reaction was initially worked up with an aqueous quench followed by extraction with diethyl ether. Later this was modified to removing the reaction solvent under reduced pressure and washing the resulting crude product with methanol as this was more straightforward and gave higher yields. It is worth noting that this reaction proceeded to the alcohol due to the polar solvent THF being used.[126] DIBAL-H reductions in non-polar solvents typically end with the tetrahedral intermediate **2.24 (Scheme 2.8)**, which upon aqueous workup yields the aldehyde. However, in polar solvents the complex **2.25** is formed because a polar solvent such as THF weakly bonds to aluminium and therefore weakens the Al-O bond, thus allowing decomposition to the aldehyde before aqueous work-up. The more electrophilic aldehyde then outcompetes the original carboxylic ester for DIBAL-H and is therefore reduced further to the alcohol.



Scheme 2.8: *DIBAL-H reaction mechanism*.[126]

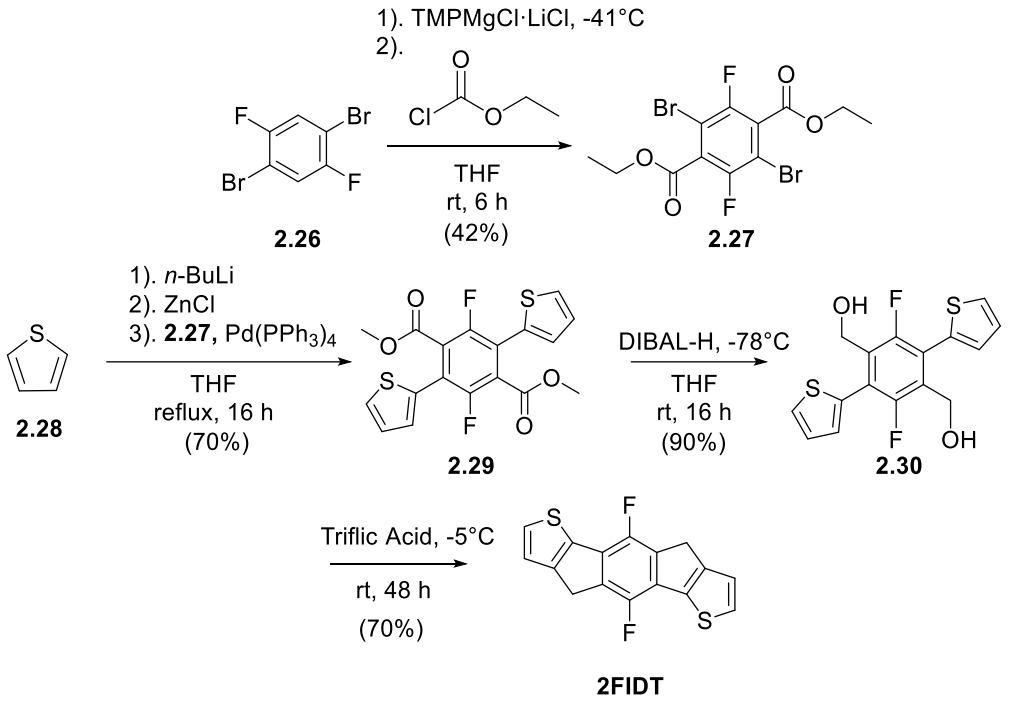
A final ring closure using triflic acid proceeded in pleasingly high 75% crude yield. The reaction entailed cooling neat **2.22** in an acetone-dry ice bath and carefully adding a known volume of triflic acid from a measuring cylinder. The use of syringes was avoided as the markings on plastic syringes melted when they were loaded with triflic acid, risking contamination of the reaction. The acidic mixture was left stirring for 60 h and was then poured into ice, filtered, washed with water, saturated sodium acetate, water, and methanol giving the crude product as a brown residue. Afterwards, the crude product was dissolved in boiling chlorobenzene (CB) and filtered. The residue was then again dissolved in boiling CB and filtered, with this extraction procedure being repeated five times overall and solvent removed from the combined filtrates under reduced pressure yielding the product.

The biggest difficulty in the triflic acid reaction was the insolubility of the core after its formation. This meant that standard methods of purification such as column chromatography could not be used. In addition, very poor solubility made it difficult to identify by NMR spectroscopy (**Figure 7.1.6**). The final product was therefore confirmed by a combination of mass spectrometry (MS), weak signals from ^{1}H-NMR that were visible once impurities were removed, and by the success of future alkylation reactions discussed in Chapter 3 of this thesis. As a result, it was hard to optimise the purification further, but extractions with alternative solvents instead of CB were attempted. Neither hot chloroform, hot ethyl acetate, or hot dichloromethane (DCM) however gave improved purity by NMR compared to hot CB.

The use of triflic acid in this ring closing avoids the need for formation of a ketone and further reduction to reach the unsubstituted core.[127] However, a weakness of this triflic acid ring closing is that the work-up requires boiling the crude product in CB, filtering, and then removing the solvent under reduced pressure to yield pure product. This step takes multiple extractions, is laborious and boiling large amounts of CB introduces risk due to potential carcinogenicity.[128] However, as can be seen further in this chapter, not all cores require this procedure.

2.2.2 – 2FIDT

Following the success of repeating the **IDTT** synthesis, we wished to further explore the scope of the reaction by exploring different cores. An attractive first target involved fluorination of the central phenyl ring (**2FIDT**, **Scheme 2.9**).[125] Our proposed route required a dibrominated, difluorinated terphthalic ester (**2.27**).[125] Since **2.27** was not commercially available, it was produced via a double deprotonation of **2.26** by the Knochel-Hauser base, followed by esterification of the resulting diGrignard with ethyl chloroformate.[129,130] Subsequent Negishi coupling was performed successfully, following the same conditions as for **IDTT**. Column chromatography of the crude product was simpler than after the Negishi coupling towards **IDTT**, this can be attributed to the increased solubility of **2.29** due to its smaller fused ring system and solubilising fluorine moieties. A final **DIBAL-H** reduction afforded the requisite diol in good 90% yield.

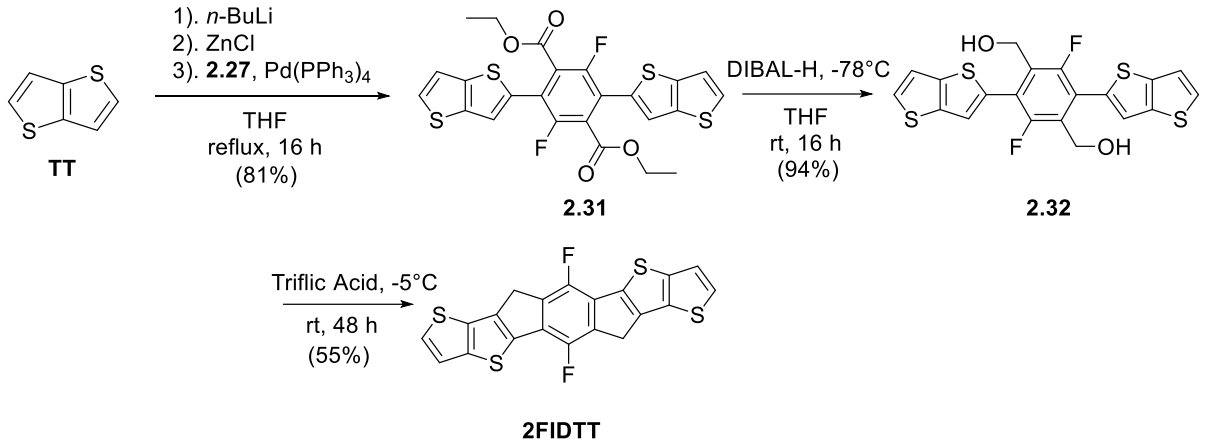


Scheme 2.9: *Synthesis of* ***2FIDT***. [125,129]

The ring closing with triflic acid was performed under identical conditions as for **IDTT**, but difficulties were faced when optimising the work-up procedure. Thankfully, the product was much simpler to identify than **IDTT** due to the presence of fluorine allowing more sensitive ^{19}F-NMR to be performed, helping optimisation. The original work-up procedure involved washes with sodium acetate, water, and methanol preceding triturating the crude product in hot chloroform. Unfortunately, neither filtering from chloroform nor DCM provided sufficient purity. Therefore, the methodology used for purifying **IDTT** was tested and the crude product was extracted with hot CB. However, this extraction did not yield pure product either, with clear impurity peaks apparent in the NMR. Additionally, attempts to recrystallise the product using a biphasic mixture of CB and methanol counter-solvent did not improve purity. As different recrystallisation solvents were tried it was noted that **2FIDT** is more soluble in chloroform than **IDTT**. Therefore, after thin layer chromatography (TLC) showed only one spot and baseline impurities a simple plug through silica with chloroform eluent was performed, yielding pure product by NMR. Repeating the process with the optimised purification procedure afforded a final optimised ring-closing yield of 70%.

2.2.3 – 2FIDTT

Building on the synthesis of **2FIDT**, a route to the novel core **2FIDTT** was proposed (Scheme 10). This core was chosen because of improvements in performance observed in both OPV and OFET devices through ring extension of **IDT**.[108,113] These improvements have been both due to improved charge conductivity through greater π-π interactions between cores increasing crystallinity for fast intermolecular transport and the rigid fused ring system allowing rapid intramolecular transport. In addition, lower bandgaps caused by increased conjugation in the cores improved optoelectronic properties.



Scheme 2.10: *Synthesis of* ***2FIDTT***.

The initial Negishi coupling between **2.27** and the organozinc reagent proceeded well in terms of crude yield (**Scheme 2.10**). As for the earlier cores, it was difficult to purify the product of the Negishi coupling step by column chromatography, this was perceived to be mainly due to the poor solubility of **2.31** causing streaking. After analysis of the ^{1}H-NMR of the product after trituration with methanol, it was found that the main impurity was the self-coupled dimer of **TT**. Therefore, as this side-product was perceived not to have an adverse effect on the next **DIBAL-H** reduction step due to a lack of reducible functional groups, the crude product was used in the reduction. An additional ice-cold DCM wash was added to the work-up of the **DIBAL-H** reduction, using the weak solubility of the alcohol in chlorinated solvents to purge the **TT** dimer from the previous step.

Finally, the triflic acid ring-closure proceeded in a high 75% yield. The same purification procedure to that for **IDTT** was initially used, with a series of washes followed by extraction of the product using hot CB. An addition to the procedure was the introduction of an isopropanol wash after the extraction with CB to remove more impurities.

2.2.4 – IDTBt

To further establish the suitability of the triflic acid route towards synthesis of cores for organic electronics another core **IDTBt** was envisioned (**Figure 2.9**). This core was designed to be a wider bandgap acceptor for OPV by using a benzothiophene moiety (**Bt**) rather than **TT**. The HOMO energy level for benzothiophene (**Bt**) was calculated to be -5.89 eV by DFT (B3LYP, 6-31G +G(d,p) basis set) whilst for **TT** it was -5.86 eV. Because benzodithiophene has a deeper HOMO energy level than **TT**, it is predicted to widen bandgap when the full core is coupled to an electron-poor component.

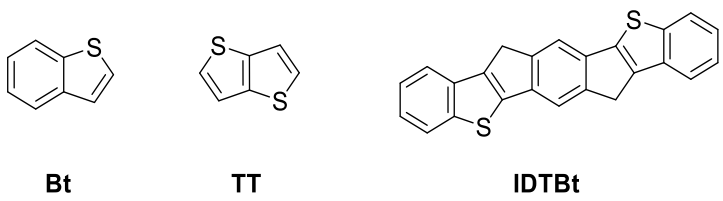
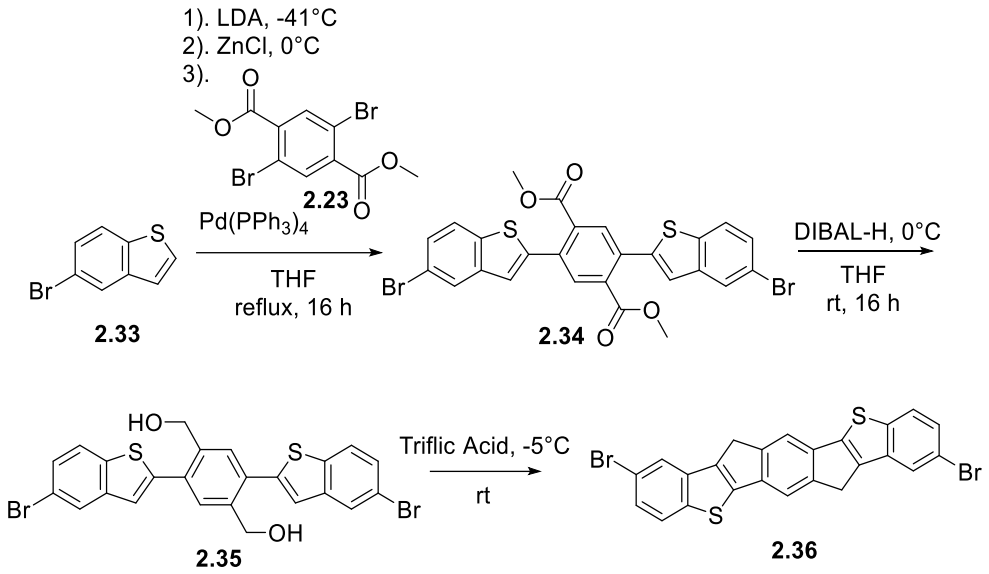


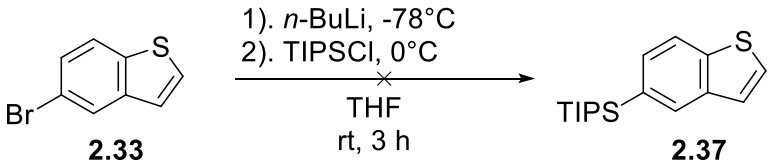
Figure 2.9*: Structures of benzothiophene,* ***TT*** *and novel* ***IDTBt*** *core.*

To allow the core to be functionalised further, a functional group such as bromine would need to be attached to the core. However, future difficulties in attaching a bromine to **IDTBt** after production of the core were predicted due to a lack of selectivity for different positions on the terminal benzene ring of **IDTBt** (**Scheme 2.11**). Therefore, the brominated starting material **2.33** was used in the synthesis of the core. In order to minimise any competing lithiation on the brominated 5 position of **2.33**, non-nucleophilic lithium diisopropylamide (LDA) was used instead of *n*-BuLi as it was perceived to be more likely to only metalate the ortho-2 position rather than perform halogen-metal exchange**.**[131,132]



Scheme 2.11: *Proposed synthesis of* ***2.35***.

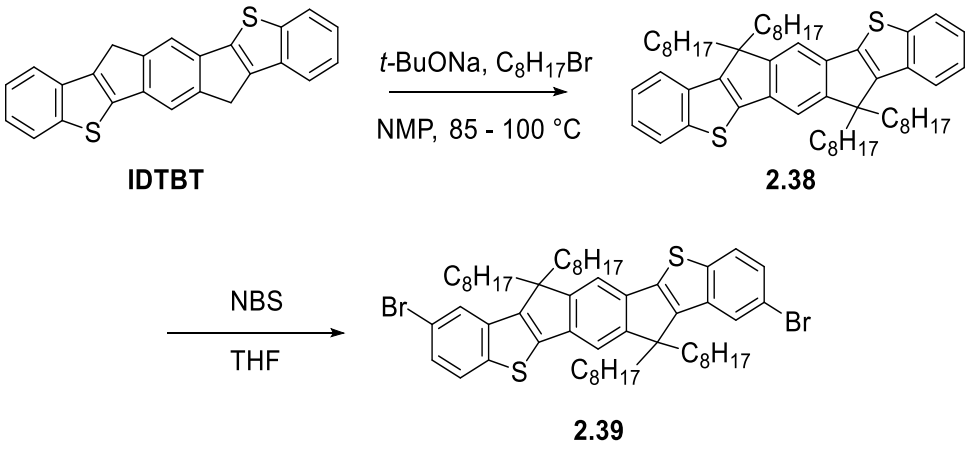
The initial synthetic plan is shown in **Scheme 2.11** and involved a Negishi coupling to attach **2.33** to **2.23** in order to avoid using toxic organotin.[133] However, after a one-pot Negishi coupling was attempted a product that was bright yellow and insoluble in common organic solvents was produced. This was theorised to be due to oligomerisation of benzothiophene through Negishi coupling between its 2 and 5 positions. As such, a protection of **2.33**, was attempted using triisopropylsilyl chloride (TIPSCl) (**Scheme 2.12**). It was predicted that lithium-halogen exchange on bromine would be significantly quicker than ortho-metalation of the acidic 2 position and therefore TIPSCl was added immediately after a colour change was observed when *n*-BuLi was added.[134]



Scheme 2.12: *Attempted TIPS protection of* ***2.33***.

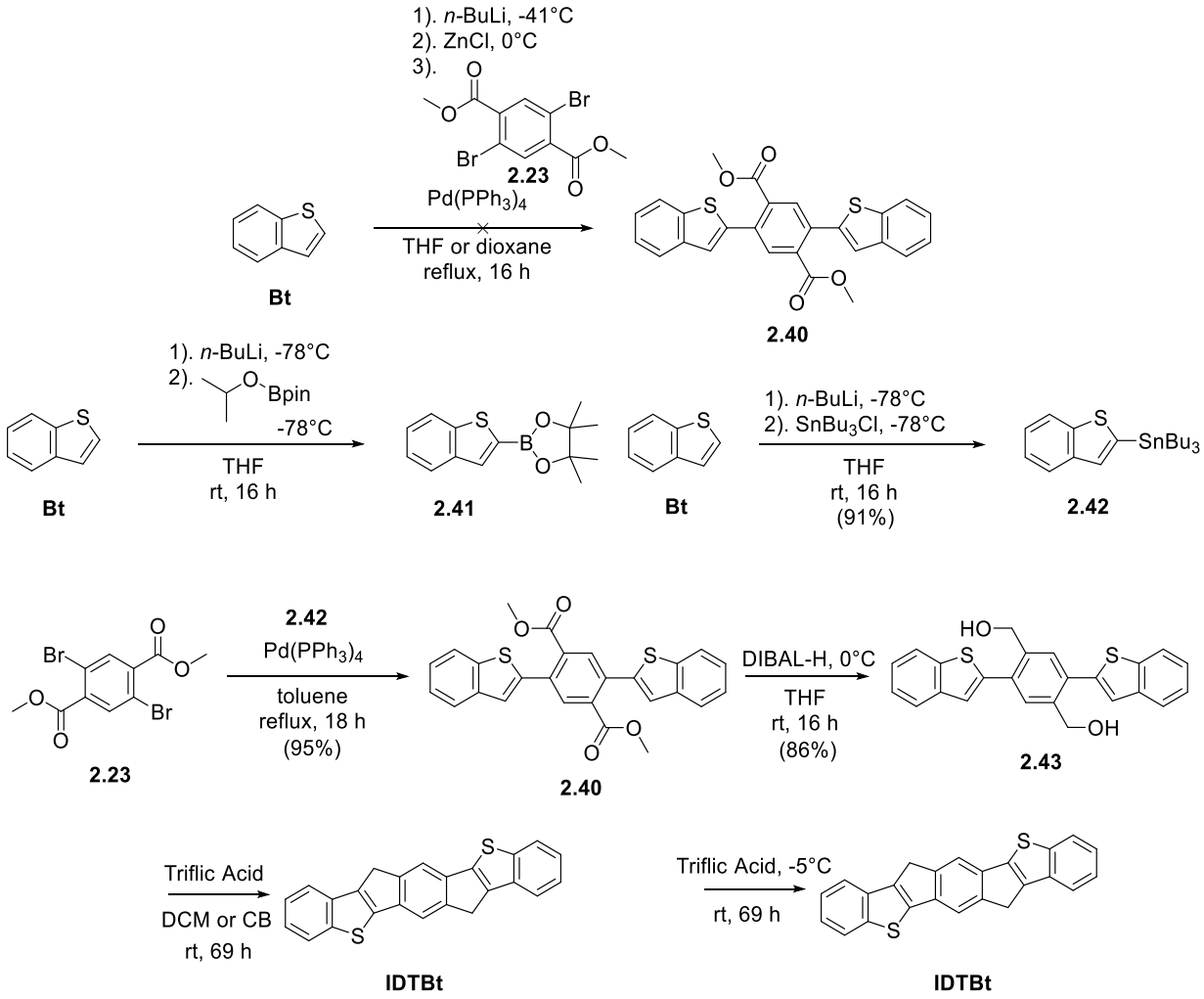
Unfortunately, a lack of selectivity was encountered with triisopropylsilyl (TIPS) substitution apparently occurring both on the 2 and 5 positions according to the ^{1}H-NMR. Due to this lack of selectivity, it was decided to first produce the unfunctionalised core and then attempt to brominate it instead. It was proposed to carry out the bromination on the alkylated **IDTBt** (**2.38**) to limit solubility problems (**Scheme 2.13**). Expected yield loss due to

selectivity problems in the bromination could be counteracted by using greater amounts of starting material to form the core and reacting at lower temperatures.



***Scheme 2.13**: Planned alkylation and bromination of **IDTBt**.*

Thus, the synthesis was modified to start with the Negishi coupling with unsubstituted **Bt** (**Scheme 2.14**). Following an overnight reaction, considerable amounts of starting material were found in crude product by ^{1}H-NMR. A second reaction with an extended reaction time of 24 h was tracked by TLC, but the reaction still had not gone to completion. After another 24 hours of reflux in THF the limiting starting material **2.23** was still seen on TLC. It was suspected that the problem related to poor solubility of **Bt** in THF, or due to the less electron rich **Bt** interfering with the reductive elimination step in the coupling cycle compared to **TT**. More forceful conditions were tested for this coupling, with THF being replaced with 1,4-dioxane due to its higher boiling point of 101 °C. Unfortunately, 1,4-dioxane couldn't be used to perform the lithiation at -78 °C due to it having a melting point of 11.8 °C and therefore the lithiation was performed at room temperature, followed by reaction with zinc chloride.[135] The Negishi coupling using 1,4-dioxane did not work, most likely due to the temperature for the lithiation being too high as the reaction mixture became brown rather than pink during the lithiation step indicating unwanted side products. Because of the difficulties faced with the Negishi coupling, a Suzuki coupling was investigated instead.



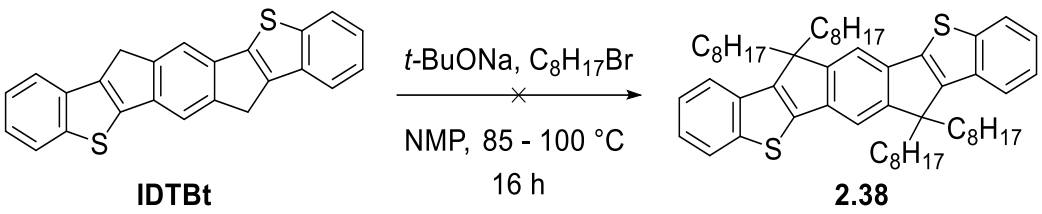
Scheme 2.14: *Synthesis of* ***IDTBt****.*[136,137]

The boronic ester **2.41** was prepared via lithiation/trapping, however, the crude product was found to have multiple impurities by ^{1}H-NMR. Therefore, column chromatography was attempted to purify out the product. However, after analysis of all the fractions including the acetone flush from the column it was found by ^{1}H-NMR that no product was present. This was believed to be due to proto-deborylation by the acidic silica.[138] A possible solution to this would be the use of boric acid impregnated silica gel. As an alternative solution, a Stille coupling was attempted instead as these couplings have had more anecdotal success in our research group and because they have been used extensively in literature to connect fused ring cores.[112,139,140] Synthesis of the necessary organotin **2.42** proceeded in high 91% yield and this was used directly for the subsequent Stille coupling without further purification (**Scheme 2.14**). The Stille coupling was performed using typical cross-coupling

conditions and $Pd(PPh_3)_4$ catalyst in toluene.[141] The product obtained was even more insoluble than the products in the equivalent steps of the syntheses of previously discussed cores. Therefore, column chromatography was immediately performed with a large column and dry loading yielding the product in excellent 95% yield. After a successful DIBAL-H reduction, triflic acid ring closing was performed as for **IDTT**. Due to an even weaker solubility in organic solvents than **IDTT**, **IDTBt** faced significant difficulties in its purification. After the same purification procedure was employed as for **IDTT**, the product was confirmed by MS. It was difficult to confirm the purity of the core through ^{1}H-NMR as it was only partially soluble in both $CDCl_3$ and deuterated tetrachloroethane (d2-TCE). However, the faint ^{1}H-NMR signals clearly showed impurities and the compound was a dark brown colour as opposed to beige for purified **IDTT** and **2FIDTT** and therefore further purification was needed.

A novel methodology for the triflic acid ring closing utilised by Tobe *et al* on shorter-cored **IDT** analogues was also tested for the ring closing of **2.43**.[142] This involved solvation of the reaction in DCM and using much less triflic acid. The benefit of this methodology is a much shorter reaction time of 25 minutes and good yields, with two **IDT** derivatives produced in either 42% or 96% yields in the literature.[142] The synthesis of **IDTBt** was performed according to this methodology and yielded the product by MS. It was observed that **2.43**, had a poor solubility in DCM and therefore the reaction procedure was modified, increasing the reaction time to 1 hour. To this end, the reaction was also performed with CB as the solvent due to it being more solubilising towards these fused ring species. After reaction completion and quench with aqueous sodium bicarbonate the same workup as utilised previously was performed, with a series of washes followed by extraction with CB. Both the DCM version of the reaction and CB reaction showed the product ion at 367.1 m/z after the work-up procedure; however, the CB reaction was deemed to have fewer impurities by MS and CB was therefore chosen as the solvent for the scaled-up reaction. Following the same work-up, the scaled-up crude product was investigated by TLC to confirm a suitable eluent. All tested eluents resulted in significant smearing (or baseline retention), therefore a simple silica plug with hot chloroform was attempted. Although NMR suggested improved purity, there were still impurities present.

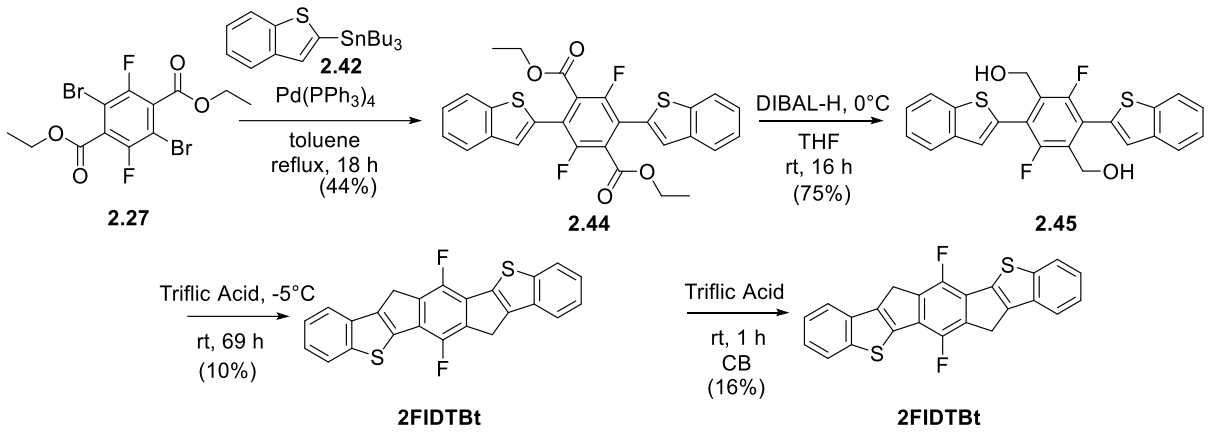
The difficulties in purification were proposed to result from poor solubility, so the alkylation step was attempted to afford a soluble product (**Scheme 2.15**). Attempted reaction with *t*-BuONa in N-methyl-2-pyrrolidone (NMP) followed by the addition of 1-bromooctane unfortunately afforded no identifiable product. This was theorised to be either due to the poor solubility of the core as opposed to **IDT** or due to its low purity. In any case, due to lack of starting materials no further investigations were performed, and the route was abandoned.



Scheme 2.15: *Attempted alkylation of* ***IDTBt****.*

2.2.5 – 2FIDTBT

To improve the solubility of the core and therefore the ease of its purification, a new core **2FIDTBt** was envisioned with fluorine group substitution (**Scheme 2.16**). This modification was made based on the synthesis of **2FIDTT** where the core was found to be more soluble in chlorinated solvents than **IDTT**. Furthermore, fluorination would lower the HOMO energy levels of the core, therefore leading to wider bandgap acceptors for indoor and ternary cell OPV applications after orbital hybridisation with an electron poor monomer. An additional benefit of fluorination is the possibility of using highly sensitive ^{19}F-NMR to confirm products that may not be visible or may be too complex to identify in ^{1}H-NMR.



Scheme 2.16: *Synthesis of* ***2FIDTBt****.*

Coupling of fluorinated ester **2.27** with **2.42** afforded **2.44** in 44% yield. This was much lower than was obtained for the Stille coupling of the non-fluorinated ester. This was possibly due to the excessive streaking observed during purification by column chromatography, which necessitated a second round of column chromatography, leading to potential loss through adsorption to silica. Alternatively, the increased steric bulk from F and OEt groups compared to OMe used en route to **IDTBt** could have hindered oxidative addition in the Stille coupling cycle, as this step is known to be affected by steric hindrance.[143] The steric hindrance hypothesis is also supported by the mechanistically similar Negishi coupling en route to **2FIDTT** proceeding in a maximum 81% yield, significantly lower than the 95% yield obtained by Negishi coupling en route to **IDTT** (**Schemes 2.10** and **2.7**). The following DIBAL-H reduction proceeded without issues.

The triflic acid reaction was performed with **2.45**, both by the neat method and the solvated method used by Tobe *et al*.[142] Both reactions were performed in parallel and their performance was compared. After reaction completion, the product of the solvated method was worked up as for **IDTBt**. Due to the presence of impurities by ^{1}H-NMR further purification was attempted on this product. Firstly, a biphasic recrystallisation from CB with methanol antisolvent was employed due to the acceptable solubility of the crude product in CB. However, no improved purity was observed for this recrystallisation and therefore a second biphasic recrystallisation from chloroform with methanol antisolvent was attempted. This second recrystallisation yielded pale beige solid at a yield of 15.8% from the starting material. The product had no obvious impurities in the alkyl region and reduced

impurities in the aryl region by ^{1}H-NMR. ^{19}F-NMR showed only one relevant singlet at -116.14 ppm indicating good purification. The same work-up procedure was then applied to the crude product of the neat method. Both the neat and solvated method contained the product by MS at 402.0 m/z. However, there were slight differences in the positions of the aryl peaks in the ^{1}H-NMRs for the two methods (**Figure 2.10**) and a difference for the position of the large singlet peak attributed to the product in their ^{19}F-NMRs. The neat method had a peak at -131.38 ppm whilst the solvated method showed a signal at -116.14 ppm (**Figures 7.1.25 and 7.1.27**).

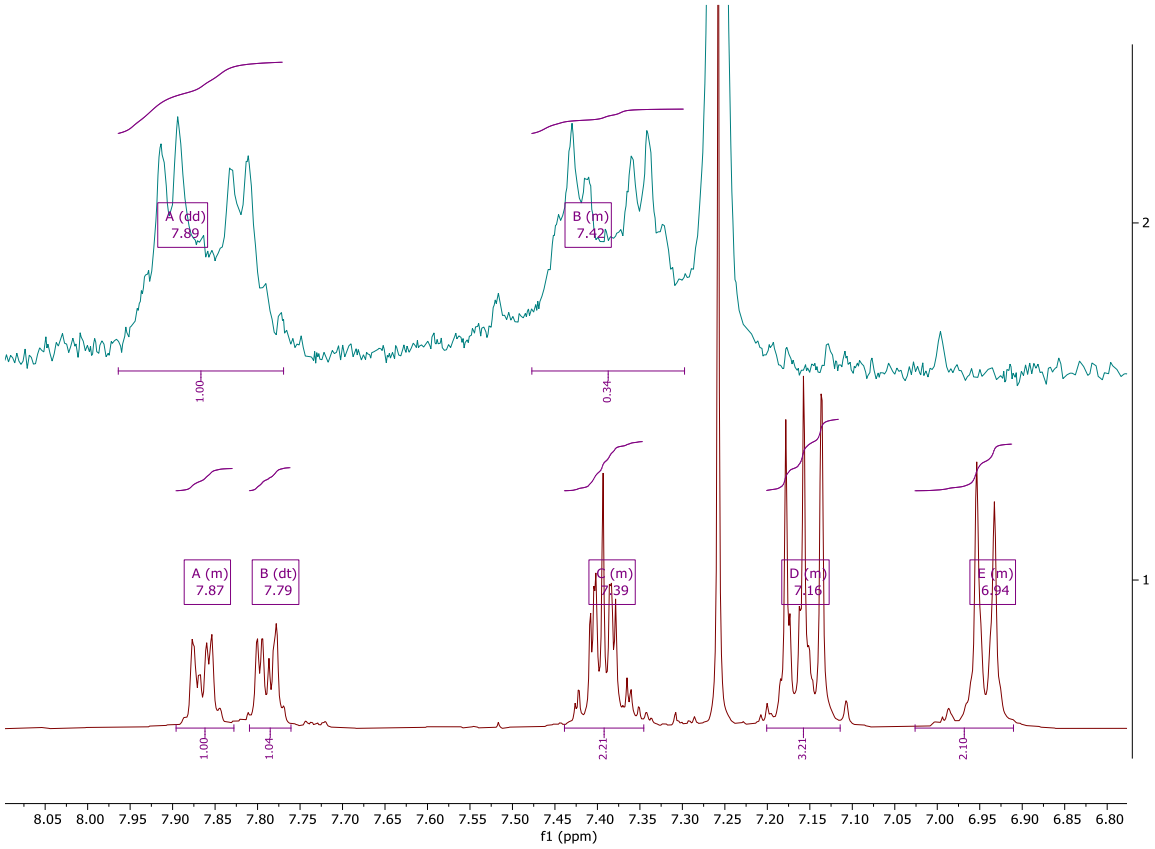
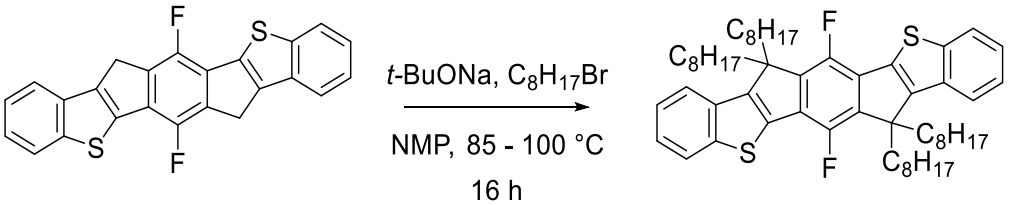


***Figure 2.10**: ^{1}H-NMR of purified **2FIDTBt** made by the neat method (top) and solvated method (bottom).*

This difference was first attributed to the presence of varying amounts of solvent such as CB in each product, however after intense drying under strong vacuum the NMRs for the products stayed the same. This difference made selecting the optimal method for cyclisation very difficult, but since both methods confirmed the product by MS both were theoretically viable. However, although the neat product had less-clear peaks indicating impurity at the

chemical shift of the product, the solvated method showed greater obvious impurity between 6.9 – 7.25 ppm in the aromatic region missing from the product of the neat method. The peaks did not correspond to those in CB and moreover any CB would have been removed from both products by long drying under strong vacuum.[144] Due to the highly reactive nature of triflic acid it is difficult to theorise what the impurity was, but it was predicted that it was formed through either the reaction of CB or by over reaction of the product due to solvation allowing pathways unachievable in the solvated method. For use in organic electronics, the core would need to later be alkylated to improve its solubility. It was feared that the larger aryl impurity would compete with **2FIDTBt** in the alkylation. Therefore, the neat method was scaled up instead.

The two scaled-up runs performed gave poor yields of 10% and 5%, this may be either due to intrinsic problems in the reaction or loss in the silica plug step of the work-up as the poorly soluble product may crash out and stay in the silica. To investigate the suitability of this core for further use in plastic electronics, a test alkylation was performed and purified by column chromatography (**Scheme 2.17**). Due to the low amount of available core because of the low yields in its synthesis the column of the product was problematic. Fractions collected from the column were essentially collected blindly due to the fractions being too dilute to visualise by ultraviolet light on TLC. After analysis of each fraction, one was found to have a significant ^{19}F-NMR signal. Because of its low concentration the fraction could not be analysed by ^{1}H-NMR. However, the target product was produced in at least trace amounts as it was detected by MS at 846.4 m/z. Whilst this synthesis of **2FIDTBt** is more promising than that of **IDTBt**, further work on its development was halted due to time constraints.

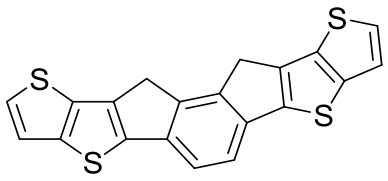


2FIDTBt **2.46**

Scheme 2.17: *Alkylation of* ***2FIDTBt****.*

2.2.6 – meta-IDTT

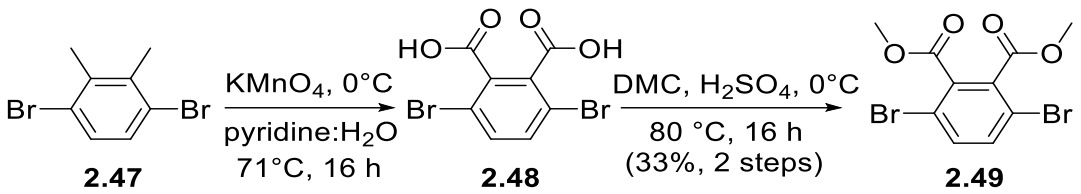
In order to investigate the potential benefits of introducing dipole moments to NFAs as in the **Y6** acceptor (**Figure 2.7**), a bent cored **IDTT** derivative **meta-IDTT** was envisioned (**Figure 2.11**).[72]



meta-IDTT

Figure 2.11: *Proposed* ***meta-IDTT*** *core.*

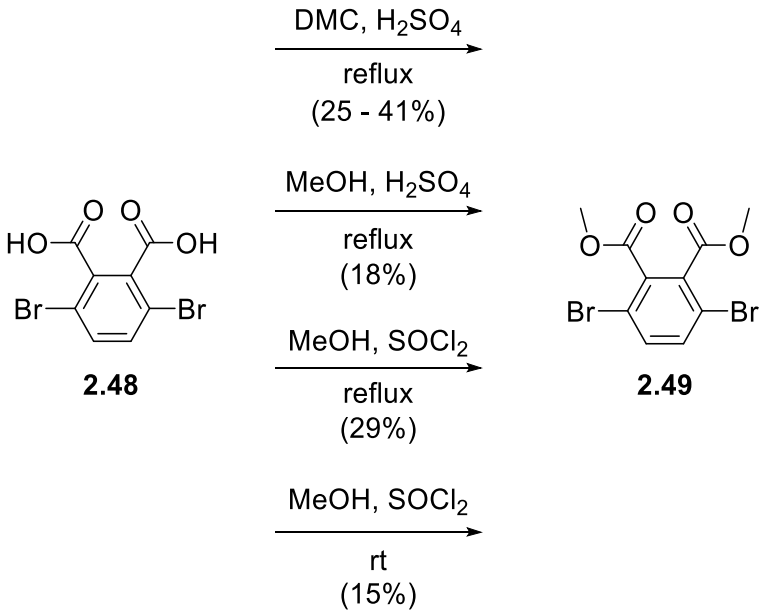
The synthetic route towards this acceptor built on the route taken by Tobe *et al* to **IDT** derivatives.[142] Similarly to the syntheses of the fluorinated acceptors, the required ester was not commercially available. Therefore, it first had to be made from **2.47** by oxidation followed by esterification. Following a literature procedure, the oxidation was carried out using potassium permanganate (**Scheme 2.18**).[142] Batches of four equivalents of potassium permanganate with water were added to **2.47** under reflux every 30 mins eight times and the reaction was monitored by TLC. However, as the TLC had spots that were very close to each other there was difficulty in identifying the disappearance of the starting material and finding when the reaction stopped. Therefore, a "mini work-up" with extraction using diethyl ether from a 10 mL aliquot of the reaction was performed. After removal of solvent *in vacuo* the aliquot-product was analysed by ^{1}H-NMR and found to be mainly mono-substituted with carboxylic acid. Resultantly, another 40 equivalents of potassium permanganate were added in batches of eight equivalents hourly. After filtration through celite the crude product was confirmed by ^{1}H-NMR. Protection as an ester was performed without further purification. The protection was carried out using dimethyl carbonate (DMC) in sulfuric acid at 80 °C overnight. Unfortunately, after work-up for both steps together only a 33% yield was obtained. The yield of crude carboxylic acid was 79% and therefore the loss of yield was predominantly from the esterification that proceeded in 42% yield.



2.47 **2.48** **2.49**

Scheme 2.18: *Synthesis of ester en route to* ***meta-IDTT****.*[142]

The oxidation was scaled-up and again required addition of very large amounts of potassium permanganate, completing in 100% yield. Further esterification using DMC gave a poor 25% yield. Therefore, attempts to improve the esterification yield were investigated. A series of esterifications using different reagents and conditions were attempted (**Scheme 2.19**).

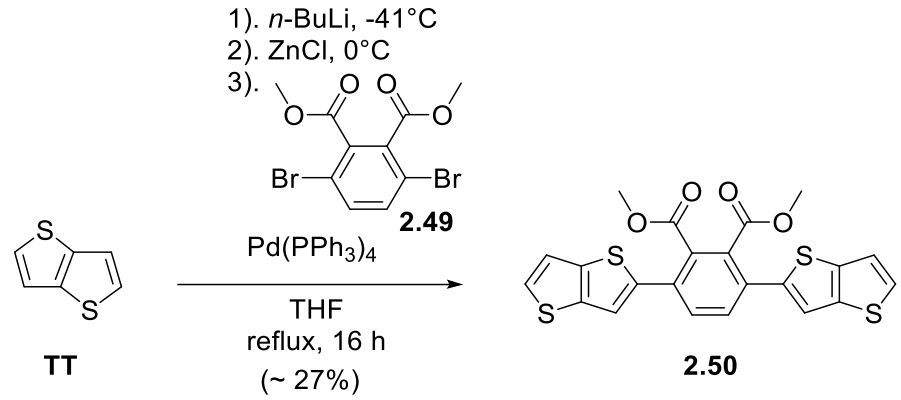


2.48 **2.49**

Scheme 2.19: *Modified ester syntheses with four sets of reaction conditions and their yields shown.*[142,145,146]

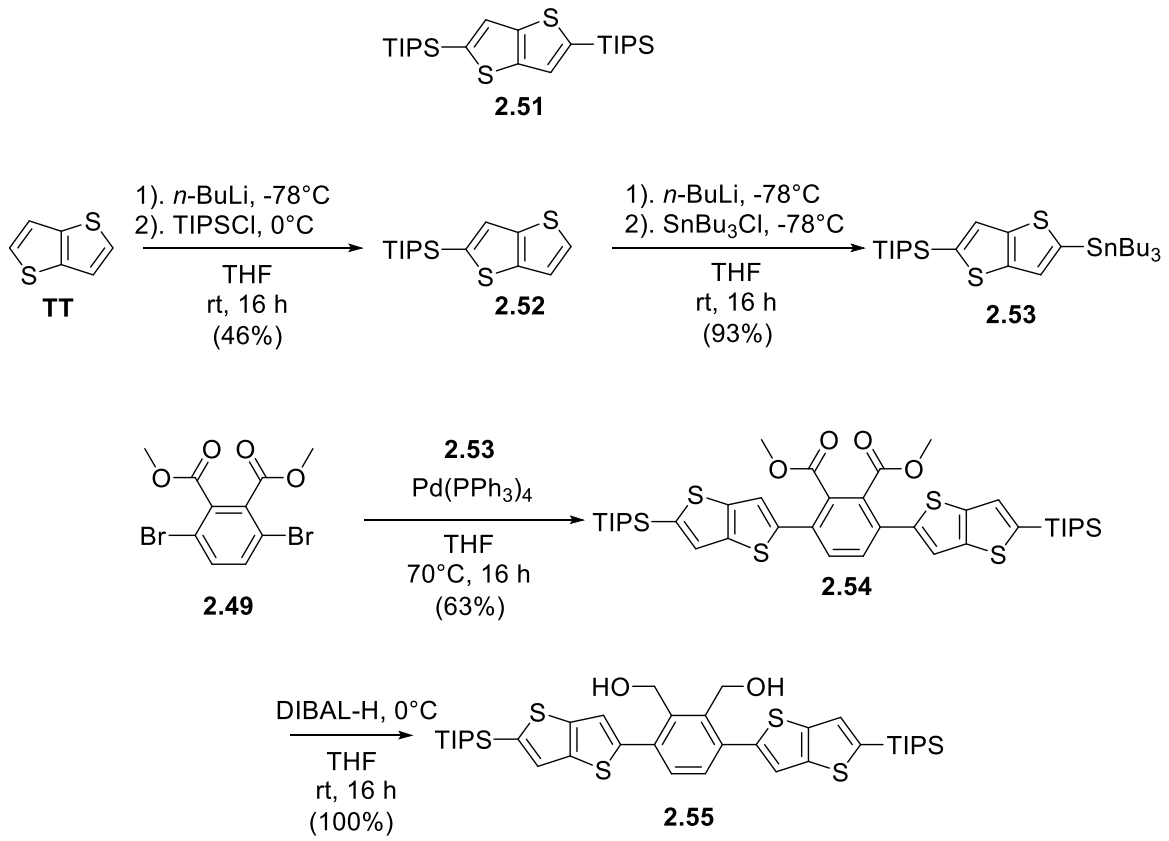
Esterification using methanol instead of DMC was performed according to literature procedure, giving only 18% yield.[147] The $SOCl_2$ method has been performed in literature both with heating and at room temperature and therefore both methods were attempted.[145,148] However, neither $SOCl_2$ reaction gave high yields, with the refluxed reaction giving a 29% yield. To confirm that this yield wasn't reduced by the presence of water having a greater effect on degrading $SOCl_2$ in the small-scale reaction, a scale-up was performed. However, on scale-up the reaction still gave a poor 20% yield, leaving DMC as the best option for protection.

The first coupling attempted with **TT** was a one-pot Negishi cross-coupling, as most used for previously mentioned cores (**Scheme 2.20**). Unfortunately, after column chromatography the product was still impure due to streaking in the column and close R_F values for bands of impurities and product. Moreover, the mass of this crude product gave a reaction yield of only 27%. Due to the poor yield of the crude product, further purification was not attempted, and other methods of coupling were investigated for scale up. It was hypothesised that a low yield was obtained because the steric interactions between the ester groups may partially block the approach of the organozinc species more than in the equivalent step for the synthesis of **IDTT** (**Scheme 2.7**).



Scheme 2.20: *Attempted Negishi coupling.*

To maximise the yield of this coupling step, more forcing Stille conditions that allow higher temperature reflux in toluene compared to THF were used (**Scheme 2.21**). Furthermore, the purity of **2.53** was maximised by protection with a TIPS group prior to stannylation. This additionally improves the solubility of the product, both aiding its reaction and purification.

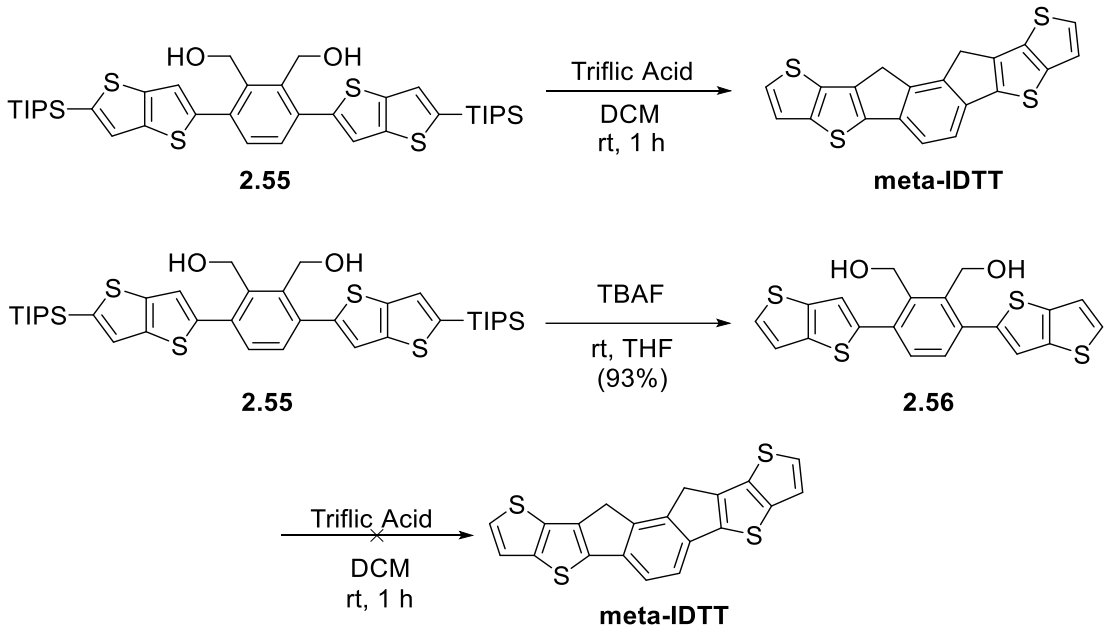


Scheme 2.21: *Route taken towards* ***meta-IDTT****.*[149]

It was predicted that **TT** would have a greater difference in R_f compared to **2.52**, than **2.52** would in comparison to **2.51**. This was because the presence of the alkyl chains on the TIPS groups would dominate and increase the R_F of the compounds in a petroleum ether-based eluent. Consequently, only 0.9 equivalents of TIPSCl were used in the synthesis of **2.52** to limit production of **2.51**. After column chromatography, **2.52** was obtained in 46% yield. Only a small fraction of **2.51** was collected, and it is believed that its small size greatly helped the purification as the fraction did not spread to overlap with **2.52**. Stannylation with tributyltin chloride proceeded successfully in a high yield.

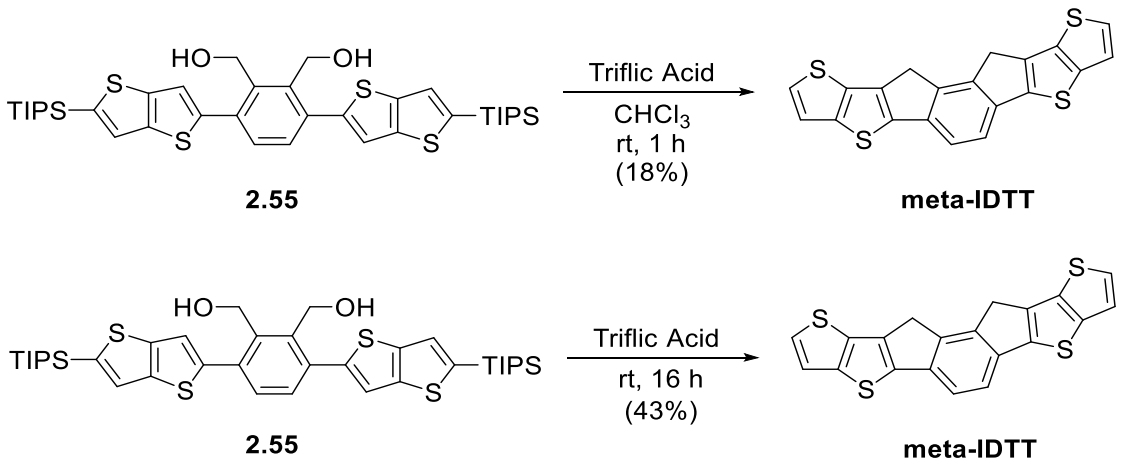
A Stille coupling repeating the conditions used towards **IDTBt** and the pure product was performed and **2.54** was obtained in a good 63% yield. The following reduction with DIBAL-H proceeded in quantitative yield with the TIPS group likely aiding the reaction by solubilising the reactant in THF. The TIPS protecting group has been shown to be resistant to acidic conditions in literature, with reaction times of 2 h using HF or 16 h with HCl being used for desilylation of the more common ether form OTIPS.[150,151] As the solvated triflic acid reaction has much shorter reaction time it was used in hope that TIPS groups would not be

removed and help with solubility for the planned future alkylation of the core, however, unfortunately the resultant **meta-IDTT** was deprotected during reaction (**Scheme 2.22**). After quench with sodium bicarbonate a TLC of the product was taken and it was found to have little streaking and apparently good solubility in a 50:50 hexane:chloroform eluent. Therefore, an aqueous work-up with extraction using chloroform in a separating funnel and drying on magnesium sulphate was performed. Afterwards, column chromatography was carried out on the crude product, however only trace product was obtained when confirmed by MS.



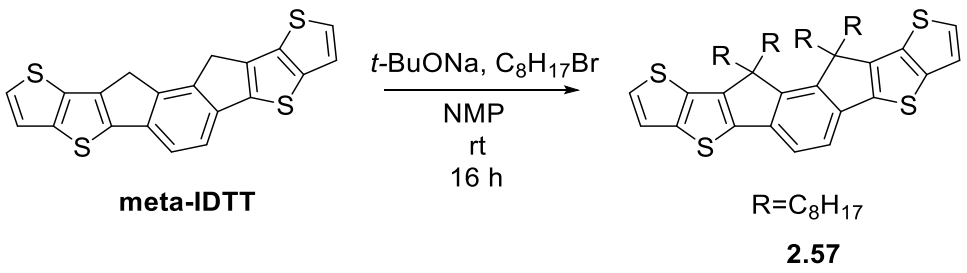
Scheme 2.22: *First synthesis of* ***meta-IDTT****.*

The poor yield of the cyclisation could have been because the TIPS groups interfered in the reaction in some way. Therefore, to reduce complexity a tetra-*n*-butylammonium fluoride (TBAF) deprotection was performed before the triflic acid step. However, after the solvated methodology for the ring closing was used on **2.56**, no significant product peak was observed in the mass spectrum of the crude product. It was hypothesised that the reaction was not very favourable and could only occur with **2.56** solubilised with TIPS groups. The reaction on **2.55** was again repeated, but with chloroform which was deemed more solubilising than DCM (**Scheme 2.23**).



Scheme 2.23: *Successful synthesis of* ***meta-IDTT****.*

Because of fears that yield may be lost through column chromatography, the reaction was purified by silica plug and washes with hexane, DCM, and acetone to collect multiple fractions were employed. The product was found largely in the hexane fraction but was not completely pure. This crude product gave a yield of 18%. Finally, it was thought that perhaps the low yields of the ring closing were in fact being caused by use of the solvated method. Therefore, the ring closing was repeated using the original triflic acid ring closing methodology without any additional solvent. The reaction mixture was quenched with sodium acetate and washed with water and methanol. Afterwards attempts to purify the product by trituration in multiple organic solvents did not improve its purity. Therefore, column chromatography was undertaken giving the pure product in a good 43% yield, indicating the improved performance of the neat reaction.



Scheme 2.24: *Alkylation of* ***meta-IDTT****.*

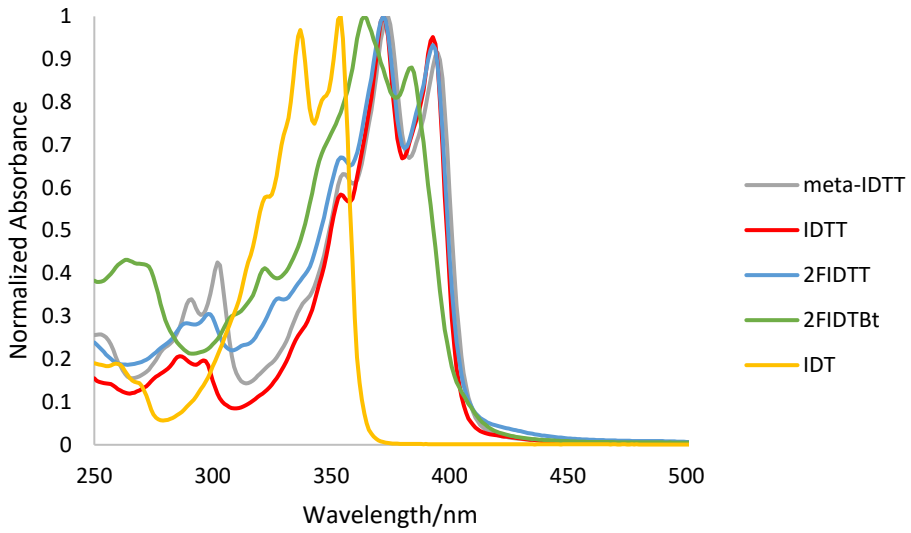
The **meta-IDTT** core was alkylated by the same procedure as used with **IDTBt** and **2FIDTBt** (**Scheme 2.24**). After aqueous work-up with chloroform extraction and removal of solvent the product was purified by column chromatography. The product was confirmed by MS but

only trace amounts were collected from the column. Because the reaction was only performed on an 11 mg scale it is possible that this extremely low yield was due to losses to adsorption on silica or because of an inaccurate mass of octyl bromide being measured out by syringe for this reaction. Alternatively, the steric hindrance between the R groups on the alkylated product may have interfered with the reaction. A repeat at larger scale would be required to confirm what the issue affecting the alkylation is. However, there was not sufficient time to perform this.

2.2.7 – Optoelectronic and Electrochemical Properties of Cores

Ultraviolet-visible (UV-Vis) spectra were taken of the cores in chloroform with optical bandgaps calculated (**Figure 2.11**). Additionally drop cast cyclic voltammetry (CV) traces were taken (**Appendix 7.1.1**). LUMO energy levels were too shallow and couldn't be estimated by CV, and therefore only the HOMO energy levels are given.

(a)



Core	Meta-IDTT	IDTT	2FIDTT	2FIDTBt	IDT
Maximum (nm)	374	372	371	363	354
Absorption Onset (nm)	452	449	413 - 485	417 - 465	374
Optical Bandgap (eV)	2.74	2.76	3.00 - 2.56	2.97 - 2.67	3.32

(b)

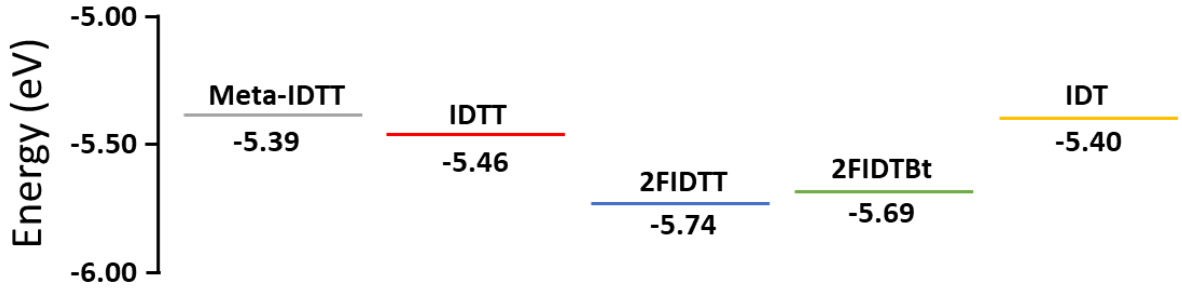


***Figure 2.11:* (a)** *Normalised UV-Vis spectra and bandgap table for cores in chloroform solution.* **(b)** *HOMO energy levels estimated for cores by CV on drop-cast films in 0.1 M solution of Bu_4NPF_6 in acetonitrile, using a ferrocene (Fc/Fc+) internal standard.*

Accurate estimation of the absorption onset for **2FIDTBT** and **2FIDTT** was difficult due to impurities in the sample contributing to the absorption onset. Therefore, approximate values are given for these cores, taking the initial absorption onset up to the major point of

inflection of the curves. As expected, **meta-IDTT** and **IDTT** have similar bandgaps as both are regioisomers and aren't cross-conjugated. Based on the data, it's impossible to say whether the two fluorinated cores are wider or shorter bandgap than the **IDTT** isomers. Logically, **2FIDTT** should have a similar bandgap to the **IDTT** isomers, with the fluorine deepening both HOMO and LUMO energy levels slightly. **2FIDTBt** would be expected to have a wider bandgap due to the deeper HOMO energy level of the **Bt** component.

The ionisation potential (IP) of each core was measured by CV as an estimation for the HOMO energy level of the core. The cores were drop cast onto the working electrode from chloroform and tested in acetonitrile solution with Bu_4NPF electrolyte. All CV traces for this thesis are given in the appendix. As the films would delaminate under measurement, it was difficult to see clear reversibility in the core's oxidation. Therefore, the onset of oxidation was referenced against a ferrocene/ferrocenium redox couple (Fc/Fc^+) giving the oxidation potential E^{OX}. This was then extrapolated from the IP of ferrocene relative to the vacuum level as per **Equation 2.1** to give the IP for the core. An IP of -4.8 eV was assumed for ferrocene as is usually done for such measurements.[152] The IP was then assumed to equal the HOMO energy level for data analysis.

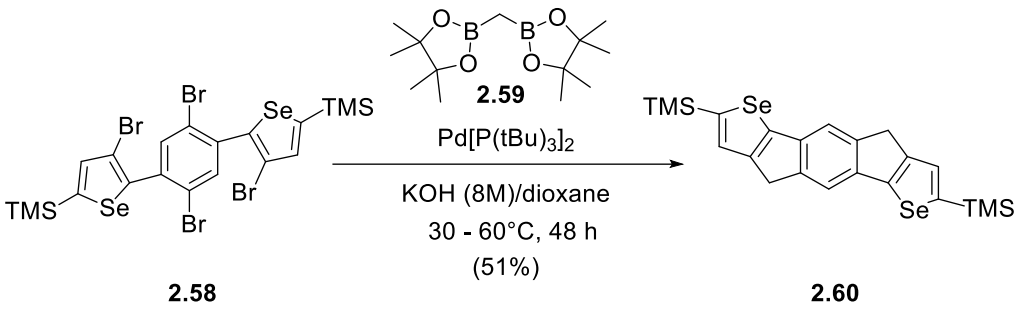
$$\boldsymbol{IP = -(E^{OX} + 4.8)eV}$$

Equation 2.1: *Formula for ionisation potential calculation from CV.*

As expected, the two **IDTT** isomers had similar HOMO energy levels, whilst fluorination lowered the HOMO levels deeper for **2FIDTT** and **2FIDTBt**. The difference in the energy levels between **2FIDTT** and **2FIDTBt** is within the error expected for CV measurements, it's likely that **2FIDTBt** has a deeper HOMO level due to the more electron accepting nature of benzothiophene as opposed to thienothiophene. Without knowing the LUMO energy levels of the fluorinated cores it's impossible to comment on their bandgap. However, the depressed HOMOs indicate that they would form wider bandgap NFAs than when **IDTT** or **meta-IDTT** are used because the HOMOs for the NFAs would be localised on the electron donating component. Unexpectedly, **IDT** has the second most shallow HOMO energy level. This is surprising because **IDT** had by far the widest optical bandgap and it's unlikely that the LUMO energy level alone is raised enough to accommodate this. It's possible that intermolecular interactions between the un-substituted **IDT** molecules in the drop cast films

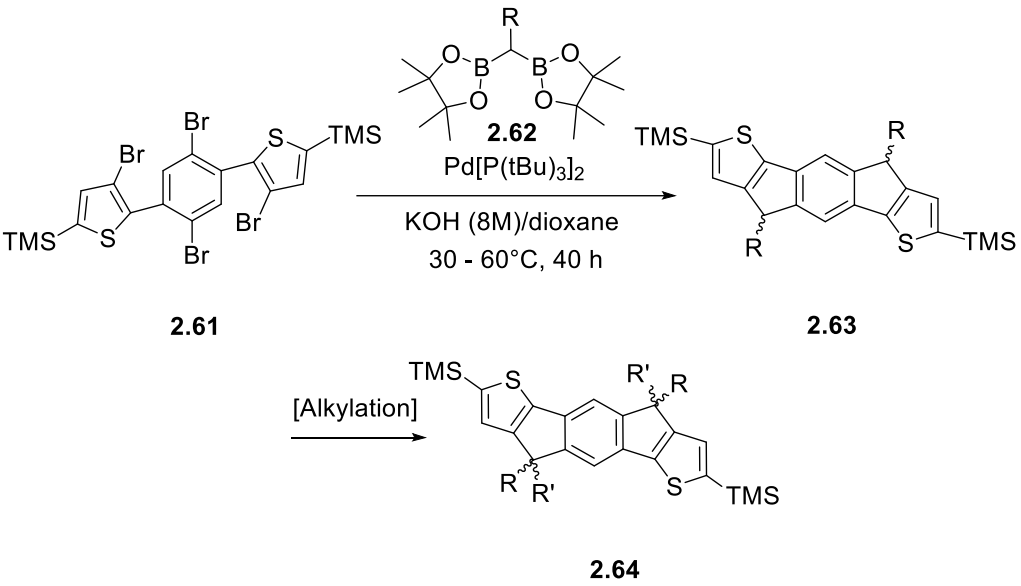
lowered their HOMOs, an effect not observed in the solution UV-Vis spectra. Alternatively, error in the CV measurements caused this pattern.

2.2.8 – Asymmetric Sidechain IDT via Double Suzuki Coupling



Scheme 2.25: *Literature double Suzuki coupling reaction.*[153]

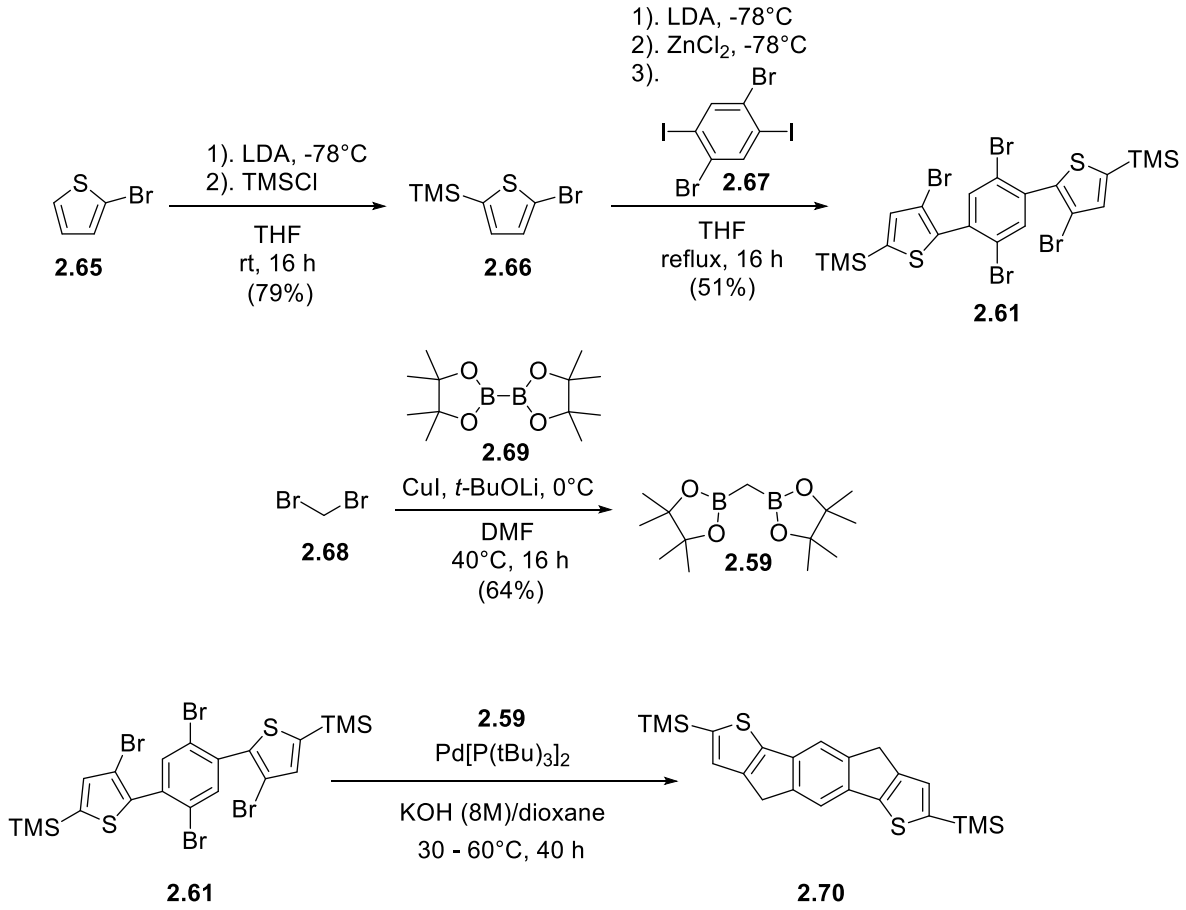
To access **IDT** with asymmetric sidechains we originally planned to build upon the double Suzuki coupling chemistry developed in our group with selenophene derivatives of **IDT** (**Scheme 2.25**).[153]



Scheme 2.26: *Proposed route towards asymmetric chain **IDT** via double Suzuki coupling.*

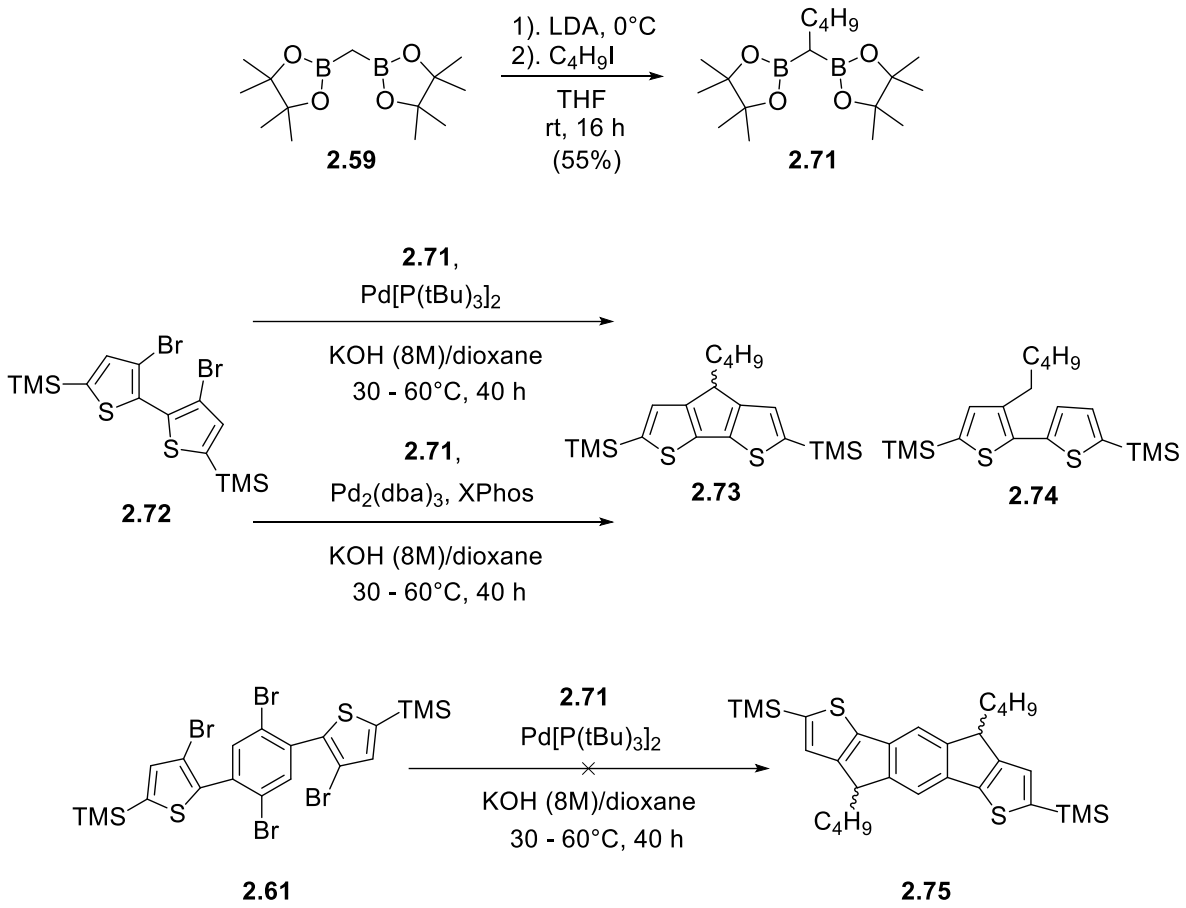
It was predicted that an alkyl (R) chained boronic ester could be used to functionalise **IDT** with an alkyl chain during ring closing via a double Suzuki coupling, forming **2.63** (**Scheme 2.26**). Alkylation would then be performed to prepare **2.64** as a racemic mixture. Further

functionalisation after removal of trimethylsilyl (TMS) groups could then be used to prepare more complex materials for use in organic electronics.



Scheme 2.27: *Synthesis of silyl-protected* ***IDT*** *via double Suzuki coupling.*[154,155]

IDT derivative **2.70** was prepared to confirm if modification of selenium to sulphur in **2.58** inhibits double Suzuki coupling (**Scheme 2.27)**. Firstly, **2.65** was successfully protected with a TMS group and used in a one-pot Negishi coupling. The coupling procedure first involved treatment of **2.66** with LDA that moved the bromine to the thiophene's "3" position via a halogen dance and abstracted a hydrogen for zinc chloride substitution.[156] After reaction with zinc chloride, Negishi coupling with **2.67** prepared **2.61** in a 51% yield, a high yield when the complexity of the one-pot reaction is considered. The boronic ester **2.59** was prepared by a copper mediated substitution on **2.68**.[157] A test double Suzuki coupling produced **2.70**, this result was confirmed by ^{1}H-NMR and MS (**Figure 7.1.36**).



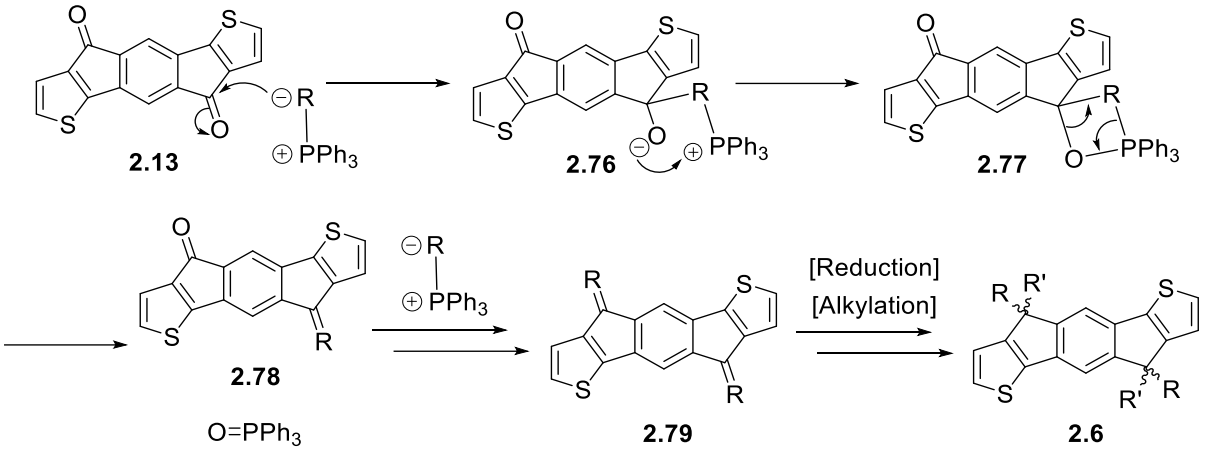
Scheme 2.28: *Synthesis of **2.72** via a double Suzuki coupling and attempted synthesis of **2.74**.* [154]

Since the double Suzuki coupling towards **2.70** proceeded successfully, alkyl chained boronic ester **2.71** was prepared by a nucleophilic substitution on butyl iodide (**Scheme 2.78**). A short alkyl chain was used to minimise the effect of steric hindrance on the double Suzuki coupling. A simpler cyclopentadiene derivative **2.73** with one ring closing site was first targeted by double Suzuki coupling to confirm its effectiveness. However, when the same conditions were used as for the synthesis of **2.70**, only trace product was obtained after recycling preparative gel permeation chromatography (GPC) was performed in chloroform on the crude product. Both **2.73** and **2.74** were detected by MS together with other unknown impurities, indicating incomplete reaction and side-products. In an attempt to prepare a greater yield of **2.73** a 2-dicyclohexylphosphino-2',4',6'-triisopropylbiphenyl (XPhos) Buckwald ligand was combined with $Pd_2(dba)_3$ to form a more reactive catalyst in-situ for double Suzuki coupling.[158] Unfortunately, **2.73** wasn't detected in the crude product's ^{1}H-NMR and only trace amounts of **2.73** were collected by recycling preparatory

GPC and confirmed by MS. A double Suzuki coupling using $Pd[P(tBu)_3]_2$ and **2.71** was also attempted on **2.61**. However**,** no product **2.75** was detected by MS indicating that the double Suzuki coupling route isn't appropriate towards asymmetric chain **IDT** synthesis.

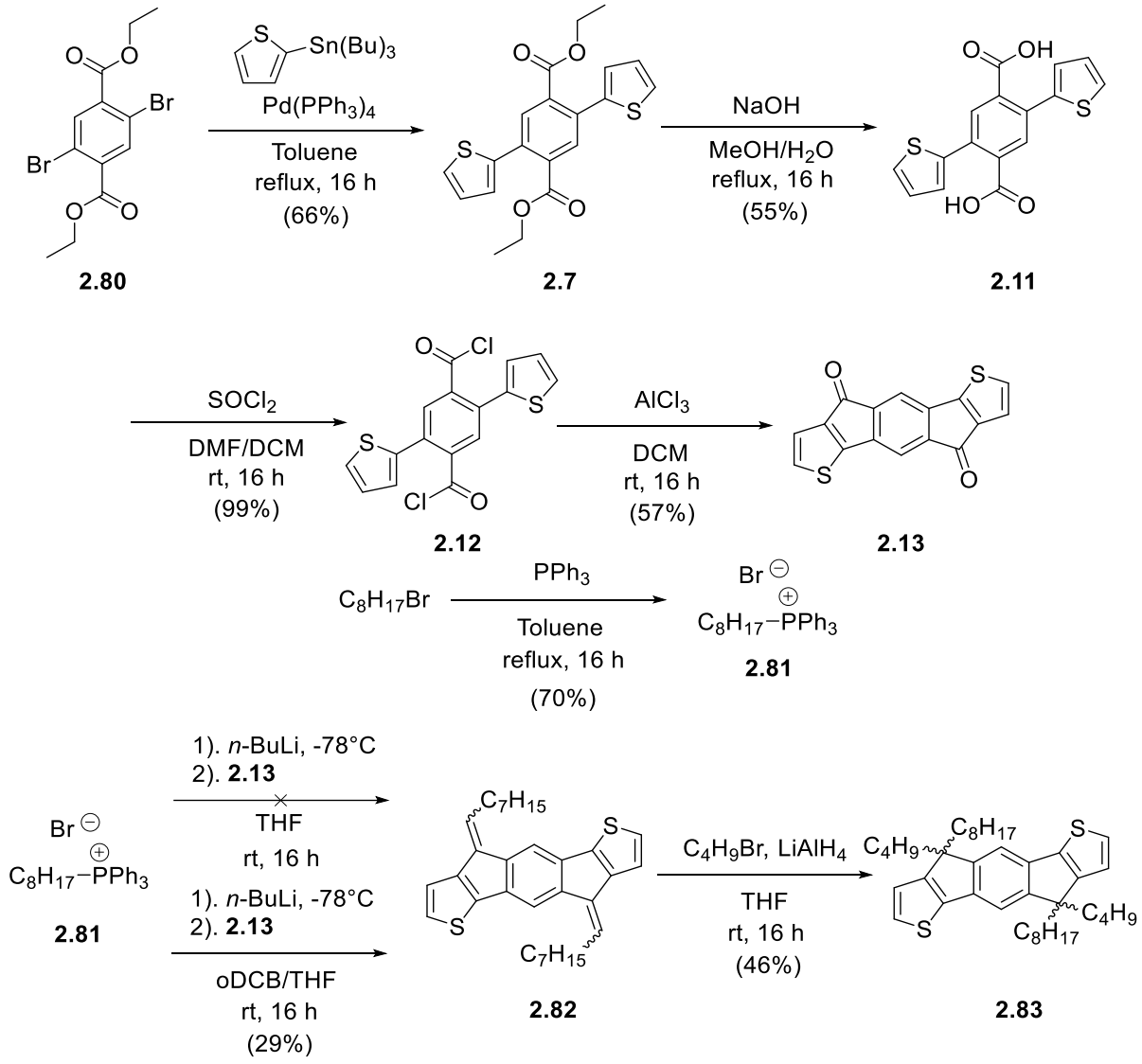
2.2.9 – Asymmetric Sidechain IDT via the Wittig Reaction

Due to the impracticality of the double Suzuki coupling route, the Wittig reaction was investigated instead to produce **IDT** with asymmetric sidechains. The Wittig reaction would be performed on the ketone **2.13** to produce **2.78**, followed by a second in-situ Wittig reaction to prepare **2.79 (Scheme 2.29)**. Further reduction and alkylation could then be carried out to produce asymmetric chain **IDT** (**2.6**). The proposed methodology is expected to produce **2.6** as a racemic mixture as with the double Suzuki coupling route.



Scheme 2.29: *Mechanism for the Wittig reaction on* ***2.13*** *and illustration of proposed subsequent steps towards asymmetric chain* ***IDT****.*

The mechanism for the required Wittig reaction begins with nucleophilic attack onto **2.13** by the ylide's anionic carbon. The produced anionic oxygen then attacks the phosphorus cation forming an oxaphosphetane intermediate. The aforementioned two steps may also occur as a concerted [2+2] cycloaddition, further mechanistic studies would be necessary to confirm this.[159] The unstable four-membered ring decomposes by a reverse [2+2] cycloaddition producing **2.78** and a phosphine oxide. The strong phosphorus-oxygen double bond formed acts as the thermodynamic driving force for the Wittig reaction.



Scheme 2.30: *Synthesis of* ***2.13*** *and subsequent Wittig reaction followed by reduction/alkylation towards* ***2.83****.*[104,108]

To perform the Wittig Reaction, the ketone **2.13** was first synthesised (**Scheme 2.30**). A Stille coupling was performed successfully using commercial 2-(tributylstannyl)thiophene to form **2.7**. The ester was deprotected to a carboxylic acid in a poor 54% yield, likely due to the poor solubility of **2.7** in methanol and an insufficient reaction time. Treatment with thionyl chloride produced the necessary acyl chloride that was successfully cyclised to **2.13** by a Friedel-Crafts acylation.

Phosphonium salt **2.81** was prepared by nucleophilic substitution of triphenylphosphine onto octyl bromide. Afterwards, deprotection with *n*-butyl lithium formed an ylide in-situ

that was reacted with **2.13**. THF was at first used for the in-situ formation of the Wittig reagent and its Wittig Reaction. However, no product was obtained as **2.13** wasn't soluble enough in THF to react. Therefore, the ylide was prepared in THF and then transferred to a solution of **2.13** in 1,2-dichlorobenzene (oDCB) instead. Due to concerns about reaction between *n*-butyl lithium and oDCB, no excess of *n*-butyl lithium was used and the phosphonium salt stirred with *n*-butyl lithium for 1 hr to ensure complete reaction. After stirring overnight, **2.82** was obtained in 29% yield. It's believed that this low yield was predominantly due to **2.13** partially crashing out of solution when THF was mixed with oDCB. The alkene was reduced using lithium aluminium hydride and alkylated in-situ with butyl bromide producing **2.83** in 46% yield.

2.3 – Conclusions

Six cores were synthesised for use in organic electronics through a triflic acid ring closing. Four cores are novel, whilst two have been produced with improvements to their synthesis (**Figure 2.12**).

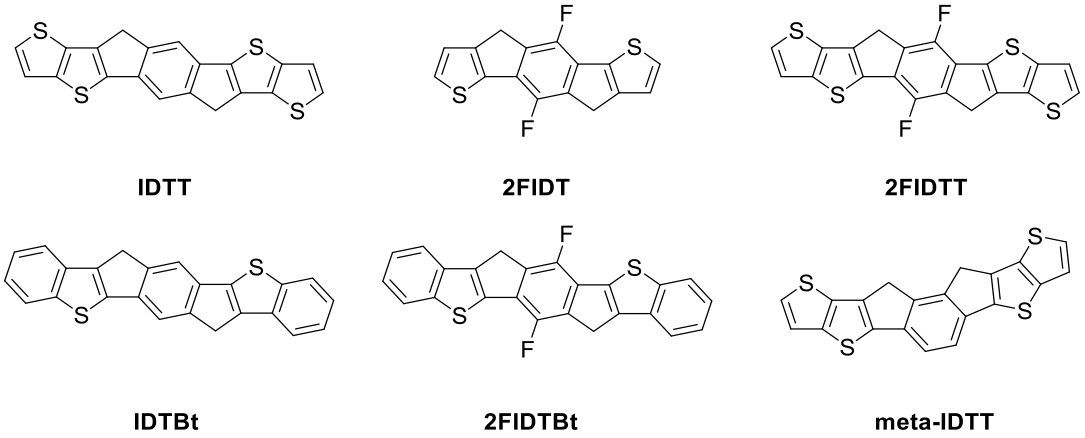


Figure 2.12: *Synthesised cores.*

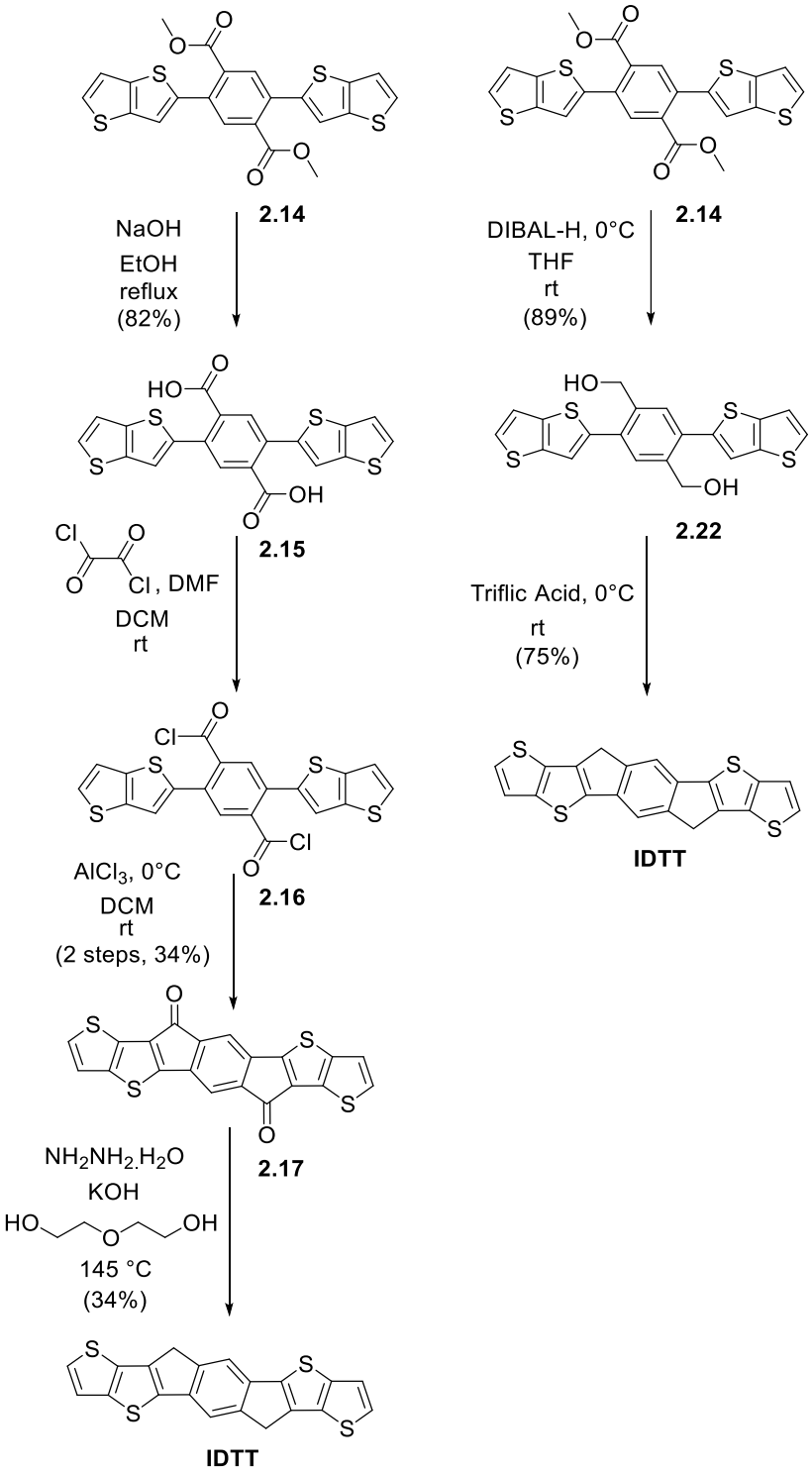
Not all cores are optimal for production by the triflic acid reaction, as may be seen in **Table 2.1**. It would not be recommended to produce **IDTBt** or **2FIDTBt** via the methodology employed in this chapter. The low yields of the triflic acid ring closings to form these cores coupled with the likely future loss in yield due to unselective bromination to allow further functionalisation of the cores make this route very low yielding overall (**Scheme 2.13**). However, the four other cores are amenable to the methodology and the route taken is suitable to produce them in sufficient amounts for further modification to organic electronics materials.

Table 2.1: *Synthetic yield of triflic acid ring closing for synthesised cores.*

CORE	IDTT	2FIDT	2FIDTT	IDTBT	2FIDTBT	META-IDTT
YIELD	75%	70%	55%	<5%	16%	43%

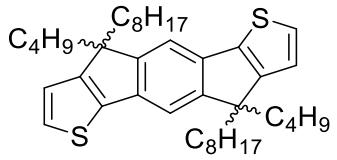
The route taken is both shorter and higher yielding than pathways taken in the past towards the cores, with a clear example being the triflic acid route towards **IDTT** taking two steps

from the ester **2.14** and proceeding in 66.8% overall yield whilst the literature route with reduction of a ketone takes four steps and proceeds in 9.5% overall yield (**Scheme 2.31**).[121]



Scheme 2.31: *Side by side view of ketone reduction route (left) and triflic acid route (right) to* ***IDTT****.*[121]

IDTT and **meta-IDTT** had similar HOMO energy levels and optical bandgaps, whilst the fluorinated cores had a reduced HOMO energy level. Due to difficulties in purification predominantly caused by the cores' insolubility, accurate optical bandgaps couldn't be obtained for the fluorinated cores.

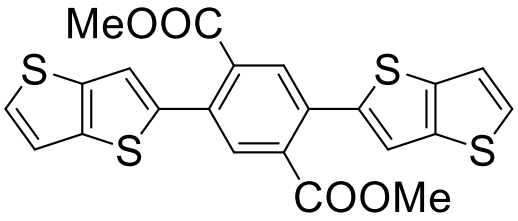


2.83

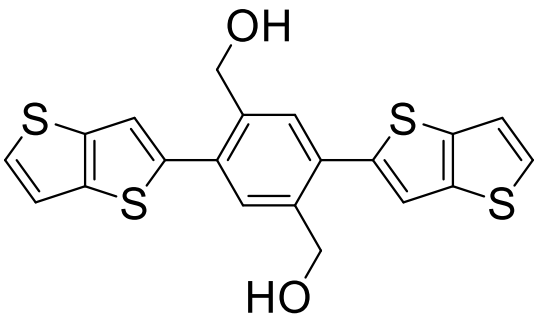
Figure 2.13*: Asymmetric IDT core synthesised by the Wittig reaction route.*

In addition to the unsubstituted cores, the novel asymmetric chain **IDT** derivative **2.83** was successfully synthesised via a Wittig reaction route (**Figure 2.13**). This novel route opens the possibility for careful tuning of the morphology of organic electronics materials that contain the **IDT** core by careful modification of each sidechain. Attempts to produce **2.83** via a double Suzuki coupling route were unsuccessful.

2.4 – Experimental

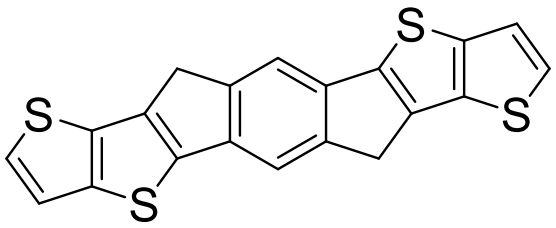


Dimethyl 2,5-bis(thieno[3,2-b]thiophen-2-yl)terephthalate (2.14): To thieno[3,2-b]thiophene (4.67 g, 30.3 mmol) in THF (120 mL) at -41 °C was added n-butyl lithium (1.6 M in hexanes, 20.8 mL, 33.3 mmol) dropwise. After 30 mins, zinc chloride (0.7 M in THF, 48.5 mL, 34.0 mmol) was added and the solution stirred for a further hour. Dimethyl 2,5-dibromoterephthalate (5.08 g, 14.4 mmol) and tetrakis(triphenylphosphine)palladium(0) (768 mg, 0.665 mmol) were added and the solution heated to reflux for 16 h. The reaction mixture was diluted with 100 mL of water and the crude product extracted with DCM (3 x 50 mL). The organic phase was washed with water (3 x 50 mL), brine (50 mL), and dried over anhydrous magnesium sulphate. After removal of solvent *in vacuo*, purification by silica gel chromatography (DCM) was performed thrice, giving the *title compound* as a light-yellow solid (5.92 g, 95%). ^{1}H NMR (400 MHz, Chloroform-d) δ(ppm) 7.89 (s, 2H), 7.41 (d, *J* = 5.0 Hz, 2H), 7.31 (s, 2H), 7.28 (d, *J* = 5.0 Hz, 2H), 3.80 (s, 6H). ^{13}C NMR (101 MHz, CDCl3) δ 167.90, 141.87, 140.07, 139.48, 133.75, 133.63, 132.15, 127.54, 119.47, 119.26, 52.78. MS (ESI-ToF) *m/z*: 470.98 (M+).

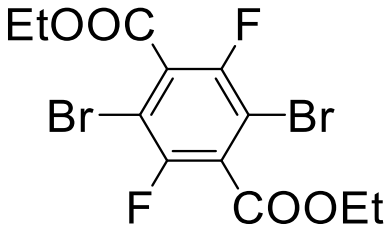


(2,5-Bis(thieno[3,2-b]thiophen-2-yl)-1,4-phenylene)dimethanol (2.22): Diisobutylaluminum hydride solution (1 M in THF, 75.4 mL, 75.4 mmol) was added over 30 mins to dimethyl 2,5-bis(thieno[3,2-b]thiophen-2-yl)terephthalate (5.82 g, 12.6 mmol) in THF (250 mL) at 0 °C and then allowed to warm to room temperature over 16 h. The solution was cooled to 0 °C and hydrochloric acid (2 M, 600 mL) was added over 30 mins followed by concentrated

hydrochloric acid (8 mL). Volatiles were removed under reduced pressure and the crude product collected by filtration. The product was washed with water (3 x 50 mL), and methanol (3 x 50 mL) giving the *title compound* as a beige solid (4.58 g 89%). ^{1}H NMR (400 MHz, DMSO) δ 7.76 – 7.67 (m, 6H), 7.51 (d, *J* = 5.3 Hz, 2H), 4.68 (s, 4H). ^{13}C NMR (101 MHz, DMSO) δ 143.02, 139.80, 139.23, 138.93, 132.66, 130.27, 128.74, 120.46, 120.33, 61.30. MS (EI-ToF) *m/z*: 413.98 (M^{+}).

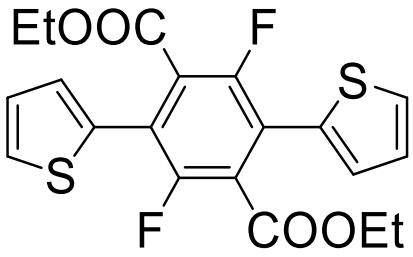


6,12-Dihydrothieno[3,2-b]thieno[2'',3'':4',5']thieno[2',3':5,6]-s-indaceno[2,1-d]thiophene (IDTT): To (2,5-bis(thieno[3,2-b]thiophen-2-yl)-1,4-phenylene)dimethanol (987 mg, 2.38 mmol) at -5 °C was added triflic acid (8 mL) over 30 mins and the reaction left at room temperature for 60 h. The reaction mixture was poured in ice (40 g), washed with water (40 mL), saturated sodium acetate (40 mL), water (40 mL), and methanol (40 mL). Afterwards the crude product was dissolved in boiling CB (50 mL) and filtered collecting the filtrate, the residue was then subjected to this extraction with CB four more times. Solvent was removed from the combined filtrates under reduced pressure yielding the *title compound* as a beige powder (680 mg, 75%). Compound decomposes above 251 °C. ^{1}H NMR (400 MHz, TCE-d2) δ 7.70 (s, 2H), 7.42 (d, *J* = 5.3 Hz, 2H), 7.39 (d, *J* = 5.2 Hz, 2H), 3.92 (s, 4H). MS (EI-ToF) *m/z*: 377.9766 (M^{+}).

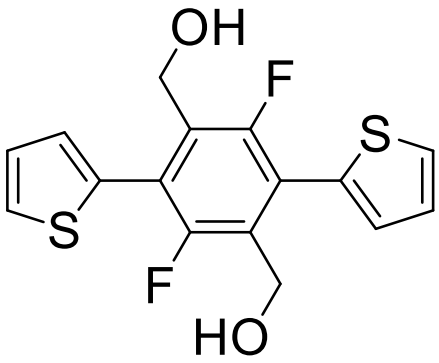


Diethyl 2,5-dibromo-3,6-difluoroterephthalate (2.27): 1,4-dibromo-2,5-difluorobenzene (5.47 g, 20.1 mmol) in THF (60 mL) was added to 2,2,6,6-Tetramethylpiperidinylmagnesium chloride lithium chloride complex solution (1M in THF:toluene, 46.3 mL, 46.3 mmol) at -41 °C over 30 mins. After 5 h at -41 °C, ethyl chloroformate (4.62 mL, 4.83 mmol) was added

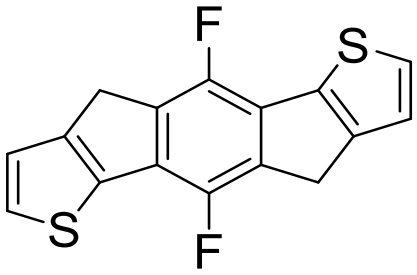
and the solution was left at room temperature for 16 h. After quenching with hydrochloric acid (1 M, 115 mL) over 30 mins, the product was extracted with diethyl ether (3 x 50 mL) and dried over anhydrous magnesium sulphate. Following removal of solvent *in vacuo*, the crude product was triturated in cold hexane, filtered, and washed with cold hexane (3 x 50 mL) yielding the *title product* as an off-white solid (3.552 g, 42%). ^{1}H NMR (400 MHz, Chloroform-d) δ (ppm) 4.47 (q, *J* = 7.1 Hz, 4H), 1.41 (t, *J* = 7.1 Hz, 6H). ^{19}F NMR (377 MHz, CDCl3) δ -108.72 (s). ^{13}C NMR (101 MHz, Chloroform-d) δ 161.43, 152.27 (dd, ^{1}J = 252.3 Hz, ^{4}J = 4.6 Hz, CF), 127.21 – 126.50 (m, CF), 107.81 – 107.03 (m, CF), 63.22, 14.03.



Diethyl 2,5-difluoro-3,6-di(thiophen-2-yl)terephthalate (2.29): To thiophene (2.52 mL, 31.5 mmol) in THF (90 mL) at -41 °C was added n-butyl lithium (1.6 M in hexanes, 19.7 mL, 31.5 mmol) dropwise. After 30 mins, zinc chloride (0.7 M in THF, 45.9 mL, 32.1 mmol) was added. After an hour, diethyl 2,5-dibromo-3,6-difluoroterephthalate (5.69 g, 13.7 mmol) and tetrakis(triphenylphosphine)palladium(0) (789 mg, 0.683 mmol) were added, and the solution heated to reflux for 16 h. The reaction mixture was poured into water (400 mL) and filtered. Washing with water (3 x 100 mL) and methanol (3 x 100 mL) yielded the *title product* as a light yellow solid (4.03 g, 70 %).^{1}H NMR (400 MHz, Chloroform-d) δ (ppm) 7.50 (dd, *J* = 5.4, 1.3 Hz, 2H), 7.21 (dd, *J* = 3.6, 1.3 Hz, 2H), 7.11 (dd, *J* = 5.4, 3.6 Hz, 2H), 4.24 (q, *J* = 7.1 Hz, 4H), 1.16 (t, *J* = 7.1 Hz, 6H). ^{19}F NMR (377 MHz, Chloroform-d) δ (ppm) -119.48. ^{13}C NMR (101 MHz, CDCl3) δ 163.53, 152.01 (d, ^{1}J = 252.6 Hz, CF), 130.96, 129.53, 128.27, 127.24, 126.21 – 125.85 (m, CF), 123.12 – 121.10 (m, CF), 62.41, 13.78.

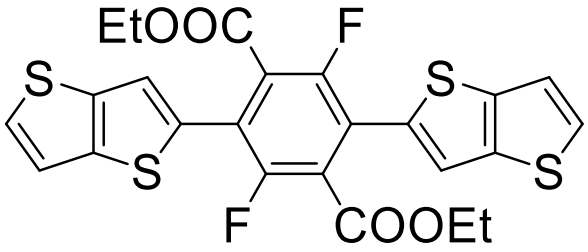


(2,5-Difluoro-3,6-di(thiophen-2-yl)-1,4-phenylene)dimethanol (2.30): Diisobutylaluminum hydride solution (1 M in THF, 1.53 mL, 1.53 mmol) was added over 30 mins to diethyl 2,5-difluoro-3,6-di(thiophen-2-yl)terephthalate (108 mg, 0.256 mmol) in THF (1 mL) at -78 °C, and the solution allowed to warm to room temperature over 16 h. The solution was cooled to 0 °C and quenched by addition of hydrochloric acid (2 M, 11 mL) over 30 mins followed by concentrated hydrochloric acid (0.1 mL). The product was extracted with diethyl ether (3 x 5 mL), washed with water (3 x 5 mL), brine (5 mL), and dried over anhydrous magnesium sulphate yielding the *title product* as a light beige solid (78 mg, 90%). ^{1}H NMR (400 MHz, DMSO-d) δ 7.80 (dd, *J* = 5.3, 1.4 Hz, 2H), 7.38 (dd, *J* = 3.5, 1.4 Hz, 2H), 7.24 (dd, *J* = 5.3, 3.5 Hz, 2H), 5.30 (t, *J* = 5.0 Hz, 2H), 4.43 – 4.35 (m, 4H). ^{19}F NMR (377 MHz, DMSO-d) δ (ppm) -119.44. ^{13}C NMR (101 MHz, DMSO) δ 154.76 (d, ^{1}J = 246.2 Hz, CF), 131.91, 130.41, 128.80, 128.72 - 128.40 (m, CF), 127.65, 123.90 – 124.82 (m, CF), 54.95.

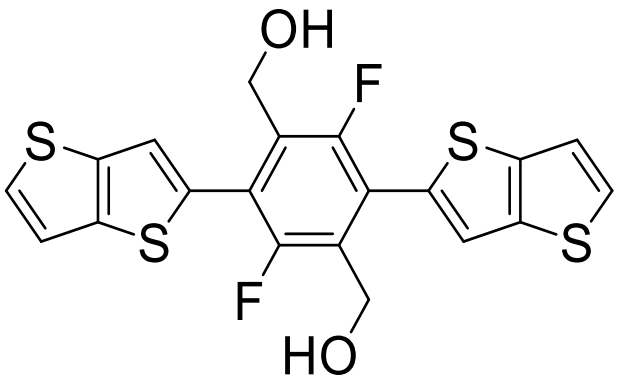


5,10-Difluoro-4,9-dihydro-s-indaceno[1,2-b:5,6-b']bisthiophene (2FIDT): To (2,5-difluoro-3,6-di(thiophen-2-yl)-1,4-phenylene)dimethanol (2.3 g, 6.8 mmol) at -5 °C was added triflic acid (25 mL) over 30 mins and the reaction allowed to warm to room temperature over 48 h. The reaction mixture was poured in ice (100 g), washed with water (100 mL), saturated sodium acetate (100 mL), water (100 mL), and methanol (100 mL). Afterwards the filtrate was dissolved in hot chloroform (200 mL) and passed through a silica plug with further washing with hot chloroform (3 x 50 mL). After solvent was removed *in vacuo*, the product

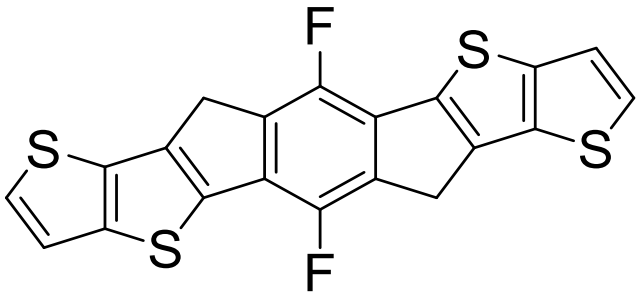
was obtained as a beige solid (496 mg, 24%). ^{1}H NMR (400 MHz, Chloroform-d) δ (ppm) 7.38 (d, *J* = 4.9 Hz, 2H), 7.12 (d, *J* = 4.9 Hz, 2H), 3.79 (s, 4H). ^{13}C NMR (101 MHz, $CDCl_3$) Chloroform-d) δ (ppm) 147.58 (dd, ^{1}J = 243.9 Hz, ^{4}J = 3.9 Hz, CF), 146.69, 138.29, 132.60 - 131.97 (m, CF), 128.94, 125.89 - 125.13 (m, CF) 122.45, 53.43. ^{19}F NMR (377 MHz, Chloroform-d) δ (ppm) -131.72. *m/z*: MS (EI-ToF): 302.00 (M^+).



Diethyl 2,5-difluoro-3,6-bis(thieno[3,2-b]thiophen-2-yl)terephthalate (2.31): To thieno[3,2-b]thiophene (4.45 g, 31.7 mmol) in THF (110 mL) at -41 °C was added n-butyl lithium (1.6 M in hexanes, 19.8 mL, 31.7 mmol) dropwise. After 30 mins, zinc chloride (0.7 M in THF, 46.3 mL, 32.4 mmol) was added. After 1 hr, diethyl 2,5-dibromo-3,6-difluoroterephthalate (5.50 g, 13.2 mmol) and tetrakis(triphenylphosphine)palladium(0) (764 mg, 0.661 mmol) were added and the solution heated to 75 °C for 16 h. The reaction mixture was poured into water (400 mL) and filtered under vacuum. After washes with water (3 x 100 mL) and methanol (3 x 100 mL) trituration with warm methanol yielded the *title product* as a light-yellow solid (6.11 g, 81%). ^{1}H NMR (400 MHz, Chloroform-d) δ (ppm) 7.45 (d, *J* = 5.3 Hz, 2H), 7.40 (s, 2H), 7.29 (d, *J* = 5.3 Hz, 2H), 4.27 (q, *J* = 7.1 Hz, 4H), 1.14 (t, *J* = 7.1 Hz, 6H). ^{13}C NMR (101 MHz, Chloroform-d) δ (ppm) 163.42, 152.16 (dd, ^{1}J = 250.8, ^{4}J = 4.7 Hz, CF), 141.28, 139.11, 132.34, 128.52, 125.61 - 125.16 (m, CF), 122.46 - 122.10 (m, CF), 121.90, 119.37, 62.61, 13.81. ^{19}F NMR (377 MHz, Chloroform-d) δ (ppm) -118.99. *m/z*: MS (APCI-ToF): 534.9972 (M^+).

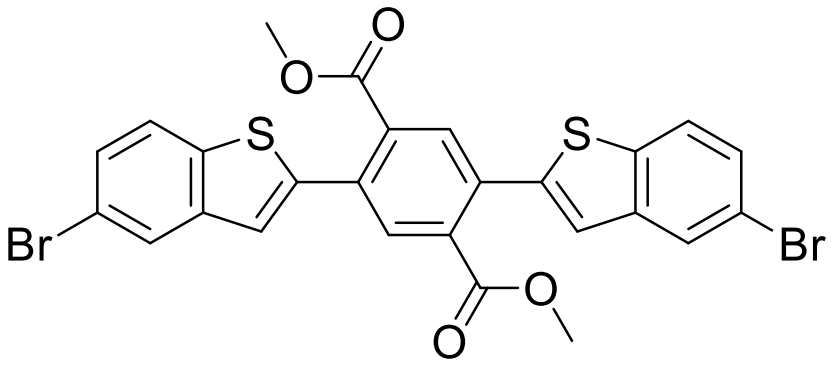


(2,5-Difluoro-3,6-bis(thieno[3,2-b]thiophen-2-yl)-1,4-phenylene)dimethanol (2.32): Diisobutylaluminum hydride solution (1 M in THF, 19.5 mL, 19.5 mmol) was added over 30 mins to diethyl 2,5-difluoro-3,6-bis(thieno[3,2-b]thiophen-2-yl)terephthalate (1.74 g, 3.25 mmol) in THF (90 mL) at -78 °C and allowed to warm to room temperature over 16 h. The solution was cooled to 0 °C and quenched by addition of hydrochloric acid (2 M, 60 mL) over 30 mins. Volatiles were removed under reduced pressure and the crude product collected by filtration. The product was washed with water (3 x 30 mL), methanol (3 x 30 mL), and cold DCM (3 x 30 mL) giving the *title compound* as a beige solid (1.37 g 94%). M.P. 251 – 253°C. ^{1}H NMR (400 MHz, DMSO-d) δ(ppm) 7.78 (d, *J* = 5.0 Hz, 2H), 7.69 (s, 2H), 7.54 (d, *J* = 5.0 Hz, 2H), 5.40 (s, 2H), 4.45 (s, 4H). ^{13}C NMR (101 MHz, DMSO) δ 154.90 (d, ^{1}J = 247.1 Hz, CF), 140.91, 138.93, 133.54, 129.41, 129.23 – 128.74 (m, CF), 124.38 – 123.99 (m, CF), 122.80, 120.38, 54.93. ^{19}F NMR (377 MHz, DMSO-d) δ(ppm) -119.94. MS (EI-ToF) *m/z*: 447.33 m/z (M^{+}).

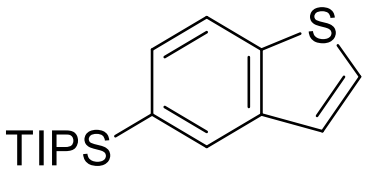


5,11-Difluoro-6,12-dihydrothieno[3,2-b]thieno[2'',3'':4',5']thieno[2',3':5,6]-s-indaceno[2,1-d]thiophene (2FIDTT): To (2,5-difluoro-3,6-bis(thieno[3,2-b]thiophen-2-yl)-1,4-phenylene)dimethanol (3.58 g, 6.50 mmol) at -5 °C was added triflic acid (25 mL) over 30 mins and the reaction allowed to go to RT over 48 h. The reaction mixture was poured in ice (100 g), washed with water (100 mL), saturated sodium acetate (100 mL), water (100 mL),

and methanol (100 mL). Afterwards the filtrate was dissolved in boiling CB (100 mL) and filtered collecting the filtrate. After this process was repeated four more times on the collected residues, the solvent was removed *in vacuo* and the residue washed with isopropyl alcohol and dried yielding the *title compound* as a beige powder (1.35 g, 55%). Compound decomposes above 237 °C. ^{1}H NMR (400 MHz, Chloroform-d)δ 7.40 (d, *J* = 5.1 Hz, 2H), 7.35 (d, *J* = 5.2 Hz, 2H), 3.98 (s, 4H). ^{19}F NMR (377 MHz, Chloroform-d) δ -131.67. MS (APCI-ToF) *m/z*: 412.94 (M^+).

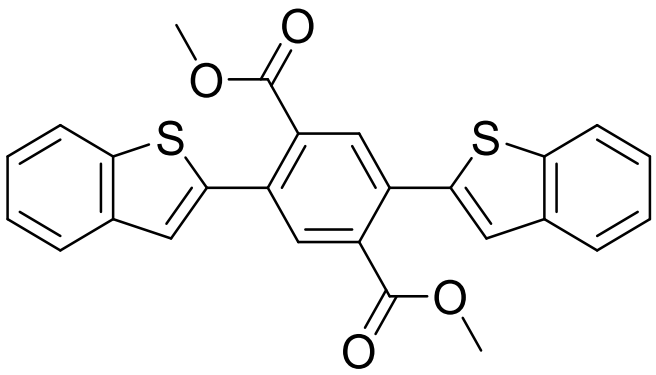


Attempted synthesis of dimethyl 2,5-bis(5-bromobenzo[b]thiophen-2-yl)terephthalate (2.34): To 5-bromobenzothiophene (2.50 g, 11.7 mmol) in THF (20 mL) at -78 °C was added LDA (2 M in THF, 5.61 mL, 11.2 mmol) dropwise. After 30 mins, the reaction was warmed to 0 °C, zinc chloride (0.7 M in THF, 17.1 mL, 12.0 mmol) was added, and the solution stirred for 30 mins. Dimethyl 2,5-dibromoterephthalate (1.96 g, 5.57 mmol) and tetrakis(triphenylphosphine)palladium(0) (295 mg, 0.260 mmol) were added at RT and the solution heated to reflux for 16 h. The reaction mixture was filtered, washed with MeOH (3 x 10 mL), and passed with chloroform through a silica plug giving a bright yellow solid.



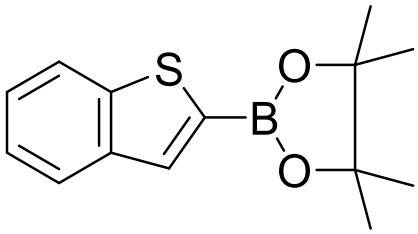
Attempted synthesis of benzo[b]thiophen-5-yltriisopropylsilane (2.37): To 5-bromobenzothiophene (100 mg, 0.47 mmol) in THF (5 mL) at -78 °C was added *n*BuLi (1.6 M in hexanes, 0.32 mL, 0.52 mmol) dropwise. After 3 h the reaction was allowed to warm to rt,

and TIPSCl (0.78 mL, 0.70 mmol) was added. After 24 h the solution was poured into THF (50 mL) and dried over anhydrous magnesium sulphate giving a brown oil.

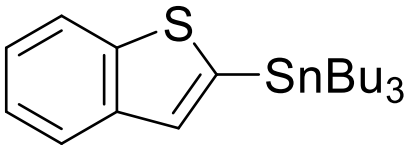


Attempted synthesis of dimethyl 2,5-bis(benzo[b]thiophen-2-yl)terephthalate by Negishi coupling (2.40): To bromobenzothiophene (500 mg, 3.73 mmol) in THF (10 mL) at -78 °C was added *n*-BuLi (1.6 M in hexanes, 2.33 mL, 3.73 mmol) dropwise. After 30 mins, the reaction was warmed to -41 °C, zinc chloride (0.7 M in THF, 17.1 mL, 12.0 mmol) was added. After an hour dimethyl 2,5-dibromoterephthalate (567 mg, 1.62 mmol) and tetrakis(triphenylphosphine)palladium(0) (295 mg, 0.260 mmol) were added at RT and the solution heated to reflux for 16 h. The reaction mixture was diluted with 20 mL of water and the crude product extracted with DCM (3 x 10 mL). The organic phase was washed with water (3 x 10 mL), brine (10 mL), and dried over anhydrous magnesium sulphate. After removal of solvent *in vacuo* an oily brown solid was obtained

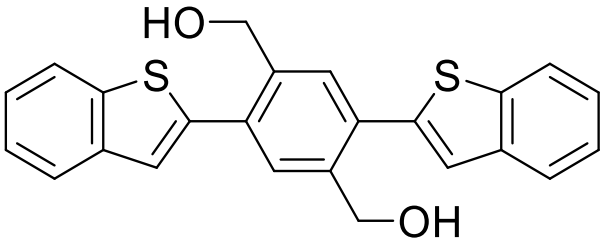
By Stille coupling: A mixture of [b]thiophen-2-yltributylstannane (4.02 g, 9.50 mmol), dimethyl 2,5-dibromoterephthalate (1.21 g, 3.18 mmol), and $Pd(PPh_3)_4$ (0.271 g, 0.230 mmol) in toluene (80 mL) was heated under reflux for 18 h. Saturated KF (100 mL) was added and after 1 h the reaction mixture was extracted with DCM (3 x 100 mL), washed with water (2 x 50 mL), and dried over anhydrous magnesium sulphate. After removal of solvent *in vacuo* the product was purified by column chromatography (DCM:hexane, 3:1) yielding the *title compound* as bright yellow crystals (1.44 g, 95%). M.P. 210 – 214 °C, ^{1}H NMR (400 MHz, Chloroform-d) δ 7.96 (s, 2H), 7.86 (d, *J* = 7.2 Hz, 2H), 7.81 (d, *J* = 7.2 Hz, 2H), 7.42 – 7.36 (m, 4H), 7.36 (s, 2H), 3.78 (s, 6H). ^{13}C NMR (101 MHz, Chloroform-d) δ 167.76, 140.54, 140.50, 139.94, 134.10, 133.91, 132.34, 124.73, 124.64, 123.95, 123.70, 122.20, 77.35, 77.03, 76.71, 52.78. M.P. 210 – 214 °C. MS (ES-ToF) *m/z*: 458.2 (M^+).



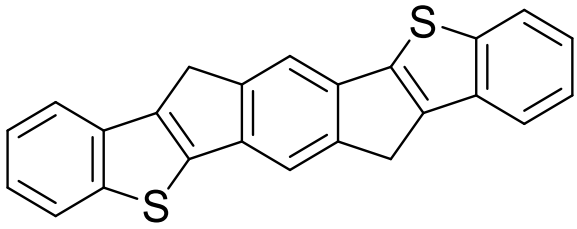
Benzo[b]thiophen-2-yltributylstannane (2.41): To benzothiophene (1.01 g, 7.49 mmol) in THF (15 mL) at -78 °C was added *n*-BuLi (5.15 mL, 1.6 M in hexanes, 8.24 mmol) dropwise. After 30 mins, 2-isopropoxy-4,4,5,5-tetramethyl-1,3,2-dioxaborolane (1.76 mL, 8.61 mmol) was added and the solution allowed to go to rt. After 16 h water (20 mL) was added and the product extracted with chloroform (3 x 40 mL), washed with water (3 x 40 mL) and dried over anhydrous magnesium sulphate. After removal of solvent *in vacuo* the crude *title product* was obtained as a clear colourless oil (1.93 g, 99%). ^{1}H NMR (400 MHz, Chloroform-d) δ 7.93 – 7.89 (m, 1H), 7.88 (s, 1H), 7.87 – 7.83 (m, 1H), 7.40 – 7.33 (m, 2H), 1.24 (s, 12H).



Benzo[b]thiophen-2-yltributylstannane (2.42): To benzothiophene (1.46 g, 10.9 mmol) in THF (15 mL) at -78 °C was added *n*-BuLi (1.6 M in hexanes, 7.5 mL, 12 mmol) dropwise. After 30 mins the mixture was warmed to 0 °C and tributyltin chloride (3.25 mL, 12 mmol) was added and the solution allowed to go to rt. After 12 h water (20 mL) was added and the product extracted with diethyl ether (3 x 30 mL), washed with water (3 x 30 mL) and dried over anhydrous magnesium sulphate. After removal of solvent *in vacuo* the *title product* was obtained as an orange oil and used in the next step without further purification (4.20 g, 91%). ^{1}H NMR (400 MHz, Chloroform-d) δ 7.93 (d, *J* = 7.9 Hz, 1H), 7.86 (d, *J* = 7.9 Hz, 1H), 7.49 – 7.40 (m, 1H), 7.40 – 7.25 (m, 2H), 1.76 – 1.55 (m, 6H), 1.47 – 1.34 (m, 9H), 1.26 – 1.17 (m, 9H), 1.00 - 0.90 (m, 9H). ^{13}C NMR (101 MHz, CDCl3) δ 144.36, 141.10, 139.82, 132.10, 123.73, 123.34, 122.76, 121.87, 29.04, 27.35, 13.74, 10.85.

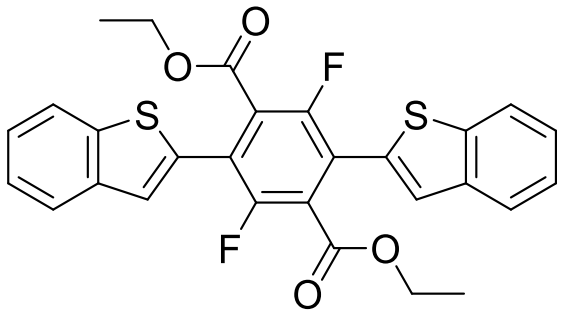


(2,5-bis(benzo[b]thiophen-2-yl)-1,4-phenylene)dimethanol (2.43): DIBAL-H (1 M in THF, 3.86 mL, 3.86 mmol) was added over 30 mins to dimethyl 2,5-bis(thieno[3,2-b]thiophen-2-yl)terephthalate (295 mg, 0.64 mmol) in THF (8 mL) at 0 °C and allowed to go to room temperature over 16 h. The solution was cooled to 0 °C and hydrochloric acid (2 M, 20 mL) was added over 30 mins. Volatiles were removed under reduced pressure and the residue was triturated with MeOH, followed by filtration and washing with 2 M HCl (10 mL) and MeOH (2 x 10 mL). Recrystallisation from THF:MeOH with a few droplets of water gave the product as a yellow solid (222 mg, 86%). M.P. 233 – 237 °C, ^{1}H NMR (400 MHz, DMSO-d6) δ 8.08 – 7.98 (d *J* = 6.8 Hz, 2H), 7.98 – 7.88 (d, *J* = 6.8 Hz, 2H), 7.81 (s, 2H), 7.68 (s, 2H), 7.49 – 7.37 (m, 4H), 4.73 (s, 4H). ^{13}C NMR (101 MHz, DMSO – d6) δ 141.40, 140.59, 139.68, 139.28, 132.53, 130.57, 125.22, 125.14, 124.48, 124.39, 122.72, 61.26. MS (EI-ToF) *m/z*: 402.07 (M^{+}).

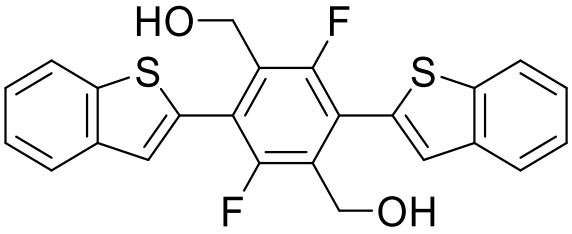


IDTBt by neat method: To triflic acid (1.3 mL) at -5 °C was added (2,5-bis(benzo[b]thiophen-2-yl)-1,4-phenylene)dimethanol (0.143 g, 0.355 mmol) over 30 mins and the reaction allowed to warm to RT over 69 h. The reaction mixture was poured in ice (20 g) and then washed with water (40 mL), saturated sodium acetate (40 mL), water (40 mL), and methanol (40 mL). Afterwards the filtrate was dissolved in boiling CB (200 mL) and filtered collecting the filtrate, the collected residue was subjected to this extraction procedure a further five times and solvent was removed *in vacuo* from the combined filtrates yielding the crude *title compound* as an orange powder.

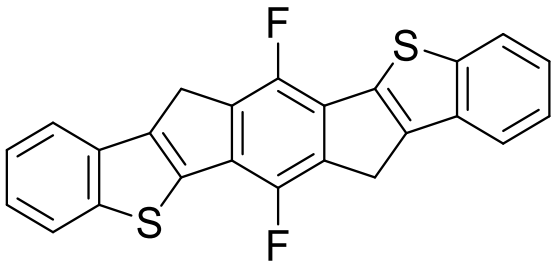
By solvated method: To (2,5-bis(benzo[b]thiophen-2-yl)-1,4-phenylene)dimethanol (0.41 g, 1.01 mmol) in CB (140 mL) was added triflic acid solution (1.6 mL triflic acid in 18 mL CB) over 20 mins. After 1 h the reaction was neutralised with saturated sodium bicarbonate (100 mL). After extraction with CB (3 x 100 mL), the solvent was removed under reduced pressure and the crude product washed with water (50 mL) and methanol (50 mL). Afterwards the residue was dissolved in boiling CB (250 mL) and filtered collecting the filtrate, this was repeated three more times. After removal of solvent *in vacuo* the solids were dissolved in hot chloroform and passed through a silica plug yielding the crude *title compound* as an orange powder (0.3292 g, 89%) after further removal of solvent. Product solubility was too low for ^{1}H-NMR. MS (MALDI-ToF) *m/z*: 367.1 (M^{+}).



Diethyl 2,5-bis(benzo[b]thiophen-2-yl)-3,6-difluoroterephthalate (2.44): Benzo[b]thiophen-2-yltributylstannane (9.18 g, 21.7 mmol), diethyl 2,5-dibromo-3,6-difluoroterephthalate (3.02 g, 7.26 mmol), and $Pd(PPh_3)_4$ (0.426 g, 0.369 mmol) in toluene (180 mL) were heated under reflux for 18 h. Saturated KF (200 mL) was added and after 1 h the reaction mixture was extracted with DCM (3 x 200 mL), washed with water (2 x 100 mL), and dried over anhydrous magnesium sulphate. After removal of solvent *in vacuo* the product was purified by silica gel chromatography (DCM:hexane, 3:1) twice, yielding the *title compound* as pale yellow crystals (1.67 g. 44%). M.P. 201 – 204 °C, ^{1}H NMR (400 MHz, Chloroform-d) δ 7.94 – 7.74 (m, 4H), 7.46 (s, 2H), 7.44 – 7.34 (m, 4H), 4.24 (q, *J* = 7.0 Hz, 4H), 1.09 (t, *J* = 7.0 Hz, 6H). ^{13}C-NMR (101 MHz, CDCl3) δ 163.23, 152.30 (d, ^{1}J = 253.8 Hz, CF), 140.99, 139.23, 131.33, 126.65, 125.80 – 125.43 (m, CF), 125.25, 124.72, 124.19, 122.83 - 122.42 (m, CF), 122.12, 62.59, 13.76. ^{19}F NMR (377 MHz, Chloroform-d) δ -118.50. MS (ES-TOF) *m/z*: 523.3 (M^{+}). IR (FTIR) vmax/cm^{-1}: 2921, 1722 (C=O) s, 1408, 1296, 1180, 1008, 744, 722, 437.

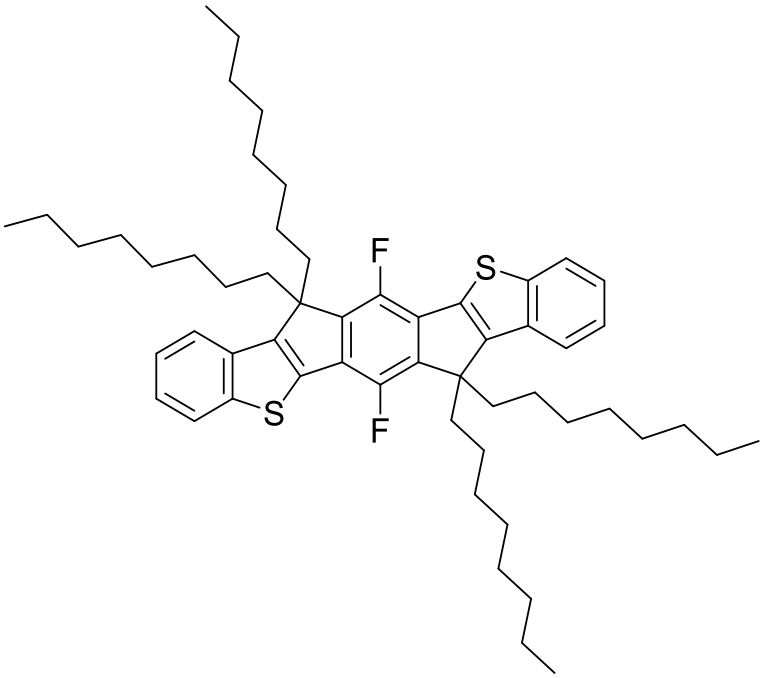


(2,5-bis(benzo[b]thiophen-2-yl)-3,6-difluoro-1,4-phenylene)dimethanol (2.45): DIBAL-H (1 M in THF, 18 mL, 18 mmol) was added over 30 mins to diethyl 2,5-bis(benzo[b]thiophen-2-yl)-3,6-difluoroterephthalate (1.50 g, 2.87 mmol) in THF (60 mL) at 0 °C and allowed to warm to room temperature over 16 h. Hydrochloric acid (2 M, 190 mL) was added to the solution over 30 mins and volatiles were removed under reduced pressure. The residue was triturated with MeOH followed by filtration and washing with 2 M HCl (50 mL) and MeOH (2 x 50 mL). Recrystallisation from THF:MeOH gave the *title compound* as pale cream crystals (0.946 g, 75%). M.P. 261 – 263 °C, ^{1}H NMR (400 MHz, Chloroform-d) δ 7.99 – 7.78 (m, 4H), 7.49 (s, 2H), 7.45 – 7.34 (m, 4H), 4.72 (s, 4H). ^{19}F NMR (377 MHz, Chloroform-d) δ -119.94. MS (ES-ToF) *m/z*: 483.1 (M^+). IR (FTIR) vmax/cm^{-1}: 3673, 3324 (O-H) br, 1408, 1268, 1005, 749, 723, 568, 429.

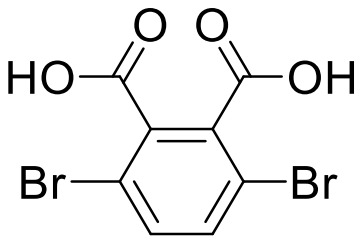


2FIDTBT by neat method: To triflic acid (2.5 mL) at -5 °C was added (2,5-bis(benzo[b]thiophen-2-yl)-3,6-difluoro-1,4-phenylene)dimethanol (0.306 g, 0.698 mmol) over 30 mins and the reaction allowed to go to RT over 45 h. The reaction mixture was poured in ice (40 g) and then washed with water (80 mL), saturated sodium acetate (80 mL), water (80 mL), and methanol (80 mL). Afterwards the filtrate was dissolved in boiling CB (400 mL) and filtered, this was repeated five more times, and the filtrates combined yielding the crude *title compound* after removal of solvent *in vacuo* as an orange solid (28.1 mg, 10%). ^{1}H NMR (400 MHz, $CDCl_3$) δ 7.91 (d, *J* = 8.2 Hz, 2H), 7.82 (d, *J* = 8.2 Hz, 2H), 7.46 – 7.32 (m, 4H), 4.03 (s, 4H). ^{19}F-NMR (377 MHz, CDCl3) δ -131.41. MS (APCI) *m/z*: 403.0 (M^+).

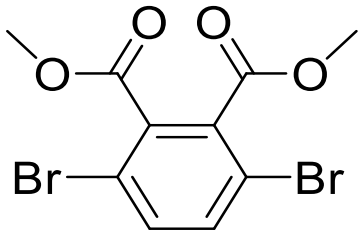
By solvated method: To (2,5-bis(benzo[b]thiophen-2-yl)-3,6-difluoro-1,4-phenylene)dimethanol (53.0 mg, 0.121 mmol) in CB (16 mL) was added triflic acid solution (0.19 mL triflic acid in 2 mL CB) over 20 mins. After 1 h the reaction was neutralised with saturated sodium bicarbonate (10 mL). After extraction with CB (3 x 10 mL), the solvent was removed under reduced pressure and the crude product washed with water (5 mL) and methanol (5 mL). Afterwards the residue was dissolved in boiling CB (25 mL) and filtered, this was repeated three more times and the filtrates combined. After removal of solvent *in vacuo* the solids were dissolved in hot chloroform and passed through a silica plug yielding the crude *title compound* as a beige solid (7.70 mg, 16%) after further removal of solvent. ^{1}H-NMR (400 MHz, Chloroform-d) δ 7.93 – 7.84 (m, 2H), 7.85 – 7.78 (m, 2H), 7.46 – 7.35 (m, 4H), 4.07 (s, 4H). ^{19}F NMR (377 MHz, Chloroform-d) δ -116.14. MS (APCI) *m/z*: 402.0 (M^+).



C8-2FIDTBT (2.46): To a suspension of **2FIDTBT** (14.2 mg, 0.0324 mmol) in NMP (0.58 mL) was added sodium tert-butoxide (18.9 mg, 0.196 mmol) portion-wise. After the suspension was heated at 80 °C for 1 h, 1-bromooctane (0.04 mL, 0.232 mmol) was added and the reaction heated at 100 °C for 16 hours. After cooling to rt the mixture was poured into ice (30 g) and the solid collected by filtration. Further washing with water (40 mL) and methanol (40 mL), followed by purification by silica gel chromatography (petroleum ether) yielded the crude *title compound* as an orange solid (1.1 mg, 4%). ^{19}F NMR (377 MHz, Chloroform-d) δ -118.73. MS (ES-ToF) *m/z*: 846.4 (M^+).



3,6-dibromophthalic acid (2.48): To 1,4-dibromo-2,3-dimethylbenzene (1.03 g, 3.09 mmol) in water (54.6 mL) and pyridine (27.3 mL) was added potassium permanganate (8 x 2.47 g, 8 x 15.6 mmol) with water (8 x 7.70 mL) in 30 mins intervals as the mixture was heated to reflux. After 12 h potassium permanganate (VII) (8 x 2.47 g, 8 x 15.6 mmol) was added with water (8 x 7.70 mL) in 30 mins intervals, while continuing heating to reflux. The solution was allowed to cool to rt and was filtered through celite with the aid of methanol washes. Pyridine was removed under reduced pressure and the mixture acidified using hydrochloric acid (2 M, 10 mL). The product was extracted with diethyl ether (50 mL x 3), washed with water (2 x 50 mL) and dried over anhydrous magnesium sulphate yielding the *title compound* (1.26 g, 100%). The product was used in the next step without further purification. ^{1}H NMR (400 MHz, DMSO-d6) δ 7.69 (s, 2H).

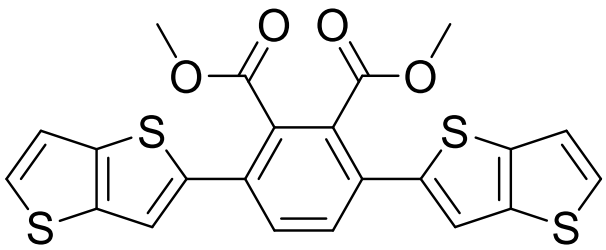


Dimethyl 3,6-dibromophthalate (2.49): To 3,6-dibromophthalic acid (390 mg, 1.20 mmol) was added concentrated sulfuric acid (0.4 mL), dimethyl carbonate (1.33 g, 14.8 mmol) and the mixture heated to 80 °C. After 16 h, sulfuric acid (0.4 mL) was added again, and the mixture heated for another 16 h. Saturated sodium bicarbonate was added (10 mL) and the product extracted with chloroform (3 x 30 mL), followed by washing with water (2 x 30 mL) and drying over anhydrous magnesium sulphate. After removal of solvent *in vacuo* silica gel column chromatography (DCM) was employed yielding the *title compound* as a white solid (176 mg, 42%). ^{1}H-NMR (400 MHz, Chloroform-d) δ 7.53 (s, 2H), 3.92 (s, 6H). ^{13}C NMR (101 MHz, Chloroform-d) δ 165.66, 135.79, 135.32, 119.35, 53.12.

To 3,6-dibromophthalic acid (189 mg, 0.617 mmol) was added concentrated sulfuric acid (0.10 mL), methanol (2 mL) and the mixture heated to 90 °C. After 16 h saturated sodium bicarbonate was added (8 mL) and the product extracted with chloroform (3 x 20 mL), followed by washing with water (2 x 20 mL) and drying over anhydrous magnesium sulphate. After removal of solvent *in vacuo* silica gel column chromatography (DCM) was employed yielding the *title compound* as a white solid (40 mg, 18%).

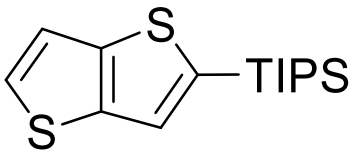
To 3,6-dibromophthalic acid (79 mg, 0.244 mmol) in methanol (2 mL) at 0 °C was added thionyl chloride (0.09 mL, 1.23 mmol). The reaction was heated to 65 °C over 16 h and saturated sodium bicarbonate was added (4 mL) and the product extracted with chloroform (3 x 10 mL), followed by washing with water (2 x 10 mL) and drying over anhydrous magnesium sulphate. After removal of solvent *in vacuo* silica gel column chromatography (DCM) was employed yielding the *title compound* as a white solid (25 mg, 29%).

To 3,6-dibromophthalic acid (42 mg, 0.130 mmol) in methanol (0.75 mL) at 0 °C was added thionyl chloride (0.1 mL, 1.37 mmol). After 16 h of stirring at RT saturated sodium bicarbonate was added (4 mL) and the product extracted with chloroform (3 x 10 mL), followed by washing with water (2 x 10 mL) and drying over anhydrous magnesium sulphate. After removal of solvent *in vacuo* a silica gel plug (DCM) was employed yielding the *title compound* as a white solid (7 mg, 15%).

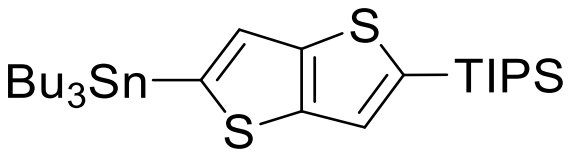


Dimethyl 3,6-bis(thieno[3,2-b]thiophen-2-yl)phthalate (2.50): To thieno[3,2-b]thiophene (170 mg, 1.21 mmol) in THF (10 mL) in a reflux setup at -78 °C was added n-butyl lithium (1.6 M in hexanes, 0.76 mL, 1.22 mmol) dropwise. After 30 mins, zinc chloride (0.7 M in THF, 1.77 mL, 1.24 mmol) was added and the solution stirred for a further hour. Dimethyl 3,6-dibromophthalate (176 mg, 0.500 mmol) and tetrakis(triphenylphosphine)palladium(0) (26.0 mg, 0.0225 mmol) were added and the solution heated to 75 °C for 16 h. The reaction mixture was poured into water (20 mL), extracted with chloroform (3 x 10 mL), washed with

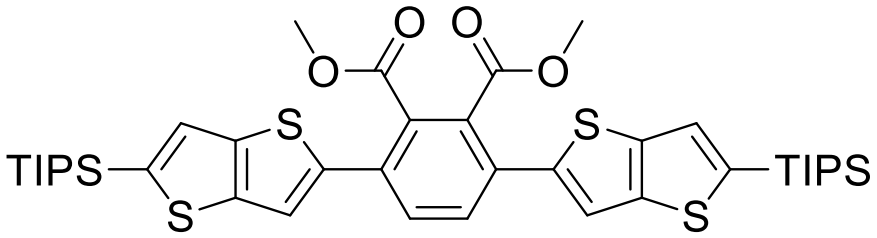
water (3 x 10 mL), brine (10 mL) and dried over anhydrous magnesium sulphate. After removal of solvent under reduced pressure the product was subjected to silica gel chromatography (petroleum ether:DCM, 1:1) yielding the crude *title compound* (62 mg, 26%). ^{1}H NMR (400 MHz, Chloroform-d) δ 7.64 (s, 2H), 7.41 (d, *J* = 5.2, 2H), 7.30 (s, 2H), 7.28 (d, *J* = 5.2 Hz, 2H), 3.76 (s, 6H).



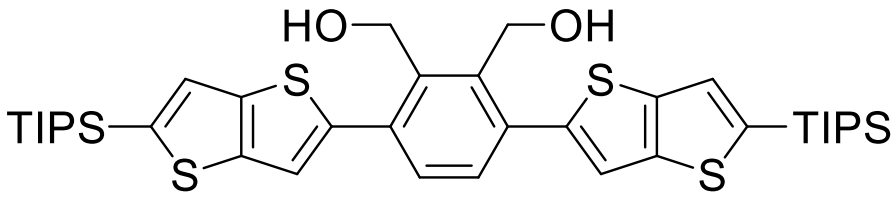
Triisopropyl(thieno[3,2-b]thiophen-2-yl)silane (2.51): To TT (2.73 g, 19.5 mmol) in THF (80 mL) at 0 °C was added *n*-BuLi (1.6 M in hexanes, 10.35 mL, 16.6 mmol) dropwise. After 30 mins triisopropylsilyl chloride (3.75 mL, 17.6 mmol) was added and the solution allowed to go to rt. After 16 h water (100 mL) was added and the product extracted with hexane (3 x 10 mL), and washed with water (1 x 10 mL). After removal of solvent *in vacuo* silica gel column chromatography was performed (hexane) yielding the *title compound* as white crystals (2.64 g, 46%). ^{1}H NMR (400 MHz, TCE-d2) δ 7.48 (d, *J* = 5.3 Hz, 1H), 7.45 (s, 1H), 7.33 (d, *J* = 5.3 Hz, 1H), 1.47 – 1.33 (m, 3H), 1.18 (d, *J* = 7.4 Hz, 18H). ^{13}C NMR (101 MHz, Chloroform-d) δ 144.67, 141.21, 138.00, 127.95, 126.93, 119.14, 18.58, 11.79.



Triisopropyl(5-(tributylstannyl)thieno[3,2-b]thiophen-2-yl)silane (2.53): To triisopropyl(thieno[3,2-b]thiophen-2-yl)silane (2.34 g, 7.88 mmol) in THF (60 mL) at 0 °C was added *n*-BuLi (1.6 M in THF, 5.42 mL, 8.67 mmol) dropwise. After 30 mins tributyltin chloride (2.45 mL, 9.03 mmol) was added. After 12 h water (100 mL) was added and the product extracted with DCM (3 x 100 mL), washed with water (3 x 100 mL) and dried over anhydrous magnesium sulphate. After removal of solvent *in vacuo* the *title compound* was obtained as brown oil and used in the next step without further purification (4.30 g, 93%). ^{1}H NMR (400 MHz, Chloroform-d) δ 7.34 (d, *J* = 0.8 Hz, 1H), 7.24 (d, *J* = 0.7 Hz, 1H), 1.68 – 1.53 (m, 12H), 1.42 – 1.27 (m, 9H), 1.16 – 1.09 (m, 18H), 0.91 (t, *J* = 7.2 Hz, 9H).

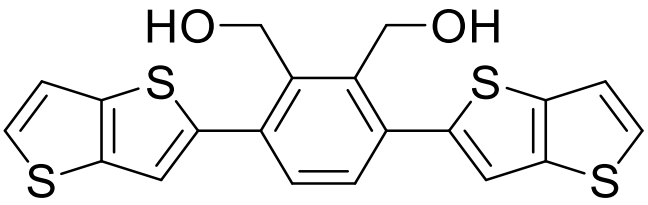


Dimethyl 3,6-bis(5-(triisopropylsilyl)thieno[3,2-b]thiophen-2-yl)phthalate (2.54): Triisopropyl(5-(tributylstannyl)thieno[3,2-b]thiophen-2-yl)silane (3.487 g, 5.95 mmol), dimethyl 3,6-dibromophthalate (340 mg, 0.966 mmol), and $Pd(PPh_3)_4$ (55.0 mg, 0.0476 mmol) in toluene (10 mL) were heated under reflux for 16 h. The mixture was poured into ethanol (40 mL), washed with ethanol (2 x 30 mL) and purified by silica gel chromatography (DCM:petroleum ether, 5:2) yielding the *title compound* as a yellow solid (477 mg, 63%). M.p. 202 – 203 °C. ^{1}H NMR (400 MHz, Chloroform-d) δ 7.64 (s, 2H), 7.37 (s, 2H), 7.29 (s, 2H), 3.80 (s, 6H), 1.44 – 1.32 (m, 6H), 1.15 (d, *J* = 7.4 Hz, 36H). ^{13}C NMR (101 MHz, Chloroform-d) δ 168.30, 144.80, 142.40, 141.62, 138.63, 132.95, 132.02, 126.89, 118.81, 53.02, 18.59, 11.82. MS (ESI-ToF) *m/z*: 783.25 (M^+).

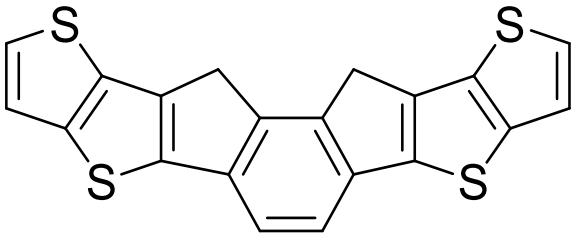


(3,6-bis(5-(triisopropylsilyl)thieno[3,2-b]thiophen-2-yl)-1,2-phenylene)dimethanol (2.55): Diisobutylaluminum hydride solution (1 M in THF, 3.06 mL, 3.06 mmol) was added over 30 mins to dimethyl dimethyl 3,6-bis(5-(triisopropylsilyl)thieno[3,2-b]thiophen-2-yl)phthalate (400 mg, 0.511 mmol) in THF (12 mL) at -78 °C, and then allowed to go to room temperature over 16 h. The solution was cooled to 0 °C and hydrochloric acid (2 M, 30 mL) was added over 30 mins. Water was added carefully (20 mL), the product extracted with chloroform (3 x 20 mL), washed with water (3 x 20 mL) and dried over anhydrous magnesium sulphate. Removal of solvent under reduced pressure yielded the *title compound* as a cream solid (365 mg, 98%). M.p. 238 – 239 °C. ^{1}H NMR (400 MHz, Chloroform-d) δ 7.54 (s, 2H), 7.44 (s, 2H), 7.39 (s, 2H), 4.98 (s, 4H), 1.45 – 1.35 (m, 6H), 1.16 (d, *J* = 7.4 Hz, 36H). ^{13}C NMR (101 MHz,

Chloroform-d) δ 144.79, 143.77, 141.21, 139.00, 137.89, 135.99, 130.77, 126.87, 119.77, 60.65, 18.61, 11.83. MS (ESI-ToF): 709.25 m/z (M^+ - H_2O).



(3,6-bis(thieno[3,2-b]thiophen-2-yl)-1,2-phenylene)dimethanol (2.56): Tetra-*n*-butylammonium fluoride (1 M in THF, 1.28 mL, 1.28 mmol) was added to (3,6-bis(5-(triisopropylsilyl)thieno[3,2-b]thiophen-2-yl)-1,2-phenylene)dimethanol (260 mg, 0.358 mmol) in THF (20 mL). After 16 h the reaction was poured into water (80 mL), filtered, and washed with water (20 x 3 mL) yielding the *title compound* as white solid (138 mg, 93%). ^{1}H NMR (400 MHz, Chloroform-d) δ 7.57 (s, 2H), 7.49 (s, 2H), 7.45 (d, *J* = 5.3 Hz, 2H), 7.32 (d, *J* = 5.2 Hz, 2H), 5.00 (s, 4H). MS (EI-ToF) *m/z*: 413.9862 (M^+).

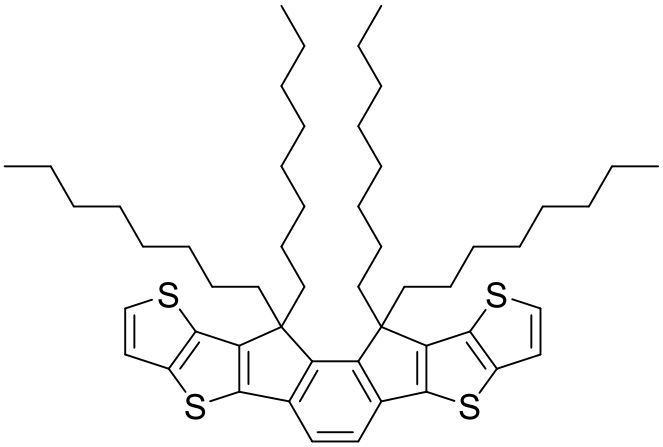


Meta-IDTT: To (3,6-bis(5-(triisopropylsilyl)thieno[3,2-b]thiophen-2-yl)-1,2-phenylene)dimethanol (40.0 mg, 0.055 mmol) in DCM (8 mL) was added triflic acid solution (0.088 mL triflic acid in 1 mL DCM) over 5 mins. After 20 mins the reaction was neutralised with saturated sodium bicarbonate (10 mL), extracted with chloroform (3 x 5 mL), washed with water (3 x 5 mL) and dried over anhydrous magnesium sulphate. After removal of solvent *in vacuo* silica gel chromatography (1:1, chloroform:petroleum ether) was employed yielding trace product.

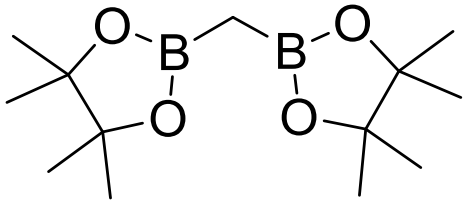
Attempted synthesis after TIPS deprotection: To (3,6-bis(thieno[3,2-b]thiophen-2-yl)-1,2-phenylene)dimethanol (122 mg, 0.0.294 mmol) in DCM (40 mL) was added triflic acid solution (0.65 mL triflic acid in 5 mL DCM) over 5 mins. After 1 h the reaction was neutralised with saturated sodium bicarbonate (50 mL), DCM removed *in vacuo*, and the

residue collected by filtration. The residue was purified by silica gel column chromatography (3:7, chloroform:petroleum ether).

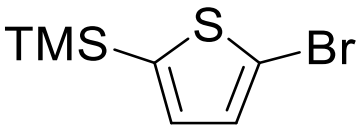
Best synthesis: To triflic acid (2.5 mL) at -5 °C was added (3,6-bis(5-(triisopropylsilyl)thieno[3,2-b]thiophen-2-yl)-1,2-phenylene)dimethanol (111 mg, 0.153 mmol) over 30 mins and the reaction allowed to go to RT over 16 h. The reaction mixture was poured in ice (40 g), filtered, washed with water (80 mL), saturated sodium acetate (80 mL), water (80 mL), and methanol (80 mL). The filtrate was heated in boiling chloroform (40 mL) and filtered; this was repeated three more times. After silica gel chromatography (chloroform) the title compound was obtained as beige solid (25 mg, 43%). Compound decomposes above 245°C. ^{1}H NMR (400 MHz, Chloroform-d) δ 7.41 (s, 2H), 7.31 (d, *J* = 5.3 Hz, 2H), 7.28 (d, *J* = 5.2 Hz, 2H), 3.79 (s, 4H). ^{13}C NMR (101 MHz, Chloroform-d) δ 142.14, 141.41, 137.55, 137.07, 134.98, 125.95, 120.98, 117.95, 30.05. MS (MALDI-ToF) *m/z*: 378.97 (M^+).



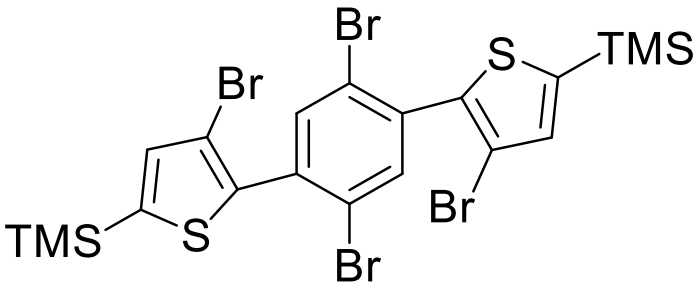
C8-meta-IDTT (2.57): To a suspension of **meta-IDTT** (11.1 mg, 0.0293 mmol) in NMP (1 mL) was added sodium tert-butoxide (16.9 mg, 0.176 mmol) portion-wise. After the suspension was heated at 80 °C for 1 h, 1-bromooctane (0.03 mL, 0.176 mmol) was added dropwise and the reaction heated at 100 °C for 40 hours. The reaction was poured into water (10 mL), extracted with ethyl acetate (3 x 5 mL), washed with water (5 x 5 mL) and dried over anhydrous magnesium sulphate. After removal of solvent *in vavuo* silica gel column chromatography was performed yielding trace *title compound*. MS (MALDI-ToF) *m/z*: 826.9 (M^+).



Bis(4,4,5,5-tetramethyl-1,3,2-dioxaborolan-2-yl)methane (2.59): To bis(pinacolato)diboron (68.7 g, 27.1 mmol), copper (I) iodide (2.30 g, 12.1 mmol), and lithium methoxide (11.6 g, 308 mmol) at 0°C was added DMF (350 mL). After 16 h at 40°C the solution was poured into water (500 mL), extracted with hexane (3 x 200 mL), washed with water (3 x 200 mL), brine (200 mL), and dried over anhydrous magnesium sulphate yielding the *title compound* (21.0 g, 64%). ^{1}H-NMR (400 MHz, Chloroform-d) δ 1.23 (s, 24H), 0.35 (s, 2H).

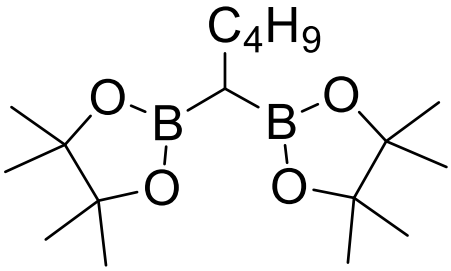


(5-bromothiophen-2-yl)trimethylsilane: To 2-bromothiophene (1.76 mL, 18.2 mmol) in THF (150 mL) at -78°C was added lithium diisopropylamide (2M in THF, 10.0 mL, 20.0 mmol) dropwise. After 1 h, TIPSCl (2.54 mL, 20.0 mmol) was added at -78°C and the solution allowed to warm to room temperature over 16 h. The solution was poured into water (200 mL), extracted with diethyl ether (3 x 100 mL), washed with water (2 x 100 mL), brine (100 mL) and dried over anhydrous magnesium sulphate yielding the *title compound* (3.39 g, 79%). ^{1}H-NMR (400 MHz, Chloroform-d) δ 7.08 (d, *J* = 3.5 Hz, 1H), 6.98 (d, *J* = 3.5 Hz, 1H), 0.30 (s, 9H).



((2,5-dibromo-1,4-phenylene)bis(4-bromothiophene-5,2-diyl))bis(trimethylsilane) (2.61): To (5-bromothiophen-2-yl)trimethylsilane (1.15 g, 4.87 mmol) in THF (50 mL) at -78°C was

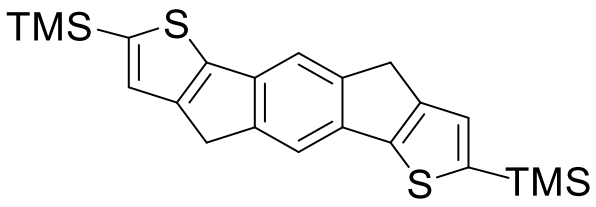
added lithium diisopropylamide (2M in THF, 2.68 mL, 5.36 mmol) dropwise. After 1 h, zinc chloride (0.7M in THF, 8.35 mL, 5.84 mmol) was added at -40°C and the solution allowed to warm to room temperature for 1 h. 1,4-dibromo-2,5-diiodobenzene (0.678 g, 1.39 mmol) and tetrakis(triphenylphosphine)palladium(0) (80.0 mg, 0.0695 mmol) were added, and the solution heated to reflux for 16 h. The reaction mixture was poured into water (100 mL), extracted with DCM (3 x 50mL), washed with water (2 x 50 mL), brine (50 mL) and dried over anhydrous magnesium sulphate. After purification by silica column chromatography (DCM:hexane, 1:1) the *title compound* was obtained as a white solid (872 mg, 51%). ^{1}H-NMR (400 MHz, Chloroform-d) δ 7.68 (s, 2H), 7.16 (s, 2H), 0.36 (s, 18H). MS (APCI-ToF) m/z 701.7423 (M+).



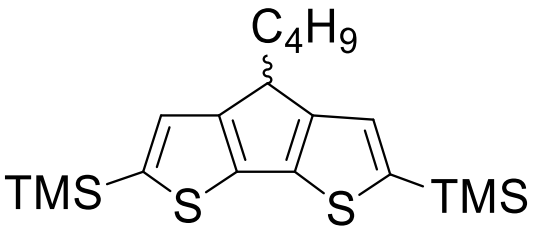
2,2'-(pentane-1,1-diyl)bis(4,4,5,5-tetramethyl-1,3,2-dioxaborolane) (2.71): To bis(4,4,5,5-tetramethyl-1,3,2-dioxaborolan-2-yl)methane (1.85 g, 6.90 mmol), in THF (80 mL) at 0°C was added lithium diisopropylamide (2M in THF, 3.8 mL, 7.59 mmol). After 30 mins, butyl iodide (0.86 mL, 7.59 mmol) was added. After 16 h at room temperature the solution was poured into water (100 mL), extracted with DCM (3 x 50 mL), washed with water (3 x 50 mL), brine (50 mL), and dried over anhydrous magnesium sulphate. After purification by silica column (1:9, ethyl acetate:hexane) the *title compound* was obtained as a white solid (1.24 g, 55%). ^{1}H-NMR (400 MHz, Chloroform-d) δ 1.59 – 1.49 (m, 2H), 1.32 - 1.16 (m, 28H), 0.90 – 0.81 (m, 3H), 0.71 (s, 1H).

General procedure for double Suzuki coupling: To bis[(pinacolato)boryl]alkane (1.5 equiv per ring closing site) and ring-closing precursor (1 equiv) was added palladium catalyst. Dioxane (2.5 mL per 0.215 mmol), and aqueous potassium hydroxide (8M, 3 equiv) were degassed over 30 mins and added. After heating to 30 °C for 16 h, more aqueous pre-degassed potassium hydroxide (8M, 6 equiv) was added to the solution and heating continued at 60 °C for a further 24 h. Water was added, and organics extracted with DCM

(x3), washed with water (x3), brine, and dried over anhydrous magnesium sulphate. The crude *title compound* was concentrated *in vacuo*.



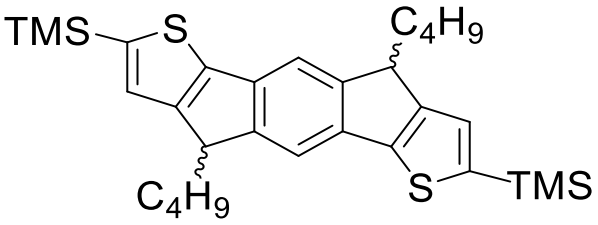
2,7-Bis(trimethylsilyl)-4,9-dihydro-s-indaceno[1,2-b:5,6-b']dithiophene (2.70): The general procedure for double Suzuki coupling was followed for this reaction using bis(4,4,5,5-tetramethyl-1,3,2-dioxaborolan-2-yl)methane (29 mg, 0.107 mmol), ((2,5-dibromo-1,4-phenylene)bis(4-bromothiophene-5,2-diyl))bis(trimethylsilane) (25 mg, 0.036 mmol), bis(tri-tert-butylphosphine)palladium(0) (3 mg, 0.005 mmol), dioxane (1 mL), potassium hydroxide (8M, 0.013 ml, 0.107 mmol) and (8M, 0.027 mL, 0.214 mmol). After work-up the crude *title compound* was obtained as a brown oil (14.2 mg, 96%). ^{1}H-NMR (400 MHz, Chloroform-d) δ (ppm) 7.59 (s, 2H), 7.50 (s, 2H), 3.71 (s, 2H), 0.36 (s, 18H). MS (MALDI-ToF) m/z 410.1 (M+).



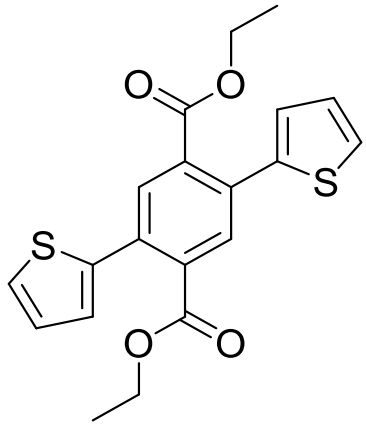
(4-Butyl-4H-cyclopenta[2,1-b:3,4-b']dithiophene-2,6-diyl)bis(trimethylsilane) (2.73): The general procedure for double Suzuki coupling was followed for this reaction using 2,2'-(pentane-1,1-diyl)bis(4,4,5,5-tetramethyl-1,3,2-dioxaborolane) (68 mg, 0.211 mmol), (3,3'-dibromo-[2,2'-bithiophene]-5,5'-diyl)bis(trimethylsilane) (33 mg, 0.0705 mmol), bis(tri-tert-butylphosphine)palladium(0) (5.4 mg, 0.0106 mmol), dioxane (1 mL), potassium hydroxide (8M, 0.02 ml, 0.211 mmol) and (8M, 0.05 mL, 0.423 mmol). After work-up the crude *title compound* was obtained as a brown oil (22.5 mg, 84%). MS (EI-ToF) m/z 378.2 (M+).

The general procedure for double Suzuki coupling was followed for this reaction using 2,2'-(pentane-1,1-diyl)bis(4,4,5,5-tetramethyl-1,3,2-dioxaborolane) (103 mg, 0.320 mmol), (3,3'-dibromo-[2,2'-bithiophene]-5,5'-diyl)bis(trimethylsilane) (100 mg, 0.213 mmol), tris(dibenzylideneacetone)dipalladium(0) (10 mg, 0.0107 mmol), XPhos (20 mg, 0.0427

mmol), dioxane (2.5 mL), potassium hydroxide (8M, 0.08 ml, 0.639 mmol) and (8M, 0.16 mL, 1.28 mmol). After work-up the crude *title compound* t was obtained as a brown oil (73 mg, 90%). MS (EI-ToF) m/z 378.2 (M+).

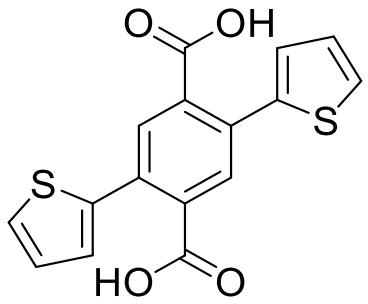


Attempted synthesis of (4,9-Dibutyl-4,9-dihydro-s-indaceno[1,2-b:5,6-b']dithiophene-2,7-diyl)bis(trimethylsilane) (2.75): The general procedure for double Suzuki coupling was followed for this reaction using 2,2'-(pentane-1,1-diyl)bis(4,4,5,5-tetramethyl-1,3,2-dioxaborolane) (38 mg, 0.117 mmol), ((2,5-dibromo-1,4-phenylene)bis(4-bromothiophene-5,2-diyl))bis(trimethylsilane) (27 mg, 0.0391 mmol), bis(tri-tert-butylphosphine)palladium(0) (3.00 mg, 5.87 mmol), dioxane (0.5 mL), potassium hydroxide (8M, 0.015 ml, 0.117 mmol) and (8M, 0.03 mL, 0.234 mmol). After work-up no product was detected by MS.

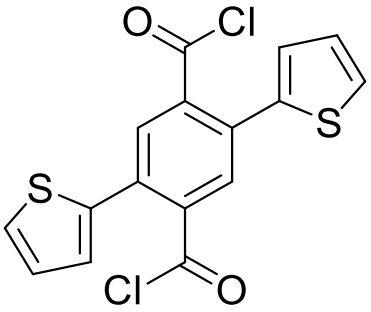


Diethyl 2,5-di(thiophen-2-yl)terephthalate (2.7): A mixture of 2-(tributylstannyl)thiophene) (7.30 mL, 23.15 mmol), diethyl 2,5-dibromoterephthalate (4.00 g, 10.5 mmol), and $Pd(PPh_3)_4$ (0.300 g, 23.2 mmol) in toluene (100 mL) was heated under reflux for 16 h. Saturated KF (100 mL) was added and after 1 h the reaction mixture was extracted with DCM (3 x 100 mL), washed with water (2 x 50 mL), and dried over anhydrous magnesium sulphate. After removal of solvent *in vacuo* the product was purified by silica column chromatography (DCM:hexane, 1:3) yielding the *title compound* as a beige solid (2.66 g, 66%). ^{1}H-NMR (400

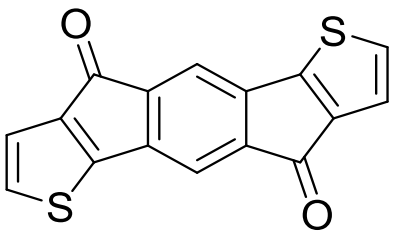
MHz, Chloroform-d) δ 7.81 (s, 2H), 7.39 (dd, *J* = 4.9, 1.4 Hz, 2H), 7.11 – 7.04 (m, 4H), 4.22 (q, *J* = 7.2 Hz, 4H), 1.15 (t, *J* = 7.1 Hz, 6H).



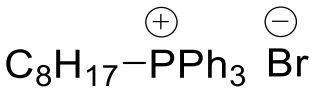
2,5-di(thiophen-2-yl)terephthalic acid (2.11): To diethyl 2,5-di(thiophen-2-yl)terephthalate (1.91 g, 3.17 mmol) and sodium hydroxide (4.00 g, 99.1 mmol) was added methanol (30 mL) and water (30 mL). After 16 h, the solution was poured into hydrochloric acid (150 mL, 2M), filtered, and washed with cold water (3 x 50mL). After drying under suction, the *title compound* was obtained as a beige solid (1.25 g, 55%). ^{1}H-NMR (400 MHz, DMSO-d6) δ 13.46 (s, 2H), 7.72 (s, 2H), 7.71 (d, *J* = 5.9 Hz, 2H), 7.30 (d, *J* = 3.5 Hz, 2H), 7.21 – 7.16 (m, 2H).



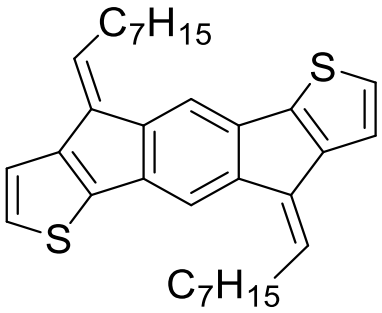
2,5-di(thiophen-2-yl)terephthaloyl dichloride (2.12): To 2,5-di(thiophen-2-yl)terephthalic acid (1.25 g, 3.78 mmol) was added thionyl chloride (1.10 mL, 15.1 mmol) and dichloromethane (25 mL), followed by dropwise addition of dimethylformamide (0.6 mL). After 16 h, the solution was purified by silica plug (DCM). After removal of solvent *in vacuo* the *title compound* was obtained as a white solid (1.37 g, 99%). ^{1}H-NMR (400 MHz, Chloroform-d) δ 7.90 (s, 2H), 7.50 (dd, *J* = 5.1, 1.2 Hz, 2H), 7.21 – 7.12 (m, 4H).



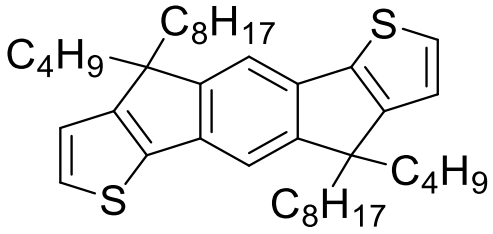
s-indaceno[1,2-b:5,6-b']dithiophene-4,9-dione (2.13): To 2,5-di(thiophen-2-yl)terephthaloyl dichloride (1.37 g, 3.73 mmol) was added aluminium trichloride (2.49 g, 18.7 mmol) and dichloromethane (50 mL). After 16 h, the suspension was slowly poured into water (100 mL), filtered, washed with water (3 x 50 mL), and cold acetone (2 x 50 mL). After drying under suction the *title compound* was obtained as a dark-blue solid (1.37 g, 99%). IR: ν(cm^{-1}) 3110, 3074 1706 (C=O). An NMR spectrum couldn't be taken for the compound due to its poor solubility in common deuterated solvents.



Octyltriphenylphosphonium bromide (2.81): To triphenylphosphine (5.45 g, 20.8 mmol) was added octyl bromide (3.00 mL, 17.3 mmol) and toluene (100 mL). After 16 h of heating under reflux, solvent was removed *in vacuo* and the crude product triturated with hexane (50 mL) giving the *title compound* as an off-white crystalline solid (5.52 g, 70%). ^{1}H NMR (400 MHz, Chloroform-d) δ 7.53 – 7.44 (m, 9H), 7.44 – 7.36 (m, 6H), 3.36 – 3.22 (m, 2H), 1.35 – 1.21 (m, 4H), 0.99 – 0.73 (m, 8H), 0.46 (t, *J* = 6.6 Hz, 3H). ^{13}C-NMR (101 MHz, Chloroform -d) δ 134.97, 134.93, 133.36, 133.27, 130.43, 130.30, 118.30, 117.45, 31.34, 30.22, 30.06, 28.76, 28.53, 22.71, 22.23, 13.81. MS (APCI-ToF) m/z 375.2237 (C16H32P+).



4,9-ioctylidene-4,9-dihydro-s-indaceno[1,2-b:5,6-b']dithiophene (2.82): To a solution of octyltriphenylphosphonium bromide (1.64 mg, 0.351 mmol) in THF (1 mL) at 0 °C was added *n*-BuLi (2M in THF, 0.15 mL, 0.307 mmol) dropwise. After 30 mins, the solution was transferred into a mixture of s-indaceno[1,2-b:5,6-b']bisthiophene-4,9-dione (26 mg, 0.0878 mmol) in oDCB (1 mL) at 0 °C. After 16 h, The reaction mixture was poured into water (4 mL), extracted with DCM (3 x 2 mL), washed with water (3 x 2 mL), brine (2 x 2 mL), and dried over anhydrous magnesium sulphate. Removal of solvent *in vacuo* and purification by silica gel chromatography (hexane) produced the *title product* as a pale-yellow solid (90 mg, 29%). ^{1}H NMR (400 MHz, Chloroform-d) δ (ppm) 7.62 (s, 2H), 7.33 (d, *J* = 4.8 Hz, 2H), 7.25 (d, *J* = 4.8 Hz, 2H), 6.62 (t, *J* = 7.6 Hz, 2H), 2.77 – 2.69 (m, 4H), 1.39 – 1.10 (m, 26H). ^{13}C-NMR (101 MHz, Chloroform-d δ 144.93, 142.15, 140.76, 133.15, 132.93, 129.28, 126.11, 122.48, 110.52, 31.82, 30.03, 29.72, 29.54, 29.25, 22.68, 14.11. (APCI-ToF) m/z 487.2483 (M+).



4,9-dibutyl-4,9-dioctyl-4,9-dihydro-s-indaceno[1,2-b:5,6-b']dithiophene (2.83): To 4,9-ioctylidene-4,9-dihydro-s-indaceno[1,2-b:5,6-b']dithiophene (20 mg, 0.043 mmol) and butyl bromide (0.01 mL, 0.0896 mmol) in THF (1 mL) was added lithium aluminium hydride (1M in hexanes, 0.09 mL, 0.0896 mmol). After 16 h, DCM (1 mL) and hydrochloric acid (2M, 0.02 mL) were added. The solution was extracted with DCM (3 x 1 mL), washed with water (2 x 1 mL), and dried over anhydrous magnesium sulphate. After column chromatography (hexane) the title product was obtained as beige solid (12 mg, 46%). ^{1}H-NMR (400 MHz,

Chloroform-d) δ 7.29 (s, 2H), 7.26 (d, *J* = 4.8 Hz, 2H), 6.97 (d, *J* = 4.8 Hz, 2H), 2.04 - 1.93 (m, 4H), 2.04 - 1.93 (m, 4H), 1.91 - 1.77 (m, 32H), 0.89 - 0.78 (m, 6H), 0.73 (t, *J* = 7.3 Hz, 6H). ^{13}C-NMR (101 MHz, Chloroform-d) δ 155.11, 153.23, 141.63, 135.56, 126.12, 121.74, 113.15, 53.61, 39.15, 38.99, 31.82, 30.02, 29.31, 29.23, 26.42, 24.16, 23.12, 22.61, 14.09, 13.94. MS (APCI-ToF) m/z 603.4069 (M+).

Chapter 3 – IDT Derivative Acceptors and their use in OPVs

3.1 – Introduction

3.1.1 – ITIC Derivatives in the Literature

After the initial synthesis of **ITIC** discussed in earlier chapters, derivatives of the structure saw a flurry of interest in the literature due to the synthetic flexibility of modular **ITIC** and its high performance.[54,58,69,160] A common modification of the structure is substitution onto the **DCI** groups (**Figure 3.1**).

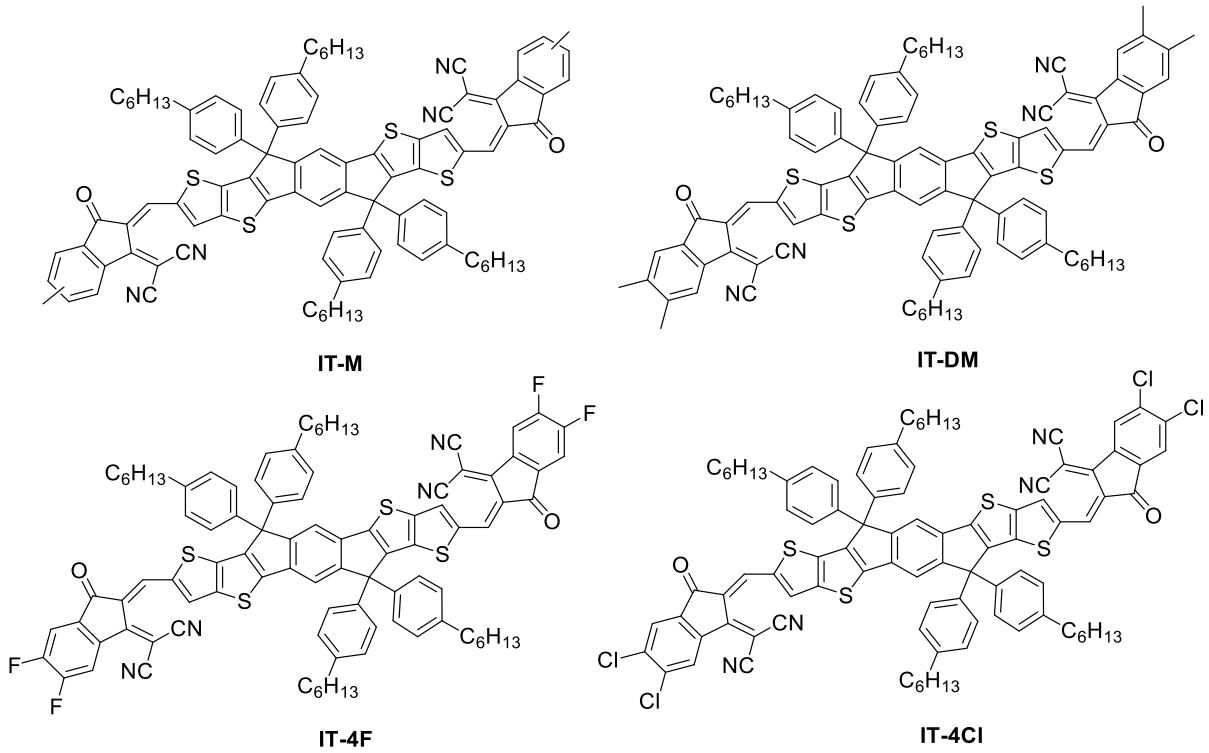


Figure 3.1: *Structures of **DCI**-substituted **ITIC** derivatives **IT-M, IT-DM, IT-4F, IT-4Cl**.*[117,161,162]

As the LUMO of **ITIC** is predominantly localised on the **DCI** groups, substitutions on these positions either lowered or raised LUMO energy levels depending on the substituted functional group, with little effect on HOMO energy levels. To raise LUMO, and therefore improve device V_{OC} **IT-M** and **IT-DM** were synthesised with substitution of electron donating methyl groups.[161] **IT-M** and **IT-DM** had LUMO energy levels 0.04 eV or 0.09 eV higher than

that of **ITIC** respectively. Short methyl groups were used to minimise any negative morphological effects that may occur due to the steric hindrance of the groups. Devices made with **IT-M**, **IT-DM**, and **ITIC** paired with the **PBDB-T** polymer were compared. It was found that V_{OC} was improved as expected, from 0.90 V for the **ITIC** devices to 0.94 V for **IT-M** and 0.97 for the **IT-DM** devices. FF was reduced as methyl groups were substituted, whilst J_{SC} was improved for **IT-M** and reduced for **IT-DM** relative to **ITIC**. The reduction in FF can be attributed to the lower domain purity of the **IT-DM** blend increasing recombination. As a result, the **IT-M** devices had the highest PCE of 11.48%, trailed by **ITIC** devices at 10.68%, and **IT-DM** at a similar 10.79%.

Halogenation on the **DCI** end groups is an alternative strategy. For example fluorination on the **DCI** end groups (**IT-4F**) was shown to deepen LUMO by 0.25 eV relative to **ITIC** and lower bandgap by 0.09 eV.[117] As observed in other fluorine substituted molecules discussed in other chapters, improved intermolecular interactions in the **IT-4F** blend increased electron mobility in the acceptor by 1.38 times relative to the **ITIC** blend. **IT-4F** was red shifted compared to **ITIC** and was therefore no-longer suited for use with **PBDB-T**. A modified polymer **PBDB-T-SF** was produced instead with a complimentary absorption spectrum and energy levels. The **IT-4F:PBDB-T-SF** blend had a PCE of 13.1%, a record for performance at the time. The high performance was obtained despite the lowered V_{OC} of 0.88 V for the blend, largely due to an improved J_{SC} of 20.88 mA/cm^2 boosted by the improved photon harvesting of the higher extinction coefficient donor and acceptor in the blend and potentially by improved charge mobility through the bulk.

To reduce LUMO even further by 0.1 eV relative to **IT-4F**, **IT-4Cl** was also synthesised and had a band gap in film of 0.07 eV lower than **IT-4F**.[162] Using an alternative **PBDB-T** derivative, **PBDB-T-2F**, blends of **IT-4Cl:PBDB-T-2F** had high PCEs of 13.45%. Whilst the change in polymer influenced device parameters, the **IT-4Cl** devices had significantly lower V_{OC} as expected and lower FF than the **IT-4F** devices, but a much higher J_{SC} of 22.67 mA/cm^2. The improvement in J_{SC} can be mainly attributed to the greatly increased extinction coefficient of the **IT-4Cl** acceptor.

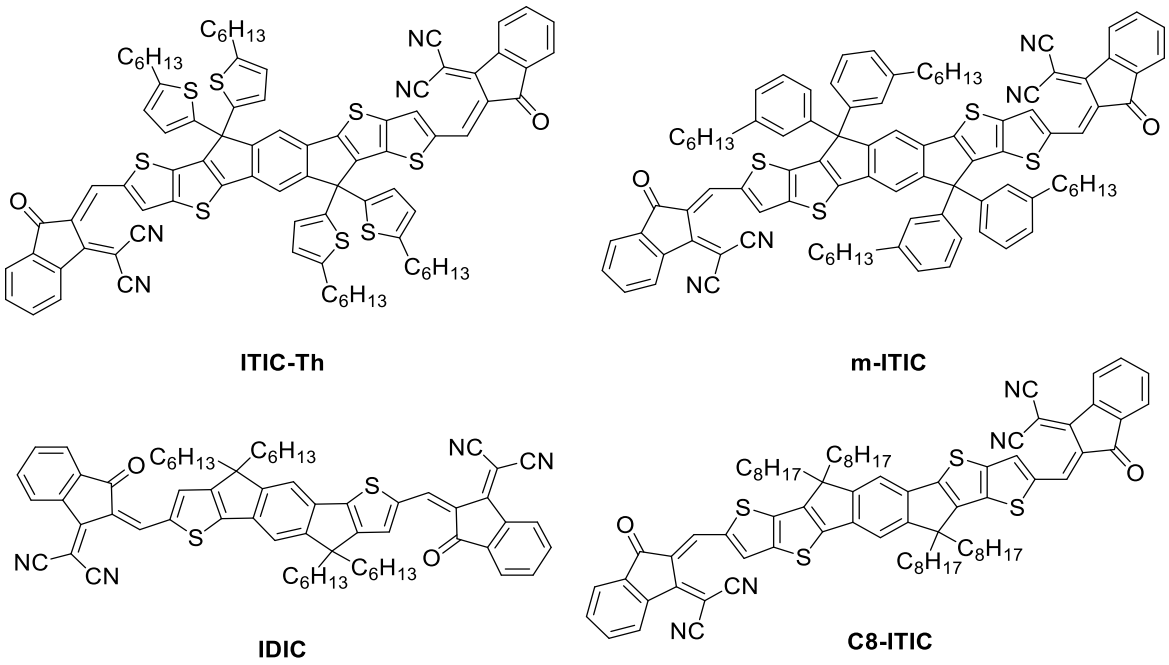


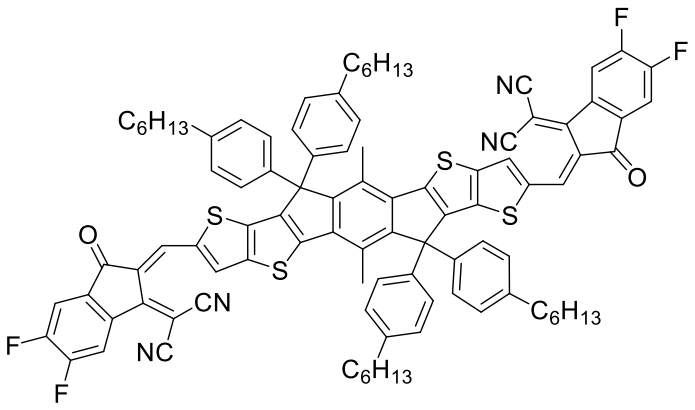
Figure 3.2: *Structures of bridge-substituted* ***ITIC*** *derivatives* ***ITIC-Th, m-ITIC, IDIC, and C8-ITIC****.*[114,122,163,164]

An alternative common point of modification is on the bridge of the **IDTT** in **ITIC**, common changes to the aryl side chains include modification of the aryl substituent as in **ITIC-Th**, isomerisation of the position of the alkyl chain as in **m-ITIC** or changing from an aryl side chain to an alkyl side chain as in **C8-ITIC** (**Figure 3.2**). Due to the σ-inductive electron withdrawing effect of the thienyl side chain **ITIC-Th** has deeper frontier orbital energy levels than **ITIC**.[163,165] When paired with a polymer appropriate to these deeper energy levels, a PCE of 10.88% largely due to a high J_{SC} of 17.6 mA/cm^2 and FF of 0.69 is obtained. The J_{SC} of the devices was improved relative to **ITIC** due to enhanced intermolecular interactions from the thienyl-alkyl chains improving electron mobility whilst the high FF was a result of well-balanced charge carrier mobilities.

More subtle modifications of the side chains in **ITIC** also lead to changes in device performance. Notably, **m-ITIC** was produced with *meta* hexyl chains instead of *para.*[164] Both **ITIC** and **m-ITIC** had almost identical HOMO-LUMO energy levels, and therefore devices of both NFAs with the **J61** polymer gave very similar V_{OC}. However, **ITIC** was found to have poorer self-organisation than **m-ITIC** as visible from grazing-incidence wide-angle X-ray scattering (GIWAXS). This was also noticeable from **m-ITIC** taking a face-on orientation whilst **ITIC** would take both either face-on or edge-on orientation. As a result, the electron

mobility of **m-ITIC** was higher and better balanced with its hole mobility, resulting in an increased J_{SC} and FF for the **m-ITIC** devices and a 10.77% PCE compared to 10.57% for the **ITIC** devices. This improvement in performance highlights how even small changes to the alkyl chains in NFAs can have a significant impact on BHJ morphology and device performance.

As discussed in the introduction to Chapter 2, **IDIC** has reduced conjugation compared to **ITIC**, yet still performs at comparable J_{SC} and PCE to **ITIC** due to having close packing because of its less sterically hindering alkyl side chains.[114] To benefit from both increased core conjugation and less bulky sidechains **C8-ITIC** was synthesised in our group.[122] The alkyl-chain form of **ITIC** was found to have a greater propensity to crystallise, a higher extinction coefficient in solution and a slightly reduced optical bandgap. Therefore, when devices of **C8-ITIC** and **ITIC** were fabricated with **PBDB-T** polymer, **C8-ITIC** performed at a maximum PCE of 12.41% compared to 10.0% for **ITIC**. This improvement was predominantly due to a 2.7 mA/cm^2 increase in maximum J_{SC} caused by increased absorptivity and a broader absorption spectrum. V_{OC} largely remained the same for both acceptors whilst FF was improved for **C8-ITIC** as the more crystalline acceptor formed a superior morphology with the polymer and had better balanced electron-hole mobilities. In addition, a further derivative of **PBDB-T** with fluorine substitution **PFBDB-T** was synthesised for use with the acceptors. This polymer slightly reduced the J_{SC} and FF of the **C8-ITIC** devices but its deeper HOMO improved V_{OC} giving a high maximum PCE of 13.2%. A remarkable effect of using **PFBDB-T** with **C8-ITIC** is the small energy loss of only 0.6 eV whilst current generation was still high at 19.6 mA/cm^2, indicating that charge splitting can occur effectively in the devices regardless of a relatively small energetic driving force at the donor-acceptor interface.



IM-4F

Figure 3.3: *Structure of central-phenyl substituted **IT-4F** derivative **IM-4F.***[166]

The NFA **IM-4F** was produced with view to further lower the bandgap of **IT-4F**, the result was a reduction in bandgap of 0.08 eV.[166] This was done by raising the HOMO of the **phenyl-IDTT** core by 0.05 eV by substituting electron donating methyl groups onto its central phenyl ring.[166] **IM-4F:PBDB-T-2F** blend devices performed at a very impressive maximum PCE of 14.17% compared to 12.80% for **IT-4F:PBDB-T-2F** blends. The lower bandgap of **IM-4F** broadened the absorption spectrum of its blend and improved J_{SC} by 2.10 mA/cm^2 compared to **IT-4F:PBDB-T-2F**, up to 22.12 mA/cm^2. Interestingly, the V_{OC} of the **IM-4F** devices was increased by 0.03 V relative to **IT-4F** devices even though **IM-4F** had a lower bandgap, a similar effect as for **C8-ITIC**. This can be explained by the reduced energy loss in the **IM-4F:PBDB-T-2F** blend of only 0.67 eV, lower than the 0.76 eV loss in **IT-4F:PBDB-T-2F** blends. It appears that modification of both the side chains as in **C8-ITIC** and substitution of electron donating groups on the central-phenyl of **IDTT** as in **IM-4F** can reduce energy loss in OPV devices.

3.1.2 – Target ITIC Derivatives

Building on previous literature research, derivatives of **ITIC** will be synthesised in this chapter from commercial material or from the cores produced in Chapter 2. Their structure will differ from **ITIC** both by substitution on the **IDTT** and **DCI** components, and by modification of the side chains and end-group **(Figure 3.4)**.

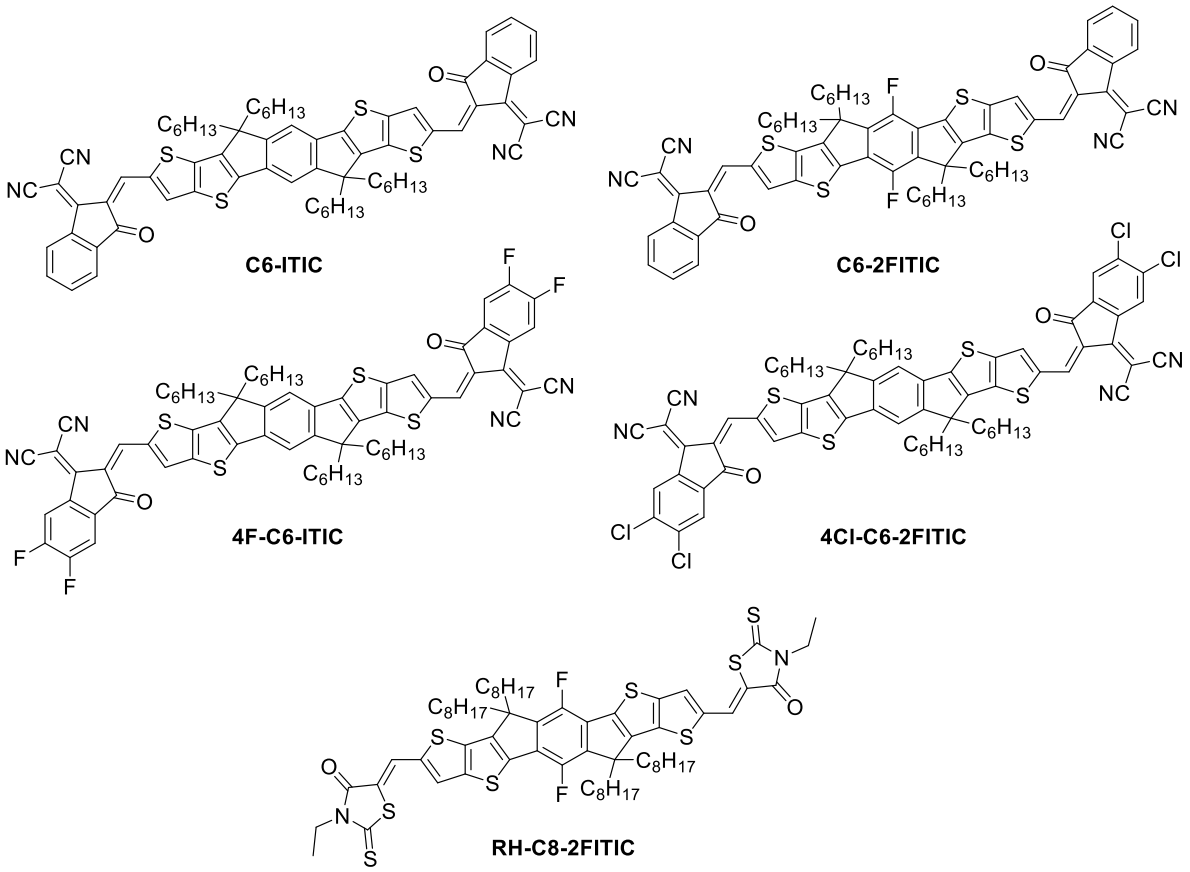


Figure 3.4: *Structure of planned* ***ITIC*** *derivatives.*

As the HOMO is localised on the electron donating moiety while the LUMO is localised on the electron accepting moiety, halogenation on the end-groups was predicted to lower bandgap by predominantly lowering the LUMO of the NFA whilst halogenation of the core was predicted to widen bandgap by predominantly lowering the HOMO. Replacement of the **DCI** end-group with the less-strongly electron accepting rhodanine group used successfully with the **IDTBR** series of acceptors (**Figure 1.11**) was predicted to raise LUMO and widen bandgap.[58,68] DFT calculations were performed to confirm our predictions for the NFAs' energy levels. The sidechains were modified to methyl groups for each acceptor to lower computational load (**Table 3.1**).

Table 3.1: *DFT results for NFAs with methyl sidechains at the B3LYP level of theory with a 6-31G +G(d,p) basis set.*

NFA	**4Cl-C6-ITIC**	**4F-C6-ITIC**	**C6-ITIC**	**C6-2FITIC**	**RH-C8-2FITIC**
LUMO (eV)	-3.69	-3.61	-3.45	-3.50	-2.97
HOMO (eV)	-5.78	-5.73	-5.59	-5.69	-5.32
Bandgap (eV)	2.09	2.11	2.14	2.19	2.36

Our predictions are confirmed by the DFT results. Fluorination on the end group in **4F-C6-ITIC** deepens the HOMO by a greater amount than the LUMO and therefore lowers bandgap while core fluorination in **C6-2FITIC** lowers the HOMO by twice the amount of the LUMO and therefore raises bandgap relative to **C6-ITIC**. Replacement of the **DCI** group with a rhodanine moiety reduces the push-pull effect in **RH-C8-ITIC** and widens bandgap.

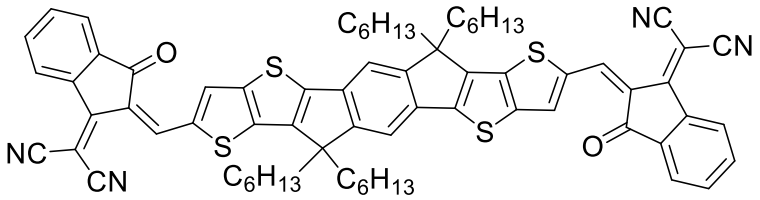
The predicted lower bandgap of **4Cl-C6-ITIC** than **4F-C6-ITIC** is counterintuitive at first as fluorine is more electronegative than chlorine and would be expected to deepen the local LUMO by a greater extent. However, the empty orbital adjacent to the 2p of fluorine is 3s, which is too high in energy to accept electrons.[167] Meanwhile chlorine has empty 3d orbitals that can accept electron pairs or π electrons and form strong noncovalent interactions such as Cl-π or Cl-S that stabilise the molecule and lower localised FMOs.[168] A further factor that reduces the bandgap of end-group chlorinated NFAs is the high dipole moment of the C-Cl bond compared to C-F. This enhances the intramolecular charge transfer between donor and acceptor components within the NFA and therefore lowers bandgap and expands absorption spectrum.[162,168]

All the NFAs were calculated to have a planar structure and are therefore expected to have similar crystallinity to **C8-ITIC (Figure 7.2.48)**. The ethyl chains on the end-groups of **RH-C8-2FITIC** may affect packing, but likely to a lesser extent than the longer sidechains on the electron donating core.

3.2 – NFA Synthesis and Properties

3.2.1 – Synthesis of C6-ITIC

The first NFA target synthesised was the hexyl-chain derivative **C6-ITIC** (**Figure 3.5**).[122] This molecule was chosen to investigate if a further increase in crystallinity will improve the performance of **C8-ITIC** devices, as **C8-ITIC** itself is an **ITIC** derivative with improved performance due to its improved self-aggregation properties. The shorter hexyl chains were projected to increase aggregation for the NFA due to their lower steric bulk compared to their octyl counterparts. It was predicted that **C6-ITIC** would retain the favourable optical properties of **C8-ITIC** upon side-chain extension, as the main chromophore isn't modified. Due to the success of **IDIC**, it was expected that **C6-ITIC** would have sufficient solubility with the reduced alkyl chain length (**Figure 2.4**).[114]

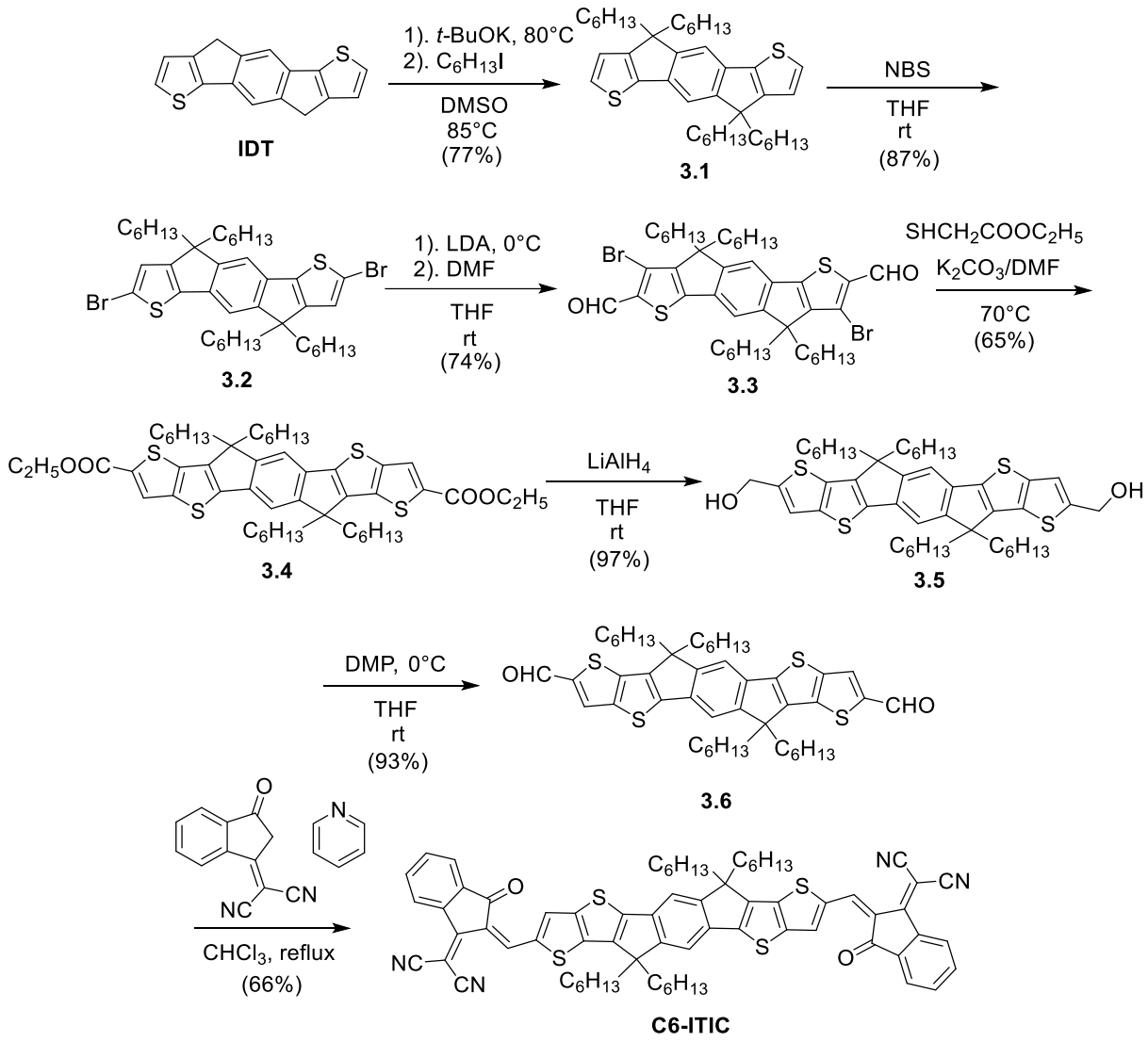


C6-ITIC

Figure 3.5: *Structure of the **C8-ITIC** derivative **C6-ITIC**.*

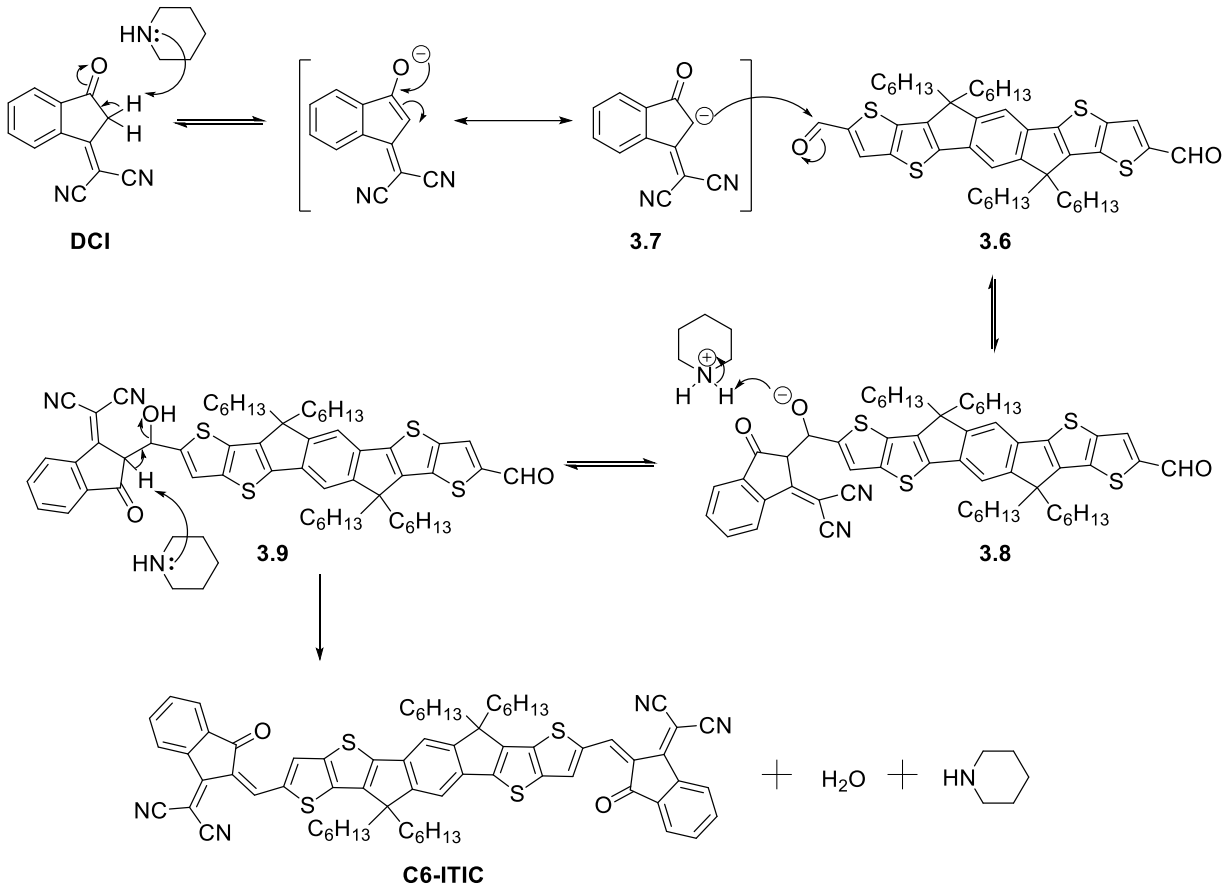
The triflic acid route towards **IDTT** was still being optimised when **C6-ITIC** was envisioned and as such the ring-extension synthetic methodology from **IDT** used by our group for **C8-ITIC** was followed (**Scheme 3.1**). **IDT** was alkylated according to literature procedure, but using 1-iodohexane rather than 1-bromohexane as iodide is a better leaving group than bromide.[122] This was followed by bromination in the absence of light with N-bromosuccinimide (NBS), with both reactions proceeding in good yield. Afterwards, a halogen dance was performed using LDA and the resulting anion was trapped with dimethylformamide (DMF) to afford the dialdehyde.[156] Further treatment with ethyl mercaptoacetate extended the ring system to **IDTT**. Functional group interconversions with reduction using lithium aluminium hydride followed by an oxidation with Dess–Martin periodinane (DMP) produced **3.6**. A significant benefit of the ring-extension methodology is the rapid preparation of this aldehyde for attachment of an end-capping acceptor group by

Knoevenagel condensation, as is required for many **ITIC** derivative NFAs. This condensation reaction produced **C6-ITIC** in a good 66% yield.



Scheme 3.1: *Synthetic route towards* ***C6-ITIC*** *following the ring-extension methodology.*[122]

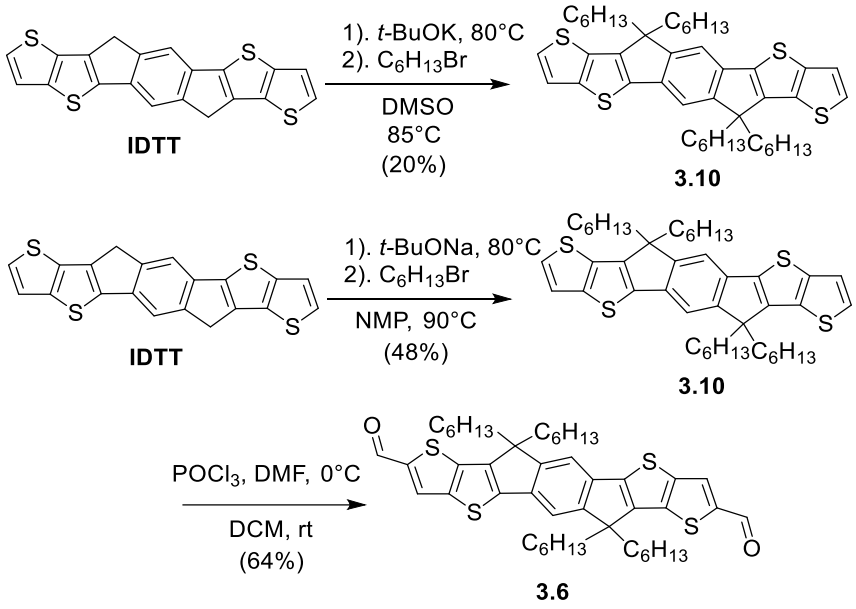
The Knoevenagel condensation is used throughout this chapter to attach accepting moieties to electron rich cores and its mechanism towards **C6-ITIC** is given in **Scheme 3.2**. The reaction begins with deprotonation α to the carbonyl in **DCI** by the pyridine base. The resulting enolate **3.7** undergoes nucleophilic addition onto the aldehyde moiety of **3.6**. Finally, protonation of the anion **3.8** and elimination of hydroxide via an E1cb type mechanism forms **C6-ITIC** by dehydration. Pyridine is regenerated throughout this reaction and is therefore catalytic.



Scheme 3.2: *Mechanism of the Knoevenagel condensation reaction towards* ***C6-ITIC****.*

As a proof of concept, the **IDTT** core synthesised by the triflic acid route was also used en route to the aldehyde **3.6**. The core was initially alkylated by the methodology used by our group to alkylate **IDTT** with the hexadecyl chain and dimethyl sulfoxide (DMSO) solvent was used. As discussed in Chapter 2, it was found that using NMP solvent produced the product in greater yields, and therefore it was used instead (**Scheme 3.3**). Both the sodium and potassium *tert*-butoxide salts gave comparable yields when NMP solvent was used. The observed yields were lower than the 77% yield obtained above in the synthesis of **3.1**, this was attributed mainly to the reduced solubility of the **IDTT** core in comparison to **IDT** (**Scheme 3.1**). Afterwards, the Vilsmeier–Haack reaction was utilised to substitute a formyl group onto the core, producing **3.6** in a 64% yield. Both reactions from **IDTT** proceeded in good yield and highlight how the triflic acid reaction route can be used successfully towards

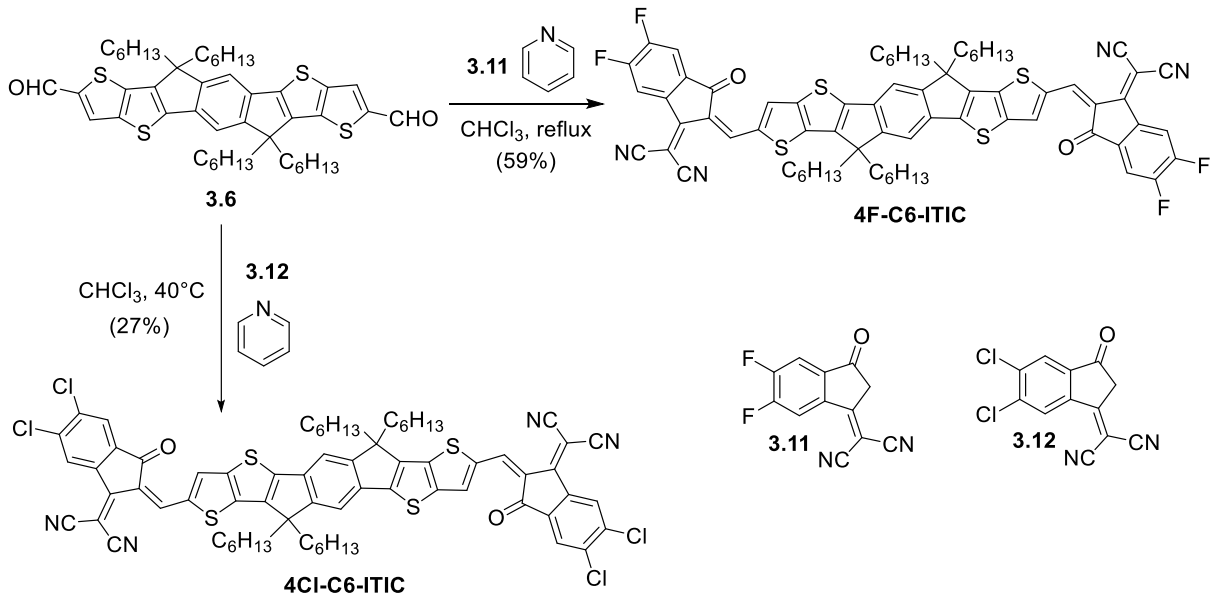
C6-ITIC and its derivatives by forming the prerequisite aldehyde for Knoevenagel condensation.



Scheme 3.3: *Alkylation of **IDTT** with a hexyl sidechain and subsequent Vilsmeier-Haack reaction.*

3.2.2 – Synthesis of End-Group Halogenated C6-ITIC

Two additional lower bandgap acceptors were envisioned, **4F-C6-ITIC**, and **4Cl-C6-ITIC** (**Scheme 3.4**). The inductive effects from the halogens in **4F-C6-ITIC** and **4Cl-C6-ITIC** were expected to reduce their bandgaps by predominantly deepening the localised LUMO orbital, as in **IT-4F** and **IT-4Cl** respectively (**Figure 3.1**). Moreover, the addition of halogens was predicted to enhance intermolecular packing through halogen-sulphur and halogen-hydrogen non-covalent interactions. In addition, a benefit of using the chlorinated **DIC** instead of fluorinated is the increased dipole moment in the C-Cl bond compared to the C-F bond. This has been known to improve the intermolecular charge transfer effect between the donor and acceptor in the BHJ and to therefore expand the overall absorption spectrum for the bulk.[162] Moreover, as discussed in the introduction to this chapter chlorine acts to stabilise the localised LUMO and therefore lower bandgap further by an additional electron accepting effect.

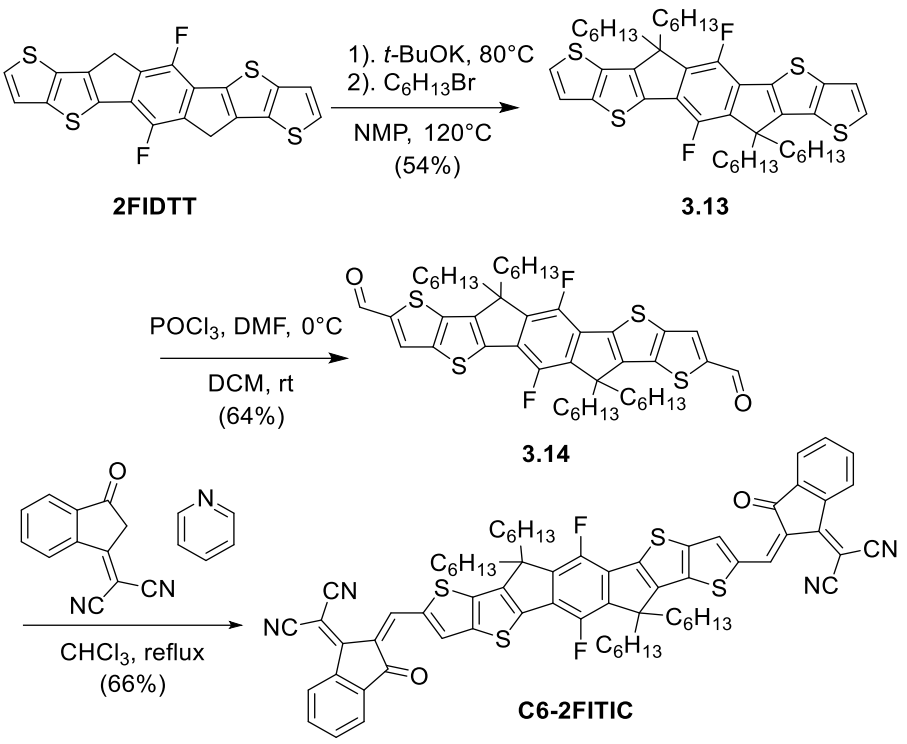


Scheme 3.4: *Knoevenagel condensation reactions towards* ***C6-ITIC*** *derivatives.*

The end-group halogenated acceptors were prepared from **3.6** produced by the ring-extension methodology. The Knoevenagel condensation from **3.6** to **4F-C6-ITIC** was facile and proceeded in a good 59% yield (**Scheme 3.4**). However, **4Cl-C6-ITIC** appeared to decompose at high reaction temperatures from **3.6** and a yield of only 8% was obtained. The reaction was instead performed at 40°C overnight and proceeded in a passable 27% yield.

3.2.3 – Synthesis of Core Fluorinated C6-ITIC

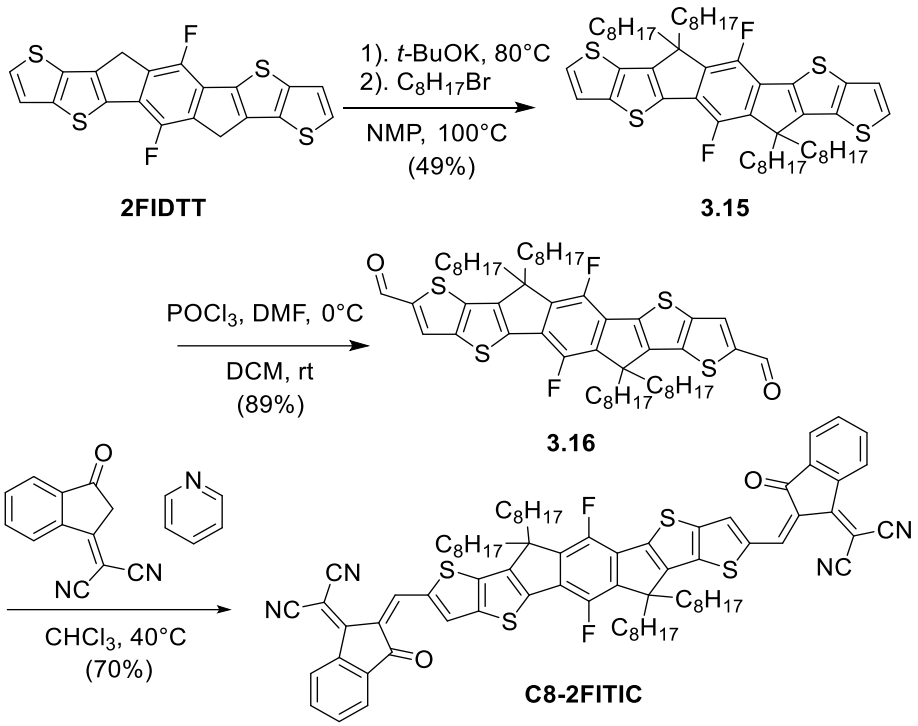
To make a wider bandgap variation of **C6-ITIC** for indoor light applications, and tertiary or tandem OPV cells the **2FIDTT** core produced by the triflic acid route was subjected to the same functionalisation as **IDTT** above (**Scheme 3.5**). Substitution of fluorine onto the central phenyl of **IDTT** is expected to widen the bandgap of **C6-2FITIC** by predominantly lowering the localised HOMO. The use of fluorine was expected to improve intermolecular interaction as would be expected for the end-group halogenated acceptors.



Scheme 3.5: *C6 alkylation and subsequent Vilsmeier-Haack reaction of* ***2FIDTT****.*

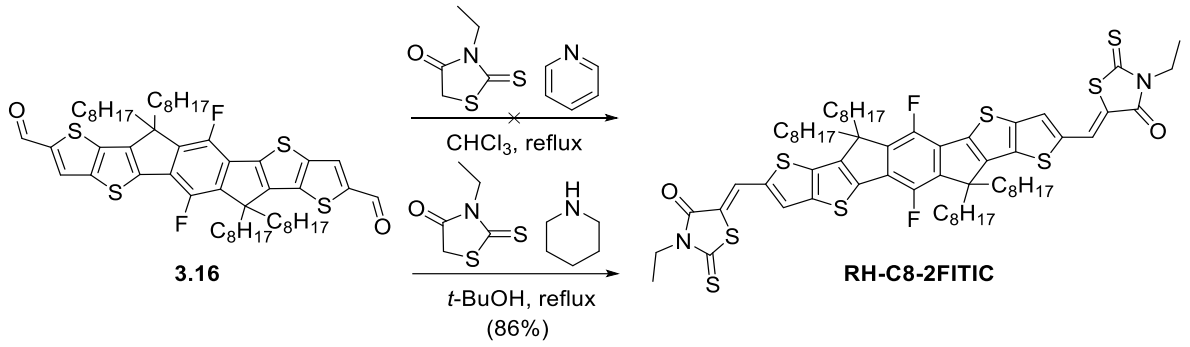
A good 54% yield was obtained for the alkylation of **2FIDTT**, a more forceful 120°C reaction temperature was used to improve the yield. Other polar aprotic solvents DMSO, dioxane, and pyridine were tested for the alkylation, but they reduced reaction yield. Vilsmeier-Haack formylation produced the requisite aldehyde **3.13**. As the unsubstituted **DIC** end group was used no stability issues were encountered for the Knoevenagel condensation and it proceeded in high 66% yield producing the novel NFA **C6-2FITIC.**

Due to concerns about the low solubility of **C6-2FITIC**, the octyl-chain alternative **C8-ITIC** was also synthesised (**Scheme 3.6**). This synthesis was performed in the same way as for **C6-2FITIC** with a major improvement being an increase in yield for the Vilsmeier-Haack reaction from 64% to 89%. This improvement was due to 13 equivalents of $POCl_3$ being used as opposed to the 5 equivalents that were used for the synthesis of **3.13**. Yield was lost in the synthesis of **3.13** due to the presence of under-reacted mono-substituted aldehyde in the crude product. It is likely that such large loadings of $POCl_3$ are required because of a loss in its purity through reaction with atmospheric water.



Scheme 3.6: *C8 alkylation and subsequent Vilsmeier-Haack reaction of* ***2FIDTT****.*

3.2.4 – Synthesis of Rhodanine End-Group C8-ITIC



Scheme 3.7: *Knoevenagel condensation reaction towards* ***RH-C8-2FITIC****.*

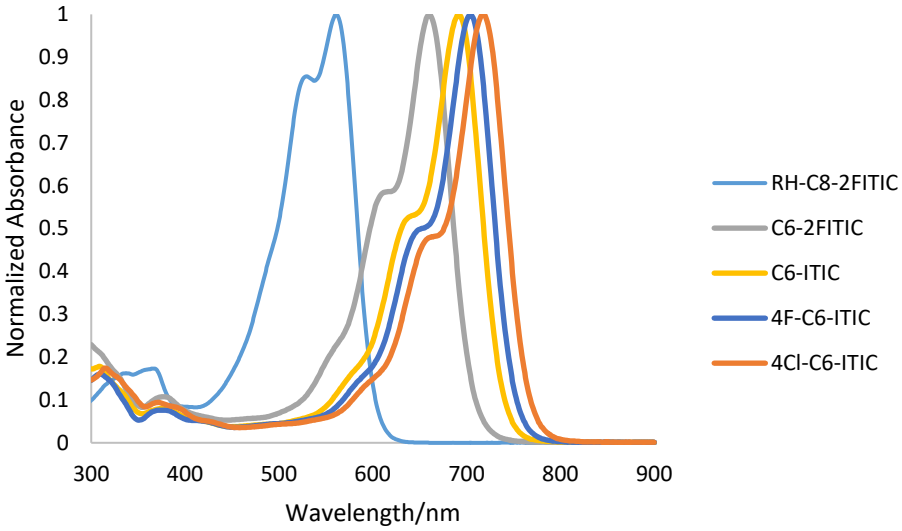
In order to make even wider bandgap acceptors for use with indoor light or ternary solar cells, a rhodanine flanked acceptor was envisioned. This acceptor was synthesised by the Knoevenagel condensation of **3.16** (**Scheme 3.7**), as for **C8-2FITIC**. The conditions used for the previous acceptors were at first attempted, yet no product was produced. Therefore, more forceful conditions were used as in the literature synthesis of **EH-IDTBR.**[10] These conditions involved the more polar *tert*-butanol to accelarate the nucleophilic addition between the rhodanine anion and the aldehyde **3.16** and to allow the reaction to be heated

to a more forcing higher temperature. Additionally the more basic piperidine was used instead of pyridine to ensure rapid deprotonation. As a result, **RH-C8-2FITIC** was obtained in excellent 86% yield.

3.2.5 – Optoelectronic and Electrochemical Properties of NFAs

The four novel acceptors were tested by UV-Vis and their optical bandgaps calculated **(Figure 3.6 (a)**). As expected, halogenation on the end-groups reduced bandgap whilst halogenation on the core increased it. Similarly, the use of a rhodanine end-group greatly widened bandgap for **RH-C8-2FITIC**.

(a)



Acceptor	4Cl-C6-ITIC	4F-C6-ITIC	C6-ITIC	C6-2FITIC	RH-C8-ITIC
Absorption Maximum (nm)	718	704	691	660	561
Absorption Onset (nm)	822	799	791	760	643
Optical Bandgap (eV)	1.51	1.55	1.57	1.63	1.93

(b)

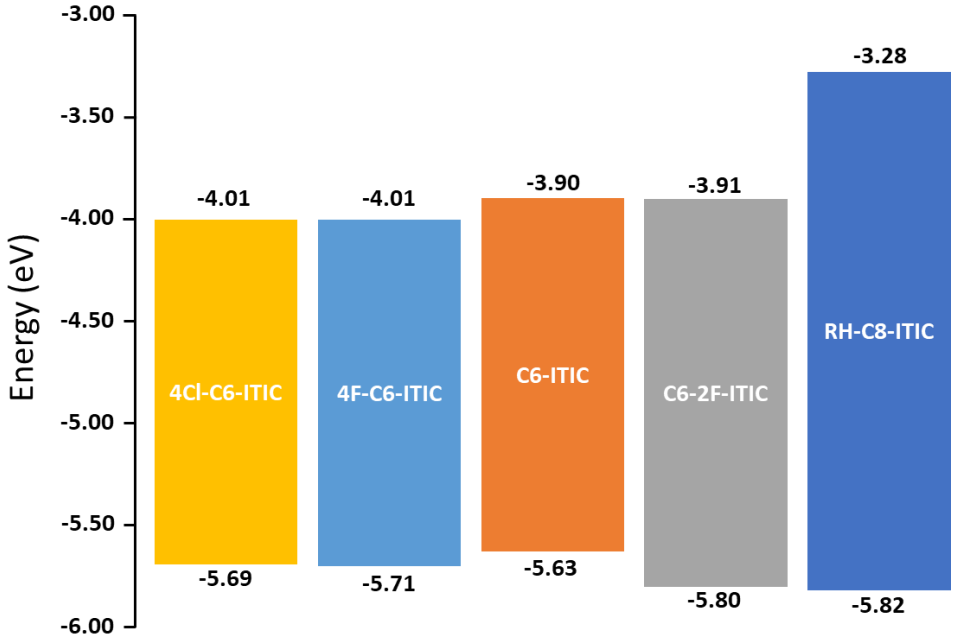


Figure 3.6: ***(a)*** *Normalised UV-Vis spectra and bandgap table for NFAs in chloroform solution.* ***(b)*** *FMO energy level diagram for novel NFAs estimated by CV on drop-cast films in 0.1 M solution of* Bu_4NPF_6 *in acetonitrile, using a (Fc/Fc+) internal standard.*

The same methodology was used for CV measurements as in Chapter 2. However, the deeper electron affinities (EAs) meant that CV could be used to estimate LUMO energy levels as well. As the NFAs were coated as films, it was difficult to see reversibility in oxidation for most due to delamination and it's likely that film thickness affected the visibility of any oxidation reversibility (**Appendix 7.2.1**). Therefore, the onsets of oxidation were used in calculations of IP. The HOMO energy levels for the NFAs were estimated as equal to the IP, this was again calculated as per **Equation 2.1**. No reversibility could be seen in the reduction of any of the NFAs. Therefore, the onset of reduction was taken and referenced against Fc/Fc^+ to give the reduction potential E^R. This was compared to the EA of ferrocene relative to the vacuum level as per **Equation 3.1** to give the EA. The EA was then assumed to equal the LUMO energy level for data analysis.

$$\boldsymbol{EA = -(E^R + 4.8)eV}$$

Equation 3.1: *Formula for electron affinity calculation from CV.*

Changes to frontier molecular orbital energy levels on halogenation have occurred as predicted, as can be seen from CV measurements depicted in **Figure 3.6 (b)**.[169] The end-group halogenated acceptors lowered bandgap by predominantly lowering LUMO orbitals while fluorination of the core raised bandgap by lowering the HOMO orbital predominantly. The trend in the electrochemical bandgap agrees to that for the optical bandgap, besides **4Cl-C6-ITIC** and **4F-C6-ITIC** having virtually identical electrochemical bandgaps whilst **4Cl-C6-ITIC** had a shorter optical bandgap. **4Cl-C6-ITIC** would be expected to have a shorter bandgap due to a greater LUMO deepening effect because of its electron-accepting stabilising effect and greater dipole moment, as discussed in the introduction of this chapter. It is likely that the lack of difference in electrochemical bandgap between the fluorinated and chlorinated acceptors is due to inherent inaccuracies in CV measurements. As expected, **RH-C6-ITIC** had a wider optical and electrochemical bandgap due to the reduced push-pull effect caused by the less electron accepting rhodanine moiety.

3.3 – Device Performance of Novel NFAs

3.3.1 – Initial Screening on Large Area Devices

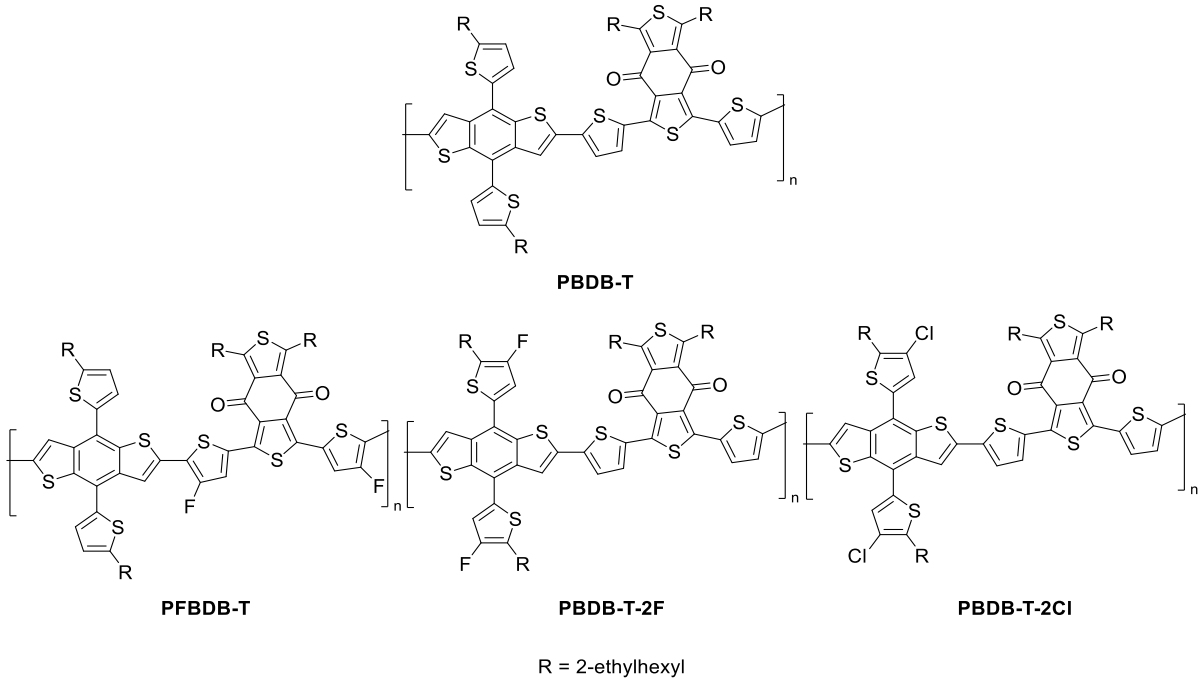
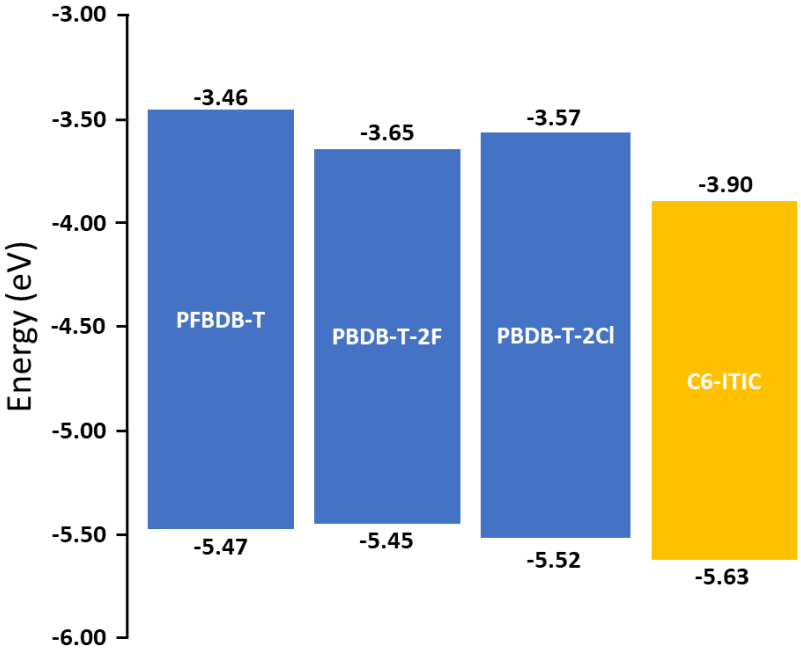


Figure 3.7: *Chemical structures of PFBDB-T, PBDB-T-2F, and PBDB-T-2Cl polymers.*[122,162,170]

After synthesis **C6-ITIC**, **4F-C6-ITIC**, **4Cl-C6-ITIC**, and **C6-2FITIC** were taken to our sponsor's site for device fabrication with view to test their potential for large-scale practical use. All devices were fabricated during an exchange visit. Three potential donor polymers with similar structures and properties were chosen for this endeavour: **PFBDB-T**, **PBDB-T-2F**, and **PBDB-T-2Cl** (**Figure 3.7**). The energy levels of these polymers by CV are depicted in **Figure 3.8 (a)** together with the energy levels of **C6-ITIC** for comparison. These polymers are all derivatives of the successful **PBDB-T** polymer.[161,171,172] It must be noted that due to inherent inaccuracies in the measurement of energy levels by CV and the varying environments in which these were taken by different research groups, the energy levels should be used as a guide rather than exact comparisons.[122,162,170] The devices were produced in an inverted stack, the energy levels of an example **PFBDB-T:C6-2FITIC** device are given in **Figure 3.8 (b)**.

(a)



(b)

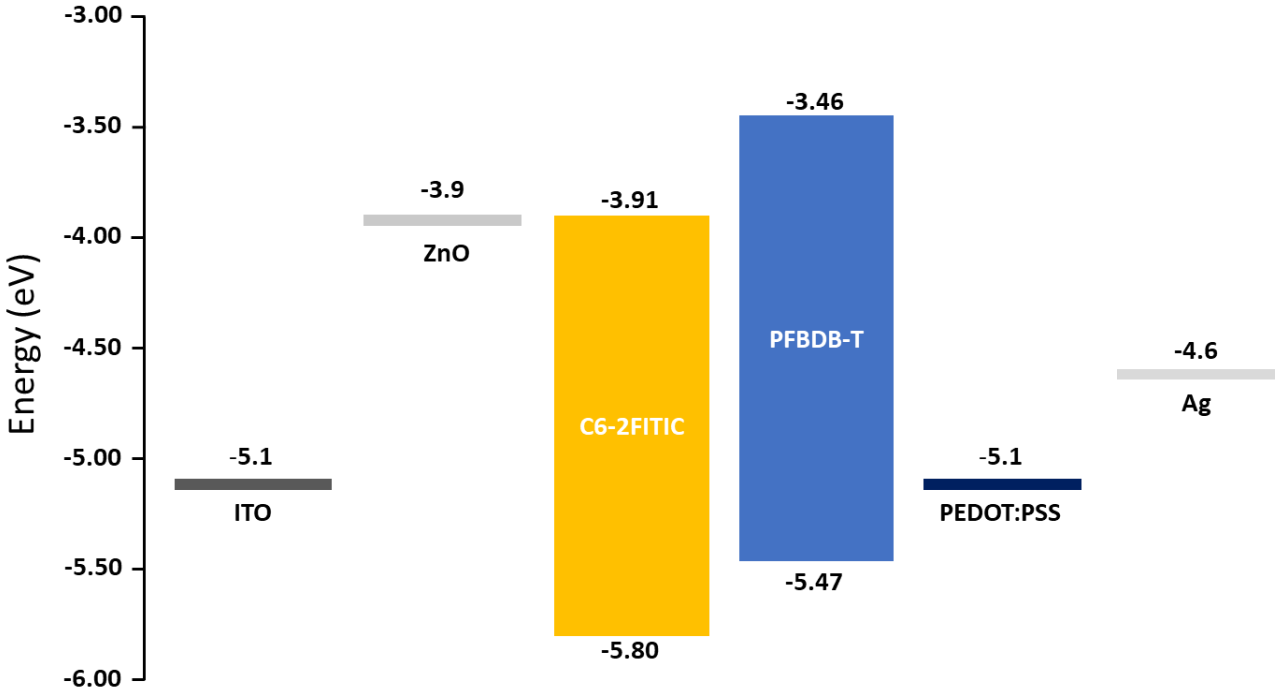


Figure 3.8: (a) *FMO energy levels of* ***PFBDB-T***, ***PBDB-T-2F***, *and* ***PBDB-T-2Cl*** *polymers from literature CV results and FMO energy levels of* ***C6-ITIC*** *by CV on drop-cast films in 0.1 M solution of* Bu_4NPF_6 *in acetonitrile, using a (Fc/Fc+) internal standard.*[122,162,170] ***(b)*** *Energy levels within the inverted device stack of* ***PFBDB-T:C6-2FITIC*** *large area devices.*[122,173]

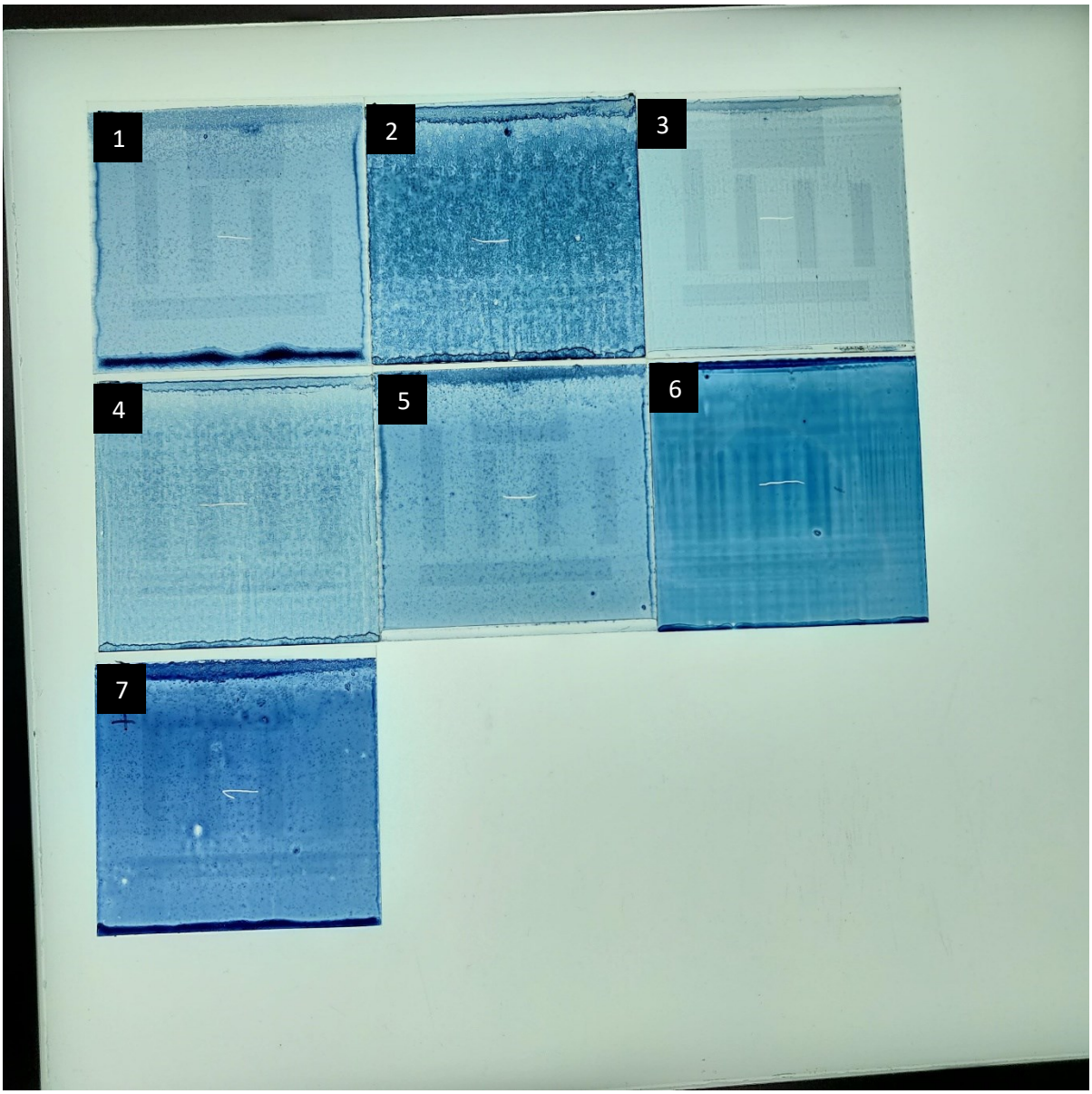
The **PFBDB-T** polymer was synthesised in our group and previously used with **C8-ITIC** to achieve 13.2% PCE devices.[122] This polymer is a modification of the prolific **PBDB-T** polymer, but with a lower HOMO energy level through fluorination resulting in higher V_{OC} devices.[161,171,172] **PBDB-T-2F** is a regioisomer of **PFBDB-T** and therefore has similar energy levels. The increased dipole moment and the stabilising acceptance of electrons by chlorine in the C-Cl bond reduces the HOMO energy level further in **PDBDB-T-2Cl** and thus gives the potential for increased V_{OC}.[168]

The devices were coated on a large 25 cm^2 substrate with 8 distinct pixels to test for scalability. However, the large area made coating homogenous films more difficult. Blade-coating was used to coat the active layers of the devices as it is a scalable and a less wasteful process in comparison to the commonly used spin-coating.

Prior to device deposition, conditions were investigated to coat test films to measure the thickness and smoothness of the active layers. Unfortunately, the poor solubility of some mixtures resulted in uneven coatings. The thickness of the test coatings was measured by profilometry and approximated by measuring the maximum absorption of a UV-vis measurement taken at the centre of the film. This absorption maximum would correspond to the maximum of absorption for the polymer for every measured film. Attempts were made to coat films to a thickness of 45 nm and 90 nm for each formulation, however this was quite difficult in practice as the relationship between DB speed varies between formulations (**Figure 3.9 (b)**).

Chlorinated solvents are often environmentally unacceptable, so our sponsor was strongly focussed on non-chlorinated solvents. The first solvent used to coat films and active layers was o-xylene, which is a non-chlorinated solvent and is therefore a good solvent choice for scalable OPV. Initially formulations were produced at 20 mg/ml, but this was reduced to 16 mg/ml as poor solubility was observed in the formulation vials. A photo of the test films is given in (**Figure 3.9 (a)**).

(a)



(b)

Film	Donor	Acceptor	DB speed mm/s	Target thickness/nm	Film Thickness/ nm	Peak UV-Vis absorbance
F1	PFBDB-T	C6-ITIC	45	45	68	0.531
F2	PFBDB-T	C6-ITIC	90	80	110	0.994
F3	PFBDB-T	4F-C6-ITIC	40	45	45	0.305
F4	PFBDB-T	4F-C6-ITIC	85	80	66	0.609
F5	PFBDB-T	C6-2FITIC	25	45	82	0.584
F6	PFBDB-T	C6-2FITIC	50	80	131	0.895
F7	PBDBT-2F	C6-2FITIC	40	45	126	0.937

Figure 3.9: (a) *Test films coated on a glass substrate, viewed with a backlight.* ***(b)*** *Table displaying formulations and coating conditions for test films. All films were processed from o-xylene at a 1:1.25 D:A ratio, 16 mg/ml concentration and a doctor blade surface temperature of 90°C.*

As can be observed above, all the test films suffered from poor morphology in both thick and thin films. Devices with **C6-ITIC** had a problem with excessive aggregation as can be seen from the multiple dark spots in the film, this effect degenerates to a very patchy film in thicker films. The **4F-C6-ITIC** devices had a very rough surface causing scattering in thin devices and had excessive aggregation in thicker devices. **PFBDB-T:C6-2FITIC** films arguably had the best coatings as they had the deepest colour and the thicker devices apparently only suffered from streaking and a small amount of excessive aggregation. **PBDB-T-2F:C6-2FITIC** films had more aggregation than those of **PFBDB-T:C6-2FITIC** at equivalent thicknesses, implying a worsened morphology when **PBDB-T-2F** is used. A major contributor to the poor morphologies of the coated films is the poor solubility of the acceptors. Because the acceptors have a deep blue colour and insoluble acceptor is left in the bottom of the formulation vial during doctor blading, the trend in the solubilities of the acceptors can be seen based on the depth of their blue colour. As such it can be assumed from the test films that **C6-2FITIC** had the best solubility, followed by **C6-ITIC**, and finally **4F-C6-ITIC**.

Table 3.2: *Maximum performance results and fabrication conditions for large area devices. The Merck reference device was made up of a confidential formulation and coated under proprietary conditions. All other devices were processed from o-xylene at a 1:1.25 D:A ratio, 16 mg/ml concentration and a doctor blade surface temperature of 90°C.*

Device	Donor	Acceptor	DB speed mm/s	Peak UV-Vis absorbance	V_{OC} (V)	FF	J_{SC} (mA/cm2)	PCE (%)
D1	PFBDB-T	C6-ITIC	40	0.552	0.91	0.41	8.4	2.4
D2	PFBDB-T	C6-ITIC	80	0.706	0.85	0.30	3.4	0.8
D3	PFBDB-T	4F-C6-ITIC	45	0.405	-	-	-	0.0
D4	PFBDB-T	4F-C6-ITIC	95	0.534	0.62	0.30	1.9	0.4
D5	PFBDB-T	C6-2FITIC	15	0.365	0.79	0.51	9.4	3.8
D6	PFBDB-T	C6-2FITIC	45	0.805	0.84	0.32	4.8	1.3
D7	PBDB-T-2F	C6-2FITIC	10	0.299	0.83	0.46	5.4	2.0
D8	PBDB-T-2F	C6-2FITIC	30	0.588	0.82	0.29	4.7	1.1
D9	Merck reference device				0.69	0.46	18.5	5.9

Afterwards, complete devices were fabricated using the same formulations as in the test films (**Table 3.2**). Reference devices performed nominally, indicating a lack of systematic error in the run.

As making profilometry measurements takes more time and can be difficult on non-homogenous active layers, active layer thickness was controlled by maximum UV-Vis absorption. Coatings of thin devices targeted a UV-Vis absorbance of 0.4 while thick devices targeted a peak absorbance of 0.8, in practice variation from these targets occurs. This methodology made the assumption that the structurally similar polymers would have similar relationships between thickness and maximum absorbance. An estimation of the thickness of active layers with each formulation can be made by taking the maximum absorbance of the device and comparing it to its equivalent film with known maximum absorbance and thickness. It must be noted that this is not a perfect approximation as the test films didn't have an HTL and were coated on ITO instead of the device's ETL, leading to a potentially different morphology and thickness.

The champion devices were D1 and D5 and this is indicative of the superior solubility of **C6-ITIC** and **C6-2FITIC**. Despite the overall poor quality of the devices, a trend can be observed. **PFBDB-T:C6-2FITIC** devices had improved FF and J_{SC} compared to **PFBDB-T:C6-ITIC** devices, but lower V_{OC}. However, due to the obvious poor solubility of the acceptors in o-xylene other solvents should be used to confirm if this relationship between the different BHJs is simply due to a difference in donor:acceptor ratio (D:A) in films. Thicker devices of each acceptor performed worse than the thinner devices. Peculiarly, this drop in performance wasn't only due to a reduction in FF as would be expected when changing to a thicker active layer, but due to a drop in J_{SC} as well. This is somewhat counterintuitive as generally thicker devices have greater J_{SC} as there is more material to absorb light. However, thicker devices were coated with a faster blade speed, which may change the microstructure of the active layer due to differences in drying dynamics, which can therefore influence charge extraction and exciton harvesting.

Both the thinner **PFBDB-T:C6-2FITIC** device D5 and the thicker device D6 outperform their respective counterpart **PDBT-2F:C6-2FITIC** devices D7 and D8. However, the devices all had significantly different thicknesses from each other, which are further complicated by the differing absorbances of the two polymers. Moreover, it's possible that optimised untested thicknesses could make the devices have a different performance relationship. Therefore, further testing is required to confirm if **PFBDB-T** or **PBDB-T-2F** is the superior polymer with **C6-2FITIC**.

4F-C6-ITIC devices had the worst performance and the measured pixels in their thinner devices were all completely shunted due to excessive aggregation (**Figure 3.10**). Increasing thickness in the **PFBDB-T:4F-C6-ITIC** devices reduced the number of shunts as aggregates are less likely to reach across the entire active layer. However, the devices still performed almost as if they had single-component active layers due to the poor solubility of **4F-C6-ITIC**, giving low J_{SC} and very poor FF JV curves.

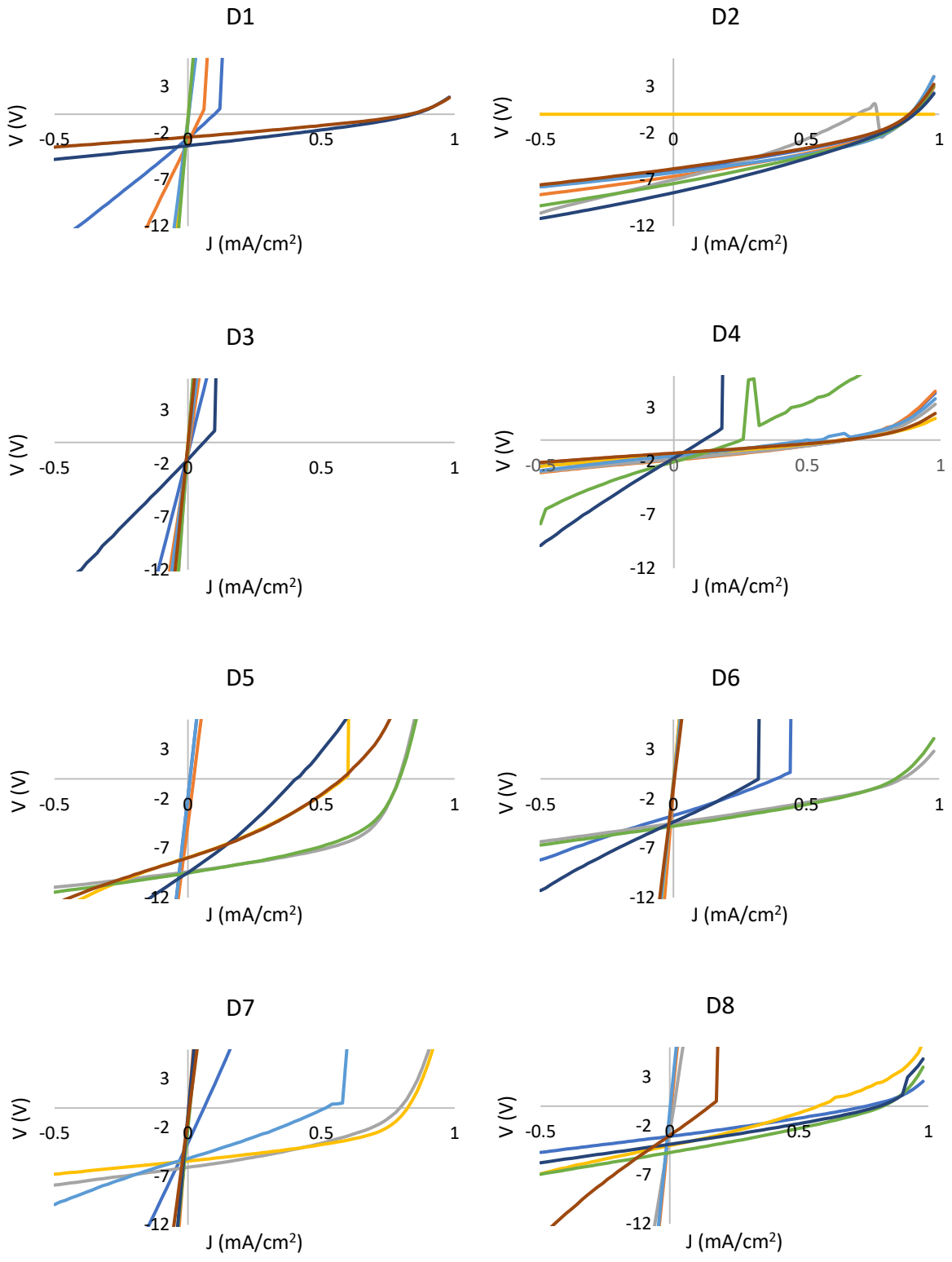
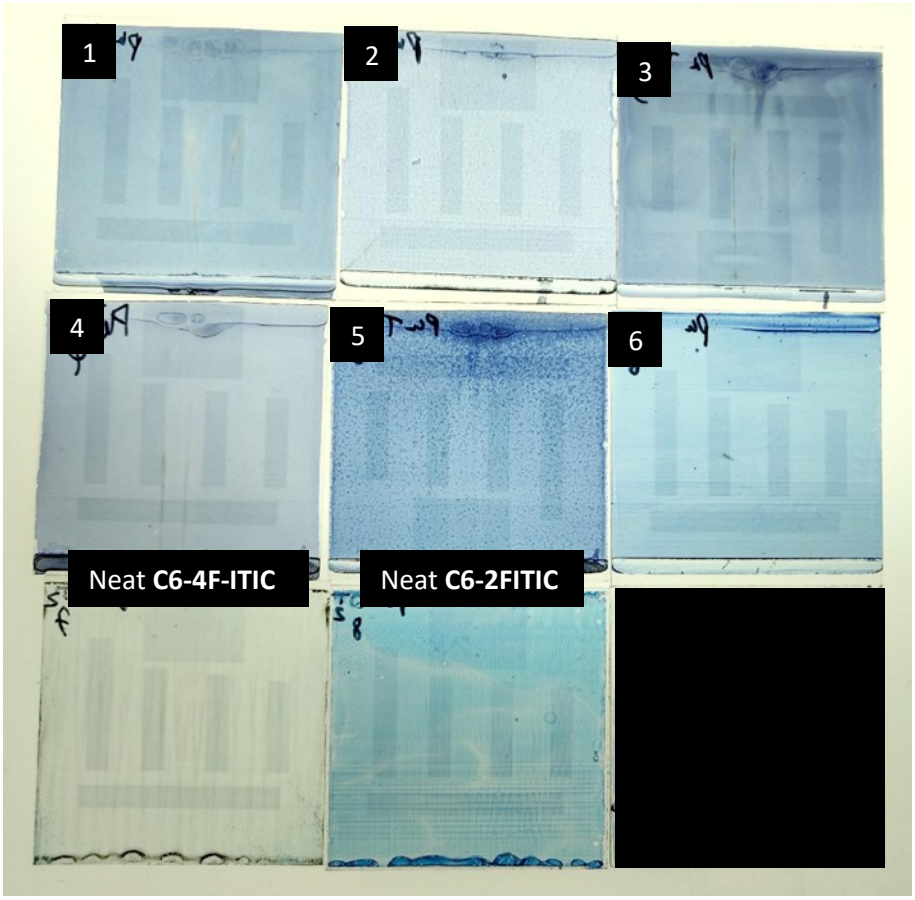


Figure 3.10: *JV curves for the completed o-xylene devices, curves for all measured pixels are shown.*

Due to the poor performance of o-xylene devices, a set of devices using the common chlorinated solvent CB were prepared instead. Although CB was an unacceptable solvent for actual application, this would at least allow comparison between materials and our previous acceptor. These devices screened the acceptors with the **PBDB-T-2F** and **PBDB-T-2Cl** polymers as they were in supply at our sponsor's site and we needed to ascertain if they were suitably high performing for us to take samples back to Imperial for future testing.

As before, test films were first coated, and their photos and coating conditions are presented below (**Figure 3.11**). After the first run, we had a better understanding of the relationship between doctor blading conditions and thickness by looking at measured test film thicknesses. Attempts were made to keep films of similar thickness based on this in the second run, but difficulties were encountered especially when the **PBDB-T-2Cl** polymer was used that had lower solubility in CB. As the coating progressed and **PBDB-T-2Cl** films were found to have lower absorbances, it was decided that **PBDB-T-2F** films and devices would target a 0.6 peak UV-vis absorbance whilst 0.3 would be targeted for **PBDB-T-2Cl**. In future work these films and devices could be optimised to have the same absorbance, and their thickness could be confirmed by profilometry.

(a)



(b)

Test Film	Donor	Acceptor	DB speed mm/s	Peak UV-Vis absorbance
F1	PBDB-T-2F	C6-ITIC	30	0.561
F2	PBDB-T-2Cl	C6-ITIC	30	0.323
F3	PBDB-T-2F	4F-C6-ITIC	35	0.699
F4	PBDB-T-2Cl	4F-C6-ITIC	40	0.385
F5	PBDB-T-2F	C6-2FITIC	20	0.618
F6	PBDB-T-2Cl	C6-2FITIC	30	0.394

Figure 3.11: (a) *Test films coated on a glass substrate, viewed with a backlight.* ***(b)*** *Table displaying fabrication conditions for the test films. All formulations were stirred at 105°C in a glovebox overnight, had a 20 mg/ml concentration in CB, a 1:1.25 D:A ratio, 16 mg/ml concentration and were coated at a doctor blade surface temperature of 90°C.*

Surprisingly, test films processed from CB were of equally poor quality to those processed from o-xylene, if not worse. F1, F3, and F4 were very rough and caused scattering, while other films suffered from aggregation. As **C6-4F-ITIC** again appeared to be less soluble than

C6-2F-ITIC, neat films of just acceptor were coated as test films. As expected, the neat **C6-4F-ITIC** is almost colourless whilst the neat **C6-2FITIC** has a light blue colour, indicating that most of the **C6-4F-ITIC** remained in the formulation vial upon coating. Test films of **4Cl-C6-ITIC** weren't coated due to a lack of material.

Table 3.3: *Maximum performance results and fabrication conditions for large area devices. The Merck reference device was made up of a confidential formulation and coated under proprietary conditions. All other device formulations were stirred at 105°C in a glovebox overnight and were processed from CB at a 1:1.25 D:A ratio, 20 mg/ml concentration and a doctor blade surface temperature of 105°C.*

Device	Donor	Acceptor	DB speed mm/s	Peak UV-Vis absorbance	V_{OC} (V)	FF	J_{SC} (mA/cm2)	PCE (%)
D1	PBDB-T-2F	C6-ITIC	30	0.621	0.87	0.31	3.7	1.0
D2	PBDB-T-2Cl	C6-ITIC	30	0.333	0.44	0.00	2.3	0.3
D3	PBDB-T-2F	4F-C6-ITIC	30	0.589	0.42	0.00	1.3	0.1
D4	PBDB-T-2Cl	4F-C6-ITIC	37	0.392	0.27	0.00	1.0	0.1
D5	PBDB-T-2F	C6-2FITIC	20	0.580	0.86	0.59	12.2	6.2
D6	PBDB-T-2Cl	C6-2FITIC	25	0.416	0.88	0.50	9.9	4.3
D7	PBDB-T-2F	4Cl-C6-ITIC	30	0.578	0.02	0.00	0.4	0.0
D8	PBDB-T-2Cl	4Cl-C6-ITIC	30	0.346	0.10	0.00	0.6	0.0
D9	Merck reference device				0.69	0.46	19.2	6.0

Afterwards, complete devices were fabricated using the same formulations as in the test films (**Table 3.3**). Reference devices performed nominally, indicating a lack of systematic error in the run.

Only novel NFA devices D1, D5, and D6 had any significant FF and behaved as two-component solar cells. The others suffered from a lack of acceptor in the active layer due to poor solubility, or the presence of multiple shunts. D5 outperformed D6 due to improved FF and J_{SC} that can be attributed to improved morphology, perhaps due to the lack of solubility of **PBDB-T-2Cl.** As expected, the **PBDB-T-2Cl C6-2FITIC** devices had slightly improved V_{OC} because of the increased stabilising effect of introducing the C-Cl bond, albeit within error.[168] The greatest correlation from this data however, is the relationship between the amount of NFA in the active layer and PCE, this is shown in **Figure 3.14** where the NFA's peak in the overall device UV-Vis spectrum grows as more soluble acceptors are used.

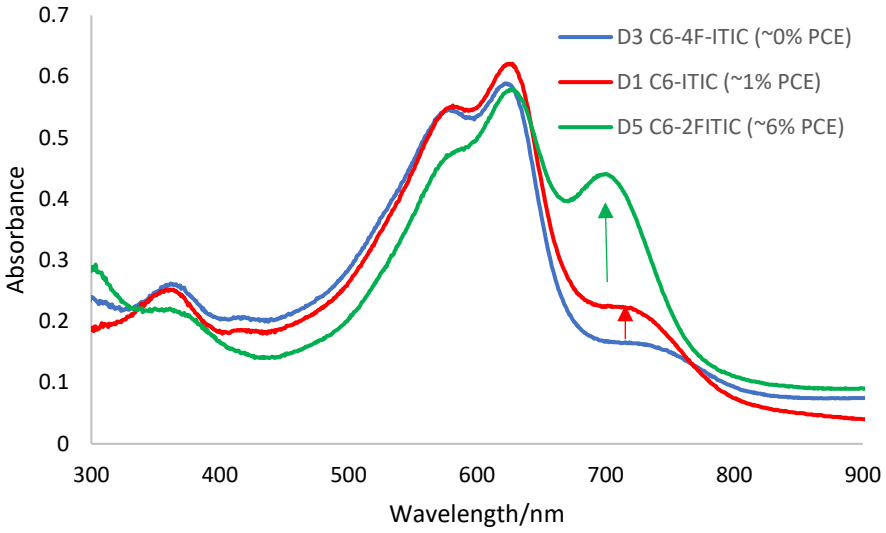


Figure 3.14: *UV-Vis spectra of completed CB devices, increases in NFA absorption are shown by arrows. The PCEs of the devices are given.*

All our acceptors suffered from poor PCEs due to a low Jsc, Voc, and FF due to poor solubility. Devices made with **C6-2FITIC** had the best performance, yet no pixels of the devices performed above the 6.5% mark. On initial screening **PFBDB-T** appears to be more suitable for use with **C6-2FITIC** than **PBDB-T-2F** and **PBDB-T-2Cl**, however more testing is required to confirm this. Reference devices performed nominally during our tests, and therefore these results weren't due to systematic error in the device fabrication process. As formulations coated from both o-xylene and CB suffered from solubility problems, a change in coating conditions, formulation content or synthetic modification of the acceptors would be required to improve device performance.

3.3.2 – Small Area Devices – Influence of Fabrication Facility

After making use of the equipment at our sponsor's site we produced small area devices in the Molecular Sciences Research Hub clean room. Unfortunately, the clean room had only become fully operational in late 2019, whilst we began testing our devices at the start of 2020. As such systematic errors were observed with our devices due to the clean room equipment not being fully optimised.

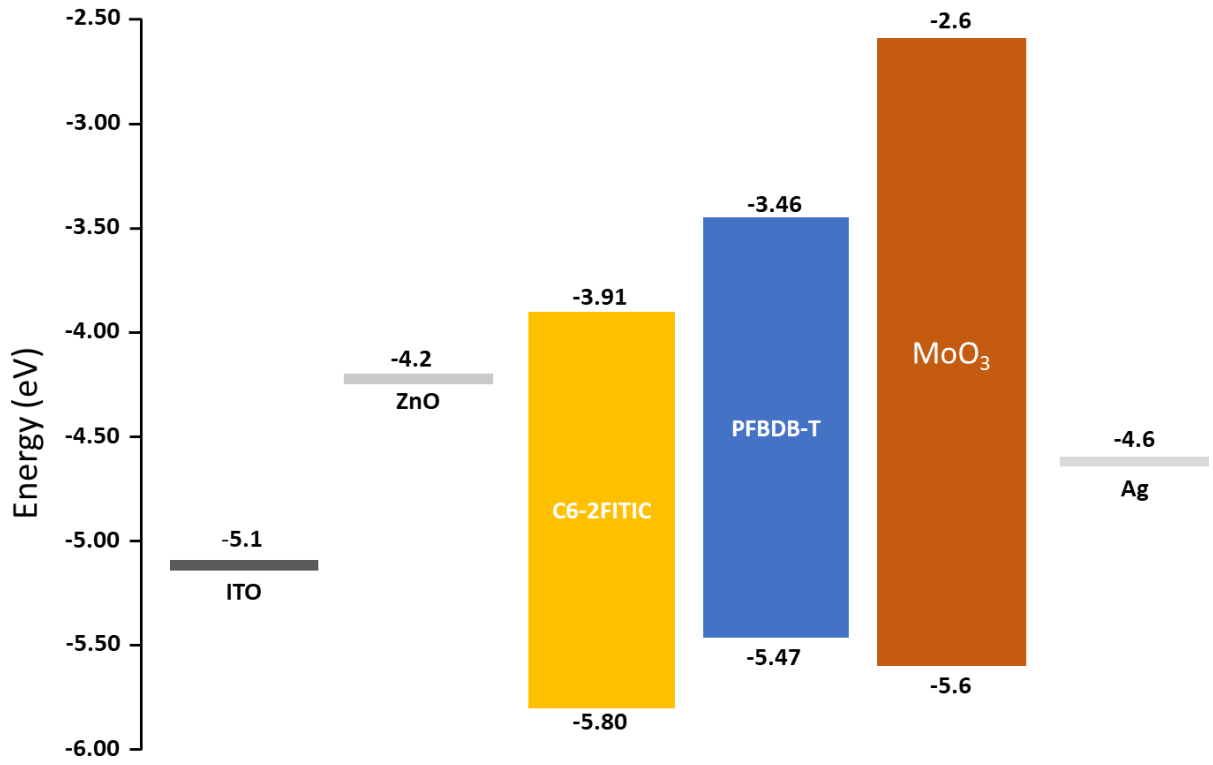


Figure 3.15: *Energy levels within the inverted device stack of* ***PFBDB-T:C6-2FITIC*** *small area-devices.*[173]

The devices produced in the clean room used more forgiving smaller 1.2 cm^2 substrates with six measured pixels that were coated by spin coating, as such optimisation was simpler than at our sponsor's site. The devices used a similar stack to the large area devices, but with a MoO_3 HTL and solgel ZnO rather than ZnO nanoparticles to coat the ETL (**Figure 3.15**).

Initial film formation utilised CB but it was found that poor coatings were obtained for all the **C6-ITIC** derivatives due to poor solubility. Solubility was improved when switching to chloroform. However, due to the low boiling point of chloroform the usual spin coating technique wherein the formulation is deposited and then spinning commences from rest could not be used. Instead, dynamic spin coating was performed where the substrate was first allowed to accelerate, and the formulation deposited upon it. An issue with dynamic spin coating is that whilst it allows for coating from low boiling solvents, it can make coating to consistent thicknesses difficult. Additionally, active layers prepared by dynamic spin coating tend to be thicker and therefore a low 12.5 mg/ml formulation concentration was used with **C6-2FITIC** devices to account for the fast-drying speed of chloroform. Attempts were made to optimise coating conditions for test films containing **C6-ITIC**, **4F-C6-ITIC**, and

4Cl-C6-ITIC. However, very poor coatings were obtained with both CB and chloroform processing solvent, similarly to observations made for the large area devices. Therefore, **C6-2FITIC** devices were prioritised for testing.

Table 3.4: *Maximum performance results and fabrication conditions for* ***PBDB-T:ITIC****,* ***PFBDB-T:ITIC****, and* ***PFBDB-T:C6-2FITIC*** *devices. All blends were used at a 1:1.25 D:A ratio, with* ***ITIC*** *devices processed from CB and* ***C6-2FITIC*** *devices processed from chloroform.*

Device	Donor	Acceptor	Concentration (mg/ml)	Annealing Temperature (°C)	Spin speed (rpm)	V_{OC} (V)	FF	J_{SC} (mA/cm2)	PCE (%)
D1	PBDB-T	ITIC	20	140	2000	0.70	0.47	20.0	6.6
D2	PBDB-T	ITIC	20	160	2000	0.76	0.49	14.1	5.3
D3	PFBDB-T	ITIC	20	140	2000	0.80	0.41	19.9	6.5
D4	PFBDB-T	ITIC	20	160	2000	0.85	0.45	16.6	6.1
D5	PFBDB-T	C6-2FITIC	12.5	120	4000	0.82	0.57	18.9	8.9
D6	PFBDB-T	C6-2FITIC	12.5	140	4000	0.74	0.47	16.7	5.8
D7	PFBDB-T	C6-2FITIC	12.5	140	4000	0.82	0.57	20.8	9.9
D8	PFBDB-T	C6-2FITIC	12.5	160	4000	0.82	0.48	16.6	6.7

Table 3.5: *Maximum performance results and fabrication conditions for optimised devices previously produced by our group. All blends were processed from CB at a 1:1.25 D:A ratio and 20 mg/ml concentration.*[122] ***PBDB-T:ITIC*** *formulations had 0.5% 1,8-diiiodooctane additive by volume.*

Donor	Acceptor	Annealing Temperature (°C)	V_{OC} (V)	FF	J_{SC} (mA/cm^2)	PCE (%)
PBDB-T	ITIC	160	0.89	0.66	17.1	10.0
PFBDB-T	ITIC	140	0.95	0.66	18.5	11.7
PBDB-T	C8-ITIC	n/a	0.87	0.73	19.7	12.4
PFBDB-T	C8-ITIC	n/a	0.94	0.72	19.6	13.2

A set of devices was prepared to investigate the optimal annealing temperature for **C6-2FITIC** devices and planned reference devices using **ITIC** (**Table 3.4**). It was found that devices produced in the clean room greatly trailed the performance of published devices produced in our group using the **ITIC** and **C8-ITIC** acceptors (**Table 3.5**).[122] The champion **PBDB-T:ITIC** device D1 had a poor PCE of 6.6%, in comparison to 10.0% for the champion literature device. Similarly, the champion **PFBDB-T:ITIC** device D3 only had a PCE of 6.5% as opposed to 11.7% in literature. These reductions were due to a greatly supressed V_{OC} and FF

for the clean room devices. For example, D3 had a V_{OC} that was an entire 0.15 V less than the equivalent literature device while it's FF was lower by a very significant 0.25. The clean room **ITIC** devices had greater J_{SC} than those in literature. However, it's unlikely that this difference is accurate as other groups using the clean room have reported that there were known issues with the JV trace measurement setup that led to a consistent overestimation of J_{SC}. Additionally, a mask wasn't used to correct for current generation outside of the measured pixels. However, the overestimation from not using a mask would be a lesser effect as over-conductive interlayers such as PEDOT:PSS weren't used in the devices.[174]

The optimal annealing temperature for **PBDB-T:ITIC** was 140 °C unlike in the literature, but no 1,8-diiodooctane additive was used in this run and this may have caused the difference. As expected, the highest performing **PFBDB-T:ITIC** device was annealed at 140 °C. D7 was annealed at 140 °C and had the highest value for all measured parameters out of the **PFBDB-T:C6-2FITIC** devices. However, the poor performance of D6 that was fabricated under the same conditions makes the optimal annealing temperature uncertain and invites further investigation. The **C6-2FITIC** devices had surprisingly low values for their V_{OC} and FF as for the **ITIC** devices.

After discussion with members of other research groups that used the clean room to fabricate OPV devices, we found that their measurements also suffered from low V_{OC} and FF. The performance of devices fabricated and measured by a scientist from a different research group are shown in **Table 3.6**.

Table 3.6: *Maximum performance results and fabrication conditions for OPV devices prepared in the clean room by Dr. Maxime Babics. The devices were coated from CB and remeasured after three days in a nitrogen glove box.* ***PCE10*** *is the* ***PTB7-Th*** *polymer* ***(Figure 1.5)****. Data reproduced with permission.*

Device	Remeasure?	Donor	Acceptor	Spin speed (rpm)	V_{OC} (V)	FF	J_{SC} (mA/cm2)	PCE (%)
D1	No	PCE10	EH-IDTBR	2000	0.91	0.51	17.4	8.3
D1	Yes	PCE10	EH-IDTBR	2000	1.00	0.59	18.7	11.4
D2	No	PCE10	EH-IDTBR	2000	0.56	0.37	12.7	2.8
D2	Yes	PCE10	EH-IDTBR	2000	0.73	0.58	12.8	5.7
D3	No	P3HT	O-ITDBR	800	0.64	0.62	13.5	5.6
D3	Yes	P3HT	O-ITDBR	800	0.74	0.67	14.0	7.2

Dr. Maxime Babics' devices in **Table 3.6** all had poor V_{OC} and FF that surprisingly improved when the devices were left in a nitrogen glove box for three days. It's unknown what caused this issue, but it is indicative of a problem with the clean-room equipment. When our devices from **Table 3.4** were similarly left in a glovebox for three days and remeasured an improvement in V_{OC} was seen for D6 and an improvement to FF and V_{OC} was seen for D7 (**Table 3.7**).

Table 3.7: *Maximum performance results for devices from* ***Table 3.4*** *with an additional remeasurement after 3 days in the glovebox.*

Device	Remeasure?	Donor	Acceptor	Annealing Temperature (°C)	V_{OC} (V)	FF	J_{SC} (mA/cm2)	PCE (%)
D6	No	PFBDB-T	C6-2FITIC	120	0.82	0.57	18.9	8.9
D6	Yes	PFBDB-T	C6-2FITIC	120	0.87	0.56	18.9	9.4
D7	No	PFBDB-T	C6-2FITIC	140	0.82	0.57	20.8	9.9
D7	Yes	PFBDB-T	C6-2FITIC	140	0.88	0.60	16.1	8.7

The systematic reduction in the performance of clean room devices compared to the literature was unfortunate, but steps were taken to optimise the **PFBDB-T:C6-2FITIC** system nevertheless with hope of utilising these optimised conditions in a different research lab.

Table 3.8: *Maximum performance results and fabrication conditions for* ***PFBDB-T:ITIC****, and* ***PFBDB-T:C6-2FITIC*** *devices optimised for annealing temperature and ETL. All devices were processed from CB at a 1:1.25 D:A ratio. ETL A was coated from a zinc acetate dihydrate precursor solution, whilst ETL B was coated from a purchased ZnO dispersion.*

Device	ETL	Acceptor	Concentration (mg/ml)	Annealing Temperature (°C)	Spin speed (rpm)	V_{OC} (V)	FF	J_{SC} (mA/cm2)	PCE (%)
D1	A	ITIC	20	120	2000	0.72	0.45	19.2	6.2
D2	A	ITIC	20	140	2000	-	-	-	-
D3	B	ITIC	20	120	2000	-	-	-	-
D4	B	ITIC	20	140	2000	0.73	0.47	18.8	6.5
D5	A	C6-2FITIC	12.5	100	4000	0.69	0.50	18.2	6.3
D6	A	C6-2FITIC	12.5	120	4000	0.65	0.43	16.1	4.6
D7	A	C6-2FITIC	12.5	120	4000	0.73	0.45	18.9	6.2
D8	A	C6-2FITIC	12.5	140	4000	0.77	0.55	19.9	8.5
D9	B	C6-2FITIC	12.5	120	4000	0.71	0.46	18.2	5.9

A further set of devices was prepared to confirm optimal annealing temperatures and to find out if using an ETL coated from a zinc acetate dihydrate precursor solution or pre-purchased ZnO dispersion is better for device performance (**Table 3.8**). No clear pattern is seen between the types of ETL or annealing temperature for **ITIC** reference devices. Unfortunately, errors in production lost reference devices D3 and D4 that would have helped to elucidate this issue. The run confirmed that 140°C annealing is optimal for **PFBDB-T:C6-2FITIC** devices as D8 had the highest PCE out of the ETL A devices, this was due to an improvement in all measured parameters. As for the reference devices, no clear pattern was seen for the comparison between ETL A and ETL B devices. Therefore, in future runs the pre-purchased ZnO dispersion ETL B was used due to its ease of use. As for previous devices, a peculiar improvement in PCE is seen upon remeasurement after 3 days in the glovebox due to an increase in both FF and V_{oc} (**Table 3.9**). This effect is observed for both **ITIC** and **C6-2FITIC** devices.

Table 3.9: *Maximum performance results for devices from* ***Table 3.8*** *with an additional remeasurement after 3 days in the glovebox.*

Device	ETL	Acceptor	Concentration (mg/ml)	Spin speed (rpm)	V_{OC} (V)	FF	J_{SC} (mA/cm2)	PCE (%)
D4	B	ITIC	20	2000	0.73	0.47	18.8	6.5
D4	B	ITIC	20	2000	0.87	0.51	18.5	8.7
D8	A	C6-2FITIC	12.5	4000	0.77	0.55	19.9	8.5
D8	A	C6-2FITIC	12.5	4000	0.86	0.59	20.9	10.6

Due to the poor solubility of **C6-2FITIC**, **C8-2FITIC** was synthesised as described at the start of this chapter and tested in future runs. Because of the superior solubility of **C8-2FITIC**, it was used in 20 mg/ml **PFBDB-T:C8-2FITIC** formulations and coated from CB (**Table 3.10**). CB was chosen as it is commonly used as a processing solvent in high-performing devices and doesn't require dynamic spin coating.[175]

Table 3.10: *Maximum performance results and fabrication conditions for* ***PFBDB-T:ITIC****, and* ***PFBDB-T:C8-2FITIC*** *devices optimised for spin speed. All devices were processed from CB at a 1:1.25 D:A ratio and 20 mg/ml concentration and their active layers annealed at 140 °C.*

Device	Acceptor	Spin speed (rpm)	V_{OC} (V)	FF	J_{SC} (mA/cm2)	PCE (%)
D1	ITIC	2000	0.86	0.50	12.7	5.4
D2	C8-2FITIC	3000	0.81	0.64	21.0	10.9
D3	C8-2FITIC	2000	0.82	0.62	22.6	11.4
D4	C8-2FITIC	2000	0.81	0.62	21.8	10.8
D5	C8-2FITIC	1000	0.77	0.37	15.4	4.4

The coating speed was optimised for **PFBDB-T:C8-2FITIC** devices. D3 and D4 performed at 11.4% and 10.8% PCE respectively and were coated at 2000 rpm. Meanwhile, D2 performed at 10.9% PCE and was coated at 3000 rpm. Both coating speeds give similar results, with a coating speed of 2000 rpm giving slightly improved FF whilst 3000 rpm coating yields slightly improved J_{sc}. Due to the higher overall performance of the champion 2000 rpm device, a 2000 rpm spin speed was chosen for future **PFBDB-T:C8-2FITIC** devices.

Table 3.11: *Maximum performance results and fabrication conditions for* ***PFBDB-T:ITIC****, and* ***PFBDB-T:C8-2FITIC*** *devices tested for* ***ITIC*** *batch influence and optimised for annealing temperature. All devices were processed from CB at a 1:1.25 D:A ratio, 20 mg/ml concentration and a 2000 rpm spin coating speed.*

Device	Acceptor	Annealing Temperature (°C)	V_{OC} (V)	FF	J_{SC} (mA/cm2)	PCE (%)
D1	ITIC A	140	0.75	0.46	18.7	6.4
D2	ITIC A	140	0.83	0.47	19.2	7.6
D3	ITIC B	140	0.82	0.50	18.2	7.5
D4	ITIC B	140	0.69	0.47	18.9	6.2
D5	C8-2FITIC	140	0.67	0.53	16.6	6.0
D6	C8-2FITIC	120	0.58	0.72	19.1	7.8
D7	C8-2FITIC	140	0.73	0.52	19.7	7.7
D8	C8-2FITIC	160	0.83	0.48	18.5	7.5
D9	C8-2FITIC	-	0.80	0.57	20.0	9.3

To ascertain if perhaps the cause of low FF and V_{OC} was poor quality **ITIC** in the reference devices and simply inherent problems with **2FITIC** devices, two batches of **ITIC** were tested **Table 3.11**. **ITIC A** was the same batch as used in previous runs, whilst **ITIC B** was a new batch borrowed from the clean room. No clear pattern is observed between the devices from the two **ITIC** batches. However, all have low FF under 0.50 and V_{OC} under 0.83 V indicating that PCE reduction is due to systematic issues with the clean room. **PFBDB-T:C8-2FITIC** devices were also optimised for annealing temperature. It was found that not annealing the active layer gave the best performance, as for **PFBDB-T:C8-ITIC** devices in our previous work (**Table 3.1**)[122] This optimal annealing temperature is quite different from the optimal 140°C for **PFBDB-T:C6-2FITIC** devices. This is reasonable since the **PFBDB-T:C6-2FITIC** system is peculiar due to the poor solubility of **C6-2FITIC** and coating through dynamic spin coating with chloroform. These differences changed the active layer's drying dynamics and altered morphology.

A series of diagnostic runs using only **ITIC** devices was performed to attempt to elucidate the issue with the clean room. Through comparison of results and discussion with other research groups it was found that the low V_{OC} and FF were due to unknown problems with the evaporator used for HTL and anode deposition, as using different evaporators eliminated the problem for other research groups. Therefore, our materials were taken to the physics department and devices prepared there.

Table 3.12: *Performance results and fabrication conditions for* ***PFBDB-T:ITIC****, and* ***PFBDB-T:C8-2FITIC*** *devices fabricated in the clean room and physics department. Performance data shows the spread of data points followed by their mean in brackets. All devices were processed from CB at a 1:1.25 D:A ratio, 20 mg/ml concentration and a 2000 rpm spin coating speed.*

Device	Coating Location	Acceptor	Annealing Temperature (°C)	V_{OC} (V)	FF	J_{SC} (mA/cm2)	PCE (%)
D1	Clean room	C8-2FITIC	120	0.61 ± 0.03 (0.63)	0.55 ± 0.18 (0.53)	17.5 ± 2.1 (17.6)	5.9 ± 1.9 (5.9)
D2	Physics	C8-2FITIC	120	0.78 ± 0.06 (0.78)	0.57 ± 0.04 (0.57)	15.7 ± 2.5 (16.1)	7.4 ± 1.7 (7.2)
D3	Clean room	C8-2FITIC	-	0.80 ± 0.01 (0.80)	0.57 ± 0.04 (0.53)	19.3 ± 1.4 (19.1)	8.2 ± 1.1 (8.2)
D4	Physics	C8-2FITIC	-	0.88 ± 0.00 (0.88)	0.65 ± 0.02 (0.64)	16.1 ± 1.1 (16.1)	9.4 ± 0.5 (9.2)
D5	Clean room	ITIC	140	0.80 ± 0.03 (0.81)	0.47 ± 0.05 (0.48)	15.6 ± 3.4 (16.7)	6.4 ± 1.1 (6.6)
D6	Physics	ITIC	140	0.88 ± 0.00 (0.88)	0.65 ± 0.02 (0.65)	14.3 ± 1.4 (14.5)	8.2 ± 1.0 (8.3)

The results of champion devices produced in the physics department were compared to the best from the clean room (**Table 3.12**). Both annealed and non-annealed **C8-2FITIC** devices performed at higher PCE due to improved V_{OC} and FF when prepared in the physics department. J_{SC} was higher for the clean room devices likely as error due to an overestimation in the solar simulator setup and because a mask was not used to account for current generation outside of pixels, unlike in the physics department. The **ITIC** devices made in the physics department also outperformed those from the clean room. This was again due to a greatly improved FF and an increased V_{oc}, the same pattern as for the **C8-2FITIC** devices. This repeating pattern confirms the systematic error present in devices prepared in the clean room as the fabrication conditions were the same as those used in the physics department. Therefore, all future devices would be fabricated and optimised further in the physics department.

3.3.3 – Devices Made by Collaborator

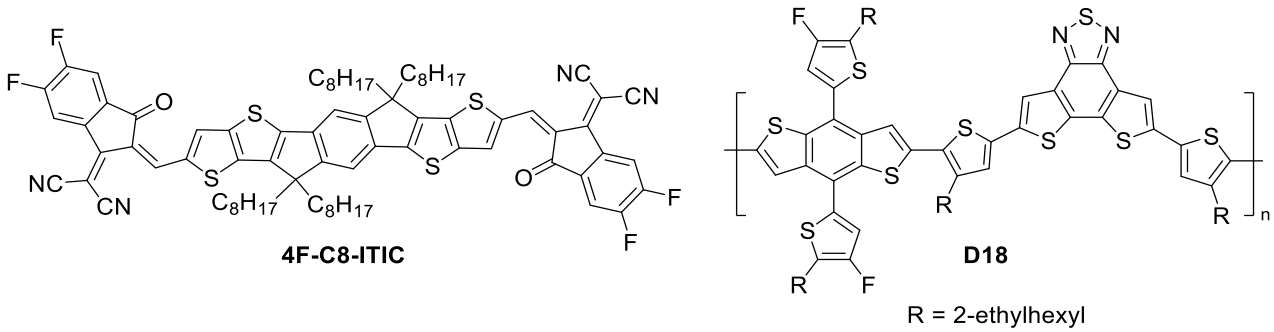
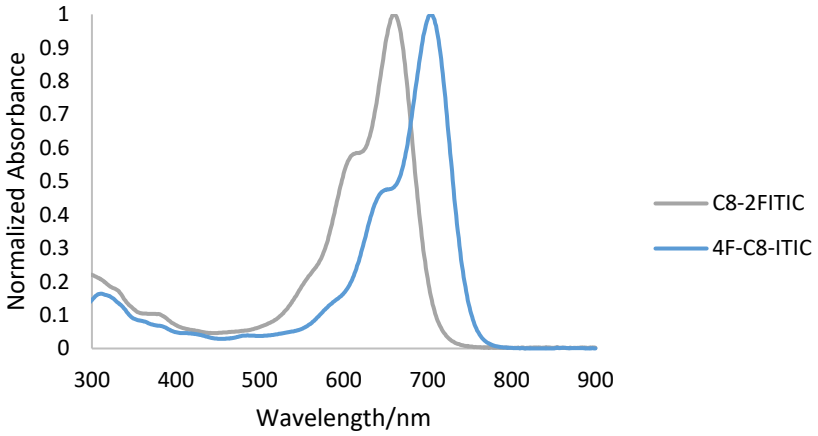


Figure 3.14: *Chemical structures of the **4F-C8-ITIC** acceptor and the **D18** donor polymer.*

Unfortunately, because of the coronavirus pandemic, I no longer had access to the physics department and could not continue testing devices myself. Therefore, the remainder of the optimisation was performed by our collaborator Dr. Flurin Eisner. Our collaborator tested the acceptor **C8-2FITIC** against **C8-ITIC** previously synthesised in our group and the novel **4F-C8-ITIC** acceptor synthesised in our group by Dr. Fei Zhuping (**Figure 3.14**). **4F-C8-ITIC** was tested to help shine a light on the relationship between fluorination location and performance. The device stack used for these devices was the same as that used in the clean room (**Figure 3.15**).

As would be expected, **4F-C8-ITIC** had a greatly reduced optical bandgap compared to **C8-2FITIC** (**Figure 3.16 (a)**). The optical bandgaps for **4F-C8-ITIC** and **C8-2FITIC** are the same as those for their hexyl-chain variants to two decimal places (**Figure 3.6 (a)**).

(a)



Acceptor	**4F-C8-ITIC**	**C8-2FITIC**
Absorption Maximum (nm)	703	660
Absorption Onset (nm)	802	762
Optical Bandgap (eV)	1.55	1.63

(b)

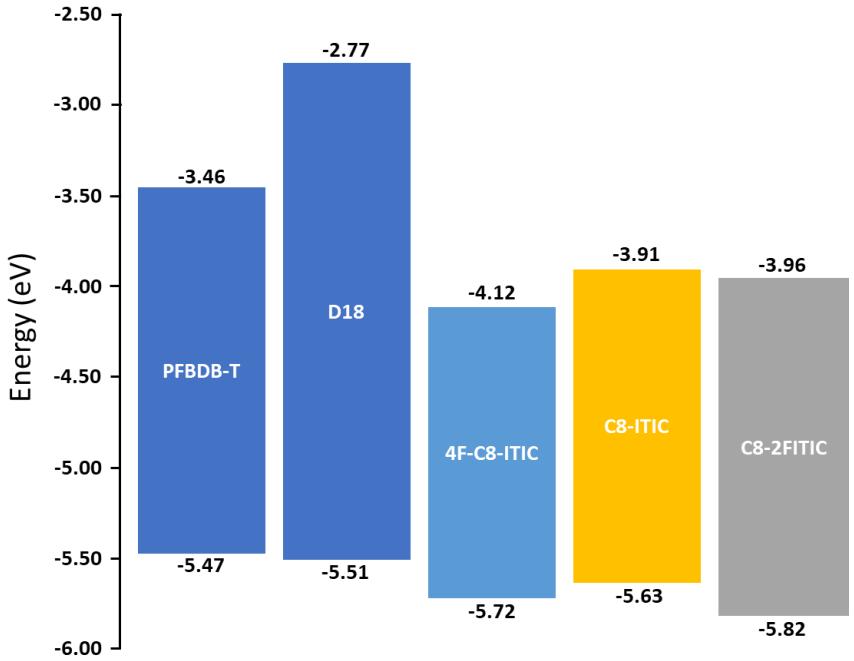


Figure 3.16: (a) *Normalised UV-Vis spectra and bandgap table for NFAs in chloroform solution.* ***(b)*** *Literature energy levels for* ***PFBDB-T***, ***D18***, *and* ***C8-ITIC*** *from thin-film CV.* [73,122] ***4F-C8-ITIC*** *and* ***C8-2FITIC*** *energy levels were estimated by CV on drop-cast films in 0.1 M solution of* Bu_4NPF_6 *in acetonitrile, using a ferrocene (Fc/Fc+) internal standard.*

In addition to **PFBDB-T**, the **D18** donor polymer was used in formulations with the acceptors. **D18** has produced record-breaking solar cells with the **Y6** acceptor that perform at 18.22% PCE.[73] The polymer has a deep HOMO that is depicted in **Figure 3.16 (b)** together with the energy levels of the tested acceptors. **4F-C8-ITIC** has a deeper LUMO than both **C8-ITIC** and **C8-2FITIC**, whilst both fluorinated acceptors have depressed HOMO energy levels compared to **C8-ITIC**. The HOMO of **C8-2FITIC** is deeper than that of **4F-C8-ITIC**, giving it a wider bandgap by CV. The same ETL and HTL coating conditions were used as in Chapter 3.3.2. The coating conditions established in the clean room for **C8-2FITIC:PFBDB-T** devices were used and the formulation optimised in terms of loading and D:A ratio. Other formulations behaved similarly and were optimised in terms of loading and D:A. No optimised devices required active layer annealing. Active layers were coated from both chloroform and CB, but it was found that coating from CB gave improved performance. The formulations used and the performance of the optimised devices are given in **Table 3.13**.

Table 3.13: *Average performance results for devices optimised by our collaborator.*

Device	Donor	Acceptor	Concentration (mg/ml)	D:A	J_{SC} (mA/cm^2)	V_{OC} (V)	FF	PCE (%)
D1	PFBDB-T	C8-ITIC	15	1:1.6	18.6	0.94	0.68	11.9
D2	PFBDB-T	C8-2FITIC	15	1:1.6	15.3	0.85	0.62	8.1
D3	PFBDB-T	4F-C8-ITIC	15	1:1.6	21.8	0.70	0.71	10.7
D4	D18	C8-ITIC	18	1:1.25	18.7	0.99	0.63	11.8
D5	D18	C8-2FITIC	18	1:1.25	15.3	0.98	0.56	8.3
D6	D18	4F-C8-ITIC	18	1:1.25	21.0	0.80	0.71	11.9

C8-2FITIC was outperformed by **C8-ITIC** and **4F-C8-ITIC** when processed with both polymers. The acceptor suffered from lower J_{SC} likely due to its wider bandgap reducing the breadth of its absorption range. Additionally, FF was depressed, and this is indicative of suboptimal packing in the bulk. A significant reduction in Voc is observed when **C8-ITIC** is replaced by **C8-2FITIC** with the **PFBDB-T** polymer, this can be attributed to the slightly deeper LUMO of the fluorinated acceptor. **C8-2FITIC** had improved performance with **D18** than **PFBDB-T** due to a large increase in V_{OC} of 0.13 V. The HOMO energy level of **D18** is only 0.04 eV deeper

than that of **PFBDB-T** and therefore it is likely that the increase in V_{OC} is also due to improved morphology or perhaps reduced energy loss. However, as the CV traces for the two polymers were taken by different groups in different locations, some natural deviation between the measurements must be assumed.

When used with **PFBDB-T**, **C8-ITIC** had the greatest PCE, although the narrow bandgap of **4F-C8-ITIC** allowed for excellent absorption and a very high J_{SC} of 21.8 mA/cm^2. The deepened LUMO of **4F-C8-ITIC** caused a lower PCE due poor V_{OC} of 0.70 V. On the other hand, when **4F-C8-ITIC** was processed with **D18** it performed at the greatest PCE. This was again due to a high J_{SC}, but this was reduced by a low V_{OC}. However, unlike for the **PFBDB-T** devices there was a greater difference in FF between **PFBDB-T:4F-C8-ITIC** and **PFBDB-T:C8-ITIC** indicating a propensity for **PFBDB-T:4F-C8-ITIC** to form appropriately sized domains of donor and acceptor, limiting recombination.

Further tests would need to be carried out in low light conditions or in ternary devices to make use of **C8-2FITIC**'s wider bandgap to improve performance. These tests could also make use of the **RH-C8-ITIC** acceptor's further widened bandgap.

3.4 – Conclusions

Six novel acceptors were synthesised both by the ring-extension methodology for **IDTT** and from **2FIDTT** produced by the triflic acid route, highlighting its suitability en route to NFAs. The novel **ITIC** derivative **C6-ITIC** was synthesised together with halogenated acceptors **4F-C6-ITIC** and **4Cl-C6-ITIC** that had a narrower bandgap. In addition, wider bandgap acceptors **C6-2FITIC**, **C8-2FITIC**, and **RH-C8-ITIC** were prepared.

The hexyl-chain NFAs were taken to our sponsor's site and tested for their potential for large-scale processing. As such, they were processed on larger substrates both from non-chlorinated o-xylene and from CB. It was found that the hexyl side chains on the acceptors were not sufficient, with **4F-C6-ITIC** and **4Cl-C6-ITIC** having negligible performance in both solvent systems due to poor solubility. The highest performing devices were obtained for **C6-2FITIC**, however the best of these only performed at around 6% PCE when processed from CB. On initial testing devices using the **PFBDB-T** polymer had higher performance with **C6-2FTIC** than **PBDB-T-2F** in o-xylene, further testing would be needed to confirm this especially for other solvent systems. Based on results from CB processed devices, **PBDB-T-2Cl** performs worse with **C6-2FITIC** than **PBDB-T-2F**, again likely due to solubility issues. Overall, longer side chains or further active layer optimisation would be required to make the tested NFAs suitable for scalable OPV.

C6-2FITIC was tested against **ITIC** reference devices in the clean room. It was found that **C6-2FITIC** had poor solubility for use even on smaller substrates with spin coating and therefore **C8-2FITIC** was synthesised. Both acceptors were tested in devices with **PFBDB-T** and their fabrication conditions partially optimised for future use. Unfortunately, the devices' performances were depressed by low V_{OC} and FF. It was found that these issues were also observed for the **ITIC** reference devices with the **PBDB-T** and **PFBDB-T** polymers and when devices were made using entirely different donors and acceptors by other researchers in the clean room. Therefore, **C8-2FITIC** was taken to the physics department and tested there instead. An improvement in V_{OC} and FF was observed immediately for the reference devices and for the **C8-2FITIC** devices in comparison to results from the clean room. Moreover, J_{SC} overestimation was not observed indicating both improved device fabrication and more accurate JV measurements in the physics department.

Due to the coronavirus pandemic blocking our access to the physics department, the remainder of the device optimisation for **C8-2FITIC** was performed by our collaborator. The NFA was tested against **C8-ITIC** and **4F-C8-ITIC** produced by a previous member of our group. The **PFBDB-T** and **D18** donor polymers were used. After optimisation, **C8-2FITIC** devices performed poorly when compared to **C8-ITIC** and **4F-C8-ITIC**. This was predominantly due to a reduction in J_{SC} because of the wider bandgap of the NFA reducing its light absorption range. The highest performing **C8-2FITIC** device was blended with **D18** and had 8.3% average PCE. The lower bandgap of **4F-C8-ITIC** increased its J_{SC} above the other NFAs, but it also had the lowest V_{OC} due to a deeper LUMO. As a result of a balance between these two parameters, the best **PFBDB-T** devices were blended with **C8-ITIC** (11.9% average PCE) whilst the best **D18** devices were blended with **4F-C8-ITIC** (11.9% average PCE).

In future work, other polymers such as **PBDB-T-2F** used in our large area devices could be tested with the novel NFAs. In addition, the **C8-2FITIC** acceptor should be tested under indoor light conditions to better match its absorption to incident light. Similarly, the wide-bandgap **RH-C8-ITIC** should be tested in this manner as well. Combinations of the wider-bandgap and narrower-band gap **C8-ITIC** derivatives could additionally be tested in ternary or tandem OPV devices.

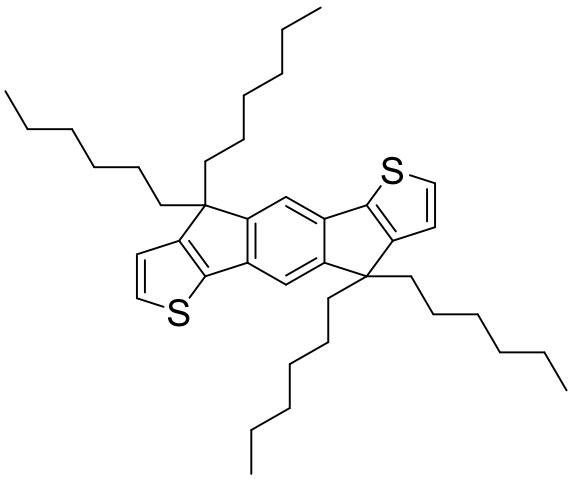
3.5 – Experimental

3.5.1 – Material Sources

PFBDB-T polymer was synthesised by Dr. Qiao He in our research group. **4F-C8-ITIC** and **C8-ITIC** were synthesised by Dr. Fei Zhuping.

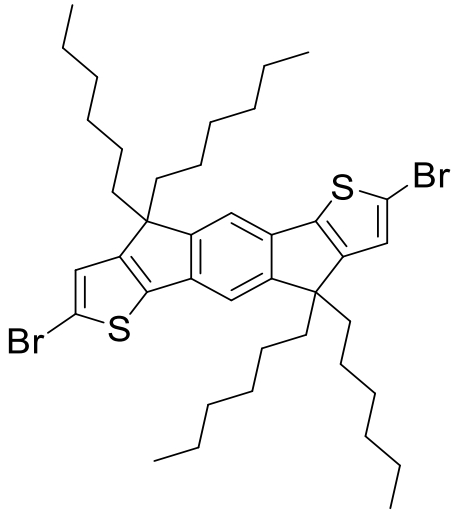
3.5.2 – Synthetic Procedures

General procedure for short-chain alkylation of cores: To a suspension of core (1.0 equiv) in DMSO or NMP was added tert-butoxide salt (6.0 equiv) portion-wise. The suspension was heated at 80 °C for 1 h, haloalkane (6.0 equiv) was added and the reaction heated for 16 hours overnight to 85 - 100 0 °C. After cooling to RT the mixture was poured into water and extracted with organic solvent (x3). The organic phase was washed with water (x3), brine and dried over anhydrous magnesium sulphate. Solvent was removed *in vacuo* and the residue purified by silica column (petroleum ether).

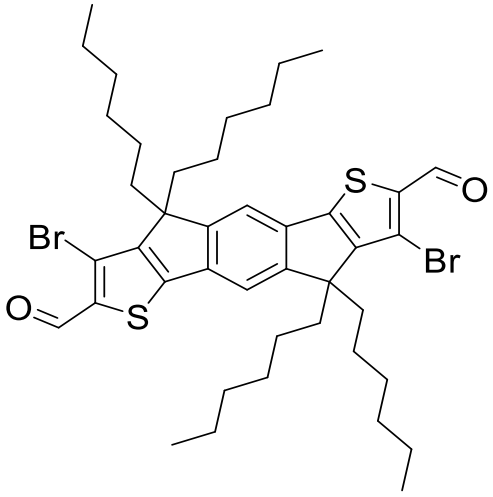


4,4,9,9-Tetrahexyl-4,9-dihydro-s-indaceno[1,2-b:5,6-b']dithiophene (3.1): The reaction was performed according to the general procedure for short-chain alkylation of cores and using **IDT** (1.53 g, 5.74 mmol), potassium *tert*-butoxide (3.87 g, 34.5 mmol), and 1-iodohexane (5.1 mL, 34.5 mmol). After work-up with DCM and purification by silica column the *title compound* was obtained as a yellow oil (2.08 g, 60.1 %). ^{1}H NMR (400 MHz, Chloroform-d) δ(ppm) 7.27 (s, 2H), 7.25 (d, *J* = 4.7 Hz, 2H), 6.96 (d, *J* = 4.8 Hz, 2H), 1.91-2.05 (m, 4H), 1.80-1.91 (m, 4H), 1.20 – 1.00 (m, 24H), 0.91 – 0.72 (m, 20H). ^{13}C NMR (101 MHz, Chloroform-d)

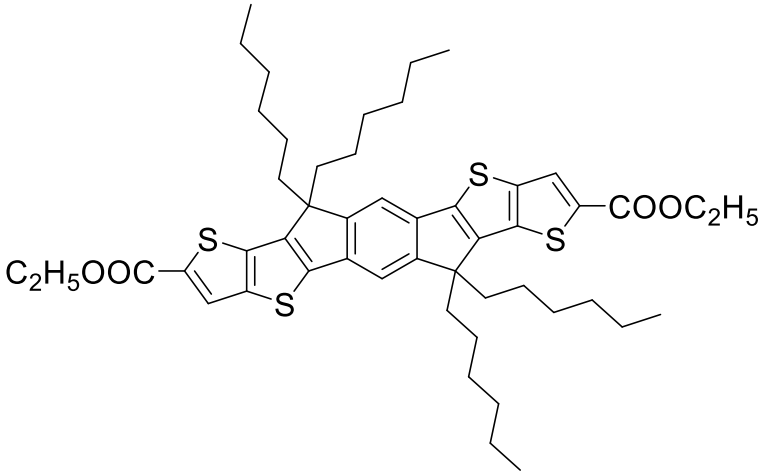
δ(ppm) 155.08, 153.21, 141.65, 135.58, 126.09, 121.70, 113.11, 53.66, 39.19, 31.60, 29.70, 24.13, 22.59, 14.01. MS (EI-ToF) *m/z* 603.4058 (M^+).



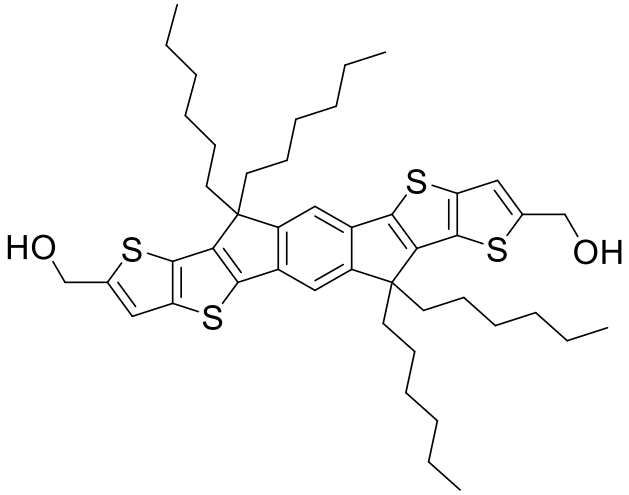
2,7-Dibromo-4,4,9,9-tetrahexyl-4,9-dihydro-s-indaceno[1,2-b:5,6-b']dithiophene (3.2): To a solution of 4,4,9,9-tetrahexyl-4,9-dihydro-s-indaceno[1,2-b:5,6-b']dithiophene (1.91 g, 3.17 mmol) in THF (120 mL) was added *n*-bromosuccinimide (1.24 g, 6.97 mmol). After 6 h in the absence of light, the solution was poured into water (100 mL) and extracted with DCM (3 x 70 mL). The organic phase was washed with water (3 x 70 mL), brine (3 x 70 mL) and dried over anhydrous magnesium sulphate. The crude product was concentrated *in vacuo* and purified by silica plug (petroleum ether), resulting in a white solid of the *title compound* (2.07 g, 86%). ^{1}H NMR (400 MHz, Chloroform-d) δ (ppm) 7.17 (s, 2H), 6.97 (s, 2H), 1.98 – 1.85 (m, 4H), 1.88 – 1.74 (m, 4H), 1.03-1.19 (m, 24H), 0.68-0.90 (m, 20H). ^{13}C NMR (101 MHz, Chloroform-d) δ 154.04, 152.13, 141.86, 135.50, 124.76, 112.99, 112.38, 54.73, 39.03, 31.57, 29.64, 24.08, 22.57, 14.00. MS (EI-ToF) *m/z* 761.2256 (M^+).



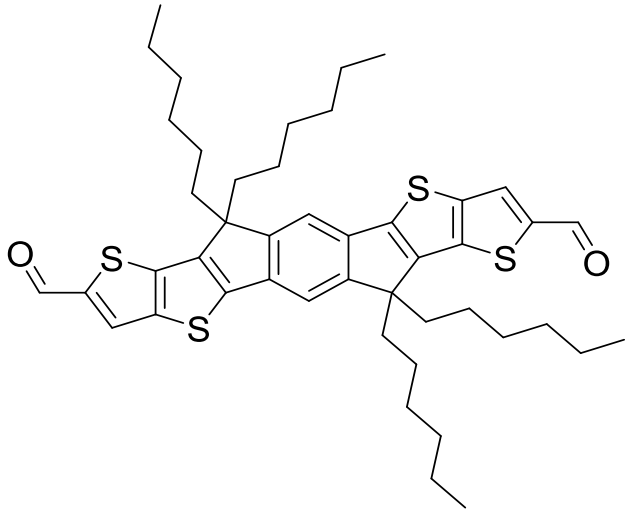
3,8-Dibromo-4,4,9,9-tetrahexyl-4,9-dihydro-s-indaceno[1,2-b:5,6-b']dithiophene-2,7-dicarbaldehyde (3.3): To a cooled (-78 °C) solution of 2,7-dibromo-4,4,9,9-tetrahexyl-4,9-dihydro-s-indaceno[1,2-b:5,6-b']dithiophene (2.17 g, 2.85 mmol) in THF (205 ml) was added lithium diisopropylamide (2M in THF, 5.69 ml, 11.4 mmol) dropwise over 30 mins. The solution was allowed to warm to RT for 16 h. It was then cooled to 0 °C over 30 mins and dimethylformamide (1.24 mL, 16.0 mmol) injected dropwise. After 30 mins water (200 mL) was added to the solution and crude product extracted with DCM (3x 100 mL). The organic phase was washed with water (3 x 100 mL), brine (2 x 100 mL) and dried over anhydrous magnesium sulphate. After removal of solvent *in vacuo* the crude product was purified by silica plug (petroleum ether) and used as off-white powder (1.62 g, 76%) in the next step without further purification. M.p. 179 – 184 °C. ^{1}H NMR (400 MHz, Chloroform-d) δ (ppm) 10.02 (s, 2H), 7.43 (s, 2H), 2.48 – 2.36 (m, 4H), 2.04 - 1.87 (m, 4H), 1.18 – 0.99 (m, 24H), 0.75 (t, J = 6.6 Hz, 12H), 0.71 – 0.60 (m, 4H), 0.47-0.59 (m, 4H). ^{13}C NMR (101 MHz, Chloroform-d) δ 183.03, 155.22, 152.81, 151.04, 137.93, 136.70, 116.27, 114.68, 56.45, 37.40, 31.38, 29.26, 23.74, 22.44, 13.96. MS (EI-ToF) *m/z* 817.2181 (M^{+}).



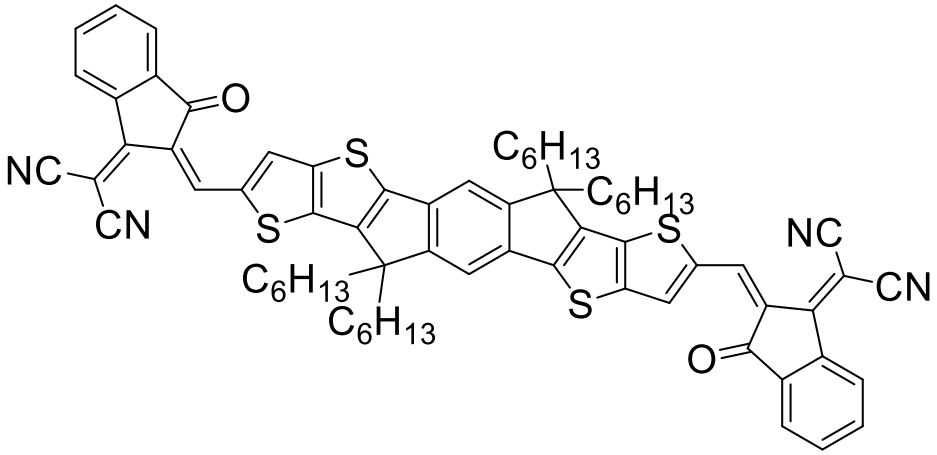
Diethyl 6,6,12,12-tetrahexyl-6,12-dihydrothieno[3,2-b]thieno[2'',3'':4',5']thieno[2',3':5,6]-s-indaceno[2,1-d]thiophene-2,8-dicarboxylate (3.4): To a solution of 3,8-dibromo-4,4,9,9-tetrahexyl-4,9-dihydro-s-indaceno[1,2-b:5,6-b']dithiophene-2,7-dicarbaldehyde (1.46 g, 1.79 mmol) and potassium carbonate (1.48 g, 10.7 mmol) in dimethylformamide (80 mL) at 70 °C was added ethyl mercaptoacetate (0.79 ml, 7.16 mmol) dropwise. After 16 h, the solution was poured into 50 mL of water and extracted with DCM (3 x 60 mL). The organic phase was washed with water (4 x 60 mL), brine (3 x 60 mL), and dried over anhydrous magnesium sulphate. After removal of solvent *in vacuo* the product was purified by column chromatography (DCM:petroleum ether 3:2) yielding the *title compound* (1.01 g, 65.7%). M.p. 131 – 133 °C. ^{1}H NMR (400 MHz, Chloroform-d) δ (ppm) 8.07 (s, 2H), 7.37 (s, 2H), 4.41 (q, *J* = 7.1 Hz, 4H), 2.18-2.07 (m, 4H), 1.96 - 2.07 (m, 4H), 1.42 (t, *J* = 7.1 Hz, 6H), 1.16 – 0.94 (m, 24H), 0.67-0.77 (m, 20H). ^{13}C NMR (101 MHz, Chloroform-d) δ (ppm) 162.69, 153.20, 147.99, 145.81, 140.91, 138.21, 136.84, 133.09, 126.86, 113.73, 61.33, 54.40, 38.35, 31.46, 29.51, 24.07, 22.50, 14.46, 13.96. MS (EI-ToF) *m/z* 859.3931 (M^{+}).



(6,6,12,12-Tetrahexyl-6,12-dihydrothieno[3,2-b]thieno[2'',3'':4',5']thieno[2',3':5,6]-s-indaceno[2,1-d]thiene-2,8-diyl)dimethanol (3.5): To a solution of diethyl 6,6,12,12-tetrahexyl-6,12-dihydrothieno[3,2-b]thieno[2'',3'':4',5']thieno[2',3':5,6]-s-indaceno[2,1-d]thiophene-2,8-dicarboxylate (0.61 g, 0.710 mmol) in THF (60 mL) at RT was carefully added lithium aluminium hydride (1M in THF, 4.26 ml, 4.26 mmol). After 1 h, the solution was cooled to 0 °C and saturated aqueous ammonium chloride (12 ml) was slowly added, followed by potassium hydroxide (8M, 6 mL). The solution was poured into water (30 mL) and extracted with DCM (3x 30 mL). The combined organics were washed with water (3 x 30 mL), brine (2 x 30 mL), and dried over anhydrous magnesium sulphate. After removal of solvent *in vacuo* a pale-yellow solid of the *title compound* was collected (0.57 g, 97%). ^{1}H NMR (400 MHz, Chloroform-d) δ (ppm) 7.29 (s, 2H), 7.28 (s, 2H), 4.93 (s, 4H), 2.17 – 2.04 (m, 4H), 2.04 – 1.81 (m, 4H), 1.15 – 0.96 (m, 24H), 0.67-0.81 (m, 20H).

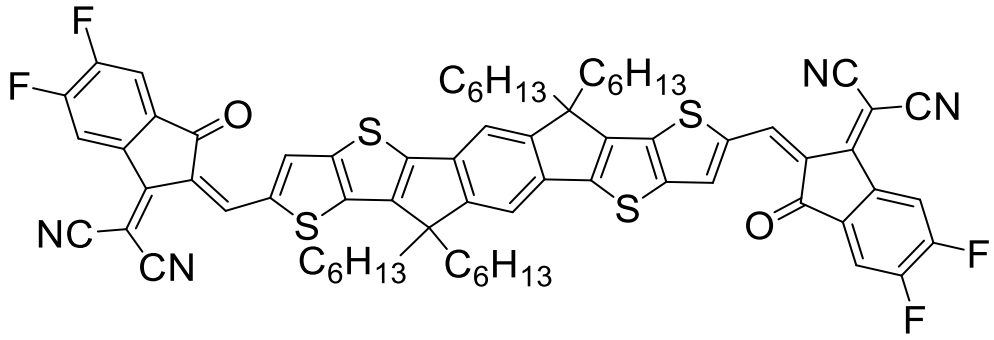


6,6,12,12-Tetrahexyl-6,12-dihydrothieno[3,2-b]thieno[2'',3'':4',5']thieno[2',3':5,6]-s-indaceno[2,1-d]thiophene-2,8-dicarbaldehyde (3.6): To a solution of (6,6,12,12-tetrahexyl-6,12-dihydrothieno[3,2-b]thieno[2'',3'':4',5']thieno[2',3':5,6]-s-indaceno[2,1-d]thiene-2,8-diyl)dimethanol (0.11 g, 0.142 mmol) in THF (3.5 mL) was added dropwise a chilled solution (0 °C) of Dess-Martin periodinate (0.18 g, 0.426 mmol) in THF (12 mL). Aqueous saturated sodium sulphite (5 mL) was added after 30 mins and it was left stirring at RT for 16 h. The crude product was extracted with DCM (3 x 5 mL) and the organic phase washed with water (3 x 5 mL), brine (2 x 5mL) and dried over anhydrous magnesium sulphate. An orange solid of the title compound was obtained after removal of solvent *in vacuo* (0.082 g, 75%). M.P. 184 – 187 °C. ^{1}H NMR (400 MHz, Chloroform-d) δ (ppm) 9.97 (s, 2H), 8.02 (s, 2H), 7.43 (s, 2H), 2.20 – 2.09 (m, 4H), 2.09 – 1.98 (m, 4H), 1.14 – 0.97 (m, 24H), 0.80 – 0.67 (m, 20H). ^{13}C NMR (101 MHz, Chloroform-d) δ (ppm) 182.82, 153.78, 150.32, 146.10, 143.82, 141.59, 140.03, 137.02, 130.19, 114.18, 54.58, 38.25, 31.42, 29.45, 24.11, 22.47, 13.93. MS (EI-ToF) *m/z* 771.3390 (M^{+})



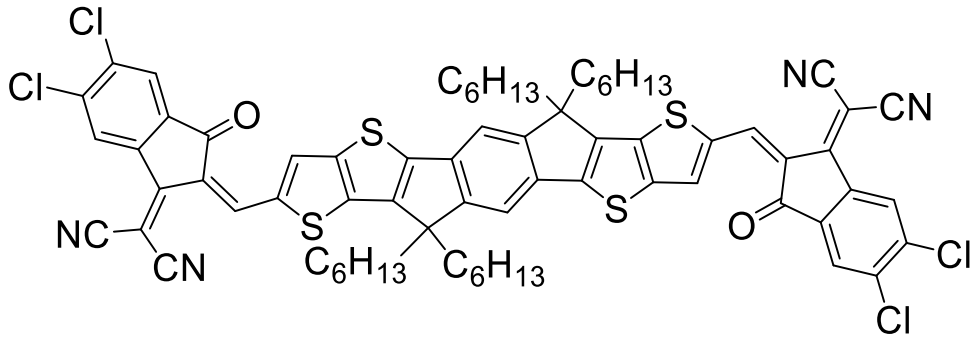
C6-ITIC:

To 6,6,12,12-tetrahexyl-6,12-dihydrothieno[3,2-b]thieno[2'',3'':4',5']thieno[2',3':5,6]-s-indaceno[2,1-d]thiophene-2,8-dicarbaldehyde (57 mg, 0.0739 mmol) and 2-(3-oxo-2,3-dihydro-1H-inden-1-ylidene)malononitrile (57 mg, 0.296 mmol) was added chloroform (8 ml) and pyridine (0.13 mL, 1.55 mmol), the reaction was stirred at 80 °C for 16 h. The reaction mixture was diluted with 8 mL of water and the crude product extracted with DCM (3 x 4 mL). The organic phase was washed with water (3 x 4 mL), brine (3 x 4 mL), and dried over anhydrous magnesium sulphate. After removal of solvent *in vacuo*, purification by silica gel chromatography (petroleum ether:DCM 1:1.5) was performed, followed by recrystallisation by slow evaporation of a biphasic mixture of DCM and methanol yielding a dark blue solid of the *title compound* (55 mg, 66%). M.P. > 400 °C. ^{1}H NMR (400 MHz, Chloroform-d) δ (ppm) 9.01 (s, 2H), 8.80 – 8.69 (m, 2H), 8.24 (s, 2H), 7.99 -7.94 (m, 2H), 7.84 – 7.74 (m, 4H), 7.52 (s, 2H), 2.36 – 2.24 (m, 4H), 2.21 – 2.05 (m, 4H), 1.19 – 1.00 (m, 24 H), 0.84 - 0.67 (m, 20H). ^{13}C NMR (101 MHz, Chloroform-d) δ (ppm) 188.47, 160.42, 154.84, 153.94, 147.21, 147.15, 143.57, 140.11, 139.13, 138.46, 137.87, 137.49, 136.89, 135.22, 134.49, 125.33, 123.75, 122.27, 114.78, 114.72, 69.21, 54.76, 38.32, 31.48, 29.45, 24.14, 22.49, 13.97. MS (EI-ToF) *m/z* 1123.4204 (M^{+})



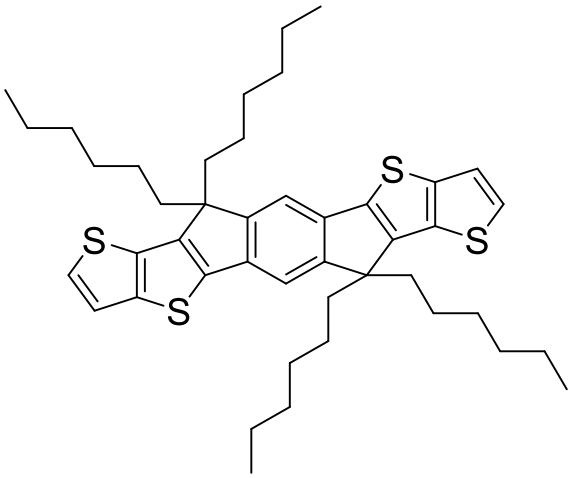
4F-C6-ITIC:

To 6,6,12,12-tetrahexyl-6,12-dihydrothieno[3,2-b]thieno[2'',3'':4',5']thieno[2',3':5,6]-s-indaceno[2,1-d]thiophene-2,8-dicarbaldehyde (82 mg, 0.106 mmol) and 2-(5,6-difluoro-3-oxo-2,3-dihydro-1H-inden-1-ylidene)malononitrile (98 mg, 0.425 mmol) was added chloroform (8 ml) and pyridine (0.18 mL, 2.23 mmol), the reaction was left at 70 °C for 16 h. The reaction mixture was diluted with 10 mL of water and the crude product extracted with DCM (3 x 5 mL). The organic phase was washed with water (3 x 5 mL), brine (3 x 5 mL), and dried over anhydrous magnesium sulphate. After removal of solvent *in vacuo*, purification by silica gel chromatography (DCM) was performed, followed by purification by preparatory chromatography, yielding a dark blue solid of the *title compound* (75 mg, 59%). M.P > 400 °C. ^{1}H NMR (400 MHz, Chloroform-d) δ(ppm) 8.97 (s, 2H), 8.59 – 8.51 (m, 2H), 8.24 (s, 2H), 7.75 - 7.67 (m, 2H), 7.51 (s, 2H), 2.33 – 2.20 (m, 4H), 2.19 – 2.06 (m, 4H), 1.18 – 0.97 (m, 24H), 0.82 - 0.66 (m, 20H). ^{13}C NMR (101 MHz, Chloroform-d) δ 186.06, 158.27, 155.81 (d, ^{2}J = 14.0 Hz, CF), 155.06, 154.78, 153.20 (dd, ^{2}J = 14.5 Hz, ^{3}J = 6.7 Hz, CF), 147.73, 147.32, 143.90, 138.99, 138.62, 138.11, 137.96, 136.73 (dd, ^{3}J = 8.6 Hz, ^{4}J = 3.5 Hz, CF), 134.47 (d, ^{3}J = 5.2 Hz, CF), 121.32, 114.96, 114.31, 114.26, 113.85 (dd, ^{1}J = 240.3 Hz, ^{2}J = 17.4 Hz, CF), 69.70, 54.80, 38.30, 31.47, 29.42, 24.15, 22.48, 13.97. ^{19}F NMR (377 MHz, Chloroform-d) δ(ppm) -122.43 (d, *J* = 19.3 Hz), -123.62 (d, *J* = 19.3 Hz). MS (EI-ToF) *m/z* 1195.3840 (M^{+}).

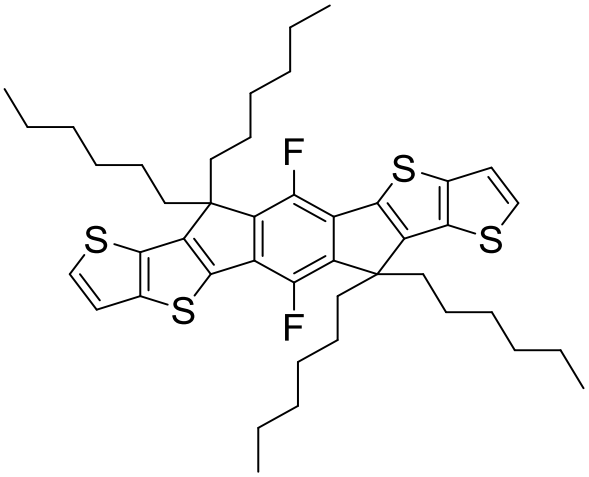


4Cl-C6-ITIC:

To 6,6,12,12-tetrahexyl-6,12-dihydrothieno[3,2-b]thieno[2'',3'':4',5']thieno[2',3':5,6]-s-indaceno[2,1-d]thiophene-2,8-dicarbaldehyde (27 mg, 0.0350 mmol) and 2-(5,6-dichloro-3-oxo-2,3-dihydro-1H-inden-1-ylidene)malononitrile (37 mg, 0.140 mmol) was added *tert*-butanol (7 ml) and pyridine (0.06 mL, 0.742 mmol), the reaction was left at 40 °C for 16 h. The reaction mixture was diluted with 6 mL of water and the crude product extracted with DCM (3 x 5 mL). The organic phase was washed with water (3 x 4 mL), brine (3 x 4 mL), and dried over anhydrous magnesium sulphate. After removal of solvent *in vacuo*, purification by silica gel chromatography (DCM) was performed, followed by purification by preparatory chromatography, yielding a dark blue solid of the *title compound* (12 mg, 27%). M.P. > 400 °C. ^{1}H NMR (400 MHz, Chloroform-d) δ(ppm) 9.00 (s, 2H), 8.79 (s, 2H), 8.25 (s, 2H), 7.99 (s, 2H), 7.51 (s, 2H), 2.32 - 2.19 (m, 4H), 2.08 – 1.96 (m, 4H), 1.16 – 0.98 (m, 24H), 0.93 – 0.67 (m, 20H). 13C NMR (126 MHz, Chloroform-d) δ 186.16, 158.22, 155.12, 155.00, 147.35, 144.01, 139.81, 139.45, 139.26, 138.74, 138.22, 137.97, 136.00, 135.25, 127.00, 125.20, 121.36, 114.97, 114.32, 114.26, 69.70, 54.78, 38.26, 31.43, 29.70, 29.38, 24.12, 22.44, 13.92. MS (LD-ToF) *m/z* 1260.8 (M^{+}).

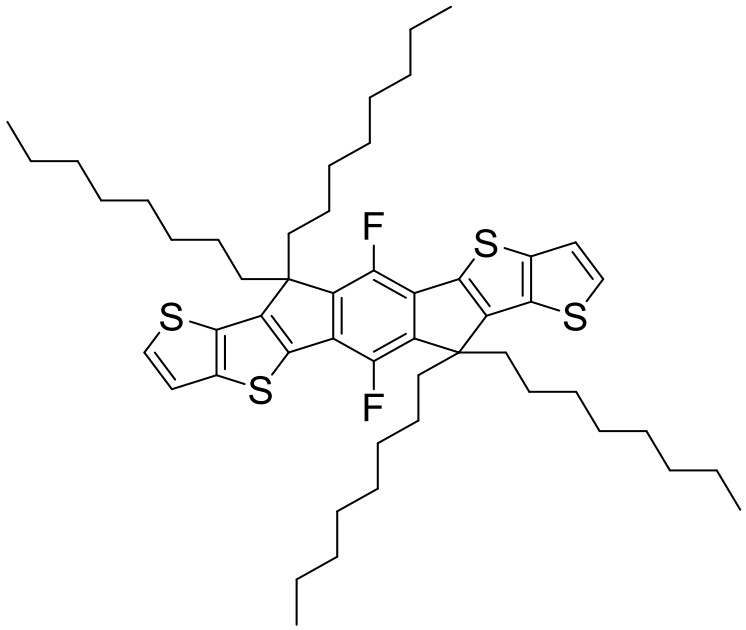


6,6,12,12-Tetrahexyl-6,12-dihydrothieno[3,2-b]thieno[2'',3'':4',5']thieno[2',3':5,6]-s-indaceno[2,1-d]thiophene (3.10): The reaction was performed according to the general procedure for short-chain alkylation of cores and using 6,12-dihydrothieno[3,2-b]thieno[2'',3'':4',5']thieno[2',3':5,6]-s-indaceno[2,1-d]thiophene (507 mg, 1.34 mmol), sodium *tert*-butoxide (772 mg, 8.04 mmol), 1-bromohexane (1.13 mL, 8.04 mmol), NMP and was heated overnight at 90 °C. After work-up with ethyl acetate and purification by silica column the *title compound* was obtained as a pale-orange solid (458 mg, 48 %). M.p. 141 – 143 °C. ^{1}H NMR (400 MHz, Chloroform-d) δ 7.39 – 7.35 (m, 4H), 7.35 (s, 2H), 2.21 – 2.10 (m, 4H), 2.08 – 1.97 (m, 4H), 1.17 – 1.04 (m, 24H), 0.96 – 0.68 (m, 20H). ^{13}C NMR (101 MHz, Chloroform-d) δ 152.29, 145.51, 143.70, 141.28, 136.57, 133.65, 125.40, 120.53, 112.99, 54.17, 38.42, 31.48, 29.57, 24.04, 22.52, 13.99. MS (LD-ToF) *m/z* 714.6 (M^{+}).



5,11-Difluoro-6,6,12,12-tetrahexyl-6,12-dihydrothieno[3,2-b]thieno[2'',3'':4',5']thieno[2',3':5,6]-s-indaceno[2,1-d]thiophene (3.13): The reaction was

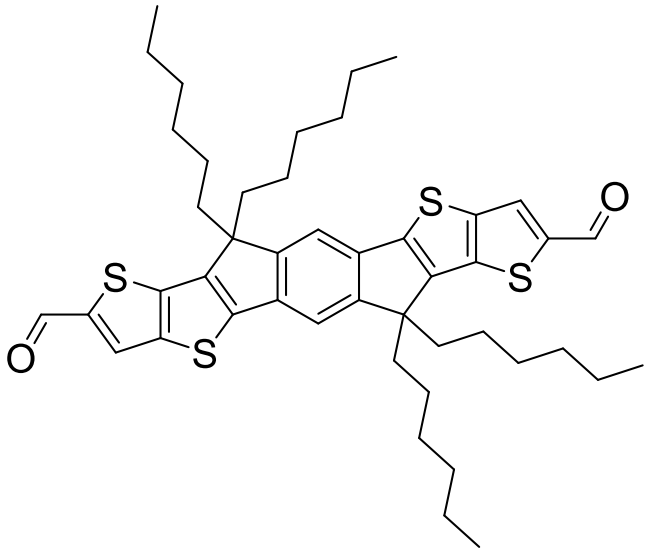
performed according to the general procedure for short-chain alkylation of cores and using 5,11-difluoro-6,12-dihydrothieno[3,2-b]thieno[2'',3'':4',5']thieno[2',3':5,6]-s-indaceno[2,1-d]thiophene (106 mg, 0.256 mmol), potassium *tert*-butoxide (172 mg, 1.53 mmol), 1-iodohexane (0.23 mL, 1.53 mmol), NMP (4 mL) and was heated overnight at 120 °C. After work-up with ethyl acetate and purification by silica column the *title compound* was obtained as a yellow solid (36 mg, 29 %). ^{1}H NMR (400 MHz, Chloroform-d) δ(ppm) 7.39 (d, *J* = 5.1 Hz, 2H), 7.36 (d, *J* = 5.1 Hz, 2H), 2.33 - 2.23 (m, 4H), 2.23 - 2.13 (m, 4H), 1.18 – 1.01 (m, 24H), 0.93 – 0.81 (m, 20H). ^{19}F NMR (377 MHz, Chloroform-d) δ(ppm) -134.13. MS (EI-ToF) *m/z*: 751.3312 (M^{+}).



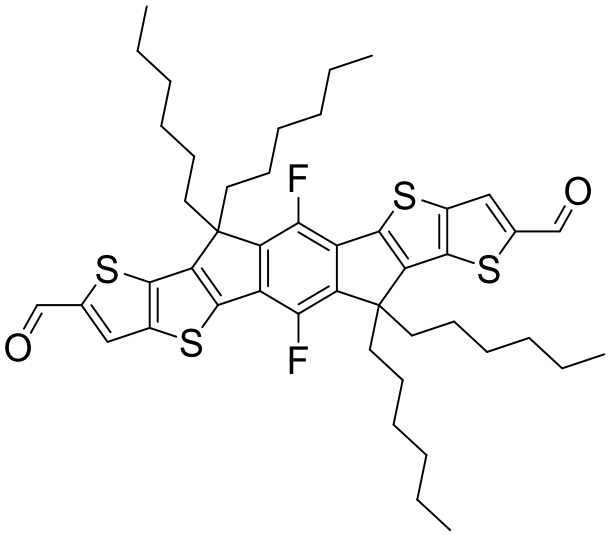
5,11-Difluoro-6,6,12,12-tetraoctyl-6,12-dihydrothieno[3,2-b]thieno[2'',3'':4',5']thieno[2',3':5,6]-s-indaceno[2,1-d]thiophene (3.15): The reaction was performed according to the general procedure for short-chain alkylation of cores and using 5,11-difluoro-6,12-dihydrothieno[3,2-b]thieno[2'',3'':4',5']thieno[2',3':5,6]-s-indaceno[2,1-d]thiophene (47.5 mg, 0.115 mmol), sodium *tert*-butoxide (66 mg, 0.688 mmol), 1-bromooctane (0.12 mL, 0.688 mmol), NMP (5mL) and was heated overnight at 100 °C. After work-up with hexane and purification by silica column the *title compound* was obtained as a yellow solid (48 mg, 49 %). M.P. 99 – 102 °C. ^{1}H NMR (400 MHz, Chloroform-d) δ(ppm) 7.39 (d, *J* = 5.0 Hz, 2H), 7.36 (d, *J* = 5.0 Hz, 2H), 2.34 – 2.23 (m, 4H), 2.23 – 2.12 (m, 4H), 1.24 – 1.01 (m, 40H), 0.93 – 0.70 (m, 20H). ^{13}C NMR (101 MHz, Chloroform-d) δ(ppm) 147.56 (dd, ^{1}J = 247.8 Hz, ^{4}J = 3.5 Hz, CF), 145.44, 143.53, 138.71 – 138.31 (m, CF), 138.02, 132.83, 126.28,

126.16 - 125.78 (m, CF), 120.53, 56.00, 36.69, 31.78, 29.69, 29.14, 24.35, 22.61, 14.06. ^{19}F NMR (377 MHz, Chloroform-d) δ(ppm) -134.09. MS (EI-ToF) *m/z*: 863.4573 (M^+).

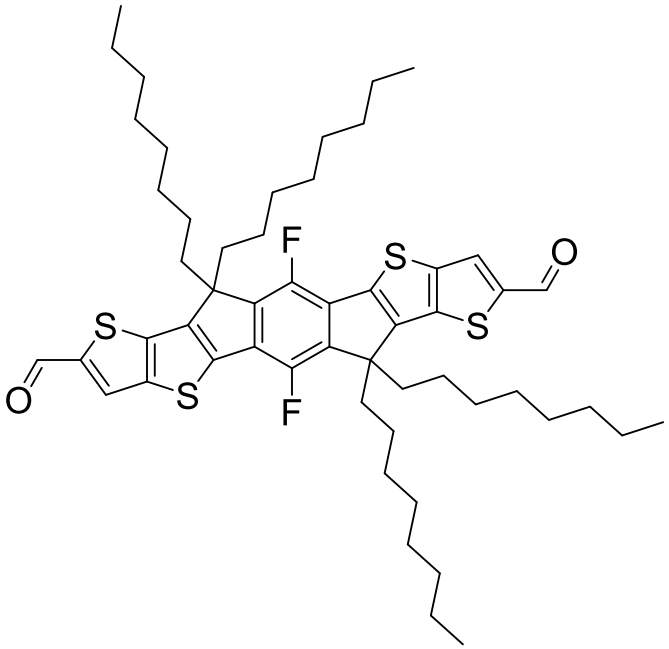
General procedure for the Vilsmeier-Haack reaction: Phosphoryl chloride (excess) was added to the starting material (1.0 equiv) dissolved in DMF (excess) and DCM or chloroform at 0 °C and the solution stirred for 16 h. Water and saturated sodium acetate were injected and the crude product extracted with DCM (x3), washed with water (x3), brine, and dried over magnesium sulphate. After removal of volatiles *in vacuo* purification by silica column (DCM) was performed.



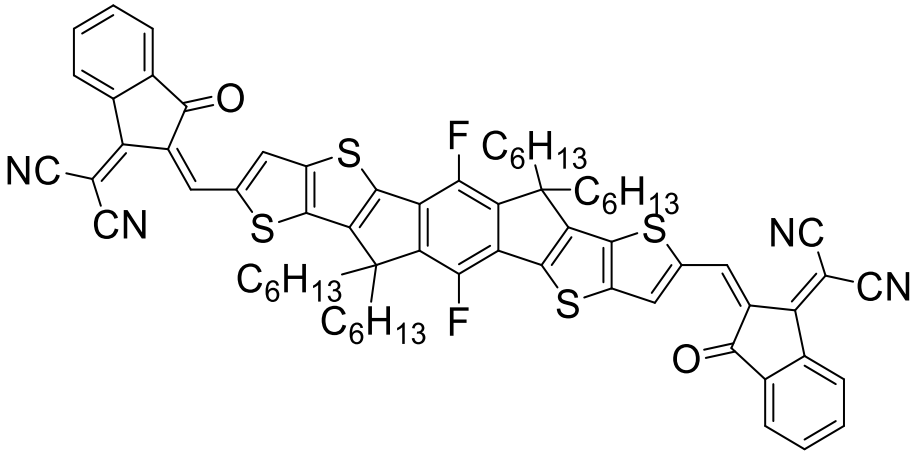
6,6,12,12-Tetrahexyl-6,12-dihydrothieno[3,2-b]thieno[2'',3'':4',5']thieno[2',3':5,6]-s-indaceno[2,1-d]thiophene-2,8-dicarbaldehyde (3.6): The reaction was performed according to the general procedure for the Vilsmeier-Haack reaction using 6,6,12,12-tetrahexyl-6,12-dihydrothieno[3,2-b]thieno[2'',3'':4',5']thieno[2',3':5,6]-s-indaceno[2,1-d]thiophene (458 mg, 0.646 mmol), phosphoryl chloride (0.36 mL, 3.88 mmol), DCM (30 mL), and DMF (0.30 mL, 3.88mmol). After purification by silica column the *title compound* was obtained as bright yellow solid (330 mg, 67 %). M.P. 184 – 187 °C. ^{1}H NMR (400 MHz, Chloroform-d) δ (ppm) 9.97 (s, 2H), 8.02 (s, 2H), 7.43 (s, 2H), 2.20 – 2.09 (m, 4H), 2.09 – 1.98 (m, 4H), 1.14 – 0.97 (m, 24H), 0.80 – 0.67 (m, 20H). ^{13}C NMR (101 MHz, Chloroform-d) δ (ppm) 182.82, 153.78, 150.32, 146.10, 143.82, 141.59, 140.03, 137.02, 130.19, 114.18, 54.58, 38.25, 31.42, 29.45, 24.11, 22.47, 13.93. MS (EI-ToF) *m/z* 771.3390 (M^+).



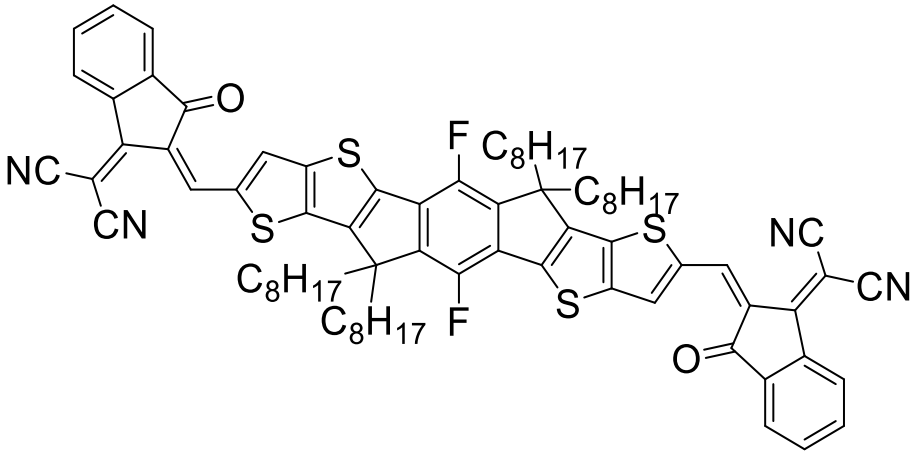
5,11-Difluoro-6,6,12,12-tetrahexyl-6,12-dihydrothieno[3,2-b]thieno[2'',3'':4',5']thieno[2',3':5,6]-s-indaceno[2,1-d]thiophene-2,8-dicarbaldehyde (3.14): The reaction was performed according to the general procedure for the Vilsmeier-Haack reaction using 5,11-difluoro-6,6,12,12-tetrahexyl-6,12-dihydrothieno[3,2-b]thieno[2'',3'':4',5']thieno[2',3':5,6]-s-indaceno[2,1-d]thiophene (57 mg, 0.0759 mmol), phosphoryl chloride (0.039 mL, 0.415 mmol), DCM (8 mL), and DMF (0.032 mL, 0.415 mmol). After purification by silica column the *title compound* was obtained as bright yellow solid (39 mg, 64 %). ^{1}H NMR (400 MHz, Chloroform-d) δ(ppm) 9.99 (s, 2H), 8.04 (s, 2H), 2.35 – 2.25 (m, 4H), 2.25 – 2.15 (m, 4H), 1.16 – 1.01 (m, 24H), 0.89 – 0.67 (m, 20H). ^{13}C NMR (101 MHz, Chloroform-d) δ(ppm) 183.00, 147.87 (dd, ^{1}J = 251.4, ^{4}J = 3.3 Hz, CF), 145.93, 144.52, 144.21, 143.50, 139.80 - 139.47 (m, CF), 138.94, 130.11, 126.77 - 126.37 (m, CF), 56.38, 36.53, 31.37, 29.28, 24.42, 22.46, 13.93. ^{19}F NMR (377 MHz, Chloroform-d) δ(ppm) -131.9. MS (EI-ToF) *m/z* 919.4489 (M^{+}).



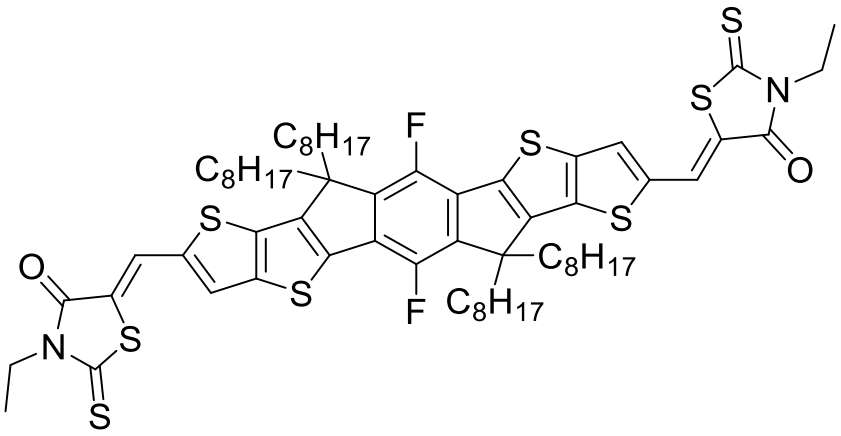
5,11-Difluoro-6,6,12,12-tetraoctyl-6,12-dihydrothieno[3,2-b]thieno[2'',3'':4',5']thieno[2',3':5,6]-s-indaceno[2,1-d]thiophene-2,8-dicarbaldehyde (3.16): The reaction was performed according to the general procedure for the Vilsmeier-Haack reaction using5,11-difluoro-6,6,12,12-tetraoctyl-6,12-dihydrothieno[3,2-b]thieno[2'',3'':4',5']thieno[2',3':5,6]-s-indaceno[2,1-d]thiophene (106 mg, 0.123 mmol), phosphoryl chloride (1.61 mL, 1.63 mmol), chloroform (10 mL), and DMF (0.25 mL, 3.23 mmol). After purification by silica column the *title compound* was obtained as bright yellow solid (100 mg, 89 %). M.P. 158 – 160 °C. ^{1}H NMR (400 MHz, Chloroform-d) δ(ppm) 9.99 (s, 2H), 8.04 (s, 2H), 2.34 – 2.24 (m, 4H), 2.24 - 2.14 (m, 4H), 1.19 – 1.01 (m, 40H), 0.91 – 0.66 (m, 20H). ^{13}C NMR (101 MHz, Chloroform-d) δ(ppm) 182.99, 147.86 (dd, ^{1}J = 249.5 Hz, ^{4}J = 5.1 Hz, CF), 145.95, 144.54, 144.23, 143.50, 139.80 - 139.48 (m, CF), 138.94, 130.10, 126.83 - 126.33 (m, CF), 56.38, 36.50, 31.71, 29.57, 29.08, 24.41, 22.58, 14.04. ^{19}F NMR (377 MHz, Chloroform-d) δ(ppm) -131.90. MS (EI-ToF) *m/z* 919.4489 (M^{+}).



C6-2FITIC: To 5,11-difluoro-6,6,12,12-tetrahexyl-6,12-dihydrothieno[3,2-b]thieno[2'',3'':4',5']thieno[2',3':5,6]-s-indaceno[2,1-d]thiophene-2,8-dicarbaldehyde (37 mg, 0.0458 mmol) and 2-(3-oxo-2,3-dihydro-1H-inden-1-ylidene)malononitrile (36 mg, 0.183 mmol) was added chloroform (5 ml) and pyridine (0.08 mL, 0.963 mmol), the reaction was left at 75°C for 16 h. The reaction mixture was diluted with 6 mL of water and the crude product extracted with DCM (3 x 4 mL). The organic phase was washed with water (3 x 4 mL), brine (3 x 4 mL), and dried over anhydrous magnesium sulphate. After removal of solvent *in vacuo*, purification by silica gel chromatography (DCM) was performed, followed by purification by preparatory chromatography, yielding a dark blue solid of the *title compound* (35 mg, 66%). M.P. > 400 °C. ^{1}H NMR (400 MHz, Chloroform-d) δ(ppm) 8.99 (s, 2H), 8.73 - 8.69 (m, 2H), 8.22 (s, 2H), 8.00 - 7.95 (m, 2H), 7.85 – 7.71 (m, 4H), 2.44 – 2.25 (m, 8H), 1.21 – 1.00 (m, 24H), 0.85 – 0.68 (m, 20H). ^{13}C NMR (101 MHz, Chloroform-d) δ(ppm) 188.41, 160.26, 148.06 (dd, ^{1}J = 255.8, ^{4}J = 3.4 Hz, CF), 147.24, 146.84, 145.71, 145.04, 140.38 - 140.14 (m, CF). 140.11, 139.49, 138.43, 137.20, 136.89, 135.39, 134.65, 127.64 - 127.22 (m, CF), 125.42, 123.89, 123.02, 114.53, 69.88, 56.51, 36.64, 31.42, 29.28, 24.47, 22.46, 13.95. ^{19}F NMR (377 MHz, Chloroform-d) δ(ppm) -130.76. MS (APCI-ToF) *m/z* 1159.33940 (M^{+}).



C8-2FITIC: To 5,11-difluoro-6,6,12,12-tetraoctyl-6,12-dihydrothieno[3,2-b]thieno[2'',3'':4',5']thieno[2',3':5,6]-s-indaceno[2,1-d]thiophene-2,8-dicarbaldehyde (50 mg, 0.0545 mmol) and 2-(3-oxo-2,3-dihydro-1H-inden-1-ylidene)malononitrile (42 mg, 0.218 mmol) was added chloroform (5 ml) and pyridine (0.10 mL, 1.14 mmol), the reaction was left at 40 °C for 16 h. The reaction mixture was diluted with 8 mL of water and the crude product extracted with DCM (3 x 4 mL). The organic phase was washed with water (3 x 4 mL), brine (3 x 4 mL), and dried over anhydrous magnesium sulphate. After removal of solvent *in vacuo*, purification by silica gel chromatography (DCM) was performed, followed by purification by preparatory chromatography, yielding a dark blue solid of the *title compound* (49 mg, 70%). M.P. > 400 °C. ^{1}H NMR (400 MHz, Chloroform-d) δ(ppm) 8.99 (s, 2H), 8.73 – 8.68 (m, 2H), 8.21 (s, 2H), 8.00 - 7.94 (m, 2H), 7.83 - 7.73 (m, 4H), 2.43 - 2.25 (m, 8H), 1.21 – 1.01 (m, 40H), 0.87 - 0.69 (m, 20H). ^{19}F NMR (377 MHz, Chloroform-d) δ(ppm) -130.74. MS (APCI-ToF): 1271.5221 (M+).



RH-C8-2FITIC: To 5,11-difluoro-6,6,12,12-tetraoctyl-6,12-dihydrothieno[3,2-b]thieno[2'',3'':4',5']thieno[2',3':5,6]-s-indaceno[2,1-d]thiophene-2,8-dicarbaldehyde (35.6 mg, 0.0387 mmol) and 3-ethyl-2-thioxothiazolidin-4-one (25.0 mg, 0.155 mmol) was added *tert*-butanol (5 ml) and pyridine (0.08 mL, 0.809 mmol). The solution was heated to reflux for 16 h. 8 mL of water were added, and the crude product extracted with ethyl acetate (3 x 4 mL). The organic phase was washed with water (3 x 4 mL), brine (3 x 4 mL), and dried over anhydrous magnesium sulphate. After removal of solvent *in vacuo*, purification by silica gel chromatography (hexane:ethyl acetate, 1:1) was performed, followed by purification by preparatory chromatography (THF), yielding a dark purple solid of the *title compound* (40.2 mg, 86%). ^{1}H NMR (400 MHz, Chloroform-d) δ 7.95 (s, 2H), 7.68 (s, 2H), 4.22 (q, *J* = 7.1 Hz, 4H), 2.36 - 2.55 (m, 4H), 2.25 – 2.13 (m, 4H), 1.35 – 1.01 (m, 54H), 0.78 (t, *J* = 7.0 Hz, 12H). ^{19}F NMR (377 MHz, Chloroform-d) δ -132.13. MS (APCI-ToF): 1205.4203 (M+).

3.5.3 – Merck Site Device Fabrication Procedure

Coating and formulation parameters for the Merck reference devices are not specified in the interest of confidentiality.

Formulations were prepared in a nitrogen glovebox the day before coating and were stirred overnight at 90°C unless otherwise specified. Devices were prepared in an inverted architecture (glass/ITO/ZnO/Donor:Acceptor/PEDOT:PSS/Ag). 25 cm^2 glass substrates with one-pre-patterned side of etched ITO were used to prepare devices whilst 25 cm^2 substrates with a full one-side ITO coating were used for test film coatings. Prior to use, each substrate was cleaned sequentially with acetone, isopropanol (IPA), and water in an ultrasonic bath. A spin-rinser was used to rinse and dry the substrates with deionised water. A layer of Nanograde N-21X-Slot ZnO dispersion was blade-coated at a DB temperature of 40°C, using 50 µL of solution, a blade speed of 5 mm/s, and a screw gap of 50 µL. The substrates were annealed at 100°C for 10 mins in air. The active layers were blade-coated onto the ETL using 80 µL of formulation, a DB temperature of 90°C unless otherwise specified, and a screw gap of 100 µm. Test films were coated under the same conditions as the device active layers but directly onto ITO-glass. Test film thicknesses were measured by a Dektak profilometer. Device active layer thickness was estimated from spectra by a UV-VIS-NIR OceanOptics spectrometer. Clevious AL4083 PEDOT:PSS was diluted at a 1:4.3 ratio by volume and blade-coated onto the active layers using 180 µL of solution, a DB temperature of 65°C, a blade speed of 20 mm/s, and a screw gap of 575 µm. The HTL layer was dried for 2 mins on the DB surface. A shadow mask was used to deposit 100 nm of Ag electrode by evaporation onto the HTL to produce 8 pixels of 16 mm^2. JV characteristics were obtained using a solar simulator at AM1.5G solar irradiation (100 mW cm^{-2}) calibrated by Si reference cell in a nitrogen glovebox.

3.5.4 – Clean Room Device Fabrication Procedure

Formulations were prepared in air the day before coating and were stirred overnight at 65°C in CB or 50°C in chloroform. Devices were prepared in an inverted architecture (glass/ITO/ZnO/Donor:Acceptor/MoO_3/Ag). 1.2 cm^2 glass substrates (Psiotec) with one-pre-patterned side of ITO were cleaned sequentially in an ultrasonic bath with Decon 90

detergent, deionised water, acetone, IPA, and left in IPA overnight. Substrates were dried and treated with oxygen plasma. ZnO ETL was spin coated from 40 µL of zinc-acetate dehydrate precursor solution (1:33.3, mono-ethanolamine:2-methoxyethanol) at 4000 rpm over 40 seconds followed by annealing at 160°C for 15 mins. Alternatively, a Sigma-Aldrich ZnO nanoparticle dispersion diluted 1:1 in IPA was spin coated at 4000 rpm over 40 seconds followed by annealing at 110°C for 10 mins. Active layers were spin coated over 35 seconds from CB or by dynamic spin coating over 35 seconds from chloroform. The active layers were used as spun or annealed for 15 mins. 10 nm of MoO_3 followed by 100 nm of Ag were evaporated onto the active layers under a shadow mask producing 5 mm^2 pixels. JV characteristics were obtained from devices sealed in a nitrogen atmosphere under a solar simulator at AM1.5G solar irradiation (100 $mWcm^{-2}$) calibrated by a Si reference cell, using a Keithley 236 source/measure unit. Some pixels were not fully measured once it was obvious that they were shunts.

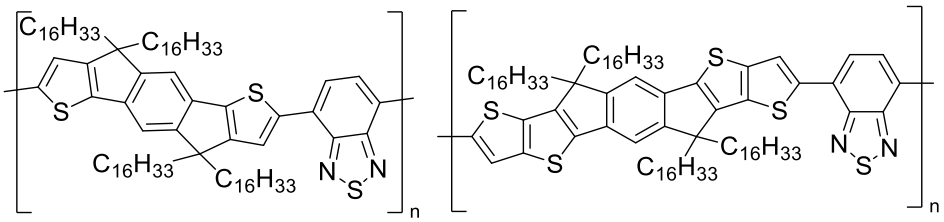
3.5.5 – Physics Department Device Fabrication Procedure

Formulations were prepared in air the day before coating and were stirred overnight at 50°C in CB. Devices were prepared in an inverted architecture (glass/ITO/ZnO/Donor:Acceptor/MoO_3/Ag). 1.2 cm^2 glass substrates (Psiotec) with one-pre-patterned side of ITO were cleaned sequentially in an ultrasonic bath with Decon 90 detergent, deionised water, acetone, IPA, and left in IPA overnight. Substrates were dried and treated with oxygen plasma. ZnO ETL was spin coated from a Sigma-Aldrich ZnO nanoparticle dispersion diluted 1:1 in IPA was spin coated at 4000 rpm over 40 seconds followed by annealing at 110°C for 10 mins. Active layers were spin coated over 35 seconds at 2000 rpm from CB. The active layers were used as spun or annealed for 15 mins. 10 nm of MoO_3 followed by 100 nm of Ag were evaporated onto the active layers under a shadow mask producing 5 mm^2 pixels. JV characteristics were obtained from devices in a nitrogen glovebox under an Oriel 300 W solar simulator at AM1.5G solar irradiation (100 $mWcm^{-2}$) calibrated by a Si reference cell, using a Keithley 236 source/measure unit. Device active layers were defined by a mask with an area of 3.86 mm^2.

Chapter 4 – Polymers for OFET

4.1 – Introduction

4.1.1 – IDT Derivative OFET Polymers



PIDT-BT **PIDTT-BT**

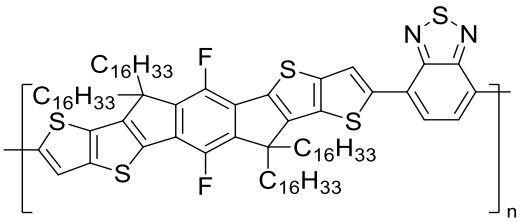
Figure 4.1: *Structures of* ***PIDT-BT*** *polymer and* ***PIDTT-BT****.*[95,121]

As briefly introduced in Chapters 1 and 2, **IDT** and **IDTT** have been used to great success in p-type polymers for OFET applications (**Figure 4.1**).[95,121] Although these polymers have less long-range order than earlier polythiophenes, they provide higher hole mobilities at high molecular weights.[96] When first synthesised, **PIDT-BT** devices were optimised up to a field effect mobility of 1.2 cm^2/Vs.[110] These devices used polymer with a number average molecular weight (Mn) of 38 kg/mol, and a weight average molecular weight (Mw) of 108 kg/mol. When significantly higher weight polymers with an Mn of 80 kg/mol and Mw of 160 kg/mol were investigated a very impressive mobility of 3.6 cm^2/Vs was obtained.[95] **PIDT-BT** was mostly amorphous in films with intermittent crystalline domains and its high mobility was obtained predominantly through rapid transport along the highly rigid and low disorder conjugated backbone. The backbone of **PIDT-BT** was found to have both a low energy barrier to planarisation and a high energy barrier for rotation, resulting in coplanarity being maintained even in amorphous regions.[176] The high molecular weight of the polymer meant that these long conjugated chains could bridge amorphous and crystalline regions in films, maintaining high charge mobility and minimising the requirement for interchain hopping.

PIDTT-BT is also semi-crystalline like **PIDT-BT** and relies on rapid transport down long chains that are resistant to disorder. As for **IDT**-based NFAs, ring extension is a viable strategy to improve the performance of OFET polymers. The lengthening of the fused ring core in

PIDTT-BT increases charge carrier mobility by increasing the rigidity of the chain. Additionally, this modification improves the polymer's relative crystallinity and therefore charge hopping between chains. OFET devices with **PIDTT-BT** had charge mobilities up to 6.6 cm^2/Vs, this was increased to 8.7 cm^2/Vs when a CuSCN electron blocking layer was used on top of the gold source/drain electrodes. **PIDTT-BT** has a relatively low LUMO of around 3.7 eV, and CuSCN blocked undesired electron transport while enhancing hole injection, highlighting the importance of device optimisation in OFET devices.

4.1.2 – Target OFET Polymer

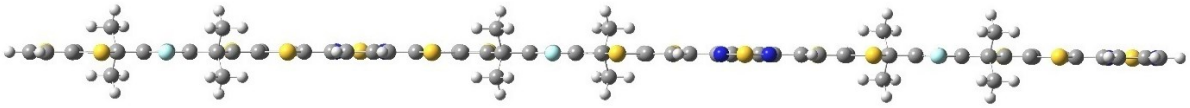


P2FIDTT-BT

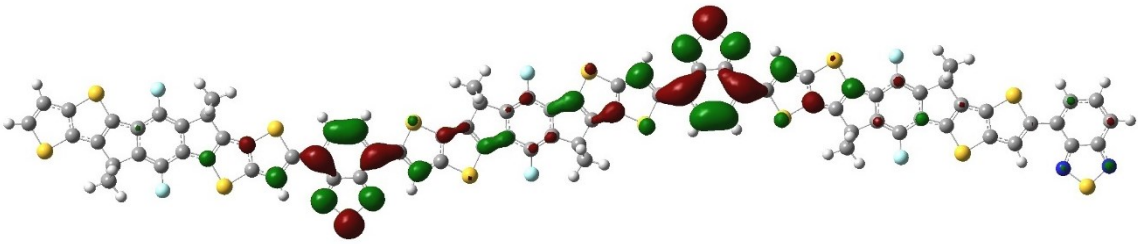
Figure 4.2: *Structure of the* ***P2FIDTT-BT*** *polymer.*

Due to the success of literature **PIDTT-BT**, the polymer **P2FIDTT-BT** was envisioned (**Figure 4.2**). The polymer was synthesised to investigate if fluorination on the central phenyl position can help improve the crystallinity of the polymer via non-covalent inter-chain interactions and thus increase charge carrier mobility for p-type OFET applications. DFT calculations were performed and showed the polymer to be highly planar similarly to its non-fluorinated counterparts and therefore suitable for rapid intrachain charge transport (**Figure 4.3 (a)**). The model used a trimer of **P2FIDTT-BT** with methyl sidechains to reduce computational load.

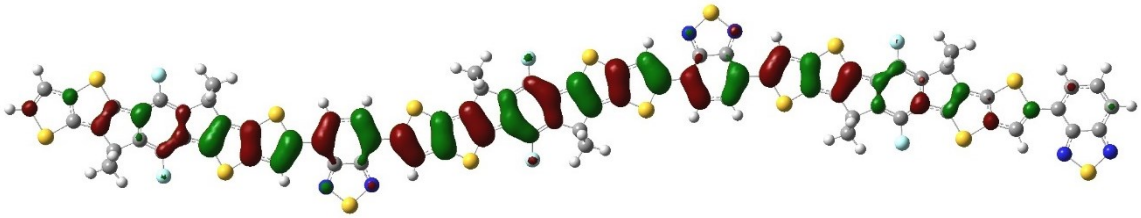
(a)



(b)



(c)



(d)

FMO	Energy (eV)
HOMO	-4.75
LUMO	-2.88

Figure 4.3: *DFT results for a trimer of* ***P2FIDTT-BT*** *with methyl sidechains at the B3LYP level of theory with a 6-31G +G(d,p) basis set.* ***(a)*** *Side view of trimer.* ***(b)*** *Trimer LUMO orbital.* ***(c)*** *Trimer HOMO orbital.* ***(d)*** *Table of calculated FMO energy levels.*

As would be expected for a p-type polymer, the LUMO of the polymer is highly localised on the electron poor **BT** units while the HOMO is distributed across the entire polymer chain, potentially allowing for rapid hole transport (**Figure 4.3 (a) and (b)**). The HOMO of the polymer is calculated to be 4.75 eV, this matches the approximately 4.74 eV work function

of a gold electrode allowing for a low hole injection barrier.[177] However, the DFT calculation only uses a trimer with methyl sidechains causing inaccuracy in the calculated HOMO value. In addition, the calculation doesn't take account of interchain interactions that would affect FMOs in films.

4.2 – Results and Discussion

4.2.1 – Polymer Synthesis

The starting point for the monomer synthesis was **2FIDTT** produced by the triflic acid-route (Chapter 2). This was alkylated with long hexadecyl alkyl sidechains, rather than the hexyl sidechains previously used for the NFA synthesis. Long linear alkyl sidechains were used to ensure the good solubility of the resulting polymer, in analogy to **PIDTT-BT**. Alkylation proceeded smoothly, albeit in a modest yield around 50%. Bromination was performed in a mixed solvent of THF/DMF at room temperature, but it was difficult to purify the produce. Analysis of both crude and purified (by column chromatography) batches consistently exhibited impurity peaks, which were first believed to be mono or tri-brominated impurities. Even attempts to purify by recycling prep GPC were unsuccessful. Eventually it was noted that the samples dissolved in $CHCl_3$ for NMR analysis resulted in a colour change from beige to light blue. TLC analysis of **4.2** in $CDCl_3$ fresh $CHCl_3$, DCM, and THF are depicted **in Figure 4.3** and show two spots only apparent in the $CDCl_3$ sample.

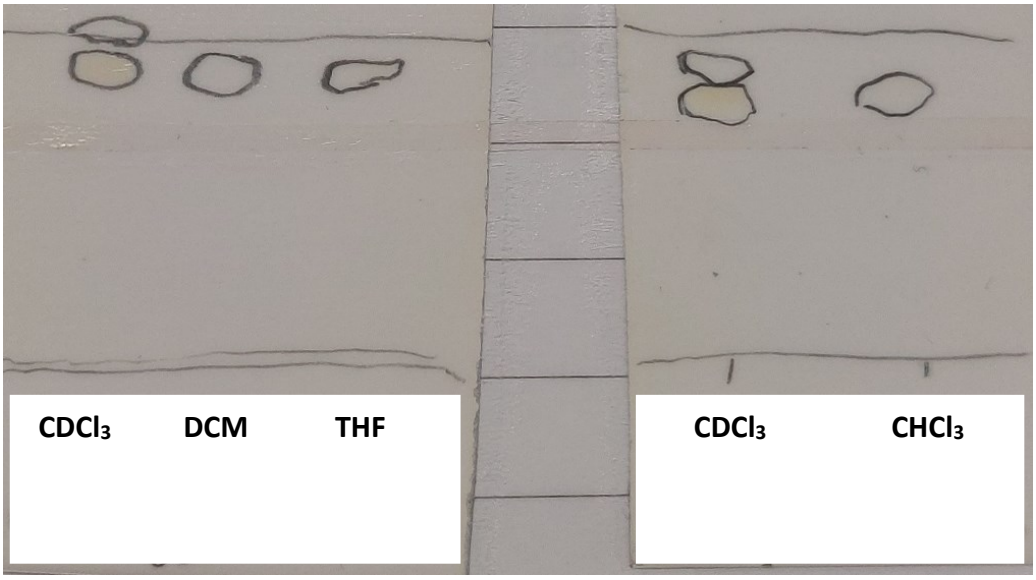
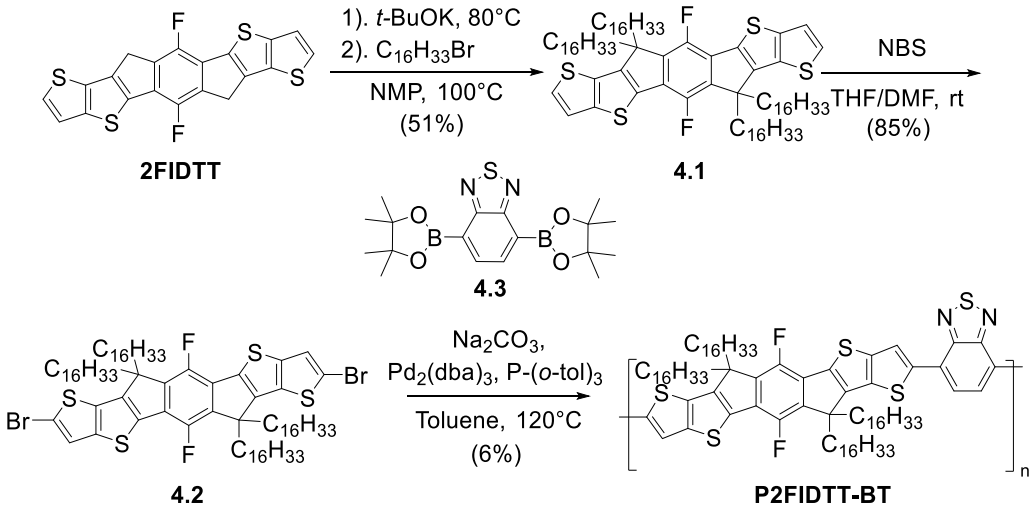


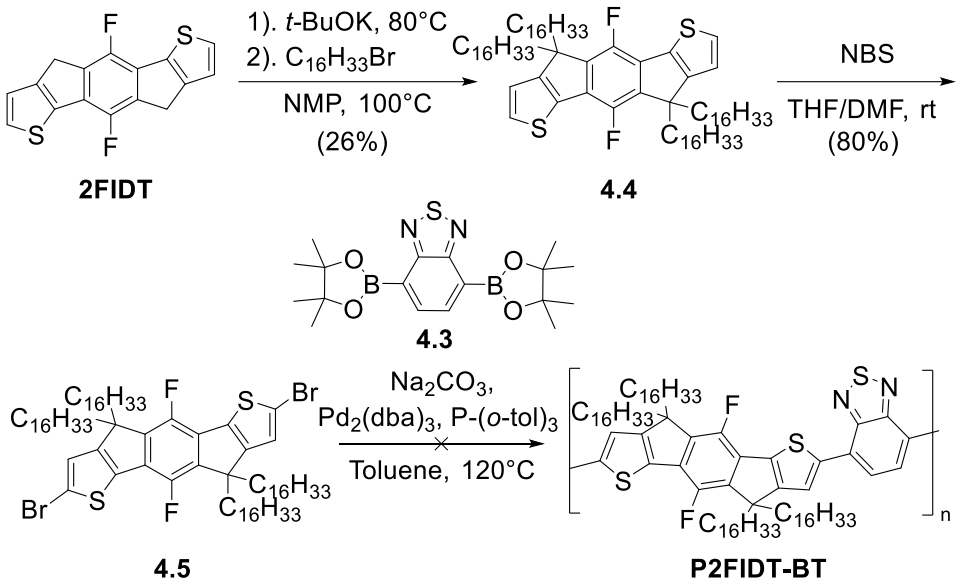
Figure 4.3: *Photo of hexane eluted TLCs taken of a sample of* ***4.2*** *in different solvents.*

Replacement of the NMR solvent with a new batch of $CDCl_3$ resulted in clean spectra, as did running the NMR in deuterated DCM. We therefore believe the problem related to the presence of HCl forming in the $CDCl_3$, which appeared to cause some irreversible degradation. Unfortunately, this issue wasn't spotted immediately, and a significant loss in yield and time resulted, as multiple attempts at purification of **4.2** to remove decomposed impurity by column chromatography, recrystallisation and preparatory GPC were attempted. The high yield value for the synthesis of **4.2** in **Scheme 4.1** refers to the yield of the product after the first purification by column chromatography, when the only impurity detected by NMR was that caused by decomposition in the $CDCl_3$ NMR solvent.



Scheme 4.1: *Synthesis of* ***P2FIDTT-BT*** *polymer from* ***2FIDTT****.*

With monomer **4.2** in hand, it was then polymerised with the bis(boronic) ester of BT under the Suzuki conditions previously used to synthesise **PIDTT-BT**.[121] Thus the mixture was heated for 2 days under nitrogen, cooled and precipitated from acidified methanol. Soxhlet extraction was performed with methanol, acetone, hexane, and THF solvent giving the polymer after removal of solvent from the fractions and precipitation from methanol. When a 0.07 M concentration of monomers was reacted in toluene, analysis of the THF fraction indicated a polymer with a poor Mn of 3.4 kg/mol and Mw of 3.7 kg/mol. The monomer concentration was increased to 0.15 M and a polymer with an improved Mn of 26 kg/mol, and an Mw of 30 kg/mol was obtained after fractionalisation. Increasing the monomer concentration to 0.2 M produced a polymer with an Mn of 13 kg/mol and a Mw of 16 kg/mol. However, a repeat of the polymerisation with a monomer concentration of 0.15 M provided polymer that was fully extracted by acetone during Soxhlet extraction, implying a very low molecular weight. As such it was assumed that the greatest factor reducing polymer Mn was the weighing error in monomer measurement. Only small amounts of monomer were used, with the 30 kg/mol polymer for example being produced from only 103.4 mg of **4.1**. Therefore, measurement errors in the weights of the monomers could reduce molecular weight as per the Carothers' equation that states that the degree of polymerisation is highly dependent on the ratio between the amount of each monomer.[178] The low 6% yield of the highest Mn forming polymerisation was due to most of the polymer being removed during washes with other solvents before THF in the Soxhlet extraction. Only a small fraction of the entire synthesised polymer was only soluble in THF.

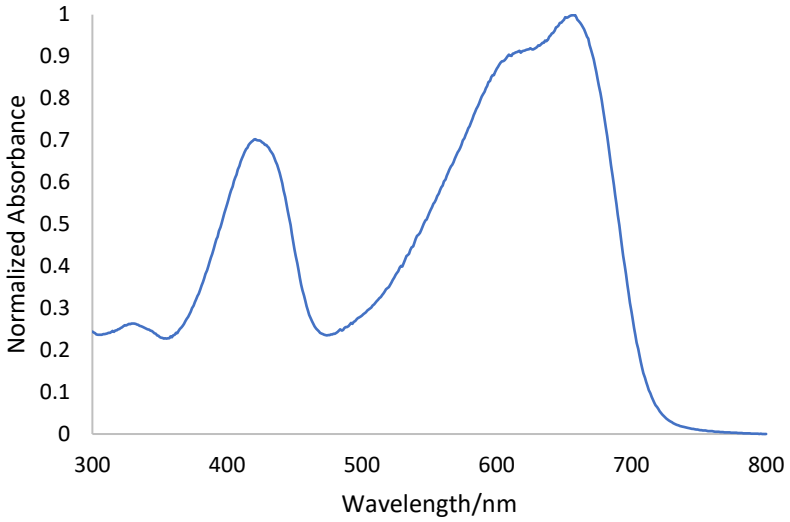


Scheme 4.2: *Attempted synthesis of* ***P2FIDT-BT*** *polymer from* ***2FIDT****. The yield value for the synthesis of* ***4.5*** *refers to the yield of the product after the first purification by column chromatography.*

In addition, the synthesis of the less-complex polymer **P2FIDT-BT** was attempted from **2FIDT** in parallel to the synthesis of **P2FIDTT-BT** (**Scheme 4.2**). Alkylation under standard conditions produced **4.4** in a poor 26% yield, most likely due to the poor solubility of **2FIDT** and uncertainty about its purity due to its poor solubility in NMR solvents. NBS bromination proceeded as expected. Unfortunately, the polymerisation was not attempted as NMR testing in $CDCl_3$ again caused decomposition and introduced impurity into the sample. Multiple attempts were taken to remove this impurity including column chromatography, preparatory GPC and recrystallisation. However, due to poor separation on silica and as the samples were constantly tested by NMR in $CDCl_3$ the decomposed impurity was always found. Because of the repeated purification attempts and decomposition, only around 20 mg of pure **4.5** was obtained once the decomposition was understood and successfully purified out. This equates to only 8.57 mg of comonomer **4.3**, not enough to polymerise as there would be too much variance between the two monomers used due to weighing error. The resultant misalignment in the amounts of each monomer would result in a very poor molecular weight according to Carothers' equation.[178]

4.2.2 – Optoelectronic and Electrochemical Properties of 2FIDTT-BT

A UV-Vis spectrum was taken of **P2FIDTT-BT** in chloroform solution showing a dual band absorption common for donor-acceptor polymers with absorption peaks at 424 nm and 658 nm.[121] An absorption onset of 715 nm was found, equating to an optical bandgap of 1.73 eV. The bandgap of 196k g/mol Mw **PIDTT-BT** films in literature is 1.71 eV, implying that either the lower HOMO on the **2FIDTT** moiety of **2FIDTT-BT** or the greatly reduced Mw of the synthesised **P2FIDTT-BT** reduced conjugation and widened bandgap.[121]



Polymer	**P2FIDTT-BT**
Absorption Maximum (nm)	658
Absorption Onset (nm)	715
Optical Bandgap (eV)	1.73

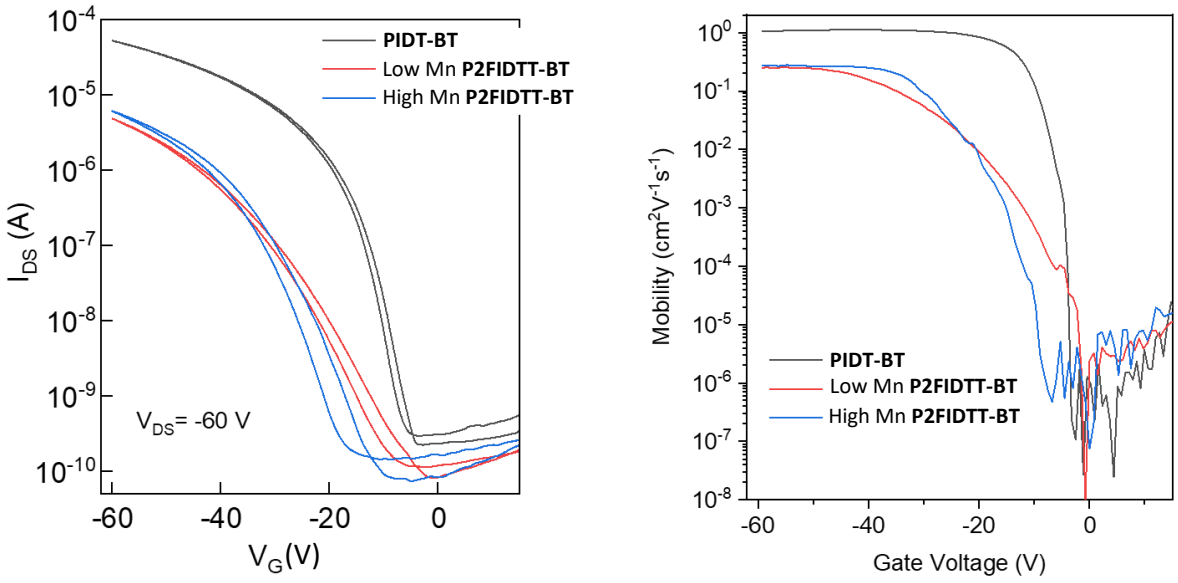
Figure 4.4: *Normalised UV-Vis spectra and bandgap table for* ***P2FIDTT-BT*** *in thin film.*

The IP of **P2FIDTT-BT** was measured to estimate a HOMO energy level by CV of drop-cast films in a 0.1 M solution of Bu_4NPF_6 in acetonitrile. Pronounced oxidation reversibility was found for the polymer films and therefore the half wave potential of the oxidation and subsequent reduction was referenced against Fc/Fc^+ and used as E^{OX} in **Equation 2.1** to find the IP. The IP was assumed to equal the HOMO energy level for the polymer. The IP of **P2FIDTT-BT** was calculated as -5.63 eV. This is deepened in comparison to the -5.40 eV

obtained in literature for films of **PIDTT-BT** by photoelectron spectroscopy in air. While variation from measurement techniques will occur, the effectively reduced HOMO of **P2FIDTT-BT** can be explained by a decreased conjugation due to a reduced molecular weight and by fluorination lowering the HOMO orbital on the **2FIDTT** moiety of the polymer.

4.2.3 – 2FIDTT-BT Device Performance

The **2FIDTT-BT** polymer was tested in OFET devices by our collaborator Dr. Aniruddha Basu at the KAUST Solar Center in Saudi Arabia. The low Mn batch of polymer with a Mn of 13 kg/mol and a Mw of 16 kg/mol was analysed together with the high Mw batch that had a Mn of 26 kg/mol and a Mw of 30 kg/mol. The polymer was tested against **PIDT-BT** (**Figure 4.5**) at a channel width and length of 1000 and 80 µm respectively, using Al/Au source and drain electrodes, a CYTOP dielectric, and an Al gate electrode. The source and drain electrodes were treated with pentafluorothiophenol self-assembled monolayer to improve hole injection.[179] Further information about coating conditions and separate device curves are given in this chapter's experimental section and the appendix respectively.



Polymer	V_T (V)	μ_{sat} (cm^2/Vs)
Low Mn **P2FIDTT-BT**	-29.90	0.24
High Mn **P2FIDTT-BT**	-29.05	0.29
PIDT-BT	-13.27	1.11

Figure 4.5: *Transfer curves, mobility curves based on the first derivative of the linear regime transfer curve and second derivative of the saturation regime transfer curve, and performance table for* ***P2FIDTT-BT*** *and* ***PIDT-BT*** *OFET devices.* ***PIDT-BT*** *had Mn = 121 kg/mol and Mw = 322 kg/mol.*

As expected, the higher Mn batch of **P2FIDTT-BT** had a higher μ_{sat} than the lower Mn batch. This is likely due to its longer polymer chains improving intrachain charge transport as well as improving connectivity between crystalline and amorphous domains.[180] The poor μ_{sat} of both polymers is likely to be predominantly due to their relatively low Mn as increased core conjugation should make the polymer chains more rigid and less disordered improving charge transport. This mobility raising molecular weight effect occurs for literature **PIDTT-BT** when compared to the **PIDT-BT** polymer.[95,121] Alternatively, fluorination impedes the ability of **P2FIDTT-BT** to self-organise thus lowering transfer integrals, increasing reorganisation energy, and therefore lowering charge mobility.[181,182] **P2FIDTT-BT** had poor current at positive gate bias highlighting its suitability as a p-type polymer. The absence of electron

conduction likely relates to the high lying LUMO level, which limits electron injection. In addition, as shown by the DFT results (**Figure 4.3**) the LUMO of the polymer is localised on the **BT** units whilst the HOMO is spread across the entire molecule allowing rapid intramolecular hole transfer but reduced electron mobility.

It is possible that barriers to injection due to energy level mismatch between polymer and electrodes also caused a reduction in mobility.[183] The HOMO energy level of **PIDT-BT** film is -5.15 eV from the literature, more shallow than that our recorded value of -5.63 eV for the high Mw **P2FIDTT-BT**.[184] The literature energy level was measured by photoemission spectroscopy and this would introduce variation when compared to our CV result. However, the energy level difference is significant and may have reduced the mobility of **P2FIDTT-BT** as the OFET system and its electrodes were initially optimised for **PIDT-BT** and aligned to its FMO energy levels. Future device investigation should focus on improving the energy level match between the FMOs of **P2FIDTT-BT** and the electrodes, perhaps by modification of the self-assembled monolayer.

As can be seen from the transfer curves for the tested polymers, **PIDT-BT** generates more charge at any measured V_G value (**Figure 4.5**). Importantly, the V_T of the **PIDT-BT** devices is less than half that of either batch of **P2FIDTT-BT** indicating greatly superior switching behaviour. The μ_{sat} of **PIDT-BT** is also greater than those of either **P2FIDTT-BT** batch. Therefore, **PIDT-BT** is a preferable polymer for p-type OFETs overall.

4.3 – Conclusions

The **PIDTT-BT** derivative **P2FIDTT-BT** was synthesised with a maximum Mn of 26 kg/mol and a Mw of 30 kg/mol. Attempts were also made to produce the **2FIDT**-based **P2FIDT-BT** polymer, however it was abandoned due to monomer decomposition and timing constraints because of the coronavirus pandemic. The **P2FIDTT-BT** polymer had a thin film optical bandgap of 1.73 eV and a HOMO energy level of -5.63 eV by CV on a drop-cast film.

OFET devices using **P2FIDTTBT** performed at a maximum μ_{sat} of 0.29 cm^2/Vs. A lower molecular weight batch of the polymer had a reduced 0.24 cm^2/Vs μ_{sat} as would be expected. Due its poor charge transport, the **P2FIDTTBT** polymer had a high minimum V_T of -29 V indicating poor switching behaviour.

Future research should focus on producing greater quantities of monomer for the polymerisations towards **P2FIDTBT** and **P2FIDTTBT** so higher Mn values can be obtained through reduced weighing error. Further optimisation could then be carried out on OFET devices to improve their performance.

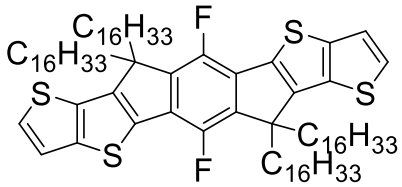
4.4 – Experimental

4.4.1 – Material Sources

PIDT-BT polymer was synthesised by Dr. Qiao He in our research group.

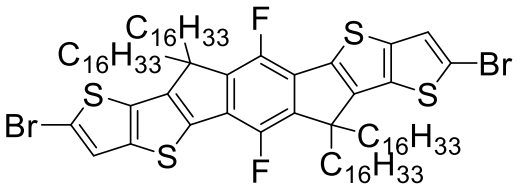
4.4.1 – Synthetic Procedures

General procedure for long-chain alkylation of cores: To a suspension of core (1.0 equiv) in NMP was added tert-butoxide salt (6.0 equiv) portion-wise. The mixture was heated at 80 °C for 1 h, haloalkane (6.0 equiv) was added and the reaction heated for 16 hours overnight. After cooling to RT the mixture was poured into water (100 mL), filtered, and washed with methanol (3 x 50 mL). The crude product was purified by silica column (petroleum ether) and afterwards by biphasic recrystallisation (chloroform:ethanol).

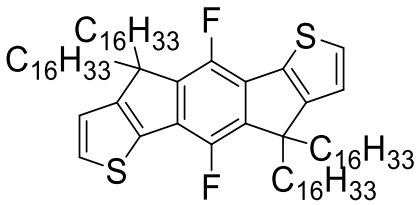


5,11-Difluoro-6,6,12,12-tetrahexadecyl-6,12-dihydrothieno[3,2-b]thieno[2'',3'':4',5']thieno[2',3':5,6]-s-indaceno[2,1-d]thiophene (4.1): The reaction was performed according to the general procedure for long-chain alkylation of cores and using 5,11-difluoro-6,12-dihydrothieno[3,2-b]thieno[2'',3'':4',5']thieno[2',3':5,6]-s-indaceno[2,1-d]thiophene (144 mg, 0.348 mmol), sodium *tert*-butoxide (200 mg, 2.08 mmol), 1-bromohexadecane (0.64 mL, 2.08 mmol), NMP (6 mL) and was heated overnight at 100 °C. Following work-up, the crude product was recrystalised to afford the title compound was obtained as a pale-yellow solid (233 mg, 51 %). M.P. 104 – 106 °C ^{1}H NMR (400 MHz, Chloroform-d) δ(ppm) 7.40 (d, *J* = 5.0 Hz, 2H), 7.38 (d, *J* = 5.0 Hz, 2H), 2.35 - 2.24 (m, 4H), 2.24 – 2.13 (m, 4H), 1.37 – 1.00 (m, 112H), 0.95 – 0.73 (m, 12H). ^{13}C NMR (101 MHz, Chloroform-d) δ 147.53 (dd, ^{1}J = 247.7, ^{4}J = 3.6 Hz, CF), 145.40, 143.49, 138.66 - 138.22 (m, CF) 137.99, 132.82, 126.24, 126.12 - 125.72 (m, CF) 120.49, 55.98, 36.63, 31.95, 30.10 –

28.92 (multiple s), 24.32, 22.72, 14.14. ^{19}F NMR (377 MHz, Chloroform-d) δ(ppm) -134.09. MS (LD-ToF) *m/z* 1312.0 (M^+).

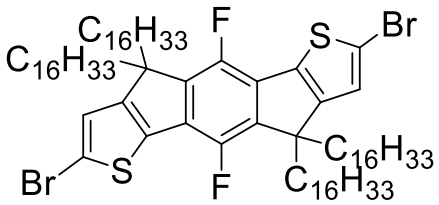


2,8-Dibromo-5,11-difluoro-6,6,12,12-tetrahexadecyl-6,12-dihydrothieno[3,2-b]thieno[2'',3'':4',5']thieno[2',3':5,6]-s-indaceno[2,1-d]thiophene (4.2): To a solution of 5,11-difluoro-6,6,12,12-tetrahexadecyl-6,12-dihydrothieno[3,2-b]thieno[2'',3'':4',5']thieno[2',3':5,6]-s-indaceno[2,1-d]thiophene (400 mg, 0.305 mmol) in THF (17.5 mL) and DMF (8.75 mL) in the absence of light was added N-bromosuccinimide (122 mg, 0.685 mmol). After 3 h the reaction mixture was poured into water (20 mL), filtered, and washed with water (3 x 10 mL). The crude product was purified by silica column chromatography (hexane) yielding the *title compound* as off-white solid (380 mg, 85%). M.P. 110 - 112 °C. ^{1}H NMR (400 MHz, Chloroform-d) δ(ppm) 7.38 (s, 2H), 2.31 - 2.21 (m, 4H), 2.16 – 2.06 (m, 2H), 1.36 – 1.02 (m, 112H), 0.94 – 0.71 (m, 12H). ^{13}C NMR (101 MHz, Chloroform-d) δ(ppm) 147.46 (dd, ^1J = 247.6, ^4J = 3.7 Hz, CF), 145.49, 141.77, 138.60 - 138.21 (m, CF), 137.29, 133.15, 126.02 - 125.59 (m, CF), 123.21, 112.48, 56.00, 36.58, 31.95, 30.01 – 28.94 (multiple s), 24.32, 22.72, 14.14. ^{19}F NMR (377 MHz, Chloroform-d) δ(ppm) -133.61. MS (LD-ToF) *m/z* 1468.0 (M^+).

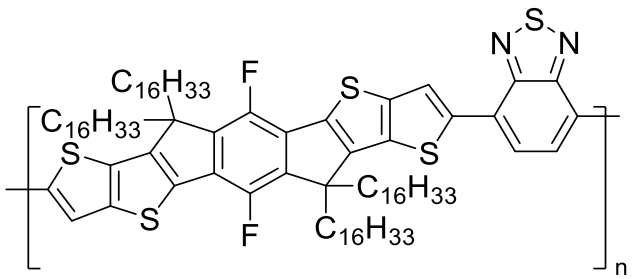


5,10-Difluoro-4,4,9,9-tetrahexadecyl-4,9-dihydro-s-indaceno[1,2-b:5,6-b']dithiophene (4.4): The reaction was performed according to the general procedure for long-chain alkylation of cores and using 5,10-difluoro-4,9-dihydro-s-indaceno[1,2-b:5,6-b']bisthiophene (126 mg, 0.417 mmol), sodium tert-butoxide (240 mg, 2.50 mmol), 1-bromohexadecane (0.76 mL, 2.50 mmol), NMP (7 mL) and was heated overnight at 100 °C. Following work-up, the crude product was recrystalised to afford the *title compound* was obtained as a pale-yellow solid (131 mg, 26 %). M.P. 81 – 83 °C. ^{1}H NMR (400 MHz, Chloroform-d) δ (ppm) 7.35

(d, *J* = 4.9 Hz, 2H), 6.95 (d, *J* = 4.9 Hz, 2H), 2.19 – 2.08 (m, 4H), 2.08 – 1.97 (m, 4H), 1.35 – 1.00 (m, 112H), 0.92 – 0.77 (m, 12H). ^{13}C NMR (101 MHz, Chloroform-d) δ (ppm) ^{13}C NMR (126 MHz, Chloroform-d) δ 154.98, 147.40 (d, ^{1}J = 248.1 Hz, CF) 139.55 – 139.24 (m, CF), 136.11, 128.71, 125.34 – 124.79 (m, CF), 121.03, 55.57, 37.39, 31.92, 29.93 – 29.15 (multiple s), 24.34, 22.69, 14.11.^{19}F NMR (377 MHz, Chloroform-d) δ (ppm) -133.78. MS (EI-ToF) *m/z* 1200.0176 (M^+).



2,7-Dibromo-5,10-difluoro-4,4,9,9-tetrahexadecyl-4,9-dihydro-s-indaceno[1,2-b:5,6-b']dithiophene (4.5): To a solution of 5,10-difluoro-4,4,9,9-tetrahexadecyl-4,9-dihydro-s-indaceno[1,2-b:5,6-b']dithiophene (131 mg, 0.109 mmol) in THF (20 mL) and DCM (5 mL) under in the absence of light was added N-bromosuccinimide (50.8 mg, 0.285 mmol). After 16 h the reaction mixture was poured into water (10 mL), filtered, and washed with water (3 x 5 mL). The crude product was purified by silica column chromatography (hexane) yielding the crude *title compound* (118 mg, 80%). M.P. 99 – 101 °C. ^{1}H NMR (400 MHz, Chloroform-d) δ(ppm) 6.96 (s, 2H), 2.14 - 2.03 (m, 4H), 2.02 - 1.91 (m, 4H), 1.36 – 1.00 (m, 112H), 0.92 – 0.71 (m, 12H). ^{13}C NMR was too weak due to solubility issues. ^{19}F NMR (377 MHz, Chloroform-d) δ(ppm) -133.48. MS (EI-ToF) *m/z* 1356.8086 (M^+).



P2FIDTT-BT

P2FIDTT-BT: To 2,8-Dibromo-5,11-difluoro-6,6,12,12-tetrahexadecyl-6,12-dihydrothieno[3,2-b]thieno[2'',3'':4',5']thieno[2',3':5,6]-s-indaceno[2,1-d]thiophene (103.4 mg, 0.0703 mmol), 4,7-bis(4,4,5,5-tetramethyl-1,3,2-dioxaborolan-2-yl)benzo[c][1,2,5]thiadiazole (27.3 mg, 0.0703 mmol), $Pd_2(dba)_3$ (1.44 mg, 1.39 x 10^{-3} mmol),

and P-(*o*-Tol)$_3$ (1.69 mg, 5.56 x 10^{-3} mmol) was added toluene (0.94 mL) and Aliquat 336 (0.1 mL) and the mixture degassed with N_2 over 30 min. Degassed Na_2CO_3 solution (2M, 0.9 mL) was added to the mixture, and the resultant mixture degassed for a further 30 min. After heating to 120°C for 48 h, the polymer was precipitated from acidic methanol (CH_3OH + HCl) and collected by filtration. After a wash with water Soxhlet extraction with methanol (8 h), acetone (8 h), hexane (8 h), and THF (8 h) was performed. Concentration of the chloroform fraction *in vacuo* followed by precipitation from methanol yielded the *title compound* as a dark blue solid (6.0 mg, 6%). M.P. > 400 °C. GPC (CB, 80°C): Mn = 26000 g/mol, Mw = 30000 g/mol. ^{1}H NMR (500 MHz, TCE-d_2 at 393 K) δ 8.72 – 8.68 (m, 2H), 8.04 (s, 2H), 2.44 (m, 8H), 1.44 – 0.94 (m, 132H). ^{19}F NMR (471 MHz, TCE-d_2 at 393K) δ -132.65.

4.4.2 – OFET device fabrication procedure

The organic field effect transistor (OFET) devices were fabricated in a top-gate, bottom-contact architecture (TG-BC). The Al/Au (5nm/35nm) source and drain electrodes were vapor deposited using a shadow mask on a glass substrate and were further treated with pentafluorothiophenol. Polymer semiconductor solutions (5 mg/ml in CB) were spin coated on the glass substrates at 2000 rpm over 1 min and then annealed at 120°C for 10 mins. 600 nm of CYTOP film was deposited on top of the semiconductor by spin coating aqueous CYTOP (67% by volume) at 1200 rpm followed by annealing at 50°C for 1hr. The capacitance of the CYTOP dielectric was measured as 3.45 nF/cm^2. 50 nm of Al was vapor deposited as a top gate electrode. The current–voltage characteristics for the devices were measured using a KEYSIGHT B2912A Precision Source/Measure Unit.

5 – General Experimental

5.1 – Materials and Reaction Conditions

Most chemicals were purchased from large commercial suppliers (Alfa Aesar, Sigma Aldrich, VWR), niche chemicals were purchased from smaller suppliers such as Fluorochem and Oscilla. All reactions were carried out under an inert nitrogen atmosphere maintained using a standard Shlenck-line. All glassware was dried in an oven at 140 °C for 1 – 16 hours prior to use. Recycling preparatory GPC was performed on a JAI LaboACE LC-5060 instrument with an in-line UV-Vis detector and fitted with 2HR and 2.5HR organic GPC columns connected in series.

5.2 – Characterisation

All NMR spectra (^{1}H, ^{19}F, ^{13}C) were measured using the residual solvent resonance of chloroform-d (unless otherwise specified) on a Bruker AV-400 (400 MHz) spectrometer, chemical shifts are given in ppm.

UV-Vis measurements were obtained on a UV-1800 Shimadzu UV-Vis spectrometer unless otherwise specified. UV-vis measurements were either taken of solutions or thin films spun cast from a 5 mg/mL chloroform solution at 2000 rpm and annealed at 100 °C for 10 mins.

Melting point measurements were obtained on a MPA1000 Melting Point Apparatus.

MS measurements were submitted to Mrs. Charlotte Rapley or Dr. Lisa Haigh at Imperial College and measured using standard procedures.

CV measurements were performed using an AUTOLAB PGSTAT 101 potentiostat with a three-electrode setup. Organic thin films were drop cast onto a glassy carbon working electrode from a 5 mg/mL chloroform solution. A platinum mesh counter electrode and an Ag/Ag^{+} reference electrode were used. 0.1M tetrabutylammonium hexafluorophosphate was used in dry deoxygenated acetonitrile as the electrolyte for all measurements, which were calibrated against ferrocene.

Infrared (IR) and Fourier-transform infrared spectroscopy measurements (FTIR) were carried out on a Bruker Alpha P spectrometer with DGTS detector and diamond ATR accessory.

Analytical GPC measurements were taken on an Agilent Technologies 1200 series GPC, with two Plgel 10 µm Mixed-B GPC columns in series (7.5 mm x 300 mm), calibrated against a polystyrene polymer internal standard.

6 – References

1 D. Jones, *Global Electricity Review 2021*, 2021.

2 T. Covert, M. Greenstone and C. R. Knittel, *J. Econ. Perspect.*, 2016, **30**, 117–138.

3 S. F. Lincoln, *R. Swedish Acad. Sci.*, 2016, **34**, 621–627.

4 S. J. Smith, H. Pitchera and T. M. L. Wigley, *Glob. Planet. Change*, 2001, **29**, 99–119.

5 F. Johnsson, J. Kjärstad and J. Rootzén, *Clim. Policy*, 2019, **19**, 258–274.

6 D. Helm, *Oxford Rev. Econ. Policy*, 2016, **32**, 191–205.

7 S. Shafiee and E. Topal, *Energy Policy*, 2009, **37**, 181–189.

8 A. Qazi, F. Hussain, N. A. B. D. Rahim, G. Hardaker, D. Alghazzawi, K. Shaban and K. Haruna, *IEEE Access*, 2019, **7**, 63837–63851.

9 P. J. Ribeyron, *Nat. Energy*, 2017, **2**, 1–2.

10 T. Saga, *NPG Asia Mater.*, 2010, **2**, 96–102.

11 V. Alex, S. Finkbeiner and J. Weber, *J. Appl. Phys.*, 1996, **79**, 6943.

12 A. Goodrich, P. Hacke, Q. Wang, B. Sopori, R. Margolis, T. L. James and M. Woodhouse, *Sol. Energy Mater. Sol. Cells*, 2013, **114**, 110–135.

13 T. D. Lee and A. U. Ebong, *Renew. Sustain. Energy Rev.*, 2017, **70**, 1286–1297.

14 M. Imamzai, M. Aghaei and Y. H. Thayoob, *Proc. Natl. Grad. Conf.*, 2011, **2012**, 8–10.

15 J. Ramanujam, D. M. Bishop, T. K. Todorov, O. Gunawan, J. Rath, R. Nekovei, E. Artegiani and A. Romeo, *Prog. Mater. Sci.*, 2020, **110**, 1–20.

16 C. Y. Liu, Z. M. Li, H. Y. Gu, S. Y. Chen, H. Xiang and X. G. Gong, *Adv. Energy Mater.*, 2017, **7**, 1601457.

17 H. Sai, T. Matsui and K. Matsubara, *Appl. Phys. Lett.*, 2016, **109**, 1–6.

18 T. Sogabe, Q. Shen and K. Yamaguchi, *J. Photonics Energy*, 2016, **6**, 040901.

19 J. Gong, K. Sumathy, Q. Qiao and Z. Zhou, *Renew. Sustain. Energy Rev.*, 2017, **68**, 234–

246.

20 P. Roy, N. Kumar Sinha, S. Tiwari and A. Khare, *Sol. Energy*, 2020, **198**, 665–688.

21 O. A. Abdulrazzaq, V. Saini, S. Bourdo, E. Dervishi and A. S. Biris, *Part. Sci. Technol.*, 2013, **31**, 427–442.

22 NREL Best Research-Cell Efficiencies, https://www.nrel.gov/pv/cell-efficiency.html, (accessed March 2022).

23 W. Ke and M. G. Kanatzidis, *Nat. Commun.*, 2019, **10**, 1–4.

24 R. E. Peierls, in *Quantum Theory of Solids*, Oxford University Press, London, 1955, pp. 108–114.

25 P. M. Grant and I. P. Batra, *Solid State Commun.*, 1979, **29**, 225–229.

26 S. A. Jenekhe, *Nature*, 1986, **322**, 345–347.

27 J. L. Brédas, J. P. Calbert, D. A. Da Silva Filho and J. Cornil, *Proc. Natl. Acad. Sci. U. S. A.*, 2002, **99**, 5804–5809.

28 C. Deibel, D. MacK, J. Gorenflot, A. Schöll, S. Krause, F. Reinert, D. Rauh and V. Dyakonov, *Phys. Rev. B - Condens. Matter Mater. Phys.*, 2010, **81**, 1–5.

29 J. Toušek, J. Toušková, J. Ludvík, A. Liška, Z. Remeš, O. Kylián, J. Kousal, R. Chomutová, I. M. Heckler, E. Bundgaard and F. C. Krebs, *Solid. State. Electron.*, 2016, **116**, 111–118.

30 Y. Tamai, H. Ohkita, H. Benten and S. Ito, *J. Phys. Chem. Lett.*, 2015, **6**, 3417–3428.

31 G. Luo, X. Ren, S. Zhang, H. Wu, W. C. H. Choy, Z. He and Y. Cao, *Small*, 2016, **12**, 1547–1571.

32 T. H. Lai, S. W. Tsang, J. R. Manders, S. Chen and F. So, *Mater. Today*, 2013, **16**, 424–432.

33 V. I. Madogni, B. Kounouhéwa, A. Akpo, M. Agbomahéna, S. A. Hounkpatin and C. N. Awanou, *Chem. Phys. Lett.*, 2015, **640**, 201–214.

34 J. Cameron and P. J. Skabara, *Mater. Horizons*, 2020, **7**, 1759–1772.

35 A. Slami and N. Benramdane, *E3S Web Conf.*, 2021, **229**, 1–5.

36 Y. X. Xu, C. C. Chueh, H. L. Yip, F. Z. Ding, Y. X. Li, C. Z. Li, X. Li, W. C. Chen and A. K. Y. Jen, *Adv. Mater.*, 2012, **24**, 6356–6361.

37 M. E. Köse, *J. Phys. Chem. A*, 2012, **116**, 12503–12509.

38 J. Wang, L. Ma, Y. W. Lee, H. Yao, Y. Xu, S. Zhang, H. Y. Woo and J. Hou, *Chem. Commun.*, 2021, **57**, 9132–9135.

39 M. C. Scharber, D. Mühlbacher, M. Koppe, P. Denk, C. Waldauf, A. J. Heeger and C. J. Brabec, *Adv. Mater.*, 2006, **18**, 789–794.

40 C. J. Brabec, S. Gowrisanker, J. J. M. Halls, D. Laird, S. Jia and S. P. Williams, *Adv. Mater.*, 2010, **22**, 3839–3856.

41 S. E. Shaheen, C. J. Brabec, N. S. Sariciftci, F. Padinger, T. Fromherz and J. C. Hummelen, *Appl. Phys. Lett.*, 2001, **78**, 841–843.

42 J. Mei and Z. Bao, *Chem. Mater.*, 2014, **26**, 604–615.

43 S. Holliday, Y. Li and C. K. Luscombe, *Prog. Polym. Sci.*, 2017, **70**, 34–51.

44 E. Bundgaard and F. C. Krebs, *Sol. Energy Mater. Sol. Cells*, 2007, **91**, 954–985.

45 T. L. Nguyen, H. Choi, S.-J. Ko, M. a. Uddin, B. Walker, S. Yum, J.-E. Jeong, M. H. Yun, T. J. Shin, S. Hwang, J. Y. Kim and H. Y. Woo, *Energy Environ. Sci.*, 2014, **7**, 3040–3051.

46 J. Huang, J. H. Carpenter, C. Z. Li, J. S. Yu, H. Ade and A. K. Y. Jen, *Adv. Mater.*, 2016, **28**, 967–974.

47 A. Wadsworth, Z. Hamid, J. Kosco, N. Gasparini and I. McCulloch, *Adv. Mater.*, 2020, **32**, 2001763.

48 NREL Best Research-Cell Efficiencies, https://www.nrel.gov/pv/cell-efficiency.html, (accessed March 2020).

49 W. Zhao, D. Qian, S. Zhang, S. Li, O. Inganäs, F. Gao and J. Hou, *Adv. Mater.*, 2016, **28**, 4734–4739.

50 I. Etxebarria, J. Ajuria and R. Pacios, *J. Photonics Energy*, 2015, **5**, 057214.

51 M. Wienk, J. Kroon, W. Verhees, J. Knol, J. Hummelen, P. van Hal and R. Janssen, *Angew. Chemie*, 2003, **115**, 3493–3497.

52 R. Kumar, S. Naqvi, N. Gupta and S. Chand, *RSC Adv.*, 2014, **4**, 15675–15677.

53 Y. He, H. Y. Chen, J. Hou and Y. Li, *J. Am. Chem. Soc.*, 2010, **132**, 1377–1382.

54 C. B. Nielsen, S. Holliday, H.-Y. Chen, S. J. Cryer and I. McCulloch, *Acc. Chem. Res.*, 2015, **48**, 2803–12.

55 D. Chen, F. Liu, C. Wang, A. Nakahara and T. P. Russell, *Nano Lett.*, 2011, **11**, 2071–2078.

56 N. Kaur, M. Singh, D. Pathak, T. Wagner and J. M. Nunzi, *Synth. Met.*, 2014, **190**, 20–26.

57 Z. Li, C. C. Chueh and A. K. Y. Jen, *Prog. Polym. Sci.*, **99**, 101175.

58 A. Wadsworth, M. Moser, A. Marks, M. S. Little, N. Gasparini, C. J. Brabec, D. Baran and I. McCulloch, *Chem. Soc. Rev.*, 2019, **48**, 1596–1625.

59 J. Zhao, Y. Li, H. Lin, Y. Liu, K. Jiang, C. Mu, T. Ma, J. Y. L. Lai, H. Hu, D. Yu and H. Yan, *Energy Environ. Sci.*, 2015, **8**, 520–525.

60 J. Liu, S. Chen, D. Qian, B. Gautam, G. Yang, J. Zhao, J. Bergqvist, F. Zhang, W. Ma, H. Ade, O. Inganäs, K. Gundogdu, F. Gao and H. Yan, *Fast charge separation in a non-fullerene organic solar cell with a small driving force*, 2016, vol. 1.

61 K. Cnops, G. Zango, J. Genoe, P. Heremans, M. V. Martinez-Diaz, T. Torres and D. Cheyns, *J. Am. Chem. Soc.*, 2015, **137**, 8991–8997.

62 Y. Kim, C. E. Song, S. Moon, E. Lim, V. A. Online, Y. Kim, C. E. Song, S. Moon and E. Lim, *Chem. Commun.*, 2014, **50**, 8235–8238.

63 S. Holliday, R. S. Ashraf, C. B. Nielsen, M. Kirkus, J. A. R??hr, C. H. Tan, E. Collado-Fregoso, A. C. Knall, J. R. Durrant, J. Nelson and I. McCulloch, *J. Am. Chem. Soc.*, 2015, **137**, 898–904.

64 D. Baran, T. Kirchartz, S. Wheeler, S. Dimitrov, M. Abdelsamie, J. Gorman, R. S. Ashraf, S. Holliday, A. Wadsworth, N. Gasparini, P. Kaienburg, H. Yan, A. Amassian, C. J.

Brabec, J. R. Durrant and I. McCulloch, *Energy Environ. Sci.*, 2016, **9**, 3783–3793.

65 M. Li, Y. Liu, W. Ni, F. Liu, H. Feng, Y. Zhang, T. Liu, H. Zhang, X. Wan, B. Kan, Q. Zhang, T. P. Russell and Y. Chen, *J. Mater. Chem. A*, 2016, **4**, 10409–10413.

66 N. Qiu, H. H. Zhang, X. Wan, C. Li, X. Ke, H. Feng, B. Kan, H. H. Zhang, Q. Zhang, Y. Lu and Y. Chen, *Adv. Mater.*, 2016, 1–5.

67 Y. Lin, Z.-G. Zhang, H. Bai, J. Wang, Y. Yao, Y. Li, D. Zhu and X. Zhan, *Energy Environ. Sci.*, 2015, **8**, 610–616.

68 S. Holliday, R. S. Ashraf, A. Wadsworth, D. Baran, S. A. Yousaf, C. B. Nielsen, C.-H. Tan, S. D. Dimitrov, Z. Shang, N. Gasparini, M. Alamoudi, F. Laquai, C. J. Brabec, A. Salleo, J. R. Durrant and I. McCulloch, *Nat. Commun.*, 2016, **7**, 11585.

69 Y. Lin, J. Wang, Z. G. Zhang, H. Bai, Y. Li, D. Zhu and X. Zhan, *Adv. Mater.*, 2015, **27**, 1170–1174.

70 A. Wadsworth, R. S. Ashraf, M. Abdelsamie, S. Pont, M. Little, M. Moser, Z. Hamid, M. Neophytou, W. Zhang, A. Amassian, J. R. Durrant, D. Baran and I. McCulloch, *ACS Energy Lett.*, 2017, **2**, 1494–1500.

71 Z. Zheng, O. M. Awartani, B. Gautam, D. Liu, Y. Qin, W. Li, A. Bataller, K. Gundogdu, H. Ade and J. Hou, *Adv. Mater.*, **5**, 1604241.

72 J. Yuan, Y. Zhang, L. Zhou, G. Zhang, H. L. Yip, T. K. Lau, X. Lu, C. Zhu, H. Peng, P. A. Johnson, M. Leclerc, Y. Cao, J. Ulanski, Y. Li and Y. Zou, *Joule*, 2019, **3**, 1140–1151.

73 Q. Liu, Y. Jiang, K. Jin, J. Qin, J. Xu, W. Li, J. Xiong, J. Liu, Z. Xiao, K. Sun, S. Yang, X. Zhang and L. Ding, *Sci. Bull.*, 2020, **65**, 272–275.

74 M. Kim, S. U. Ryu, S. A. Park, Y. J. Pu and T. Park, *Chem. Sci.*, 2021, **12**, 14004–14023.

75 B. Carsten, J. M. Szarko, H. J. Son, W. Wang, L. Lu, F. He, B. S. Rolczynski, S. J. Lou, L. X. Chen and L. Yu, *J. Am. Chem. Soc.*, 2011, **133**, 20468–20475.

76 G. Zhang, X. K. Chen, J. Xiao, P. C. Y. Chow, M. Ren, G. Kupgan, X. Jiao, C. C. S. Chan, X. Du, R. Xia, Z. Chen, J. Yuan, Y. Zhang, S. Zhang, Y. Liu, Y. Zou, H. Yan, K. S. Wong, V. Coropceanu, N. Li, C. J. Brabec, J. L. Bredas, H. L. Yip and Y. Cao, *Nat. Commun.*, 2020,

11, 1–10.

77 W. Zhu, A. P. Spencer, S. Mukherjee, J. M. Alzola, V. K. Sangwan, S. H. Amsterdam, S. M. Swick, L. O. Jones, M. C. Heiber, A. A. Herzing, G. Li, C. L. Stern, D. M. DeLongchamp, K. L. Kohlstedt, M. C. Hersam, G. C. Schatz, M. R. Wasielewski, L. X. Chen, A. Facchetti and T. J. Marks, *J. Am. Chem. Soc.*, 2020, **142**, 14532–14547.

78 P. Cheng and Y. Yang, *Acc. Chem. Res.*, 2020, **53**, 1218–1228.

79 Y. Cui, Y. Wang, J. Bergqvist, H. Yao, Y. Xu, B. Gao, C. Yang, S. Zhang, O. Inganäs, F. Gao and J. Hou, *Nat. Energy*, 2019, **4**, 768–775.

80 P. Asghari, A. M. Rahmani and H. H. S. Javadi, *Comput. Networks*, 2019, **148**, 241–261.

81 W. Shockley and H. J. Queisser, *J. Appl. Phys.*, 1961, **32**, 510–519.

82 S. Rühle, *Sol. Energy*, 2016, **130**, 139–147.

83 Y. Cui, L. Hong and J. Hou, *ACS Appl. Mater. Interfaces*, 2020, **12**, 38815–38828.

84 D. Baran, R. S. A. Ashraf, D. A. Hanifi, M. Abdelsamie, N. Gasparini, J. A. Röhr, S. Holliday, A. Wadsworth, S. Lockett, M. Neophytou, C. J. M. Emmott, J. Nelson, C. J. Brabec, A. Amassian, T. Kirchartz, J. R. Durrant, I. Mcculloch, D. Baran, R. S. A. Ashraf, S. Holliday, A. Wadsworth, S. Lockett and P. J. R. Durrant, *Nat. Mater.*, 2016, **84**, 1–18.

85 M. B. Salim, R. Nekovei and R. Jeyakumar, *Sol. Energy*, 2020, **198**, 160–166.

86 H. Kang, K. H. Kim, T. E. Kang, C. H. Cho, S. Park, S. C. Yoon and B. J. Kim, *ACS Appl. Mater. Interfaces*, 2013, **5**, 4401–4408.

87 P. Cheng, Y. Li and X. Zhan, *Energy Environ. Sci.*, 2014, **7**, 2005.

88 H. Sirringhaus, *Adv. Mater.*, 2014, **26**, 1319–1335.

89 C. R. Newman, C. D. Frisbie, D. A. Da Silva Filho, J. L. Brédas, P. C. Ewbank and K. R. Mann, *Chem. Mater.*, 2004, **16**, 4436–4451.

90 J. Zaumseil and H. Sirringhaus, *Chem. Rev.*, 2007, **107**, 1296–1323.

91 B. S. Ong, Y. Wu, P. Liu and S. Gardner, *J. Am. Chem. Soc.*, 2004, **126**, 3378–3379.

92 K. Arlauskas, M. Viliu, K. Genevic, G. Jus and H. Stubb, *Phys. Rev. B*, 2000, **62**, 235–

238.

93 B. H. Hamadani, D. J. Gundlach, I. McCulloch and M. Heeney, *Appl. Phys. Lett.*, 2007, **91**, 1–4.

94 T. Lei, J. H. Dou and J. Pei, *Adv. Mater.*, 2012, **24**, 6457–6461.

95 X. Zhang, H. Bronstein, A. J. Kronemeijer, J. Smith, Y. Kim, R. J. Kline, L. J. Richter, T. D. Anthopoulos, H. Sirringhaus, K. Song, M. Heeney, W. Zhang, I. McCulloch and D. M. DeLongchamp, *Nat. Commun.*, 2013, **4**, 2238.

96 A. F. Paterson, S. Singh, K. J. Fallon, T. Hodsden, Y. Han, B. C. Schroeder, H. Bronstein, M. Heeney, I. McCulloch and T. D. Anthopoulos, *Adv. Mater.*, 2018, 30.

97 F. Aziz and A. F. Ismail, *Mater. Sci. Semicond. Process.*, 2015, **39**, 416–425.

98 S. L. Lim, E. C. Chen, C. Y. Chen, K. H. Ong, Z. K. Chen and H. F. Meng, *Sol. Energy Mater. Sol. Cells*, 2012, **107**, 292–297.

99 Y. H. Chang, S. R. Tseng, C. Y. Chen, H. F. Meng, E. C. Chen, S. F. Horng and C. S. Hsu, *Org. Electron.*, 2009, **10**, 741–746.

100 N. Sahu, B. Parija and S. Panigrahi, *Indian J. Phys.*, 2009, **83**, 493–502.

101 S. R. Dupont, M. Oliver, F. C. Krebs and R. H. Dauskardt, *Sol. Energy Mater. Sol. Cells*, 2012, **97**, 171–175.

102 M. M. Voigt, R. C. I. MacKenzie, S. P. King, C. P. Yau, P. Atienzar, J. Dane, P. E. Keivanidis, I. Zadrazil, D. D. C. Bradley and J. Nelson, *Sol. Energy Mater. Sol. Cells*, 2012, **105**, 77–85.

103 K. T. Wong, T. C. Chao, L. C. Chi, Y. Y. Chu, A. Balaiah, S. F. Chiu, Y. H. Liu and Y. Wang, *Org. Lett.*, 2006, **8**, 5033–5036.

104 S. H. Chan, C. P. Chen, T. C. Chao, C. Ting, C. S. Lin and B. T. Ko, *Macromolecules*, 2008, **41**, 5519–5526.

105 C. P. Chen, S. H. Chan, T. C. Chao, C. Ting and B. T. Ko, *J. Am. Chem. Soc.*, 2008, **130**, 12828–12833.

106 H. N. Tsao, D. Cho, J. W. Andreasen, A. Rouhanipour, D. W. Breiby, W. Pisula and K. Müllen, *Adv. Mater.*, 2009, **21**, 209–212.

107 L. Cai, T. Moehl, S. Moon, J. Decoppet, R. Humphry-baker, Z. Xue, L. Bin, S. M. Zakeeruddin and M. Gra, *Org. Lett.*, 2014, 1–41.

108 W. Zhang, J. Smith, S. E. Watkins, R. Gysel, M. McGehee, A. Salleo, J. Kirkpatrick, S. Ashraf, T. Anthopoulos, M. Heeney and I. McCulloch, *J. Am. Chem. Soc.*, 2010, **132**, 11437–11439.

109 H. Bronstein, D. S. Leem, R. Hamilton, P. Woebkenberg, S. King, W. Zhang, R. S. Ashraf, M. Heeney, T. D. Anthopoulos, J. De Mello and I. McCulloch, *Macromolecules*, 2011, **44**, 6649–6652.

110 W. Zhang, J. Smith, S. Watkins, R. Gysel, M. Mcgehee and A. Salleo, 2010, 11437–11439.

111 J. H. Chen, C. H. Tsai, S. A. Wang, Y. Y. Lin, T. W. Huang, S. F. Chiu, C. C. Wu and K. T. Wong, *J. Org. Chem.*, 2011, **76**, 8977–8985.

112 H. H. Chang, C. E. Tsai, Y. Y. Lai, D. Y. Chiou, S. L. Hsu, C. S. Hsu and Y. J. Cheng, *Macromolecules*, 2012, **45**, 9282–9291.

113 Y. Lin, J. Wang, Z. G. Zhang, H. Bai, Y. Li, D. Zhu and X. Zhan, *Adv. Mater.*, 2015, **27**, 1170–1174.

114 Y. Lin, Q. He, F. Zhao, L. Huo, J. Mai, X. Lu, C. J. Su, T. Li, J. Wang, J. Zhu, Y. Sun, C. Wang and X. Zhan, *J. Am. Chem. Soc.*, 2016, **138**, 2973–2976.

115 X. Liu, P. Cai, D. Chen, J. Chen, S. Su and Y. Cao, *Sci. China Chem.*, 2014, **57**, 973–981.

116 Y. Lin, J. Wang, S. Dai, Y. Li, D. Zhu and X. Zhan, *Adv. Energy Mater.*, 2014, **4**, 2–6.

117 W. Zhao, S. Li, H. Yao, S. Zhang, Y. Zhang, B. Yang and J. Hou, *J. Am. Chem. Soc.*, 2017, **139**, 7148–7151.

118 C. Yao, J. Zhao, Y. Zhu, B. Liu, C. Yan, D. F. Perepichka and H. Meng, *ACS Appl. Mater. Interfaces*, 2020, **12**, 11543–11550.

119 J. Qu, D. Li, H. Wang, J. Zhou, N. Zheng, H. Lai, T. Liu, Z. Xie and F. He, *Chem. Mater.*,

2019, **31**, 8044–8051.

120 X. Zhan, A. Facchetti, S. Barlow, T. J. Marks, M. A. Ratner, M. R. Wasielewski and S. R. Marder, *Adv. Mater.*, 2011, **23**, 268–284.

121 W. Zhang, Y. Han, X. Zhu, Z. Fei, Y. Feng, N. D. Treat, H. Faber, N. Stingelin, I. McCulloch, T. D. Anthopoulos and M. Heeney, *Adv. Mater.*, 2016, **28**, 3922–3927.

122 Z. Fei, F. D. Eisner, X. Jiao, M. Azzouzi, J. A. Röhr, Y. Han, M. Shahid, A. S. R. Chesman, C. D. Easton, C. R. McNeill, T. D. Anthopoulos, J. Nelson and M. Heeney, *Adv. Mater.*, 2018, **30**, 1–7.

123 K. Reichenbächer, H. I. Süss and J. Hulliger, *Chem. Soc. Rev.*, 2005, **34**, 22–30.

124 L. Zhu, W. Gao, F. Wu, L. Li and C. Yang, *J. Mater. Chem. A*, 2018, **6**, 18044–18049.

125 WO 2019011826, 2019.

126 R. Bruckner, P. Harmata, P. Wender and W. Zettlmeier, in *Organic Mechanisms: Reactions, Stereochemistry and Synthesis*, Springer Berlin Heidelberg, Berlin, 1st edn., 2010, pp. 795–800.

127 X. Wang, H. Luo, Y. Sun, M. Zhang, X. Li, G. Yu, Y. Liu, Y. Li and H. Wang, *J. Polym. Sci. Part A Polym. Chem.*, 2012, **50**, 371–377.

128 US Department of Health and Human Services, *Natl. Toxicol. Program Tech. Rep. Ser.*, 1992, **409**, 1–171.

129 WO 2015/154845, 2015.

130 A. Unsinn, C. J. Rohbogner and P. Knochel, *Adv. Synth. Catal.*, 2013, **355**, 1553–1560.

131 M. Schlosser, *Angew. Chemie - Int. Ed.*, 2005, **44**, 376–393.

132 A. Turck, *Tetrahedron*, 2001, **57**, 4489–4505.

133 T. Greene and P. Wuts, *Protective Groups in Organic Synthesis*, Wiley-Blackwell, 3rd edn., 1999.

134 N. S. Narasimhan, N. M. Sunder, R. Ammanamanchi and B. D. Bonde, *J. Am. Chem. Soc.*, 1990, **112**, 4431–4435.

135 T. Suzuki, M. Fujisawa, S. Takagi and T. Kimura, 2006, **85**, 545–550.

136 M. E. Hoque, M. M. M. Hassan and B. Chattopadhyay, *J. Am. Chem. Soc.*, 2021, **143**, 5022–5037.

137 V. Fargeas, F. Favresse, D. Mathieu, I. Beaudet, P. Charrue, B. Lebret, M. Piteau and J. P. Quintard, *European J. Org. Chem.*, 2003, 1711–1721.

138 S. Hitosugi, D. Tanimoto, W. Nakanishi and H. Isobe, *Chem. Lett.*, 2012, **41**, 972–973.

139 S. Holliday, R. S. Ashraf, A. Wadsworth, D. Baran, S. A. Yousaf, C. B. Nielsen, C.-H. Tan, S. D. Dimitrov, Z. Shang, N. Gasparini, M. Alamoudi, F. Laquai, C. J. Brabec, A. Salleo, J. R. Durrant and I. McCulloch, *Nat. Commun.*, 2016, **7**, 11585.

140 Y. Liu, M. Li, J. Yang, W. Xue, S. Feng, J. Song, Z. Tang, W. Ma and Z. Bo, *Adv. Energy Mater.*, 2019, **9**, 1–9.

141 Y. Li, W. K. Tatum, J. W. Onorato, S. D. Barajas, Y. Y. Yang and C. K. Luscombe, *Polym. Chem.*, 2017, **8**, 5185–5193.

142 H. Miyoshi, A. Nabe, S. Chatterjee and Y. Tobe, *J. Org. Chem.*, 2019, **84**, 3927–3939.

143 P. Espinet and A. M. Echavarren, *Angew. Chemie - Int. Ed.*, 2004, **43**, 4704–4734.

144 R. J. Abraham, J. J. Byrne, L. Griffiths and M. Perez, *Magn. Reson. Chem.*, 2006, **44**, 491–509.

145 B. D. Hosangadi and R. H. Dave, *Tetrahedron Lett.*, 1996, **37**, 6375–6378.

146 S. S. Reddy, V. G. Sree, K. Gunasekar, W. Cho, Y. S. Gal, M. Song, J. W. Kang and S. H. Jin, *Adv. Opt. Mater.*, 2016, **4**, 1236–1246.

147 Ł. Skórka, J. M. Mouesca, J. B. Gosk, R. Puźniak, J. Pécaut, V. Maurel and I. Kulszewicz-Bajer, *J. Mater. Chem. C*, 2017, **5**, 6563–6569.

148 P. Holý, P. Sehnal, M. Tichý, J. Závada and I. Císařová, *Tetrahedron Asymmetry*, 2004, **15**, 3805–3810.

149 T. Wang, Y. Chen, X. Bao, Z. Du, J. Guo, N. Wang, M. Sun and R. Yang, *Dye. Pigment.*, 2013, **98**, 11–16.

150 E. . Corey and Y.-J. Wu, *J. Am. Chem. Soc.*, 1993, 8871–8872.

151 P. Magnus, M. Giles, R. Bonnert, C. S. Kim, L. McQuire, A. Merritt and N. Vicker, *J. Am. Chem. Soc.*, 1992, 4403–4405.

152 B. W. D'Andrade, S. Datta, S. R. Forrest, P. Djurovich, E. Polikarpov and M. E. Thompson, *Org. Electron.*, 2005, **6**, 11–20.

153 Z. Fei, Y. Han, E. Gann, T. Hodsden, A. S. R. Chesman, C. R. McNeill, T. D. Anthopoulos and M. Heeney, *J. Am. Chem. Soc.*, 2017, **139**, 8552–8561.

154 C. Sun, B. Potter and J. P. Morken, *J. Am. Chem. Soc.*, 2014, **136**, 6534–6537.

155 J. A. Love, I. Nagao, Y. Huang, M. Kuik, V. Gupta, C. J. Takacs, J. E. Coughlin, L. Qi, T. S. Van Der Poll, E. J. Kramer, A. J. Heeger, T. Q. Nguyen and G. C. Bazan, *J. Am. Chem. Soc.*, 2014, **136**, 3597–3606.

156 M. Schnürch, M. Spina, A. F. Khan, M. D. Mihovilovic and P. Stanetty, *Chem. Soc. Rev.*, 2007, **36**, 1046–1057.

157 C. Hwang, W. Jo and S. H. Cho, *Chem. Commun.*, 2017, **53**, 7573–7576.

158 R. Martin and S. L. Buchwald, *Acc. Chem. Res.*, 2008, **41**, 1461–1473.

159 P. A. Byrne and D. G. Gilheany, *Chem. Soc. Rev.*, 2013, **42**, 6670–6696.

160 D. He, F. Zhao, L. Jiang and C. Wang, *J. Mater. Chem. A*, 2018, **6**, 8839–8854.

161 S. Li, L. Ye, W. Zhao, S. Zhang, S. Mukherjee, H. Ade and J. Hou, *Adv. Mater.*, 2016, **28**, 9423–9429.

162 H. Zhang, H. Yao, J. Hou, J. Zhu, J. Zhang, W. Li, R. Yu, B. Gao, S. Zhang and J. Hou, *Adv. Mater.*, 2018, **30**, 1–7.

163 Z. Li, K. Jiang, G. Yang, J. Y. L. Lai, T. Ma, J. Zhao, W. Ma and H. Yan, *Nat. Commun.*, 2016, **7**, 13094.

164 Y. Yang, Z. G. Zhang, H. Bin, S. Chen, L. Gao, L. Xue, C. Yang and Y. Li, *J. Am. Chem. Soc.*, 2016, **138**, 15011–15018.

165 Y. Lin, F. Zhao, Q. He, L. Huo, Y. Wu, T. C. Parker, W. Ma, Y. Sun, C. Wang, D. Zhu, A. J.

Heeger, S. R. Marder and X. Zhan, *J. Am. Chem. Soc.*, 2016, **138**, 4955–4961.

166 Z. Zhang, H. Wang, J. Yu, R. Sun, J. Xu, L. Yang, R. Geng, J. Cao, F. Du, J. Min, F. Liu and W. Tang, *Chem. Mater.*, 2020, **32**, 1297–1307.

167 L. T. Ming, H. O. Joon, A. D. Reichardt and Z. Bao, *J. Am. Chem. Soc.*, 2009, **131**, 3733–3740.

168 Q. Zhao, J. Qu and F. He, *Adv. Sci.*, 2020, **7**, 1–25.

169 N. Elgrishi, K. J. Rountree, B. D. McCarthy, E. S. Rountree, T. T. Eisenhart and J. L. Dempsey, *J. Chem. Educ.*, 2018, **95**, 197–206.

170 Q. Fan, Q. Zhu, Z. Xu, W. Su, J. Chen, J. Wu, X. Guo, W. Ma, M. Zhang and Y. Li, *Nano Energy*, 2018, **48**, 413–420.

171 W. Zhao, D. Qian, S. Zhang, S. Li, O. Ingans, F. Gao and J. Hou, *Adv. Mater.*, 2016, 4734–4739.

172 W. Zhao, S. Li, S. Zhang, X. Liu and J. Hou, *Adv. Mater.*, 2016, 1–7.

173 R. Sorrentino, E. Kozma, S. Luzzati and R. Po, *Energy Environ. Sci.*, 2021, **14**, 180–223.

174 M. Y. Liu, C. H. Chang, K. H. Tsai, D. S. Wang, S. B. Lin, P. Y. Chen, Y. H. Lin, W. H. Lin and C. F. Lin, *Conf. Rec. IEEE Photovolt. Spec. Conf.*, 2009, 000150–000152.

175 L. Dou, J. You, Z. Hong, Z. Xu, G. Li, R. A. Street and Y. Yang, *Adv. Mater.*, 2013, **25**, 6642–6671.

176 D. Venkateshvaran, M. Nikolka, A. Sadhanala, V. Lemaur, M. Zelazny, M. Kepa, M. Hurhangee, A. J. Kronemeijer, V. Pecunia, I. Nasrallah, I. Romanov, K. Broch, I. McCulloch, D. Emin, Y. Olivier, J. Cornil, D. Beljonne and H. Sirringhaus, *Nature*, 2014, **515**, 384–388.

177 C. H. Kim, H. Hlaing, J. A. Hong, J. H. Kim, Y. Park, M. M. Payne, J. E. Anthony, Y. Bonnassieux, G. Horowitz and I. Kymissis, *Adv. Mater. Interfaces*, 2015, **2**, 1–9.

178 W. Li, L. Yang, J. Tumbleston, L. Yan, H. Ade and W. You, *Adv. Mater.*, 2014, 4456–5562.

179 J. P. Hong, A. Y. Park, S. Lee, J. Kang, N. Shin and D. Y. Yoon, *Appl. Phys. Lett.*, 2008, **92**, 2006–2009.

180 J. Yang, Z. Zhao, S. Wang, Y. Guo and Y. Liu, *Chem*, 2018, **4**, 2748–2785.

181 Z. F. Yao, J. Y. Wang and J. Pei, *Cryst. Growth Des.*, 2018, **18**, 7–15.

182 H. Bässler and A. Köhler, *Top. Curr. Chem.*, 2012, **312**, 1–65.

183 C. Liu, Y. Xu and Y. Y. Noh, *Mater. Today*, 2015, **18**, 79–96.

184 A. F. Paterson, Y. H. Lin, A. D. Mottram, Z. Fei, M. R. Niazi, A. R. Kirmani, A. Amassian, O. Solomeshch, N. Tessler, M. Heeney and T. D. Anthopoulos, *Adv. Electron. Mater.*, 2018, **4**, 1700464.

7 – Appendices

7.1 - Chapter 2

7.1.1 - CV traces

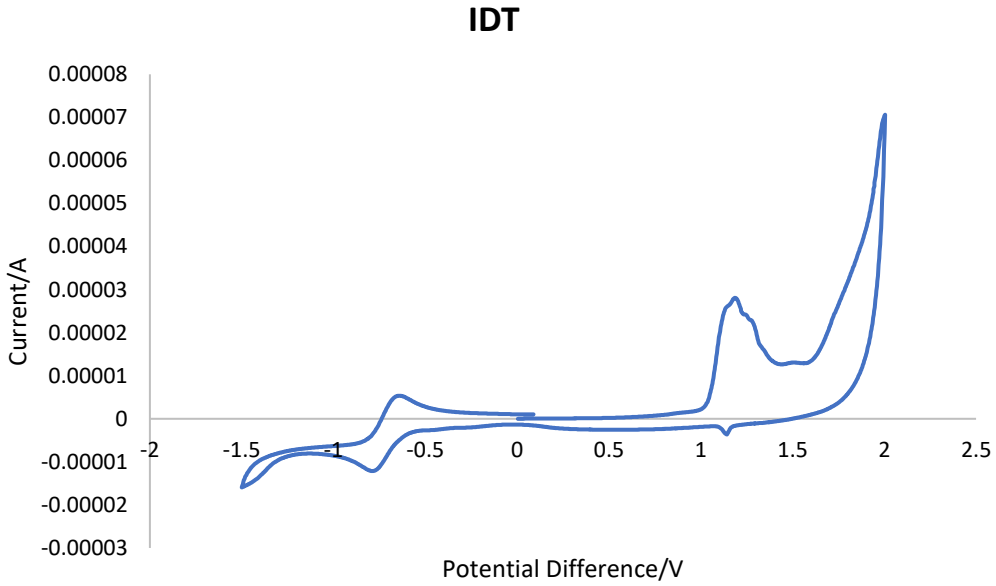


Figure 7.1.1: *CV trace of a drop-cast* ***IDT*** *film in a 0.1 M solution of* Bu_4NPF_6 *in acetonitrile.*

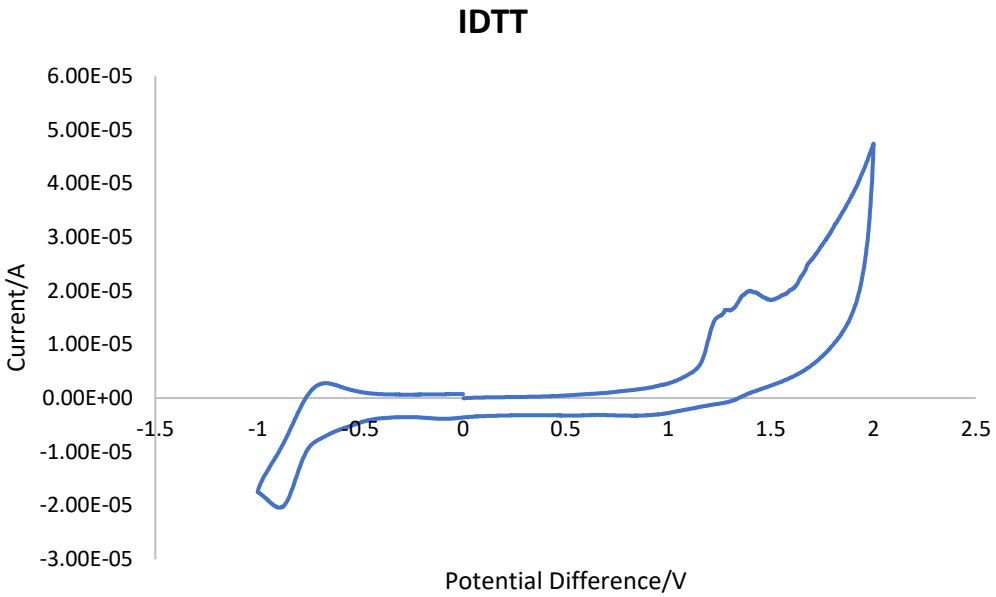


Figure 7.1.2: *CV trace of a drop-cast* ***IDTT*** *film in a 0.1 M solution of* Bu_4NPF_6 *in acetonitrile.*

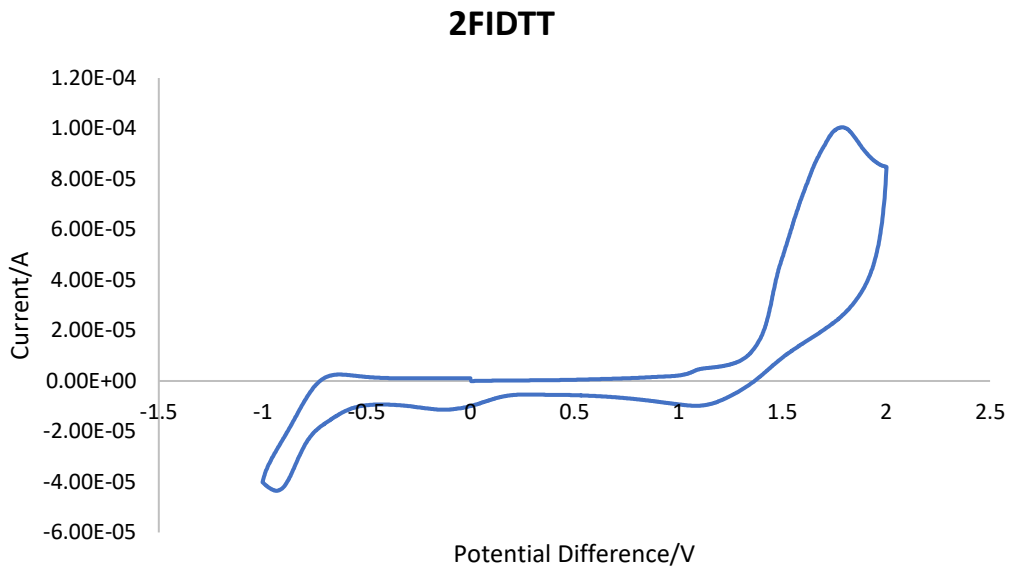


Figure 7.1.3: *CV trace of a drop-cast* ***2FIDTT*** *film in a 0.1 M solution of* Bu_4NPF_6 *in acetonitrile.*

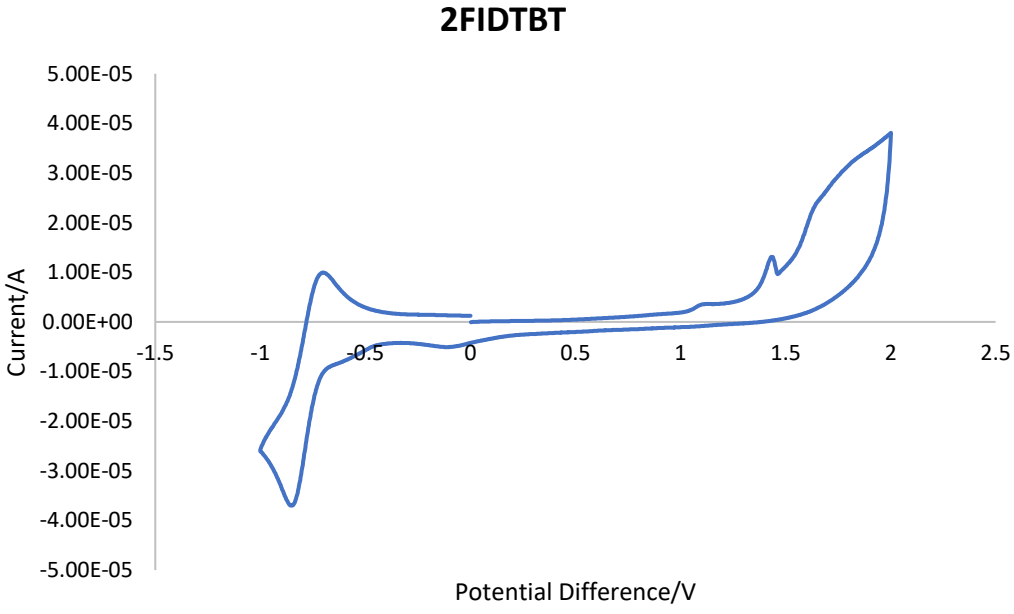


Figure 7.1.4: *CV trace of a drop-cast* ***2FIDTBT*** *film in a 0.1 M solution of* Bu_4NPF_6 *in acetonitrile.*

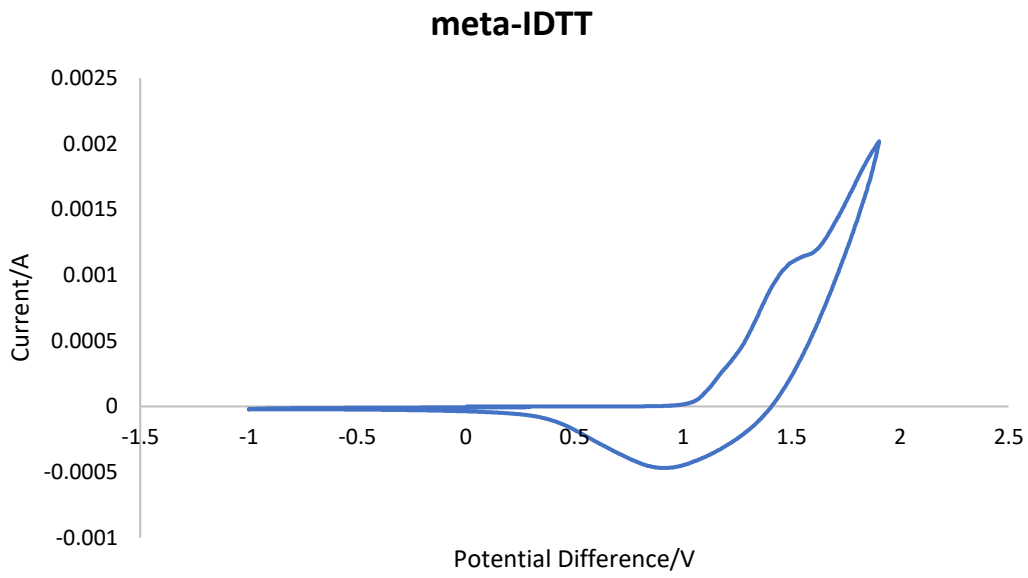


Figure 7.1.5: *CV trace of a drop-cast* ***meta-IDTT*** *film in a 0.1 M solution of* Bu_4NPF_6 *in acetonitrile.*

7.1.2 - NMR Spectra

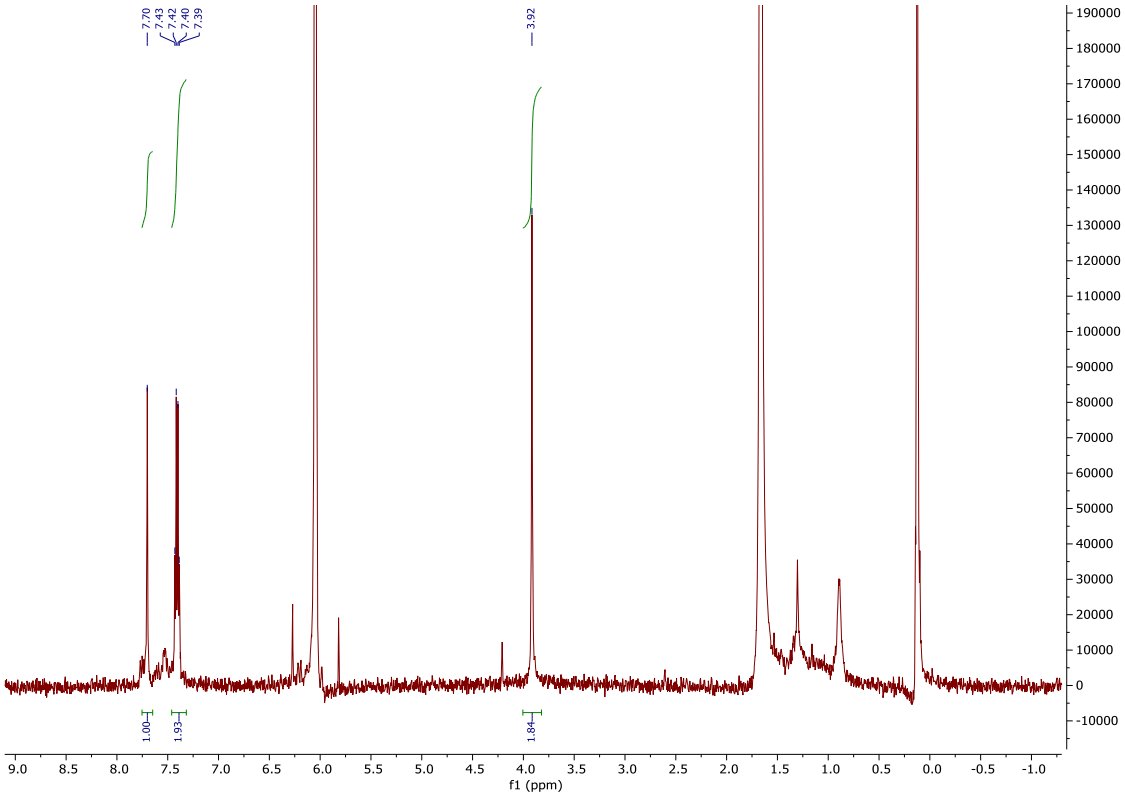


Figure 7.1.6: *^{1}H-NMR (TCE-d2) of* ***IDTT****.*

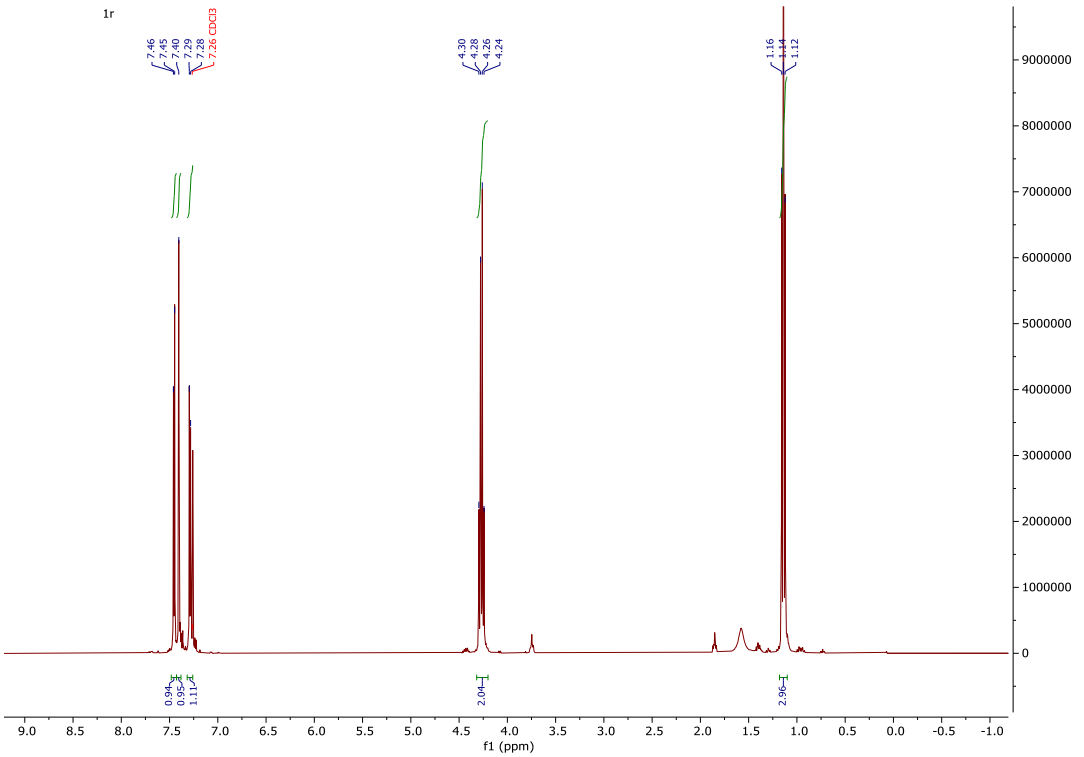


Figure 7.1.7: *^{1}H-NMR ($CDCl_3$) of Diethyl 2,5-difluoro-3,6-bis(thieno[3,2-b]thiophen-2-yl)terephthalate (**2.31**).*

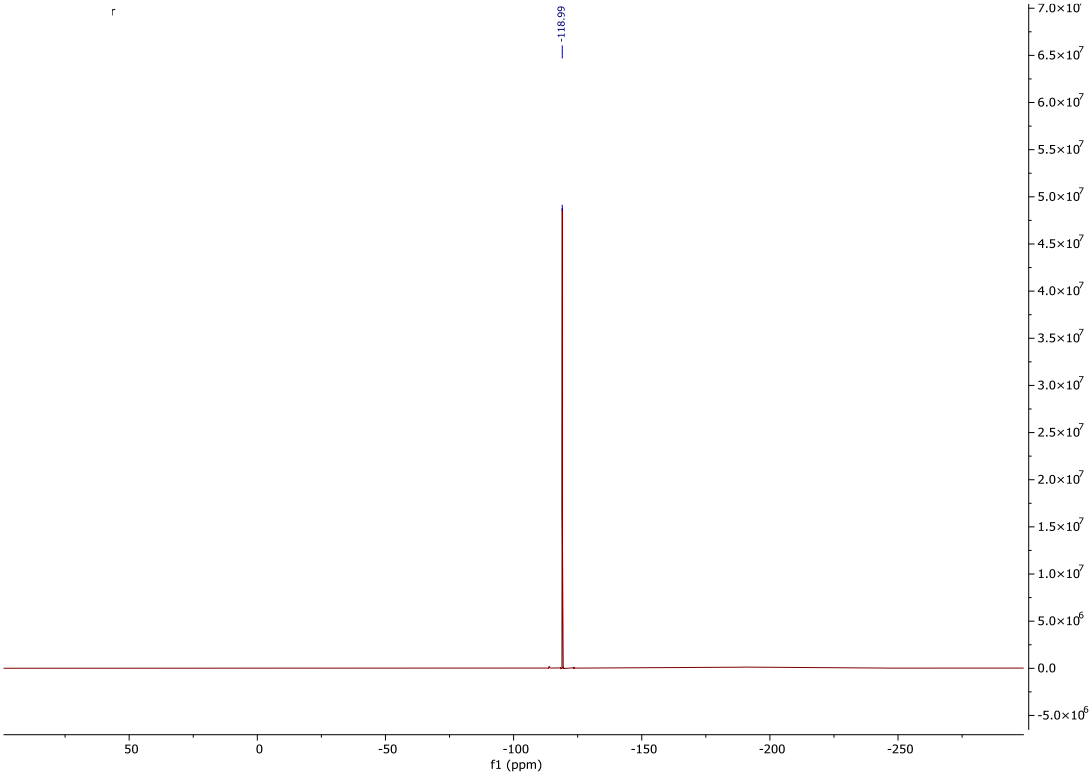


Figure 7.1.8: *^{19}F-NMR ($CDCl_3$) of Diethyl 2,5-difluoro-3,6-bis(thieno[3,2-b]thiophen-2-yl)terephthalate (**2.31**).*

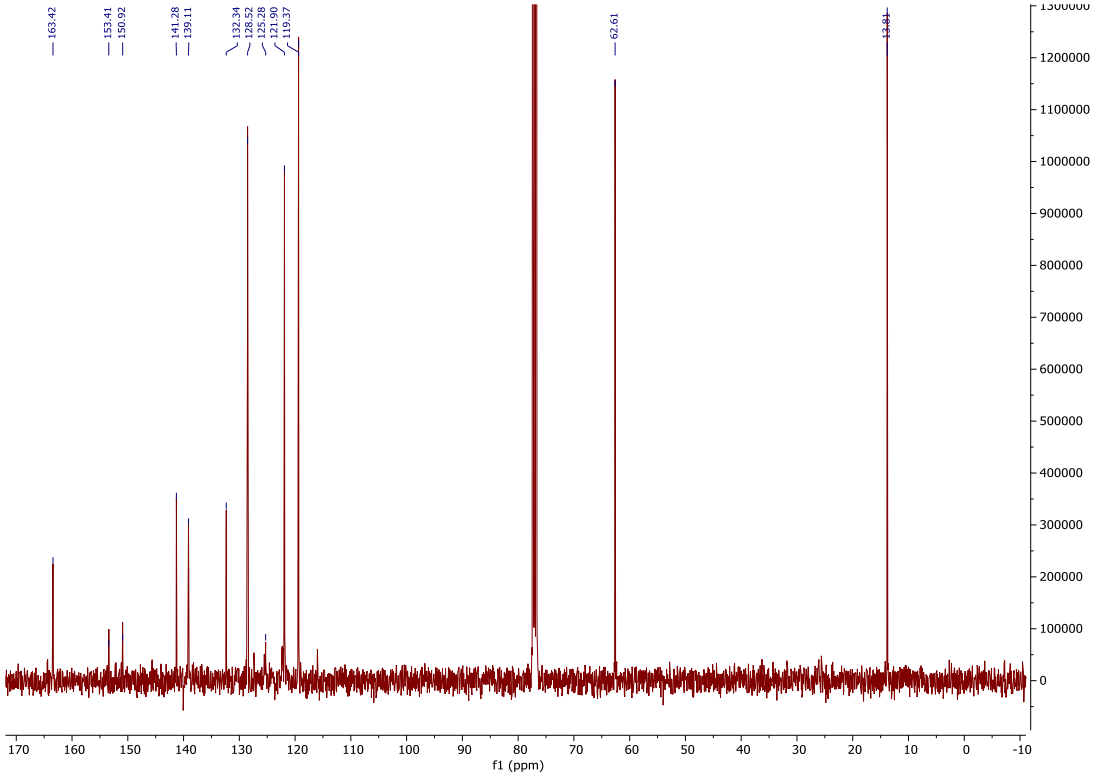


Figure 7.1.9: *^{13}C-NMR ($CDCl_3$) of Diethyl 2,5-difluoro-3,6-bis(thieno[3,2-b]thiophen-2-yl)terephthalate (**2.31**).*

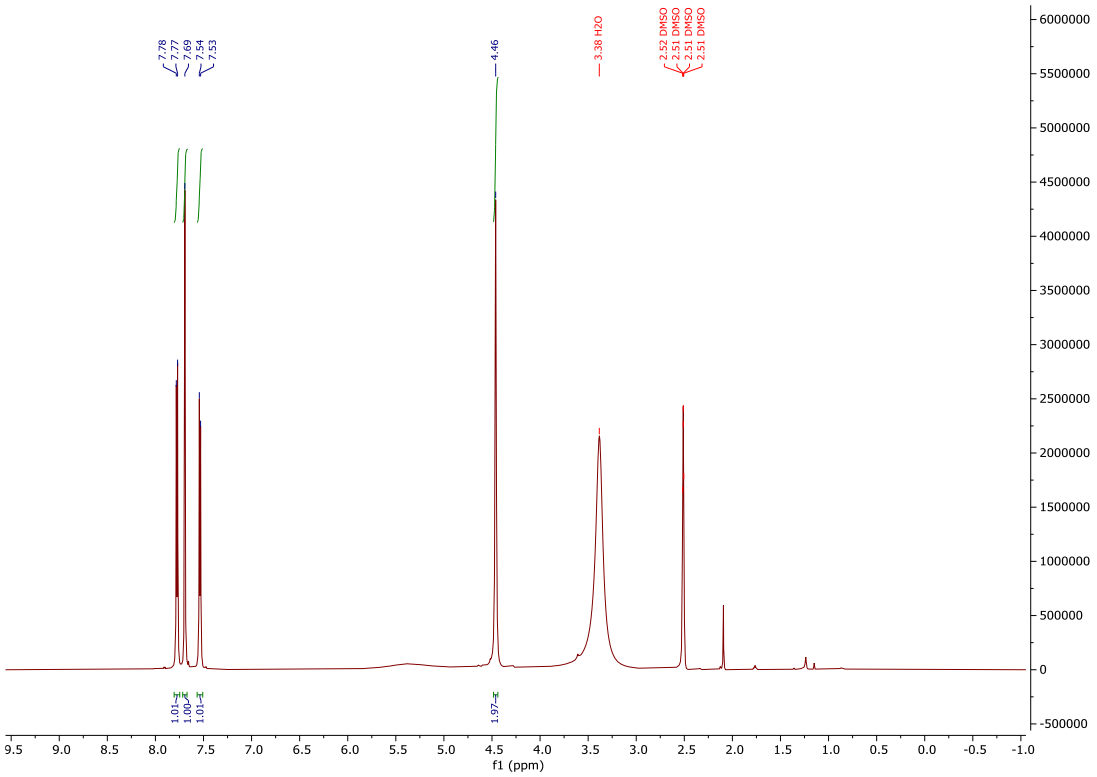


Figure 7.1.10: *^{1}H-NMR (DMSO-d_6) of (2,5-Difluoro-3,6-bis(thieno[3,2-b]thiophen-2-yl)-1,4-phenylene)dimethanol (**2.32**).*

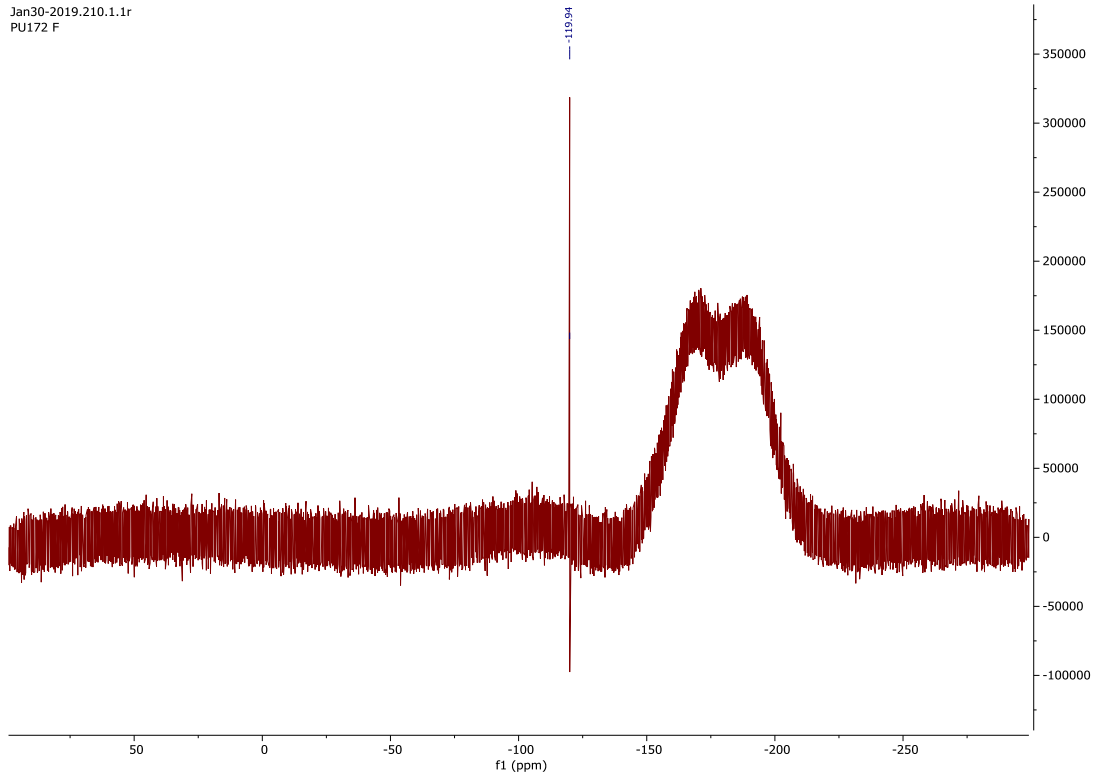


Figure 7.1.11: *^{19}F-NMR (DMSO-d_6) of (2,5-Difluoro-3,6-bis(thieno[3,2-b]thiophen-2-yl)-1,4-phenylene)dimethanol (**2.32**).*

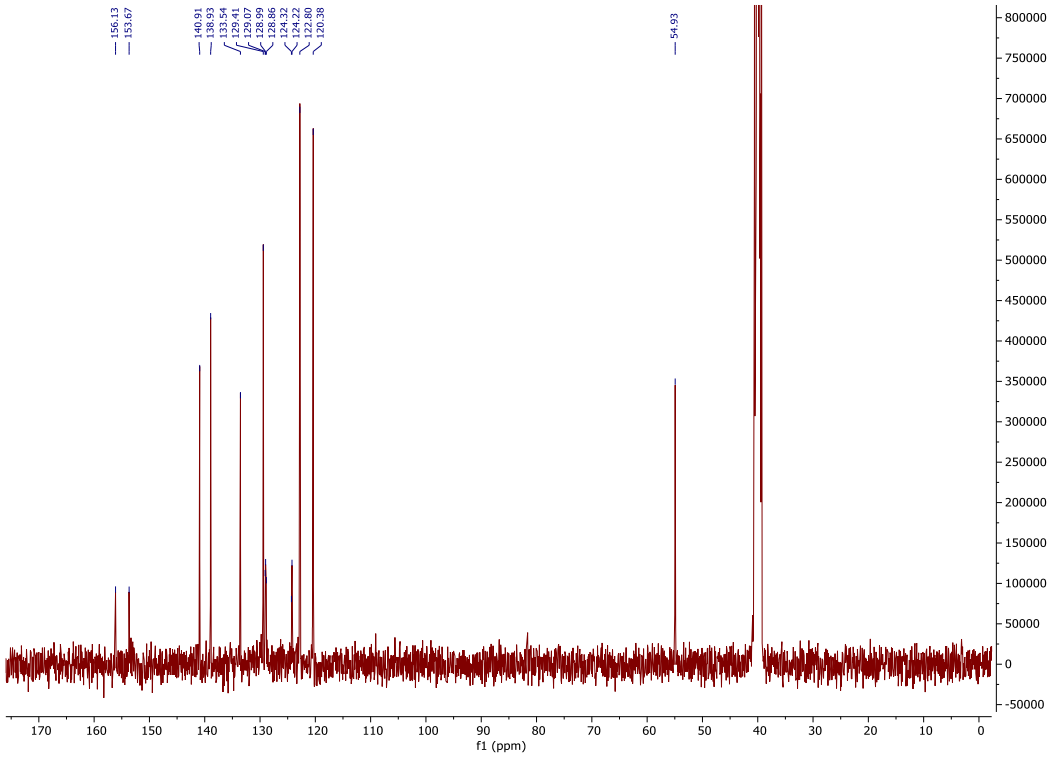


Figure 7.1.12: *^{13}C-NMR (DMSO-d_6) of (2,5-Difluoro-3,6-bis(thieno[3,2-b]thiophen-2-yl)-1,4-phenylene)dimethanol (**2.32**).*

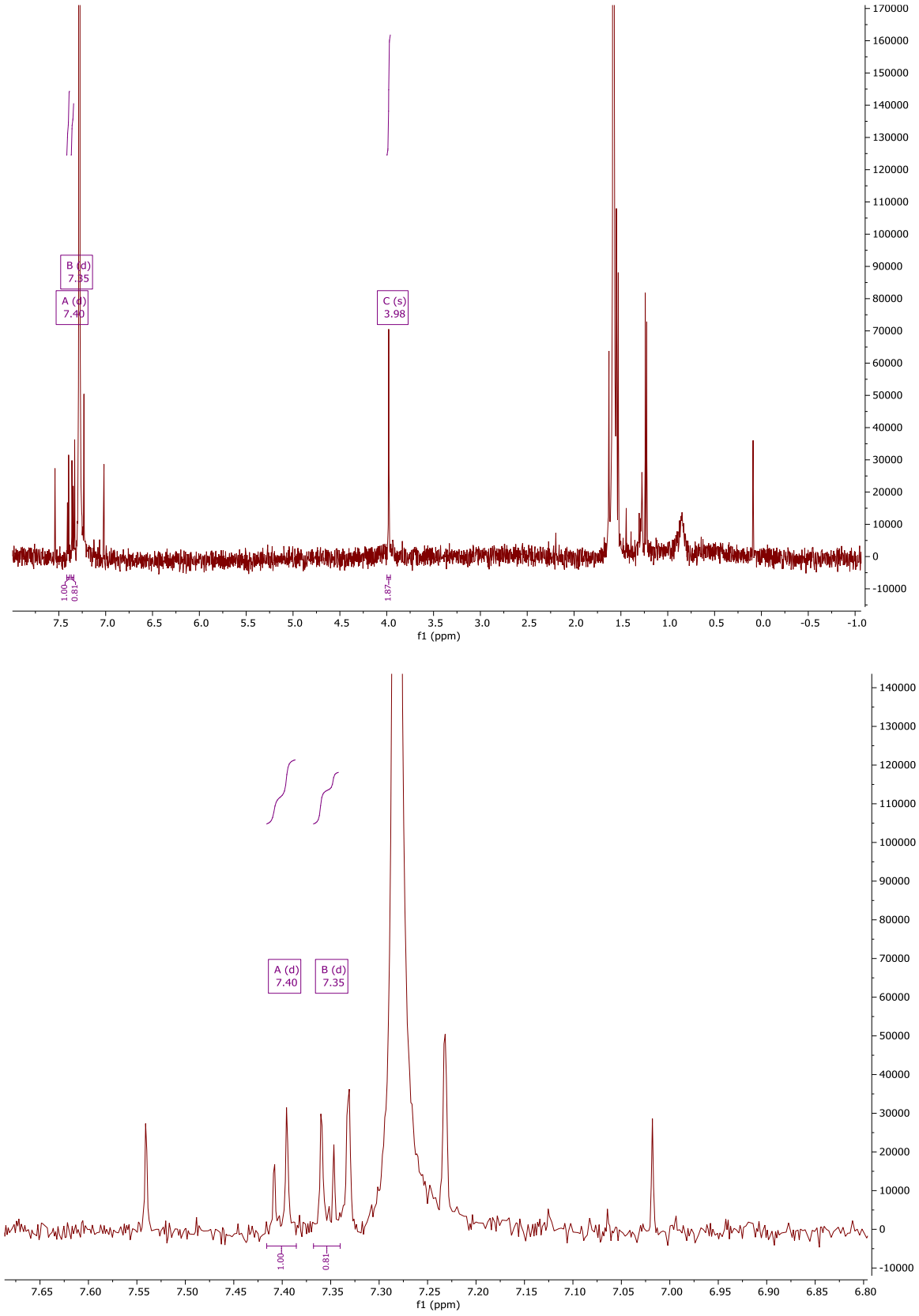


Figure 7.1.13: *^{1}H-NMR ($CDCl_3$) of* ***2FIDTT*** *at different levels of magnification.*

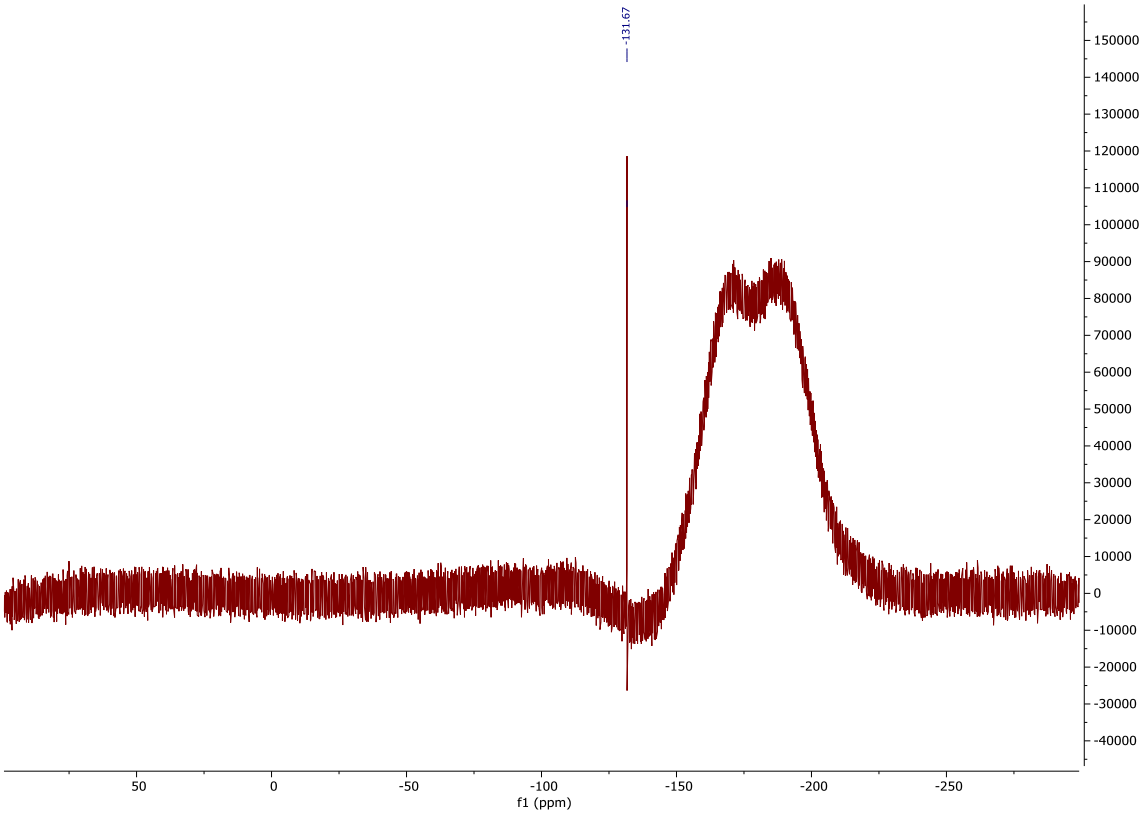


Figure 7.1.14: *^{19}F-NMR ($CDCl_3$) of* ***2FIDTT****.*

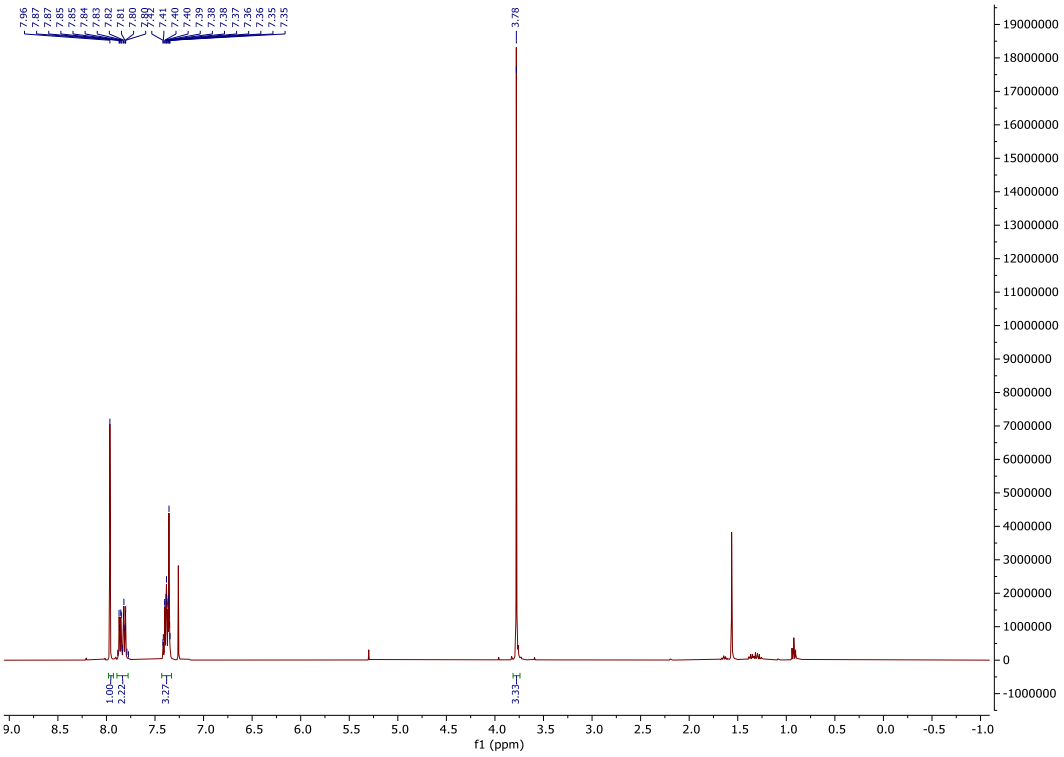


Figure 7.1.15: *^{1}H-NMR ($CDCl_3$) of Dimethyl 2,5-bis(benzo[b]thiophen-2-yl)terephthalate (****2.40****).*

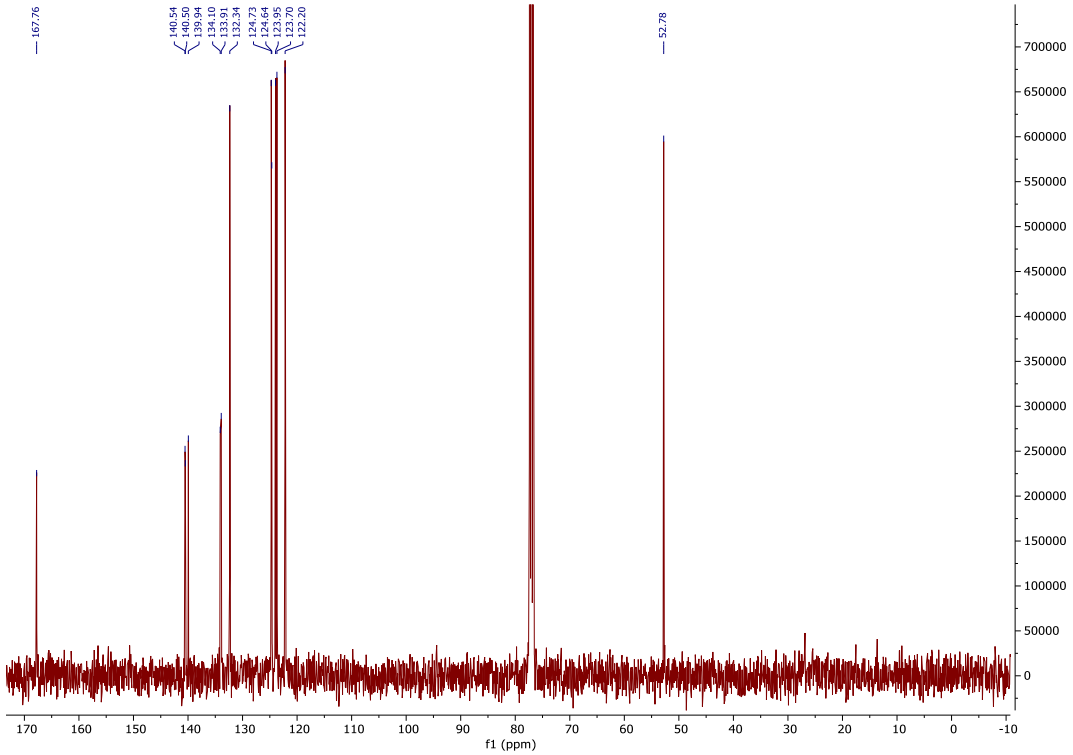


Figure 7.1.16: *^{13}C-NMR ($CDCl_3$) of Dimethyl 2,5-bis(benzo[b]thiophen-2-yl)terephthalate (**2.40**).*

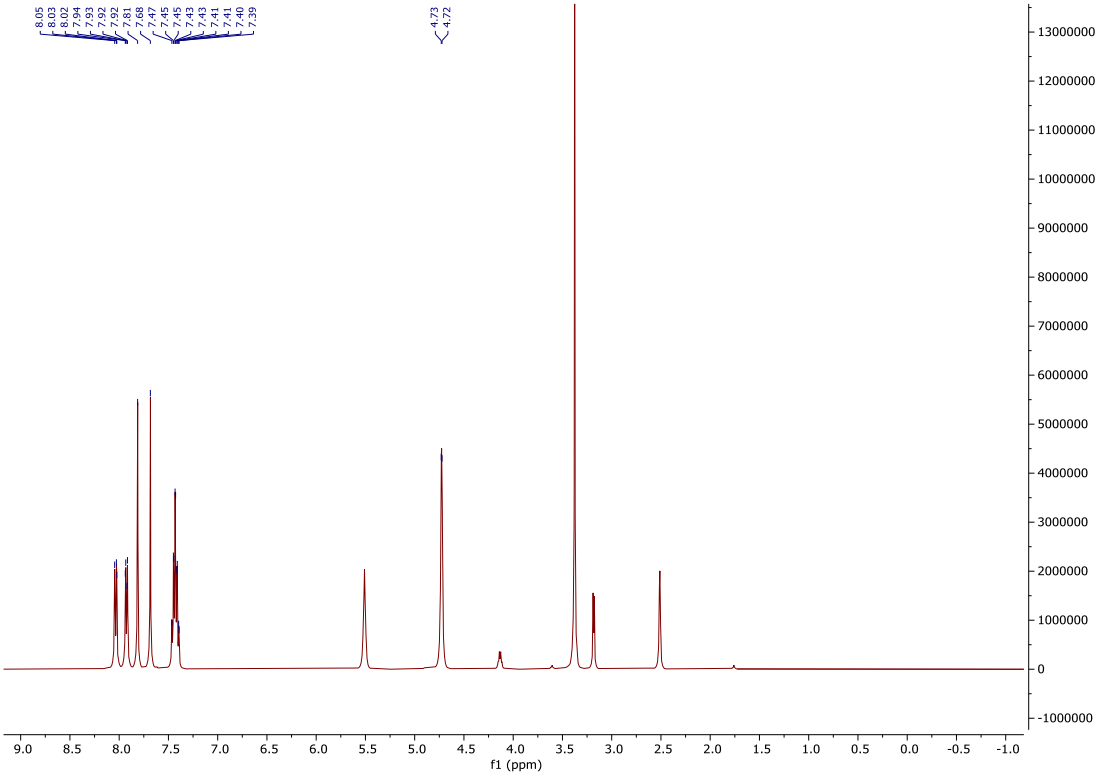


Figure 7.1.17: *^{1}H-NMR (DMSO-d6) of (2,5-bis(benzo[b]thiophen-2-yl)-1,4-phenylene)dimethanol (**2.43**).*

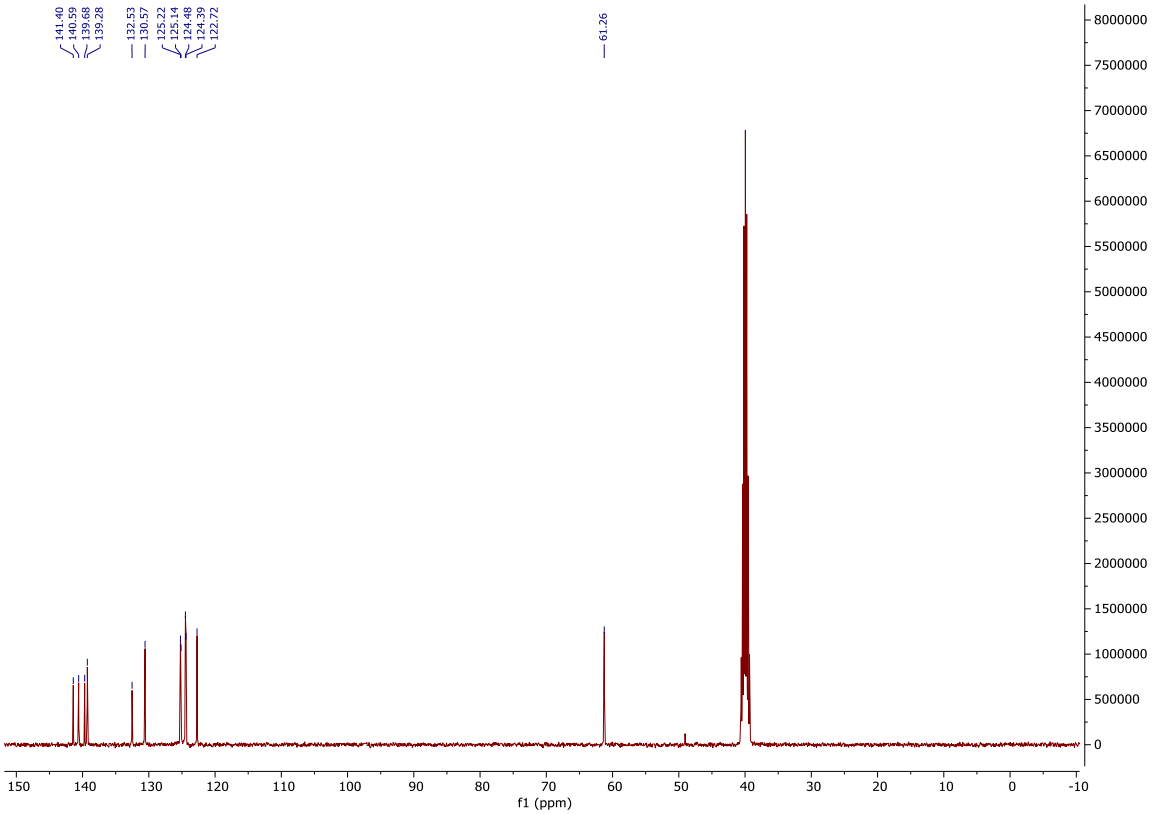


Figure 7.7.18: *^{13}C-NMR (DMSO-d6) of (2,5-bis(benzo[b]thiophen-2-yl)-1,4-phenylene)dimethanol (**2.43**).*

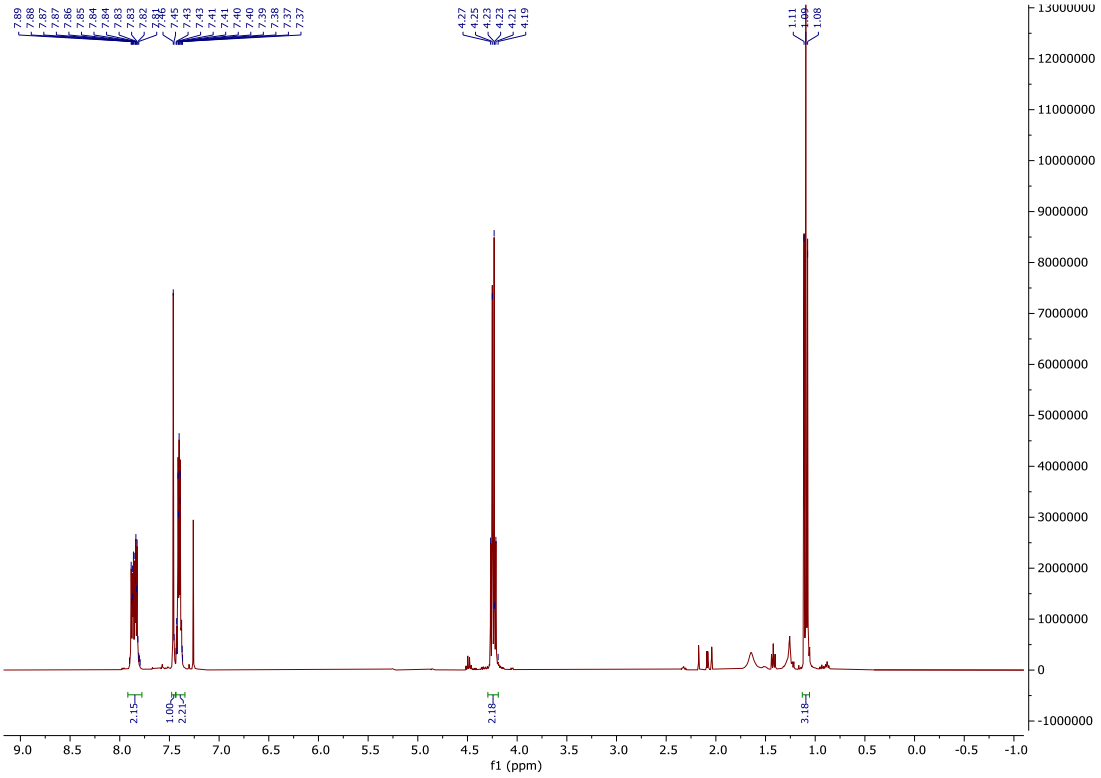


Figure 7.1.19: *^{1}H-NMR ($CDCl_3$) of diethyl 2,5-bis(benzo[b]thiophen-2-yl)-3,6-difluoroterephthalate (**2.44**).*

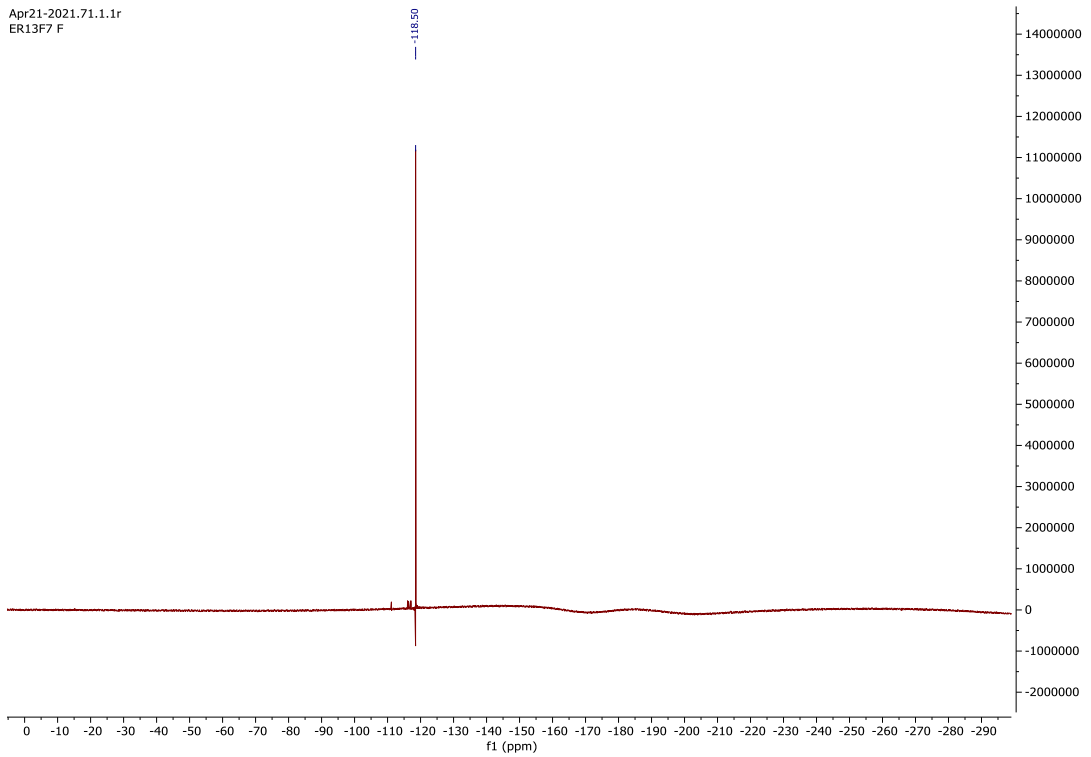


Figure 7.1.20: *^{19}F-NMR ($CDCl_3$) of diethyl 2,5-bis(benzo[b]thiophen-2-yl)-3,6-difluoroterephthalate (***2.44***).*

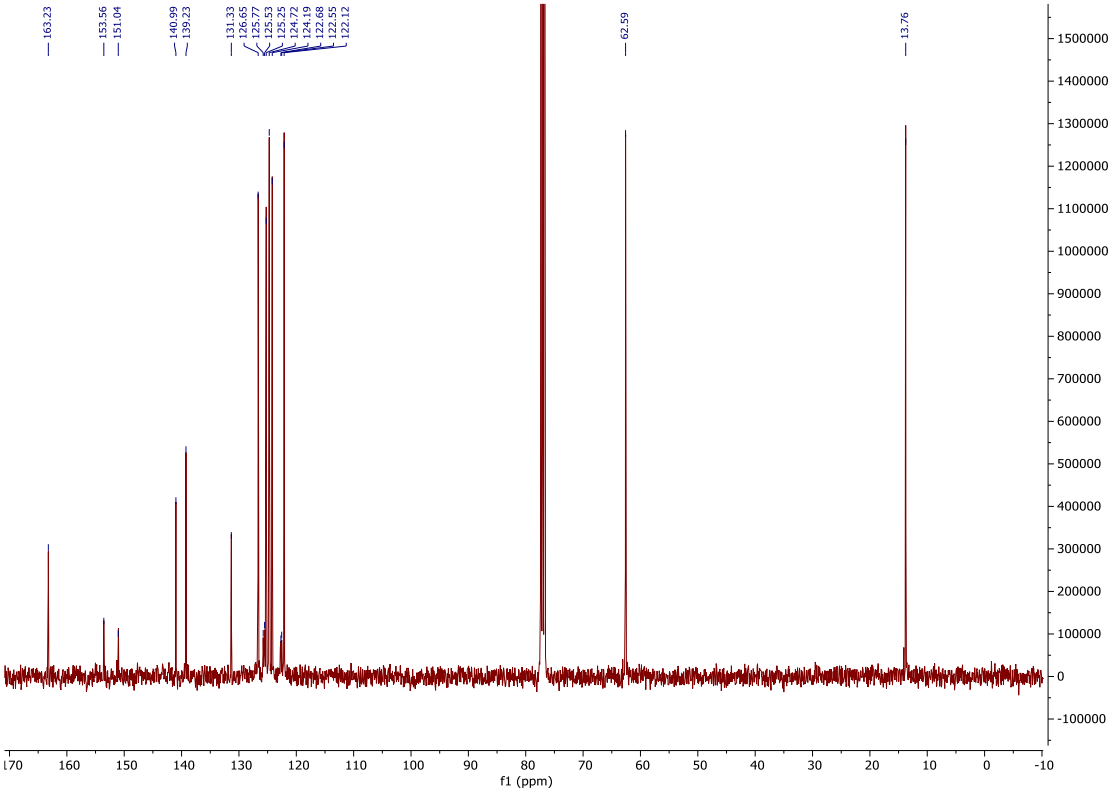


Figure 7.1.21: *^{13}C-NMR ($CDCl_3$) of diethyl 2,5-bis(benzo[b]thiophen-2-yl)-3,6-difluoroterephthalate (***2.44***).*

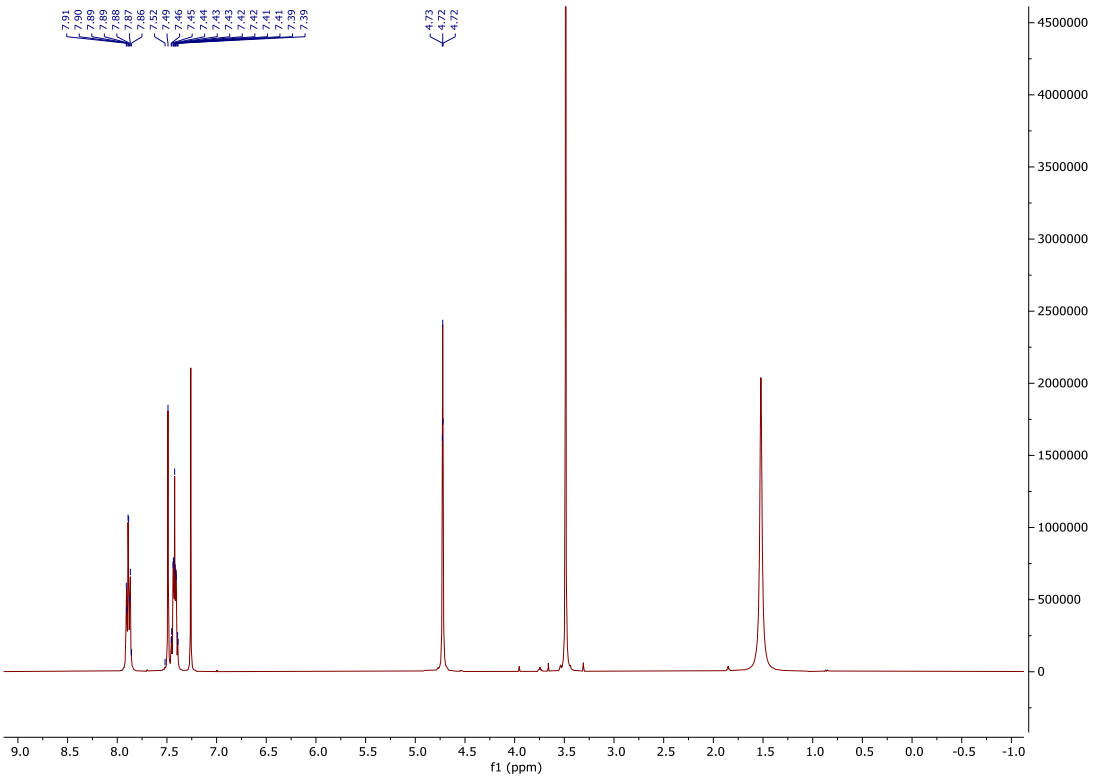


Figure 7.1.22: *^{1}H-NMR ($CDCl_3$) of (2,5-bis(benzo[b]thiophen-2-yl)-3,6-difluoro-1,4-phenylene)dimethanol (**2.45**).*

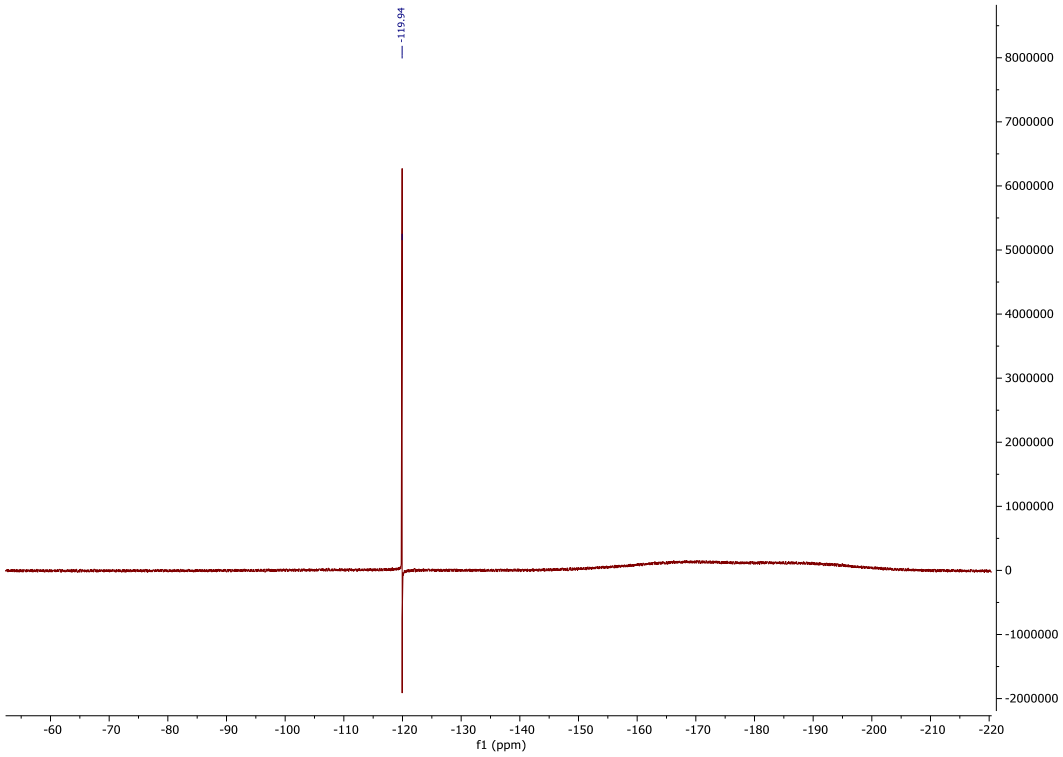


Figure 7.1.23: *^{19}F-NMR ($CDCl_3$) of (2,5-bis(benzo[b]thiophen-2-yl)-3,6-difluoro-1,4-phenylene)dimethanol (**2.45**).*

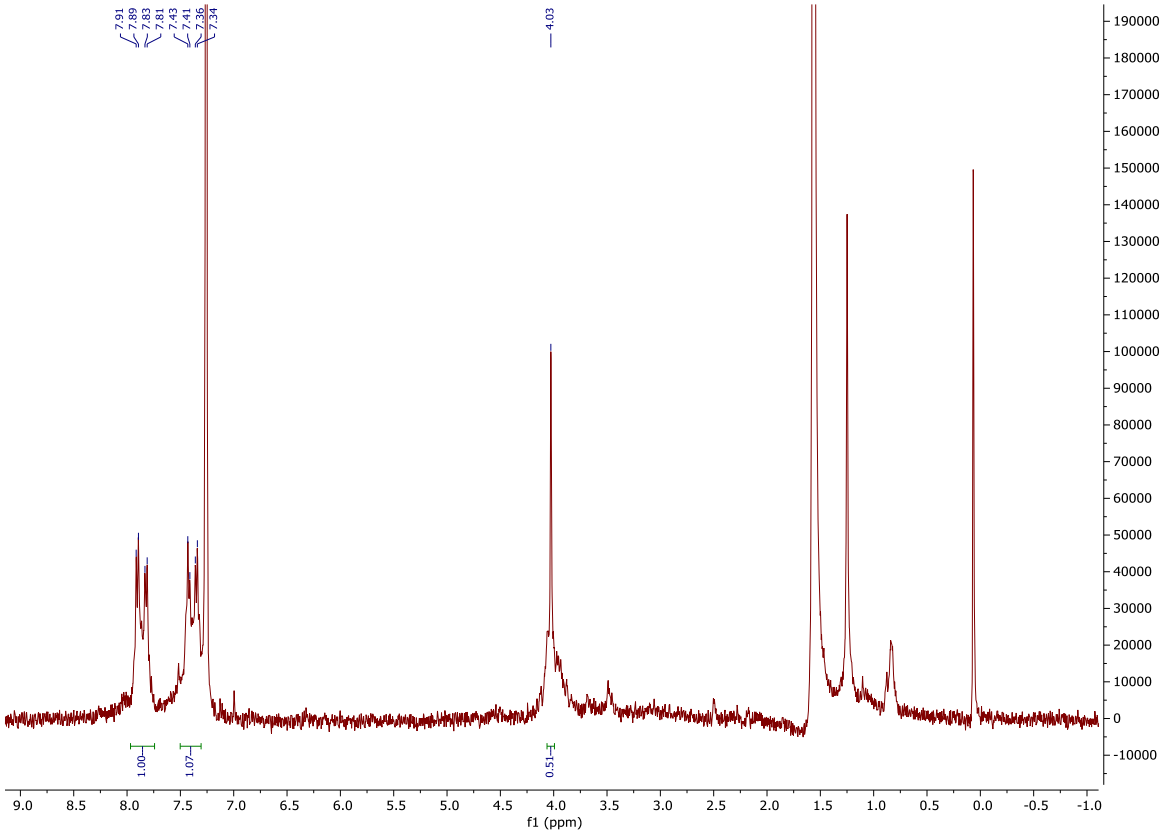


Figure 7.1.24: *^{1}H-NMR ($CDCl_3$) of* ***2FIDTBT*** *made by the neat method.*

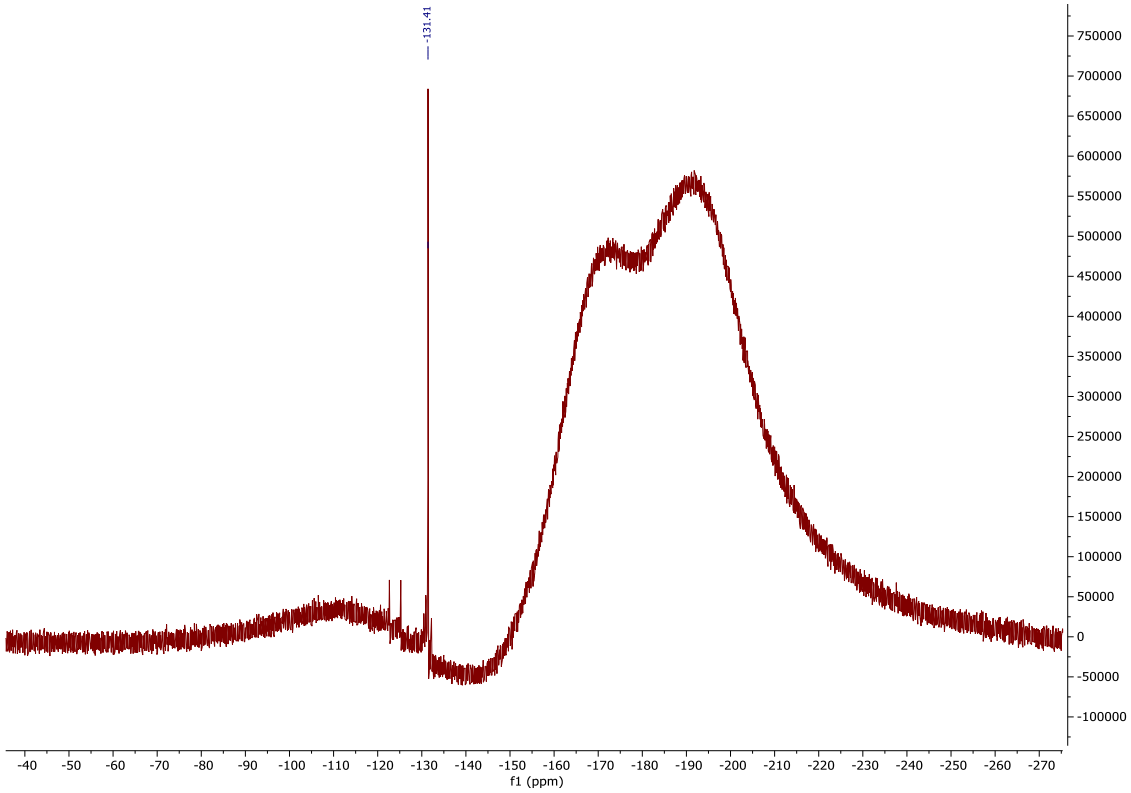


Figure 7.1.25: *^{19}F-NMR ($CDCl_3$) of* ***2FIDTBT*** *made by the neat method.*

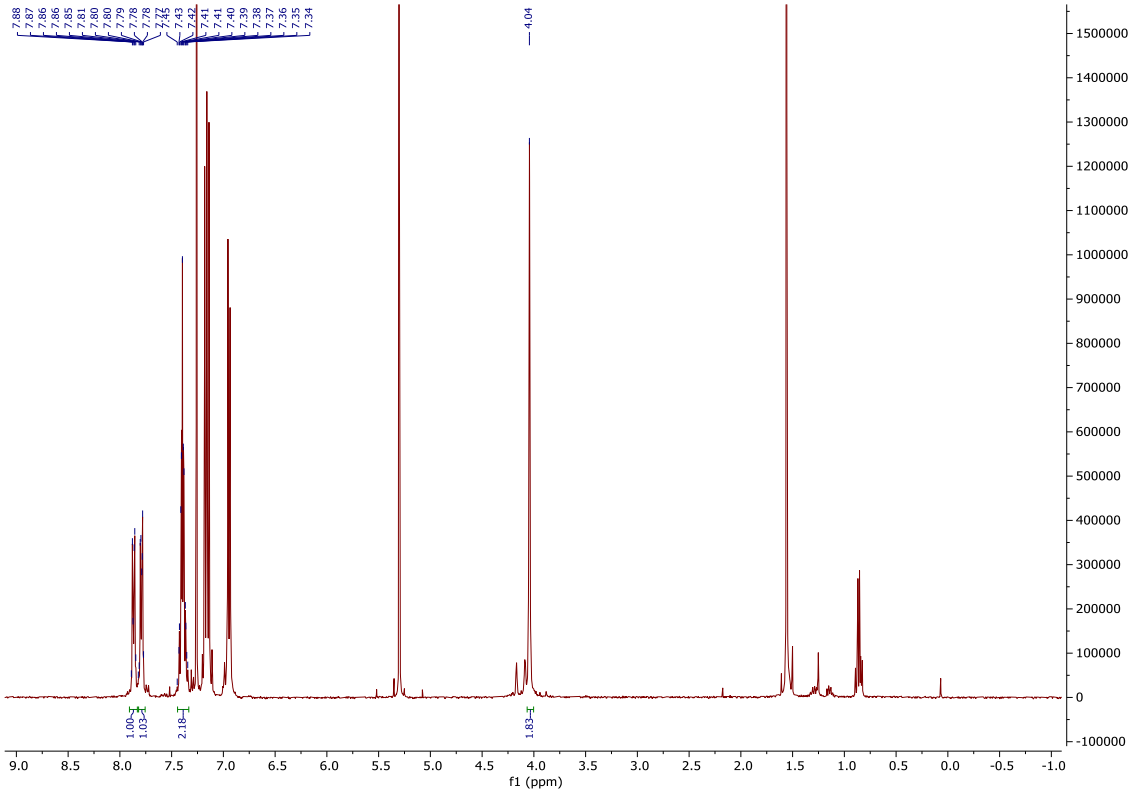


Figure 7.1.26: *^{1}H-NMR ($CDCl_3$) of **2FIDTBT** made by the solvated method.*

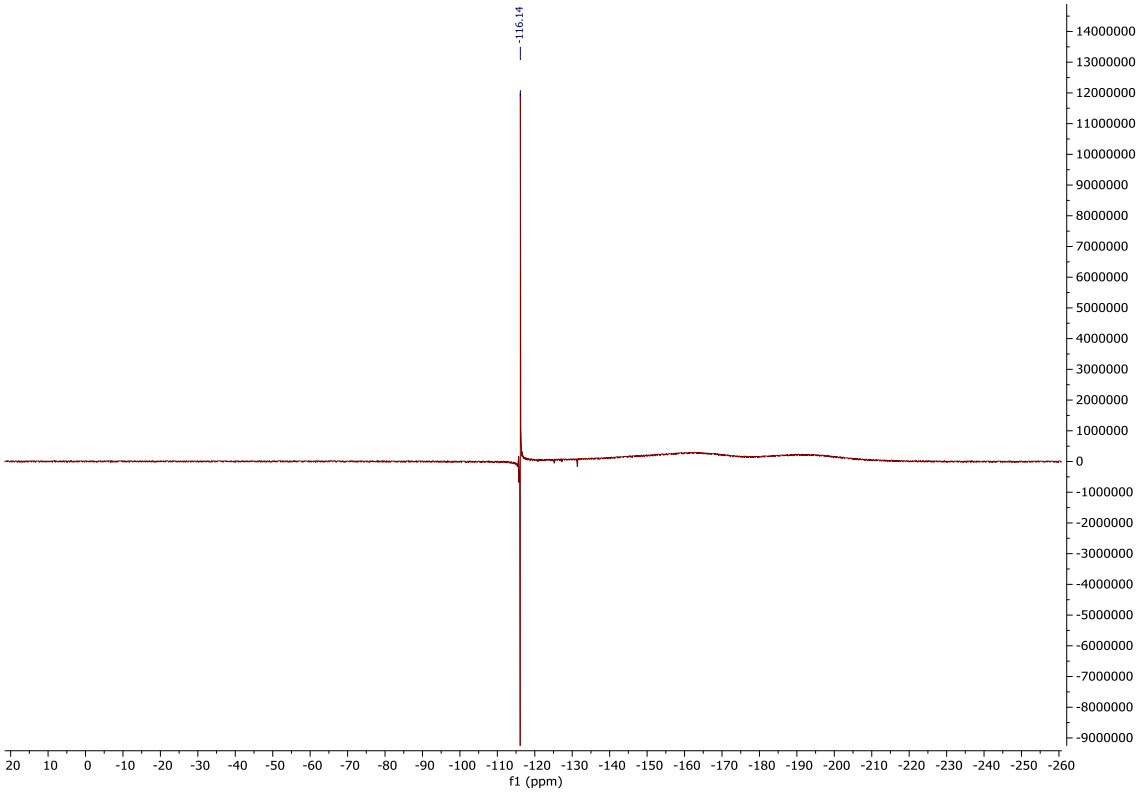


Figure 7.1.27: *^{19}F-NMR ($CDCl_3$) of **2FIDTBT** made by the solvated method.*

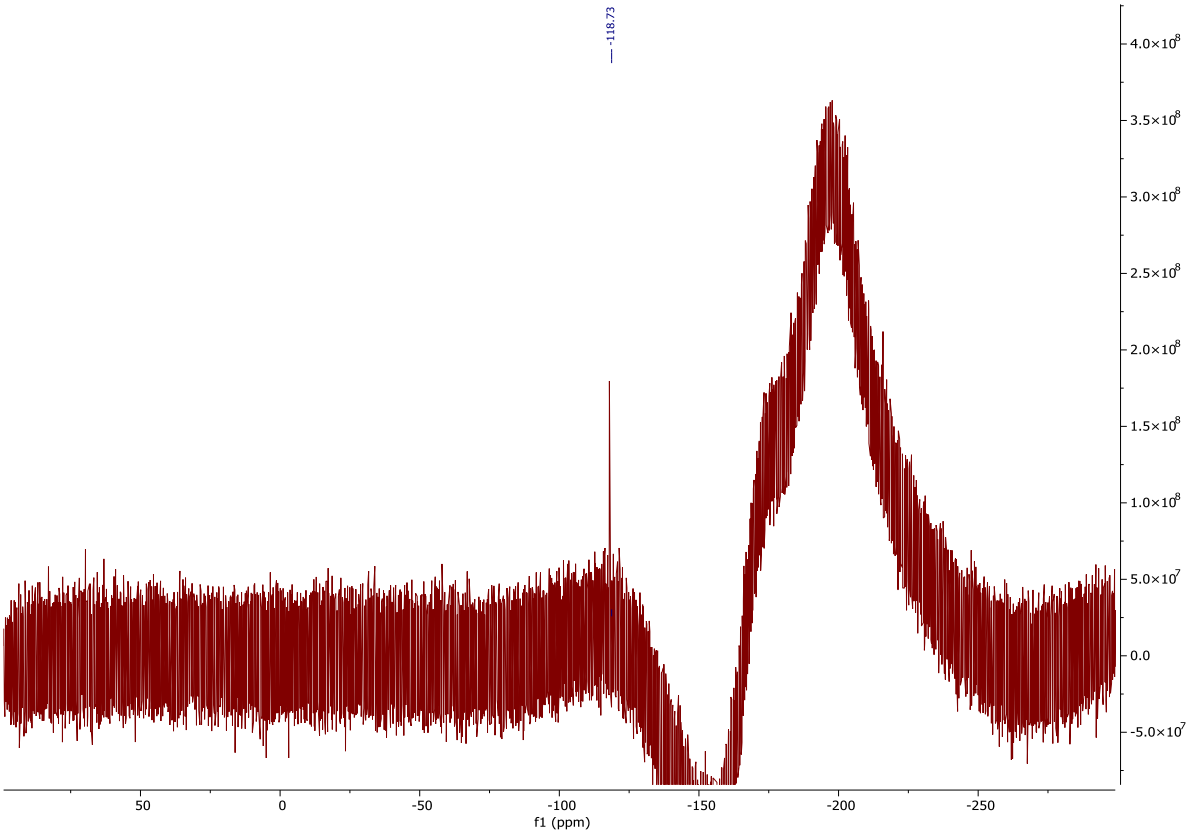


Figure 7.1.28: *^{19}F-NMR ($CDCl_3$) of* ***C8-2FIDTBT****.*

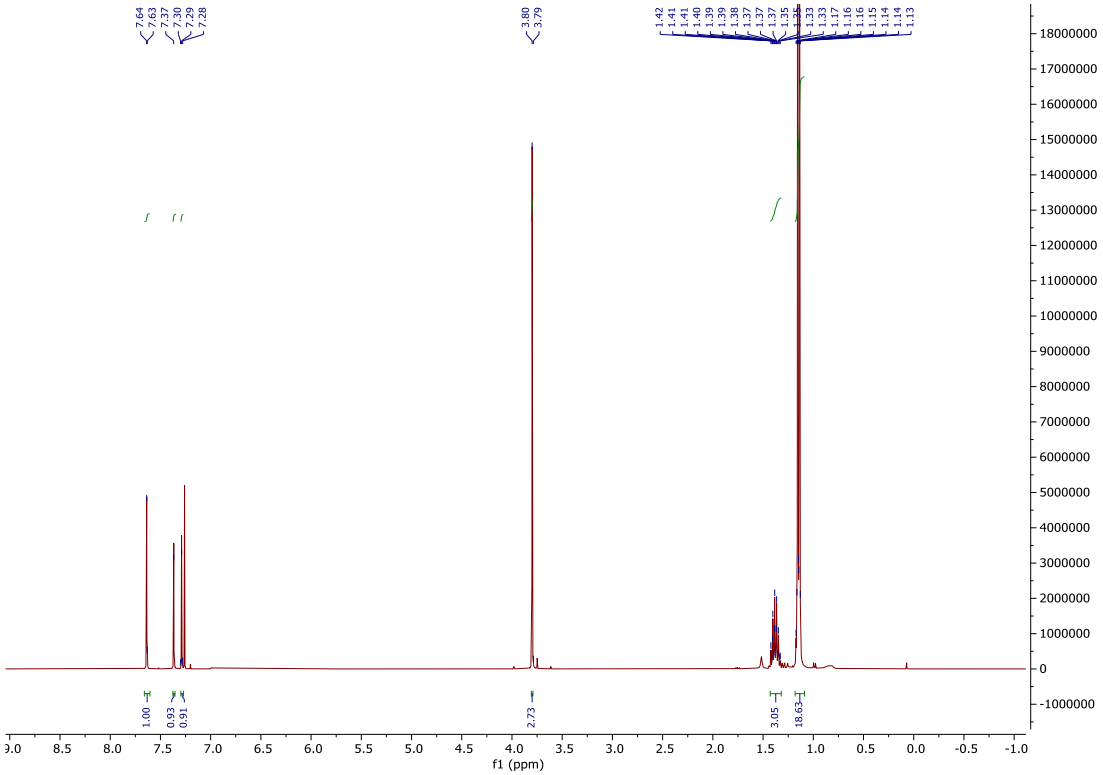


Figure 7.1.29: *^{1}H-NMR ($CDCl_3$) of dimethyl 3,6-bis(5-(triisopropylsilyl)thieno[3,2-b]thiophen-2-yl)phthalate (**2.54**).*

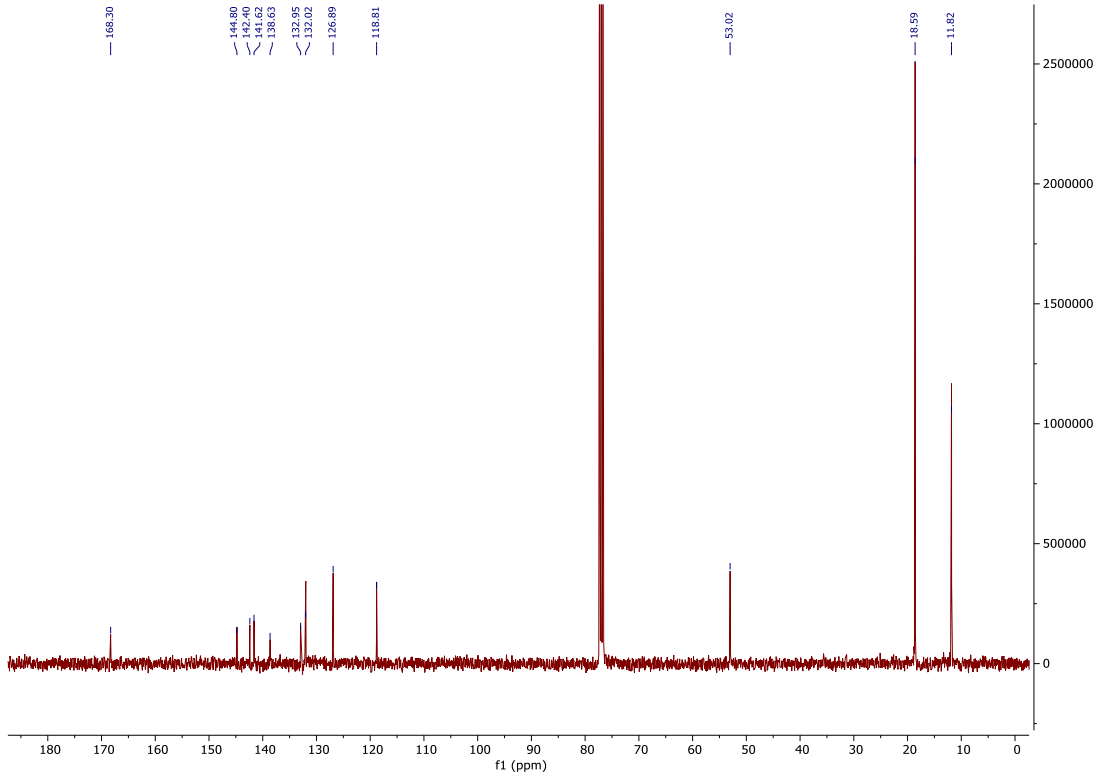


Figure 7.1.30: *^{13}C-NMR ($CDCl_3$) of dimethyl 3,6-bis(5-(triisopropylsilyl)thieno[3,2-b]thiophen-2-yl)phthalate (**2.54**).*

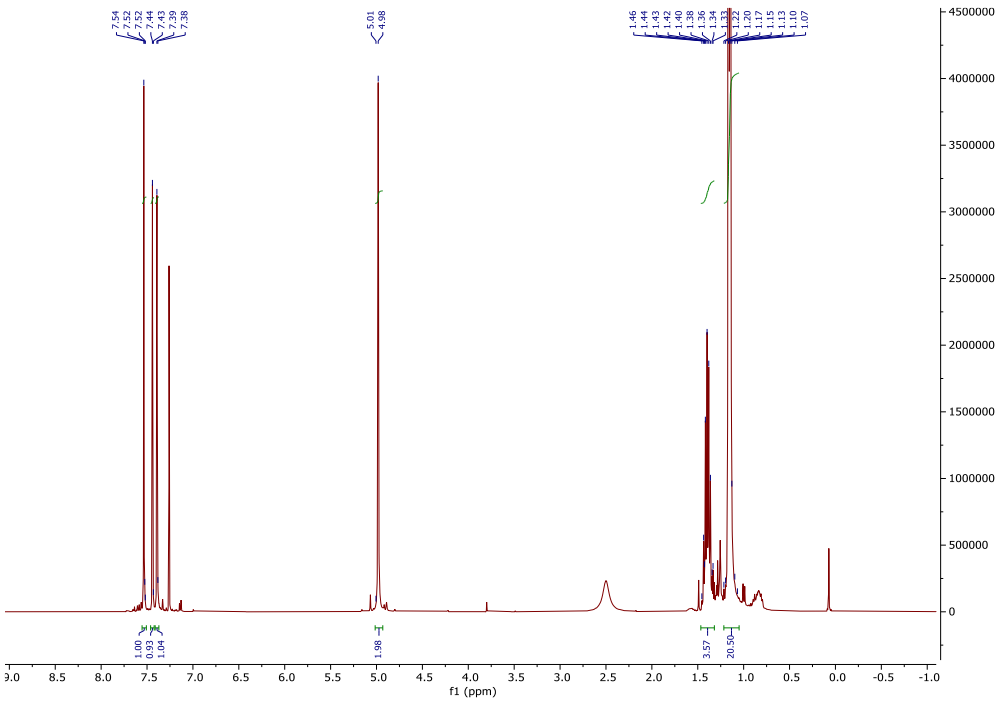


Figure 7.1.31: *^{1}H-NMR ($CDCl_3$) of (3,6-bis(5-(triisopropylsilyl)thieno[3,2-b]thiophen-2-yl)-1,2-phenylene)dimethanol (**2.55**).*

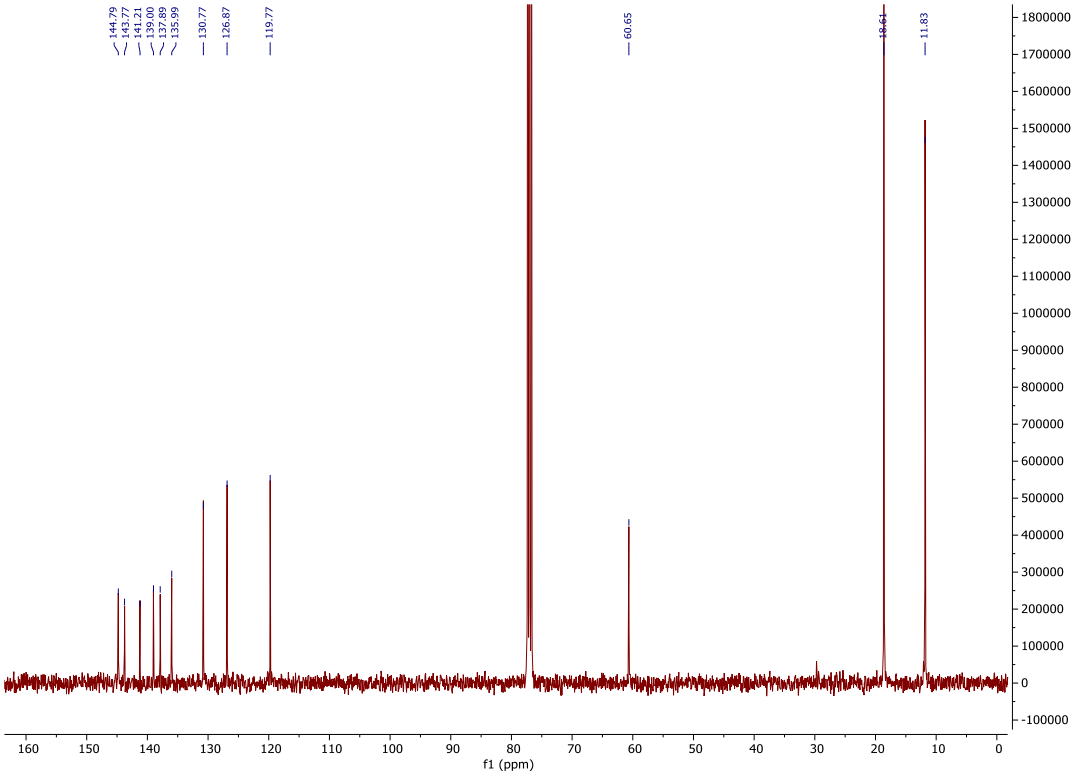


Figure 7.1.32: *^{13}C-NMR ($CDCl_3$) of (3,6-bis(5-(triisopropylsilyl)thieno[3,2-b]thiophen-2-yl)-1,2-phenylene)dimethanol (**2.55**).*

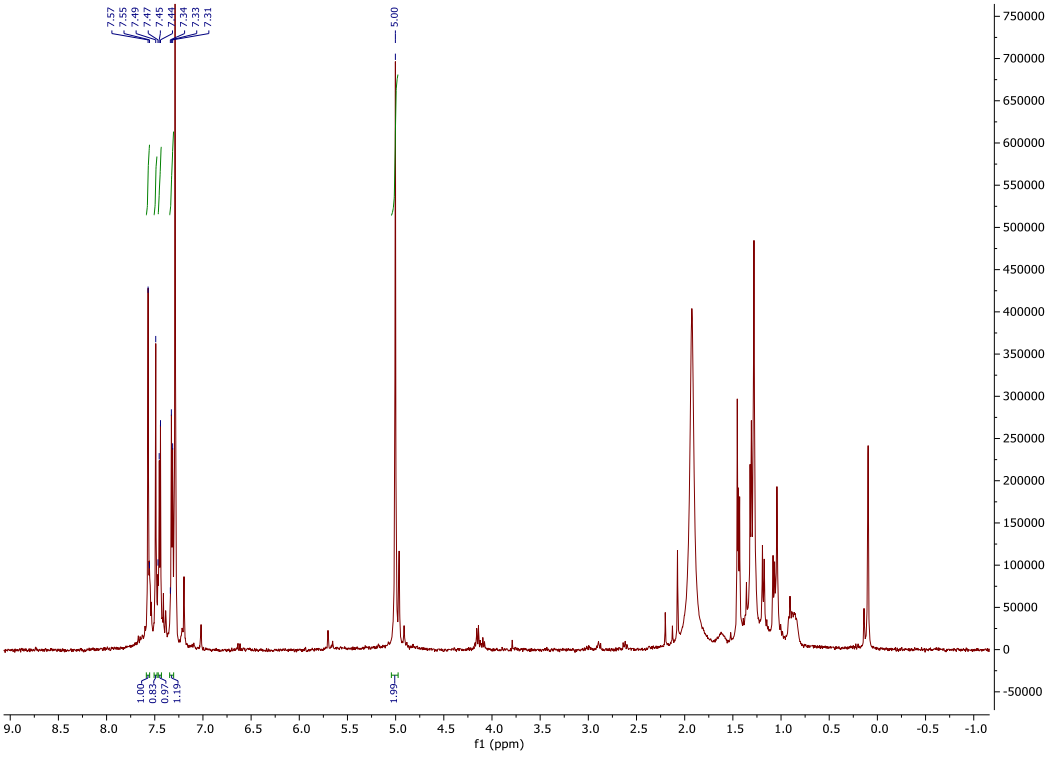


Figure 7.1.33: *^{1}H-NMR ($CDCl_3$) of (3,6-bis(thieno[3,2-b]thiophen-2-yl)-1,2-phenylene)dimethanol (**2.56**).*

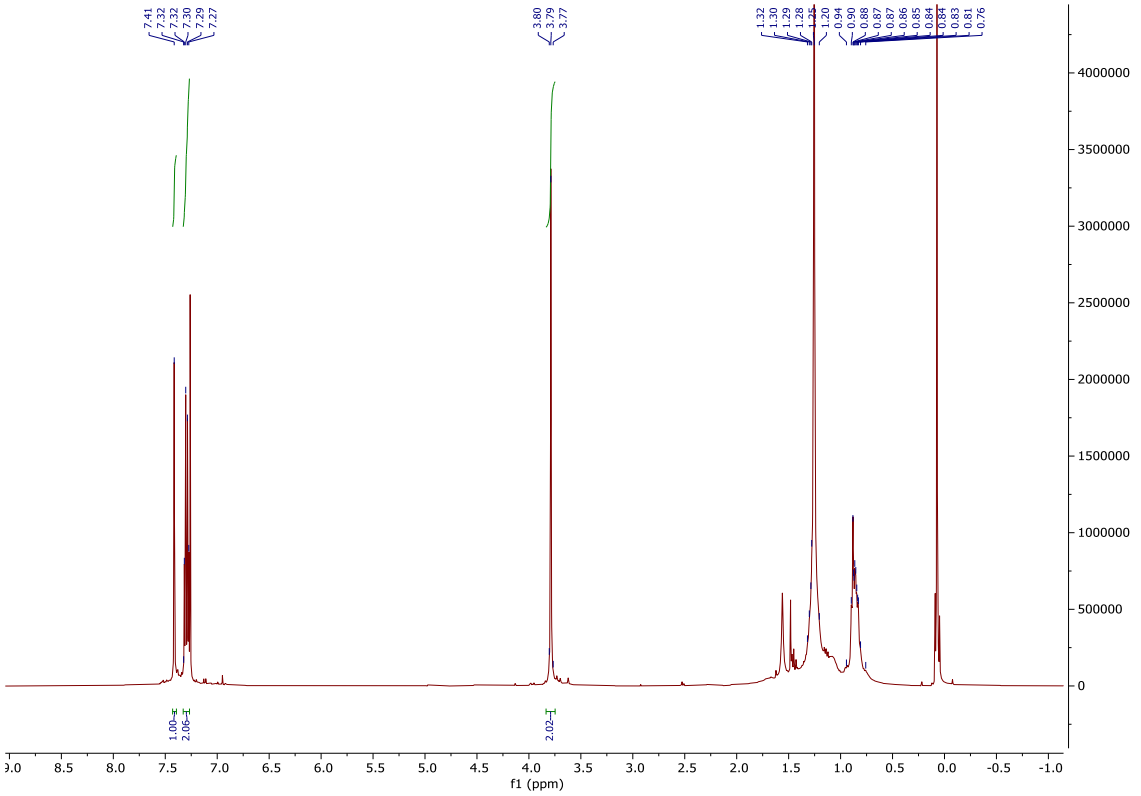


Figure 7.1.34: *^{1}H-NMR ($CDCl_3$) of* ***meta-IDTT****.*

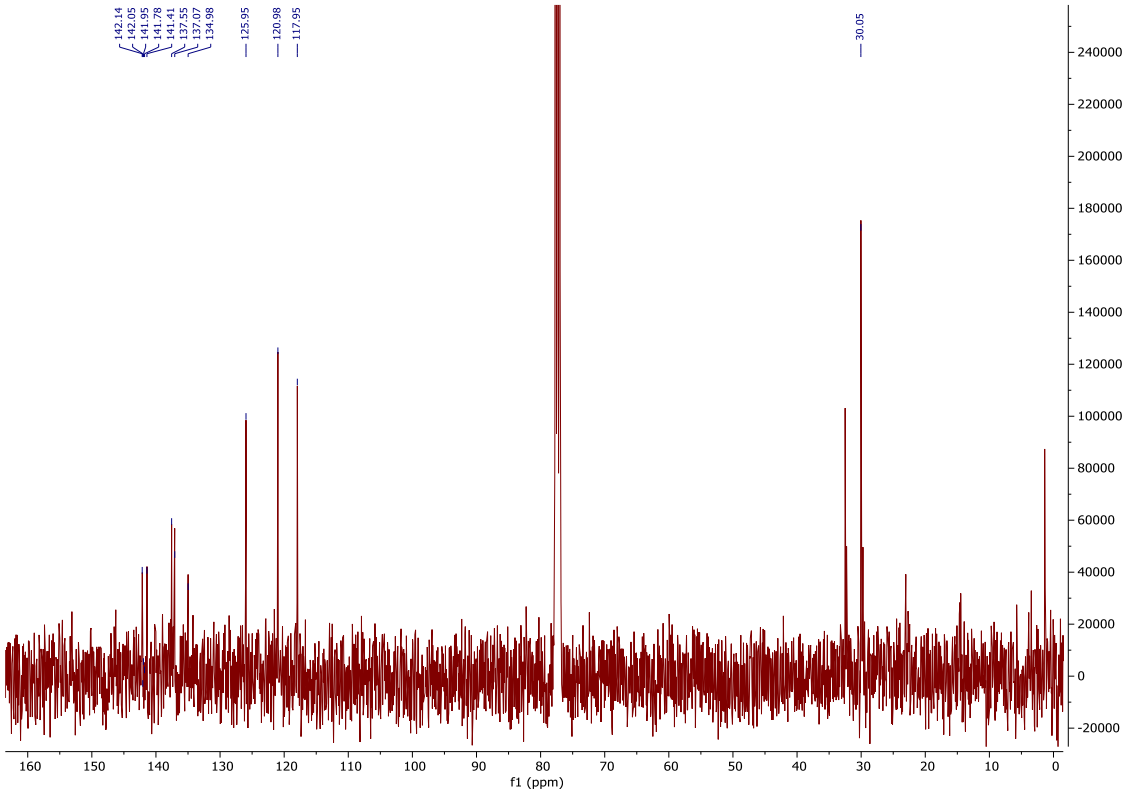


Figure 7.1.35: *^{13}C-NMR ($CDCl_3$) of* ***meta-IDTT****.*

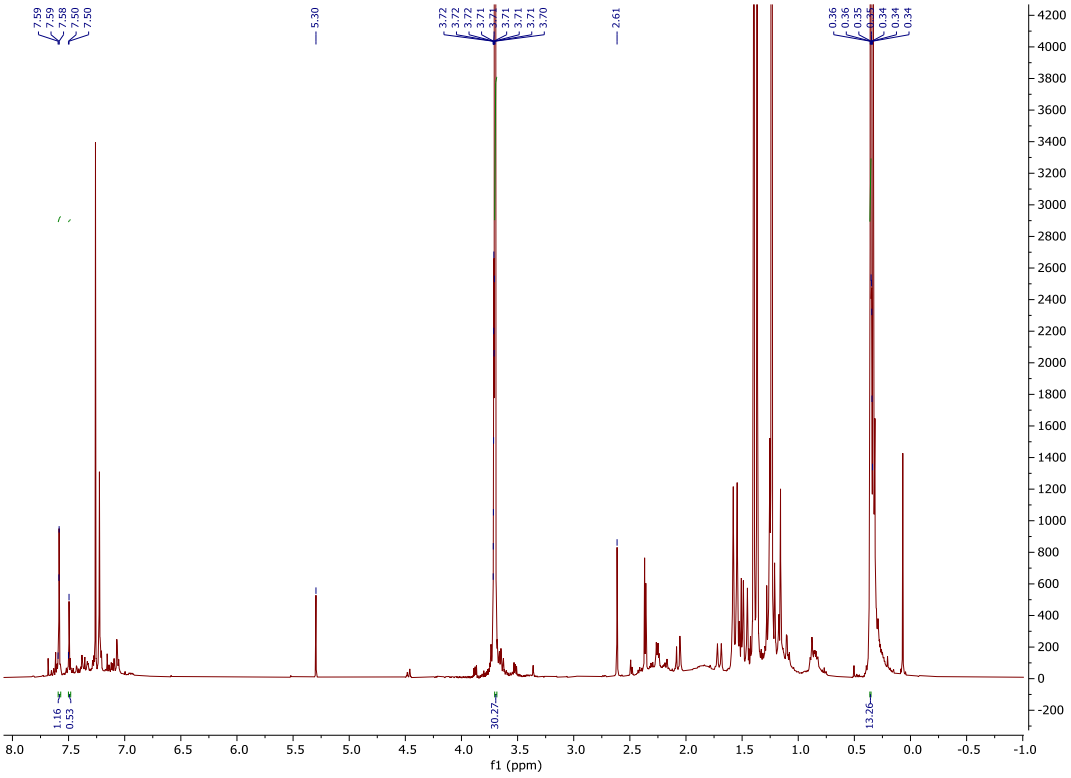


Figure 7.1.36: *^{1}H-NMR ($CDCl_3$) of 2,7-Bis(trimethylsilyl)-4,9-dihydro-s-indaceno[1,2-b:5,6-b']dithiophene (**2.70**).*

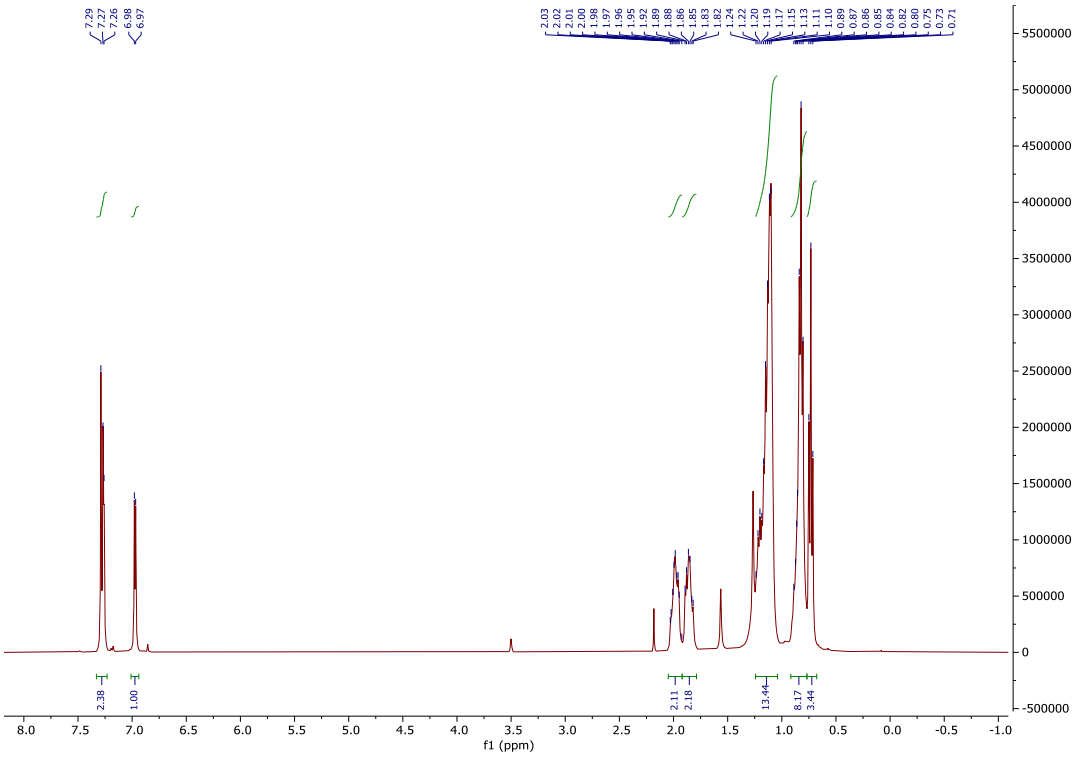


Figure 7.1.37: *^{1}H-NMR ($CDCl_3$) of 4,9-dibutyl-4,9-dioctyl-4,9-dihydro-s-indaceno[1,2-b:5,6-b']dithiophene (**2.83**).*

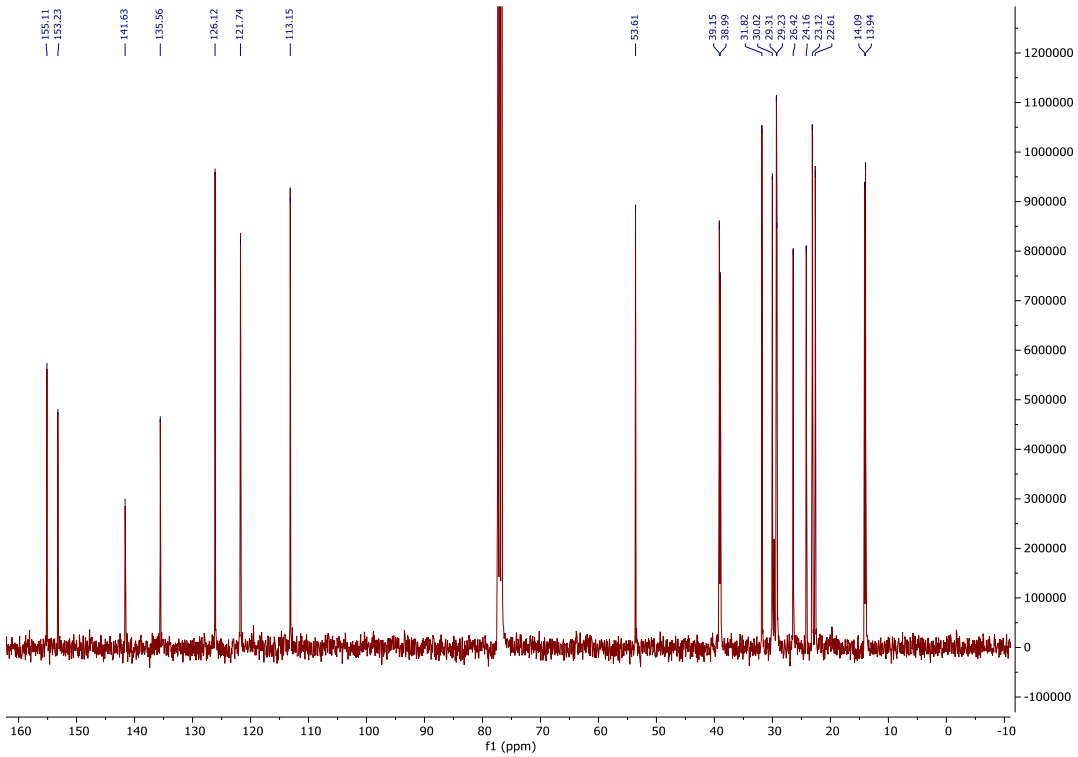


Figure 7.1.38: *^{13}C-NMR ($CDCl_3$) of 4,9-dibutyl-4,9-dioctyl-4,9-dihydro-s-indaceno[1,2-b:5,6-b']dithiophene (**2.83**).*

7.2 - Chapter 3

7.2.1 -CV traces

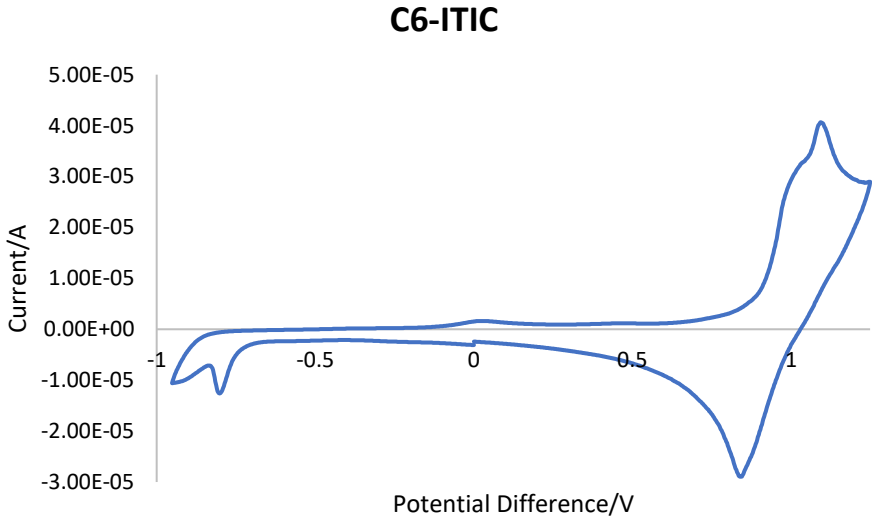


Figure 7.2.1: *CV trace of a drop-cast **C6-ITIC** film in a 0.1 M solution of Bu_4NPF_6 in acetonitrile.*

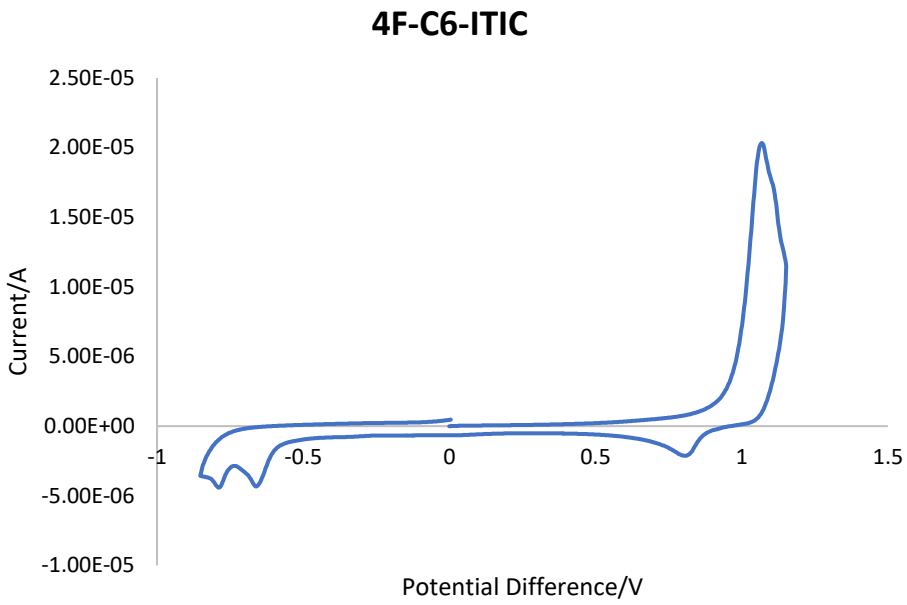


Figure 7.2.2: *CV trace of a drop-cast* ***4F-C6-ITIC*** *film in a 0.1 M solution of* Bu_4NPF_6 *in acetonitrile.*

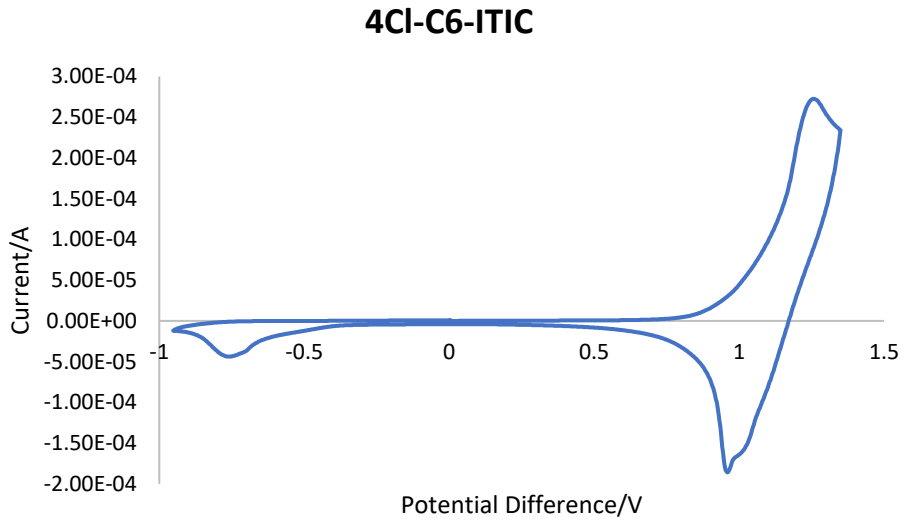


Figure 7.2.3: *CV trace of a drop-cast* ***4Cl-C6-ITIC*** *film in a 0.1 M solution of* Bu_4NPF_6 *in acetonitrile.*

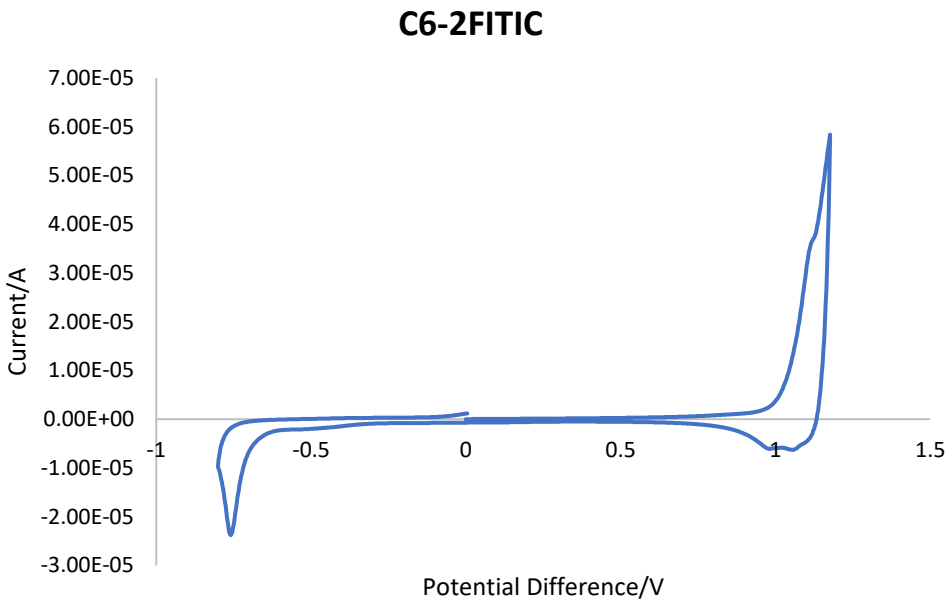


Figure 7.2.4: *CV trace of a drop-cast* ***C6-2FITIC*** *film in a 0.1 M solution of* Bu_4NPF_6 *in acetonitrile.*

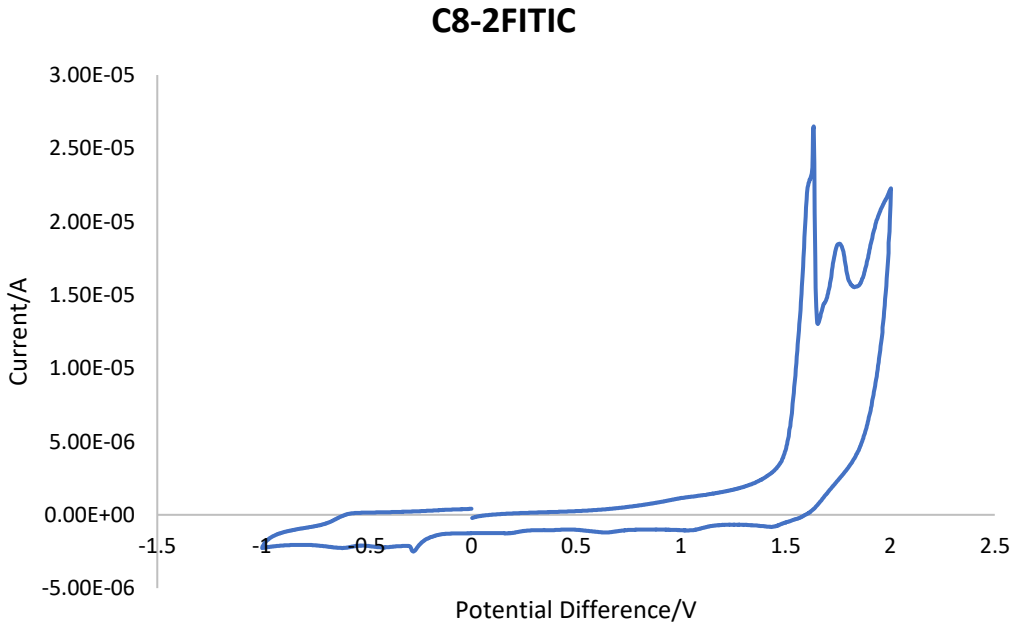


Figure 7.2.5: *CV trace of a drop-cast* ***C8-2FITIC*** *film in a 0.1 M solution of* Bu_4NPF_6 *in acetonitrile.*

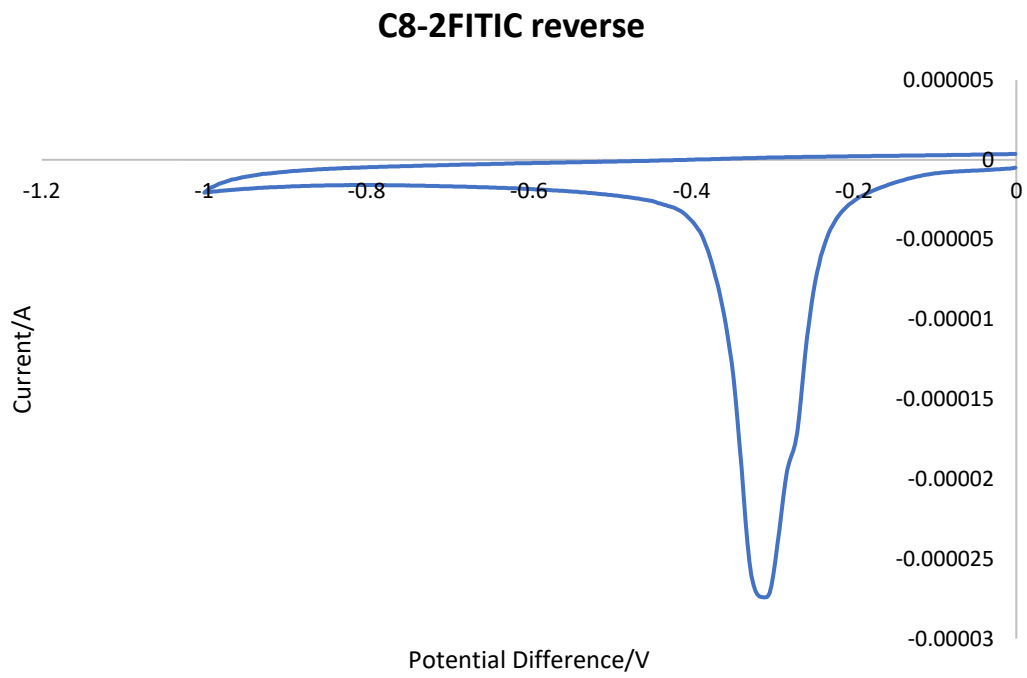


Figure 7.2.6: *Reverse sweep CV trace of a drop-cast* ***C8-2FITIC*** *film in a 0.1 M solution of* Bu_4NPF_6 *in acetonitrile.*

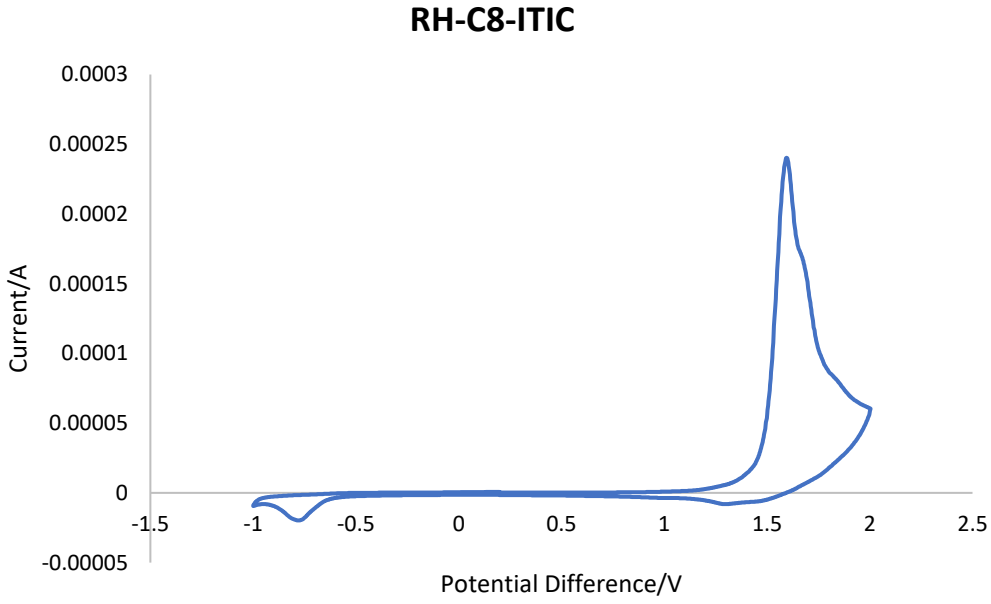


Figure 7.2.7: *CV trace of a drop-cast* ***RH-C8-ITIC*** *film in a 0.1 M solution of* Bu_4NPF_6 *in acetonitrile.*

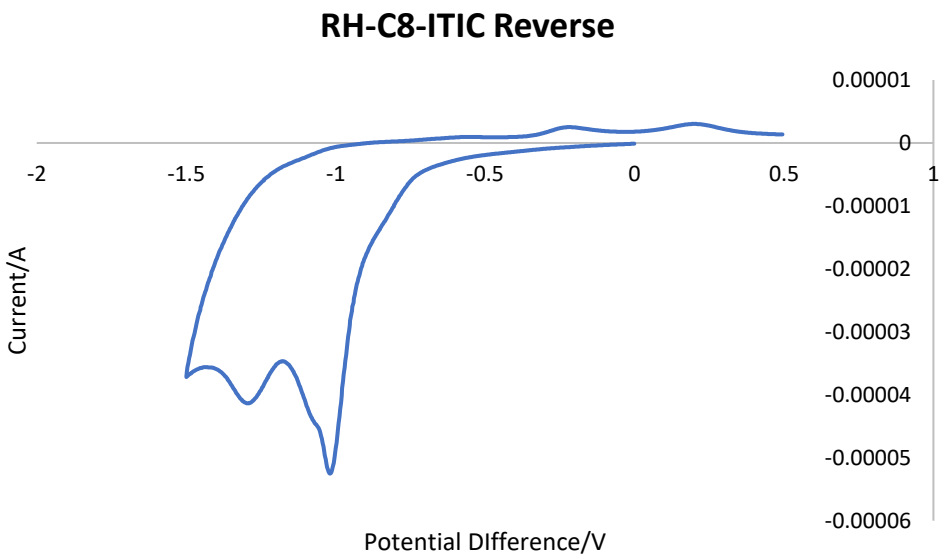


Figure 7.2.8: *Reverse sweep CV trace of a drop-cast* ***RH-C8-ITIC*** *film in a 0.1 M solution of* Bu_4NPF_6 *in acetonitrile.*

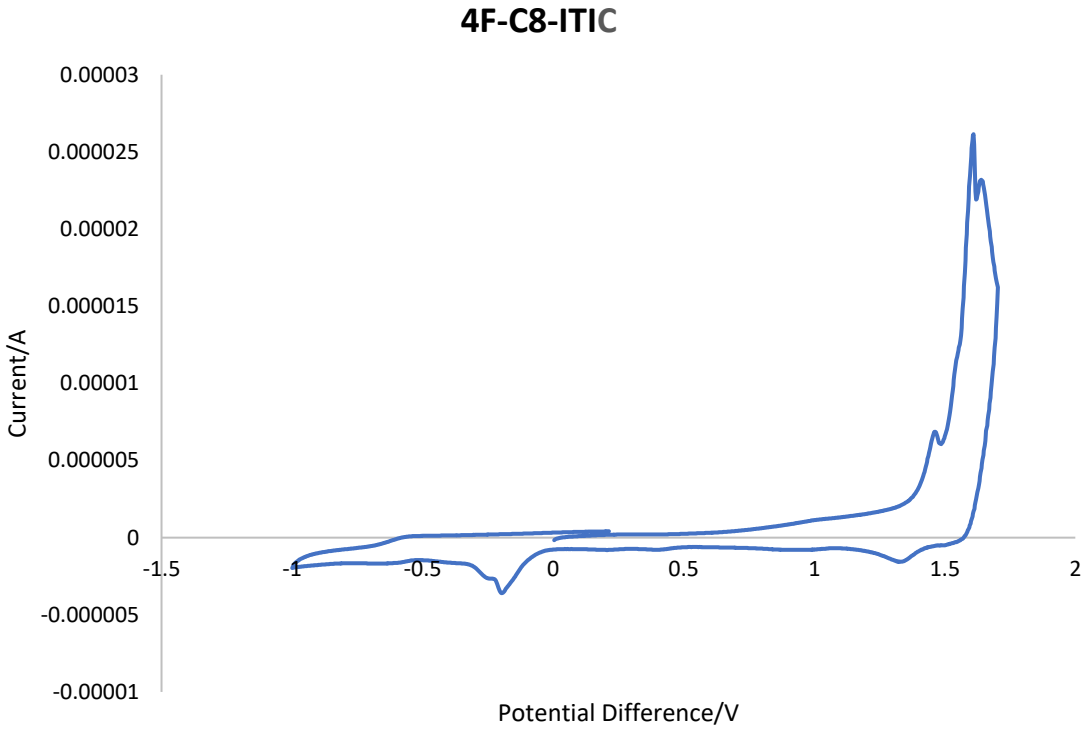


Figure 7.2.9: *CV trace of a drop-cast* ***4F-C8-ITIC*** *film in a 0.1 M solution of* Bu_4NPF_6 *in acetonitrile.*

7.2.2 - NMR Spectra

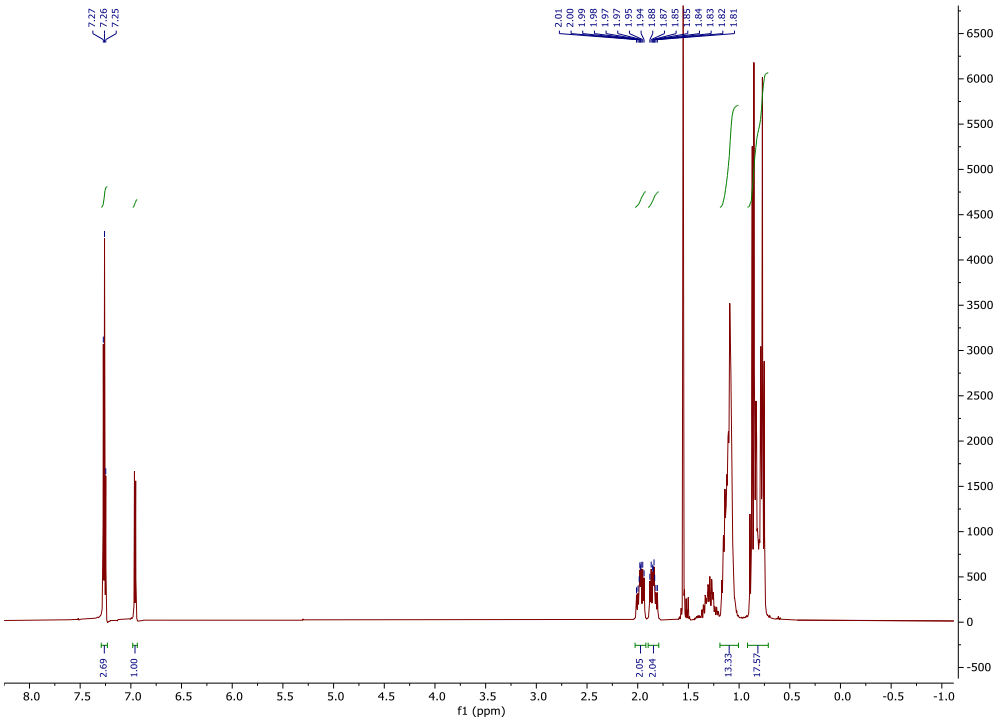


Figure 7.2.10: *^{1}H-NMR ($CDCl_3$) of 4,4,9,9-tetrahexyl-4,9-dihydro-s-indaceno[1,2-b:5,6-b']dithiophene (**3.1**).*

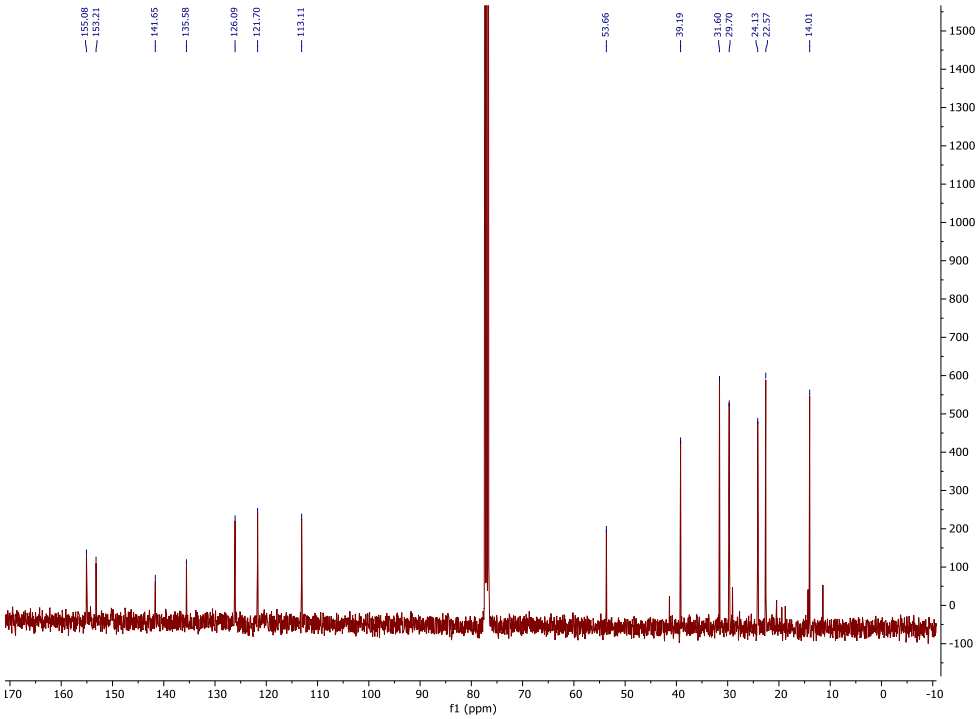


Figure 7.2.11: *^{13}C-NMR ($CDCl_3$) of 4,4,9,9-tetrahexyl-4,9-dihydro-s-indaceno[1,2-b:5,6-b']dithiophene (**3.1**).*

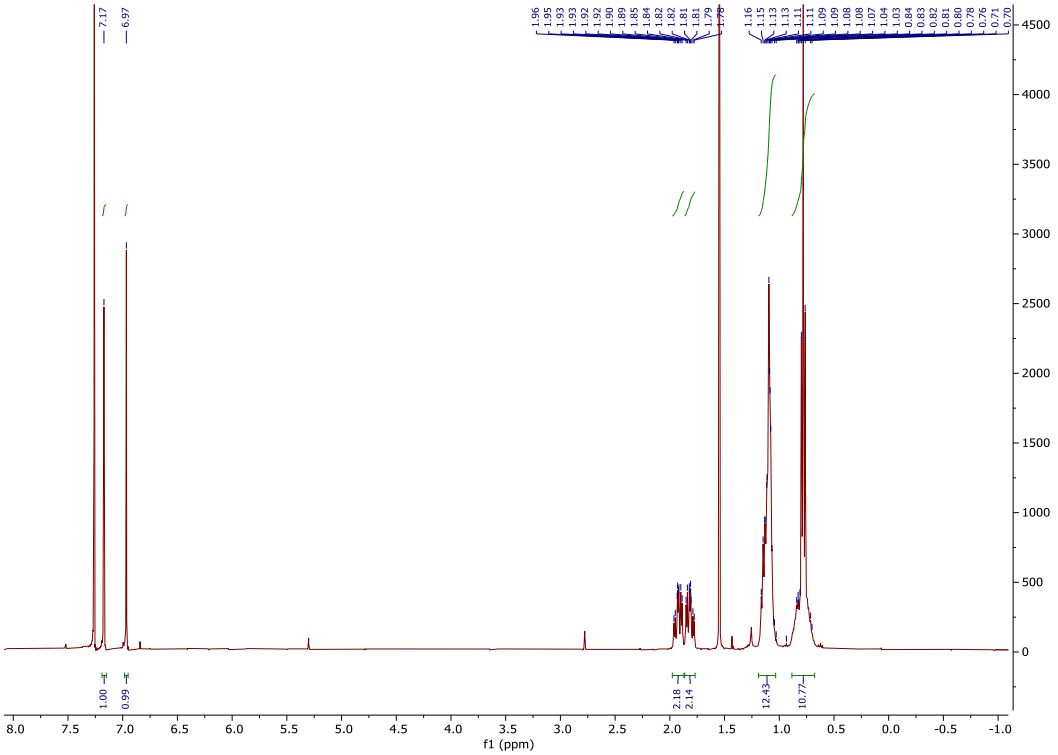


Figure 7.2.12: *^{1}H-NMR (CDCl3) of 2,7-dibromo-4,4,9,9-tetrahexyl-4,9-dihydro-s-indaceno[1,2-b:5,6-b']dithiophene (**3.2**).*

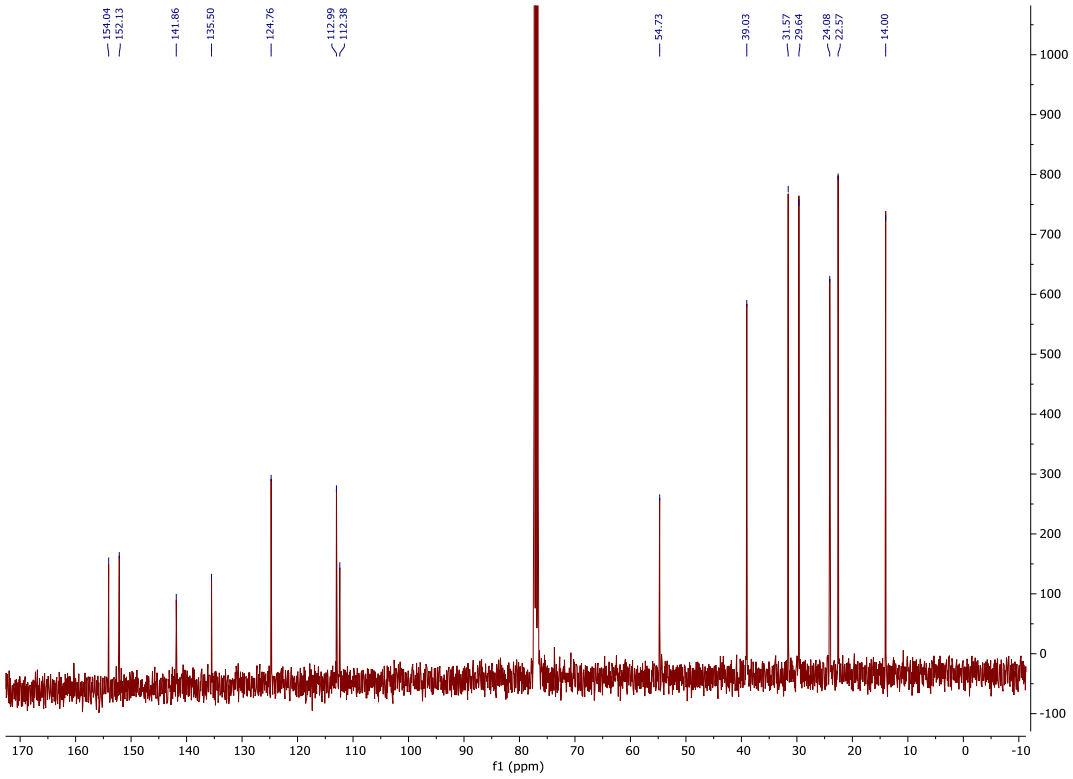


Figure 7.2.13: *^{13}C-NMR (CDCl3) of 2,7-dibromo-4,4,9,9-tetrahexyl-4,9-dihydro-s-indaceno[1,2-b:5,6-b']dithiophene (**3.2**).*

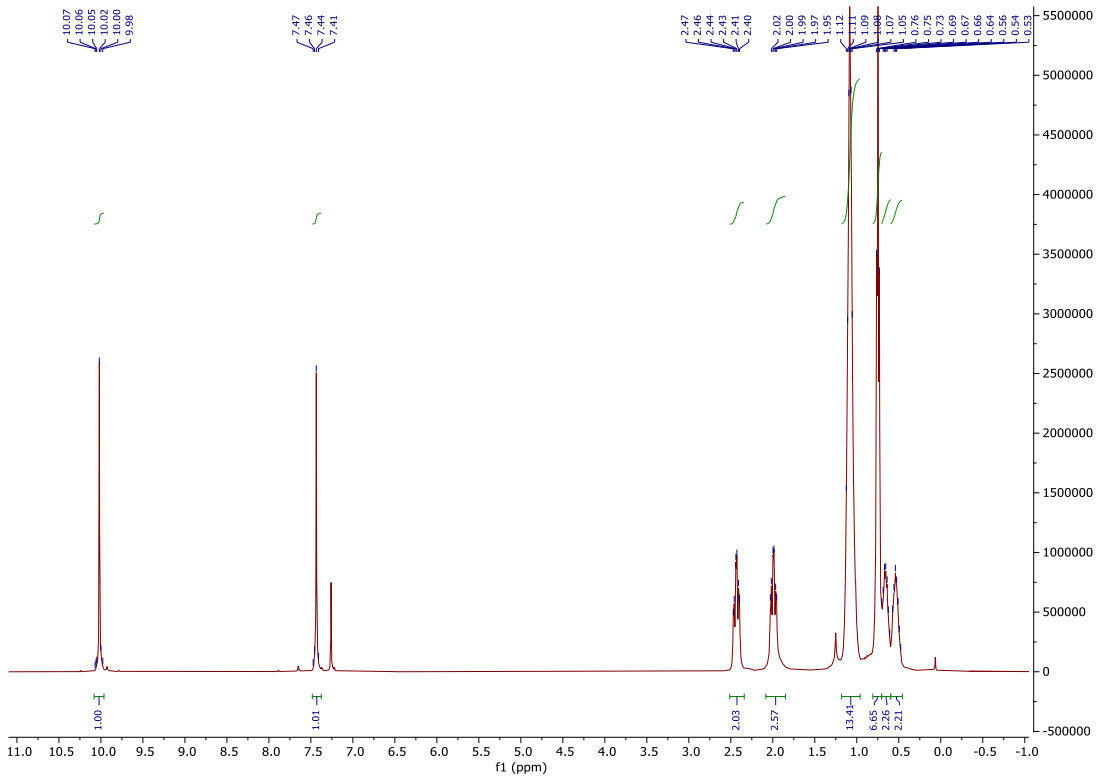


Figure 7.2.14: *^{1}H-NMR (CDCl3) of 3,8-dibromo-4,4,9,9-tetrahexyl-4,9-dihydro-s-indaceno[1,2-b:5,6-b']dithiophene-2,7-dicarbaldehyde* ***(3.3).***

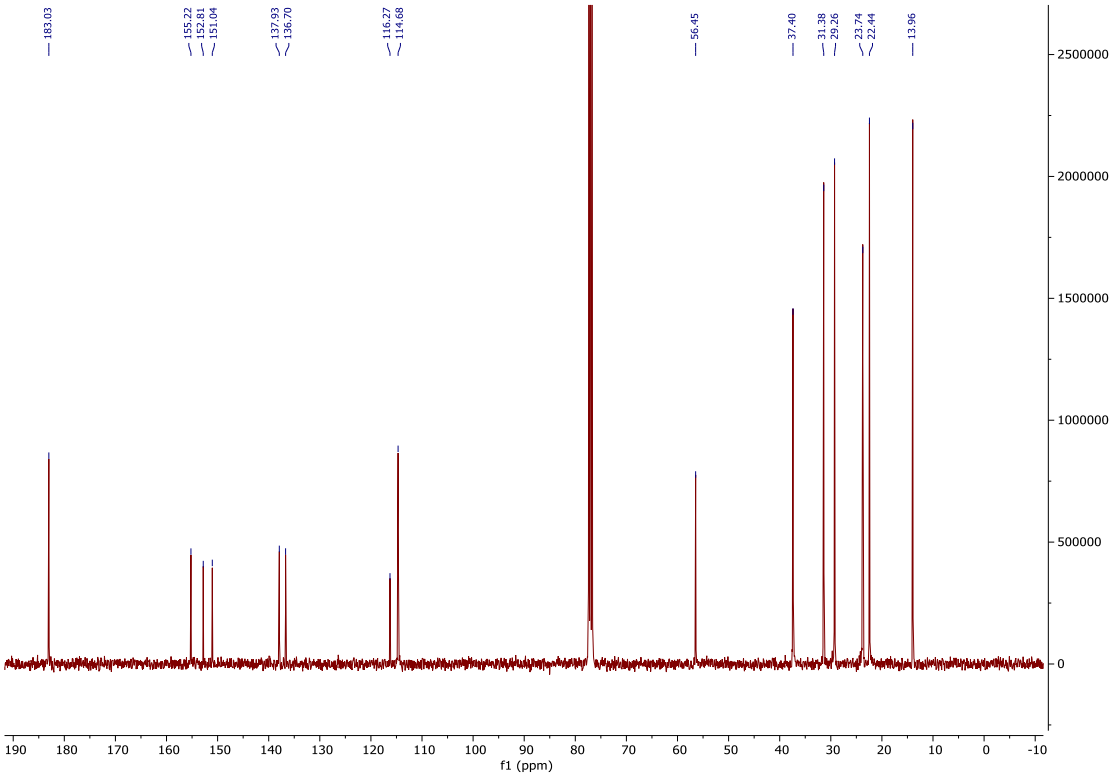


Figure 7.2.15: *^{13}C-NMR (CDCl3) of 3,8-dibromo-4,4,9,9-tetrahexyl-4,9-dihydro-s-indaceno[1,2-b:5,6-b']dithiophene-2,7-dicarbaldehyde* ***(3.3).***

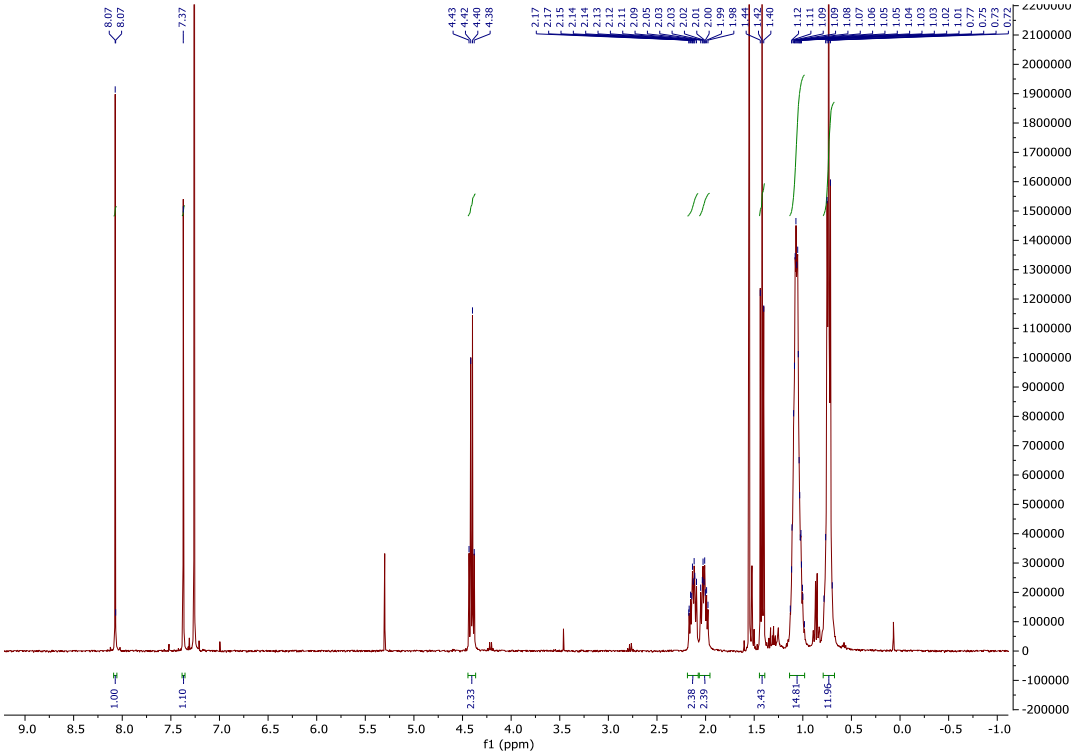


Figure 7.2.16: *^{1}H-NMR (CDCl3) of diethyl 6,6,12,12-tetrahexyl-6,12-dihydrothieno[3,2-b]thieno[2'',3'':4',5']thieno[2',3':5,6]-s-indaceno[2,1-d]thiophene-2,8-dicarboxylate* ***(3.4)****.*

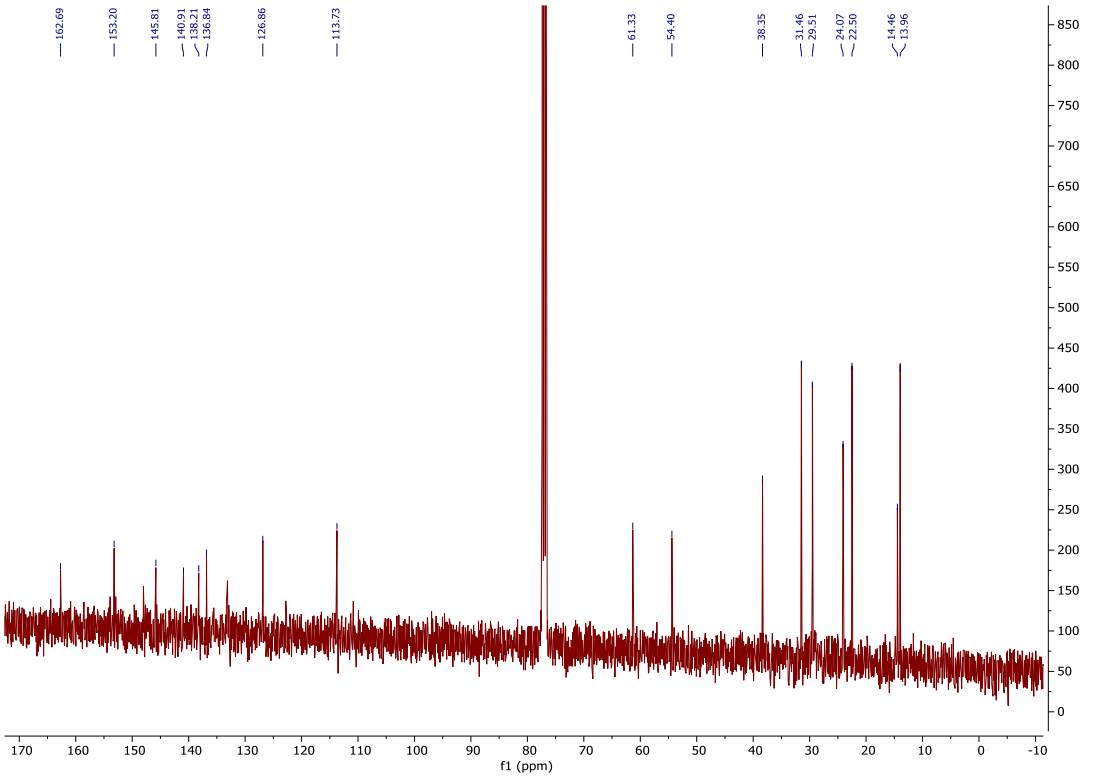


Figure 7.2.17: *^{13}C-NMR (CDCl3) of diethyl 6,6,12,12-tetrahexyl-6,12-dihydrothieno[3,2-b]thieno[2'',3'':4',5']thieno[2',3':5,6]-s-indaceno[2,1-d]thiophene-2,8-dicarboxylate* ***(3.4)****.*

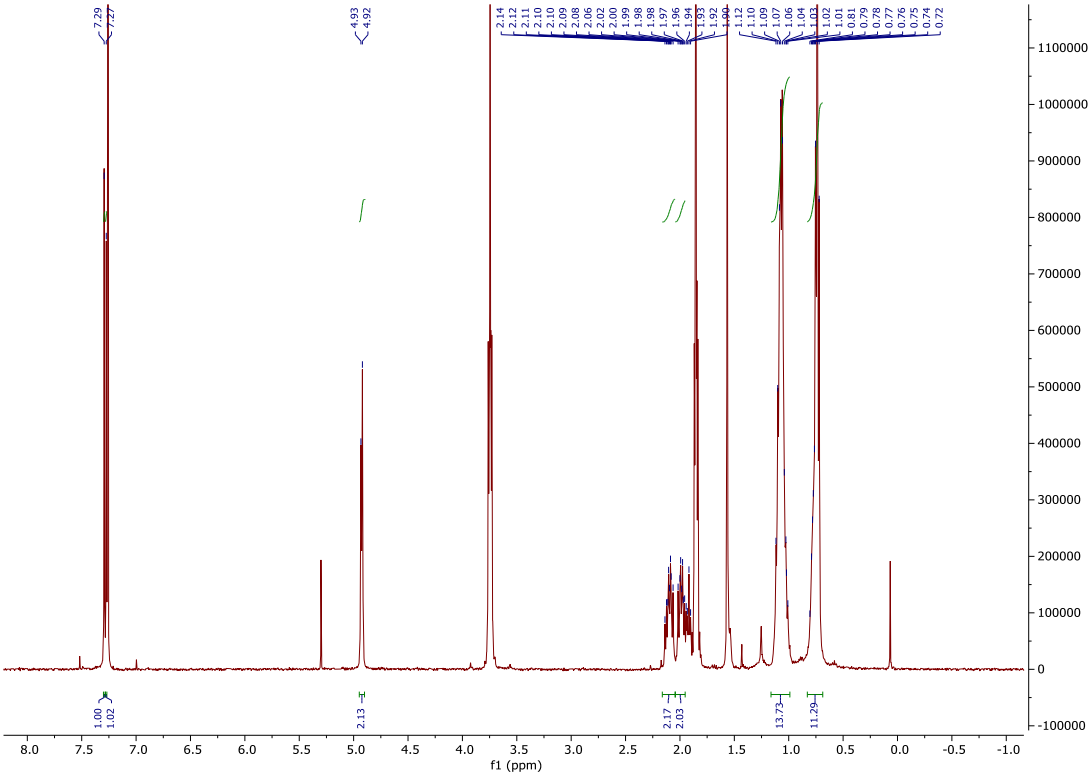


Figure 7.2.18: *^{1}H-NMR (CDCl3) of (6,6,12,12-tetrahexyl-6,12-dihydrothieno[3,2-b]thieno[2'',3'':4',5']thieno[2',3':5,6]-s-indaceno[2,1-d]thiene-2,8-diyl)dimethanol (**3.5**).*

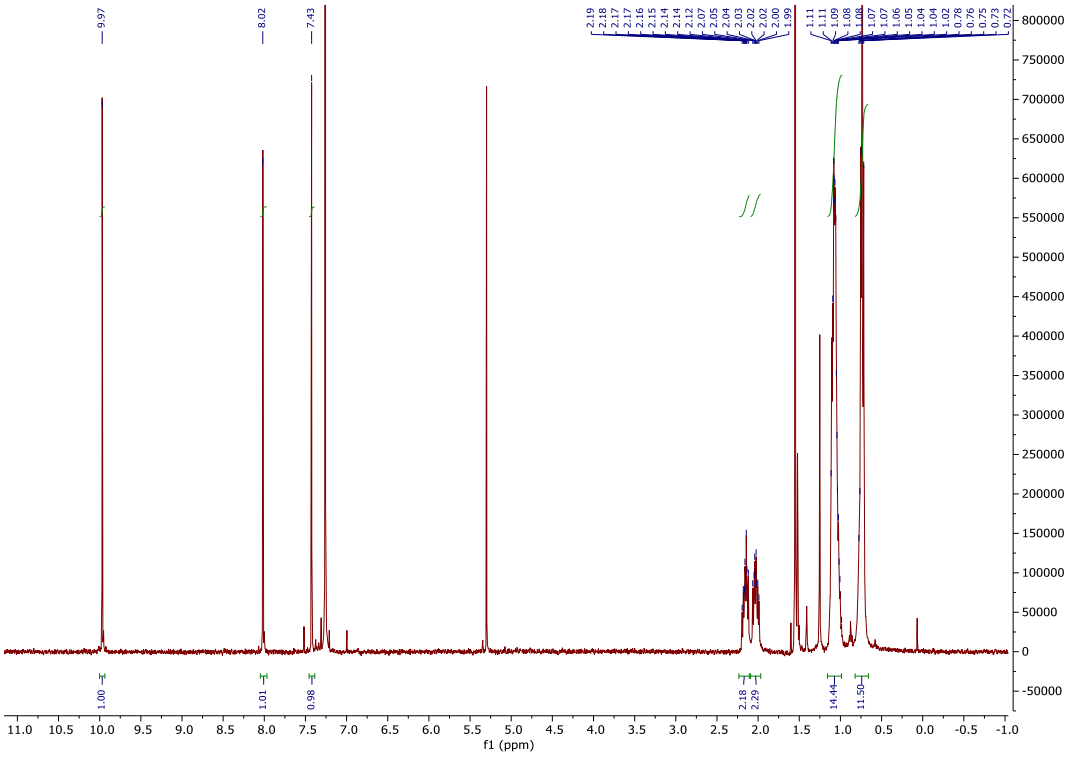


Figure 7.2.19: *^{1}H-NMR (CDCl3) of 6,6,12,12-tetrahexyl-6,12-dihydrothieno[3,2-b]thieno[2'',3'':4',5']thieno[2',3':5,6]-s-indaceno[2,1-d]thiophene-2,8-dicarbaldehyde (**3.6**).*

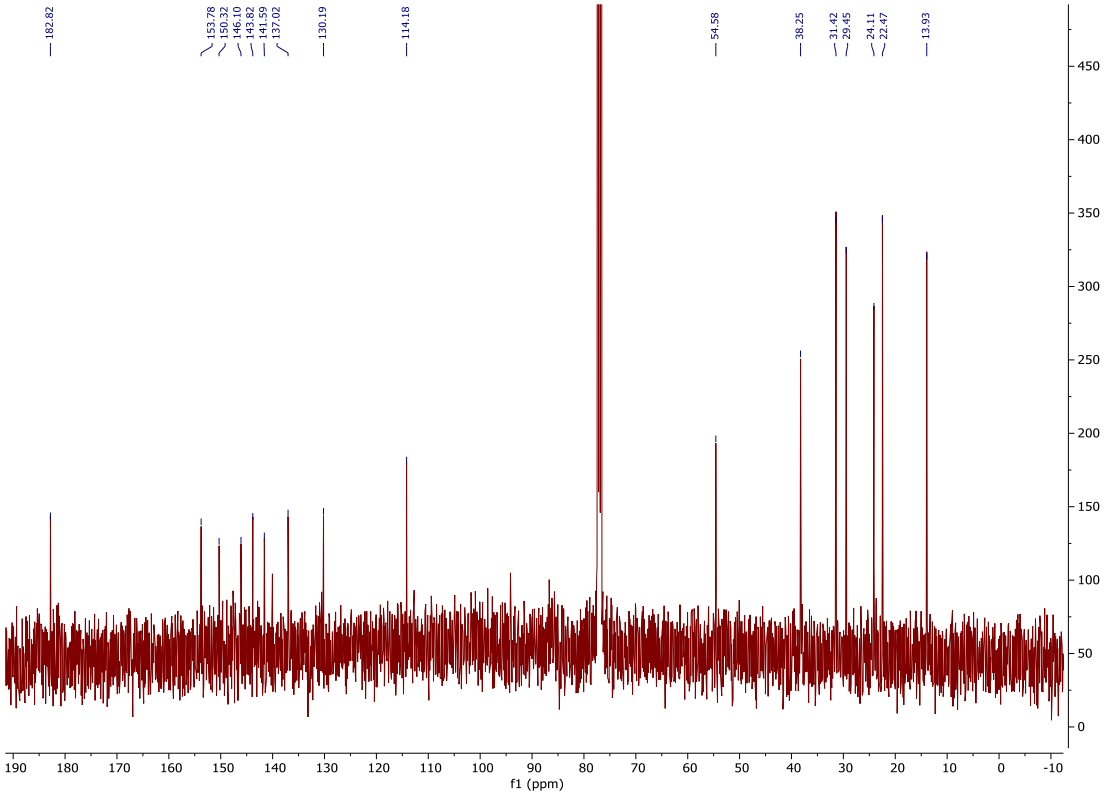


Figure 7.2.20: *^{13}C-NMR (CDCl3) of 6,6,12,12-tetrahexyl-6,12-dihydrothieno[3,2-b]thieno[2'',3'':4',5']thieno[2',3':5,6]-s-indaceno[2,1-d]thiophene-2,8-dicarbaldehyde (**3.6**).*

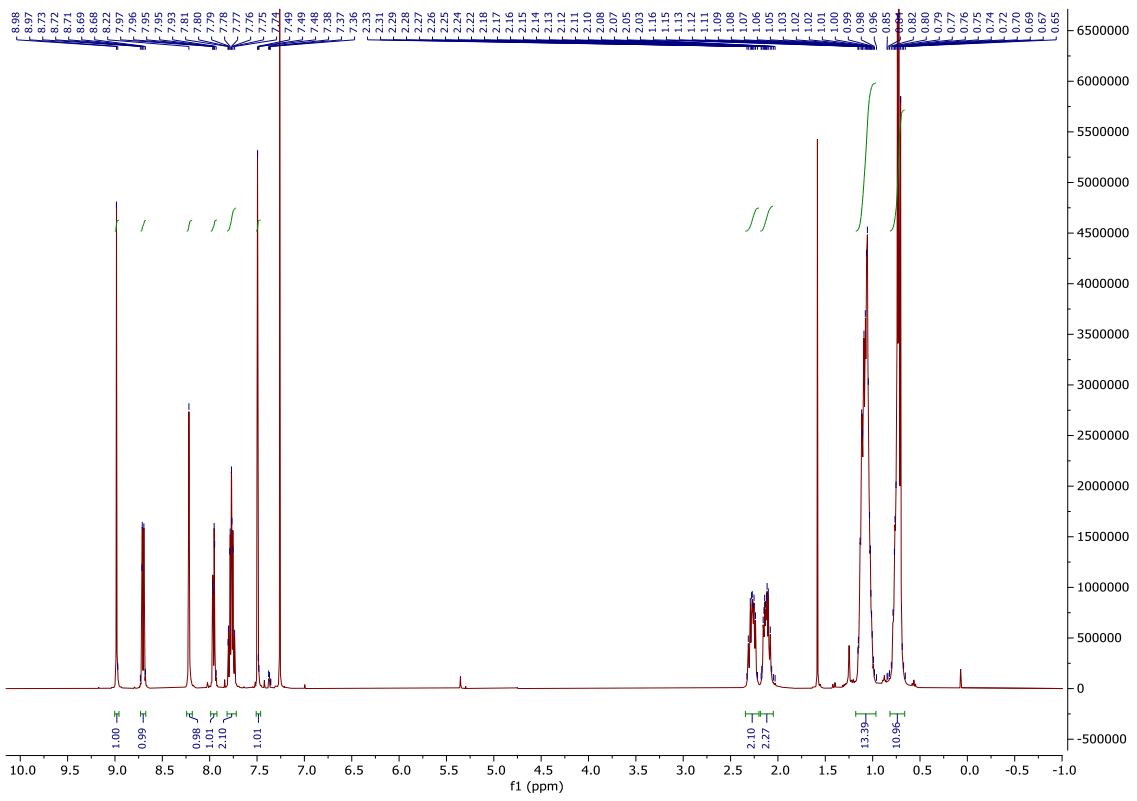


Figure 7.2.21: *^{1}H-NMR (CDCl3) of **C6-ITIC**.*

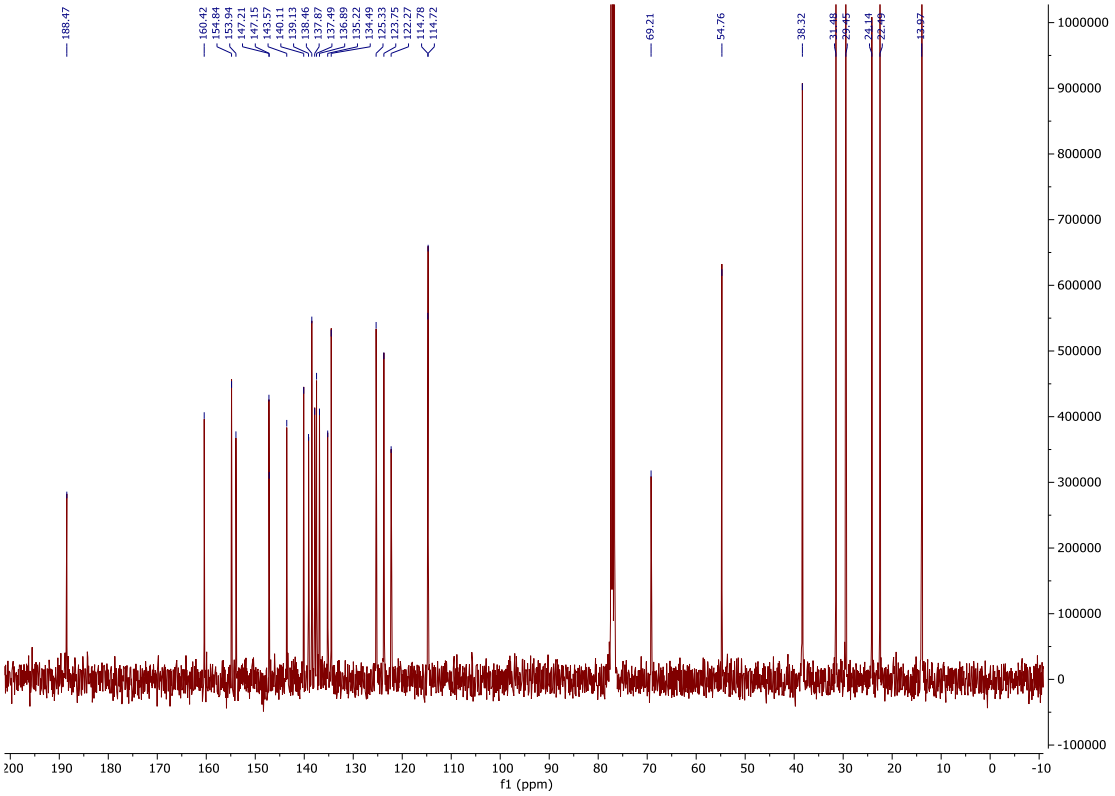


Figure 7.2.22: *^{13}C-NMR (CDCl3) of* ***C6-ITIC****.*

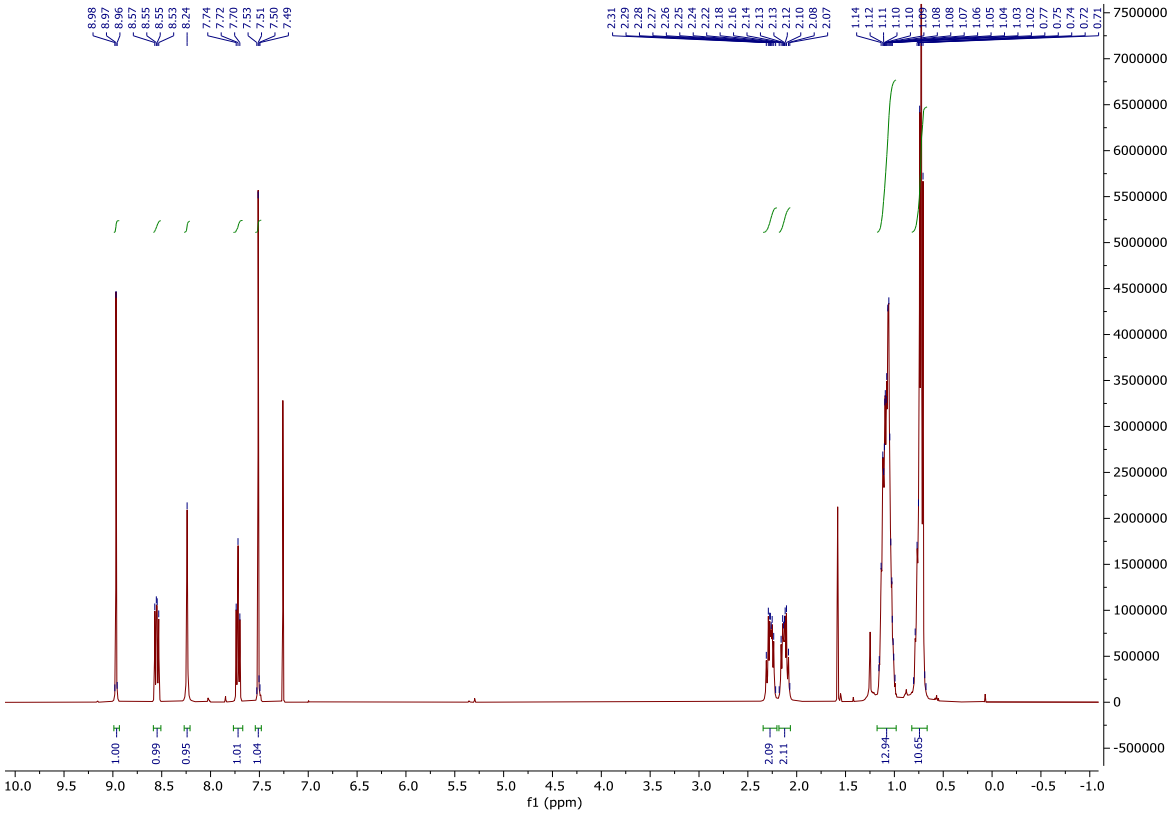


Figure 7.2.23: *^{1}H-NMR (CDCl3) of* ***4F-C6-ITIC****.*

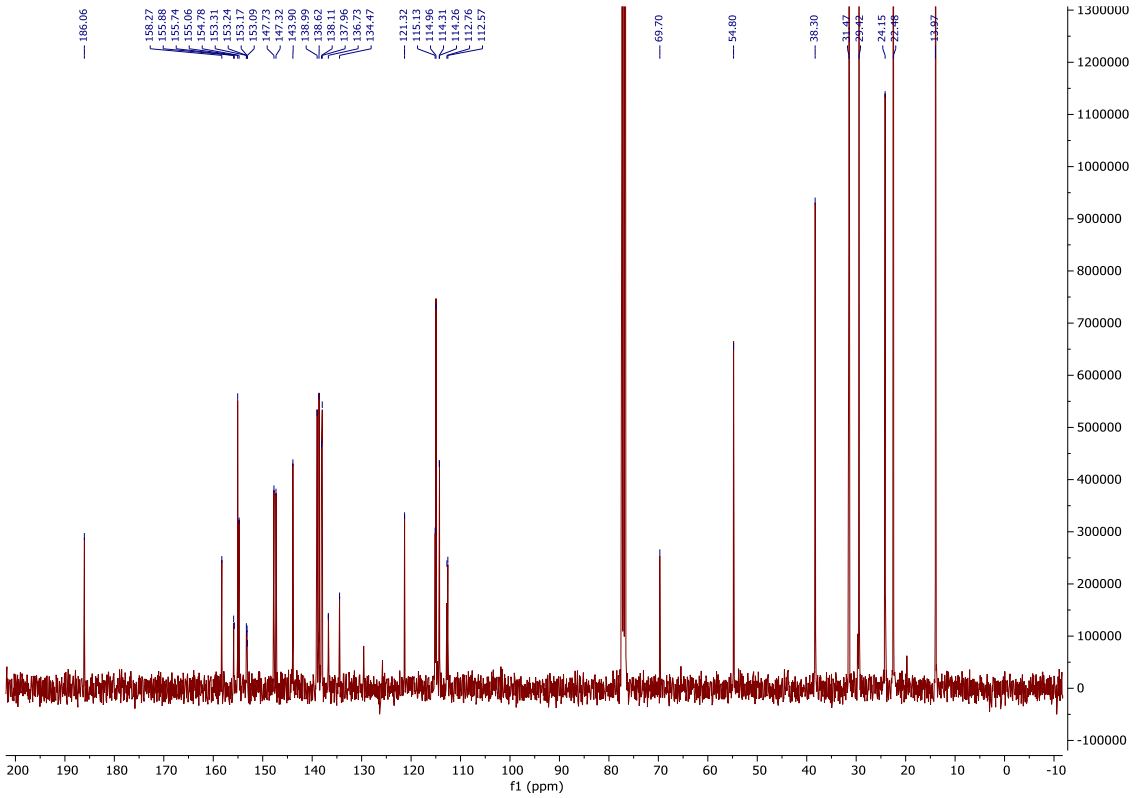


Figure 7.2.24: *^{13}C-NMR (CDCl3) of* ***4F-C6-ITIC****.*

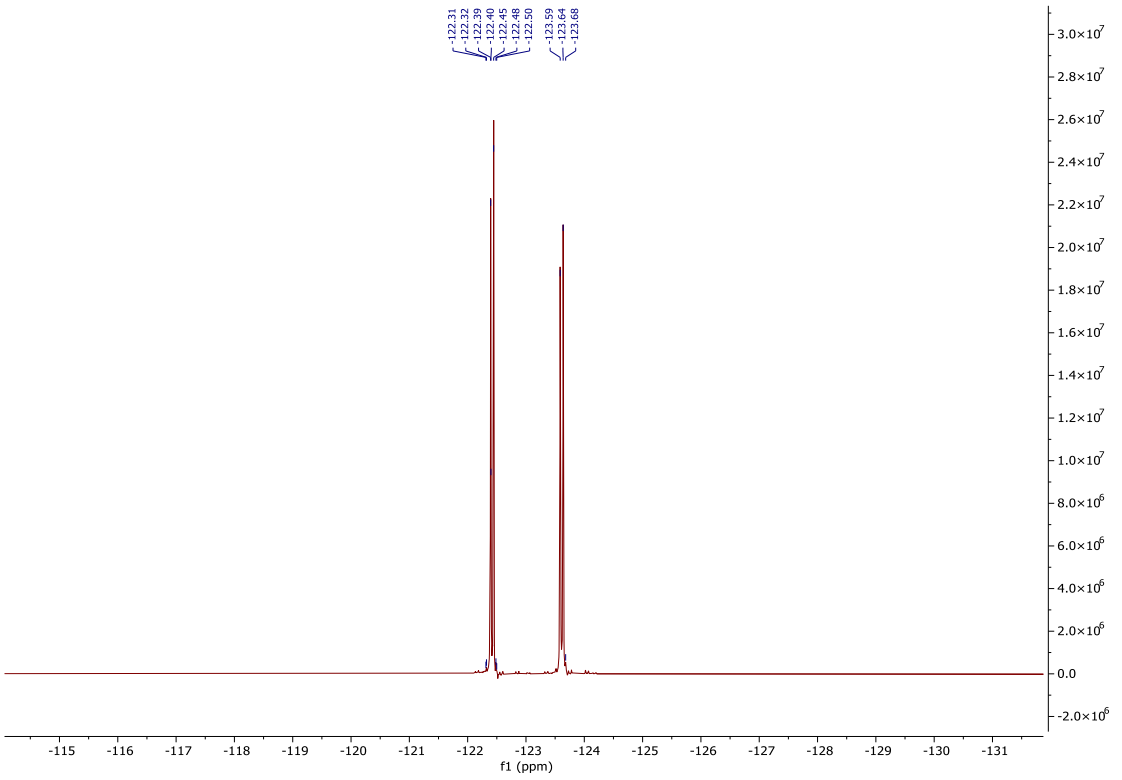


Figure 7.2.25: *^{19}F-NMR (CDCl3) of* ***4F-C6-ITIC****.*

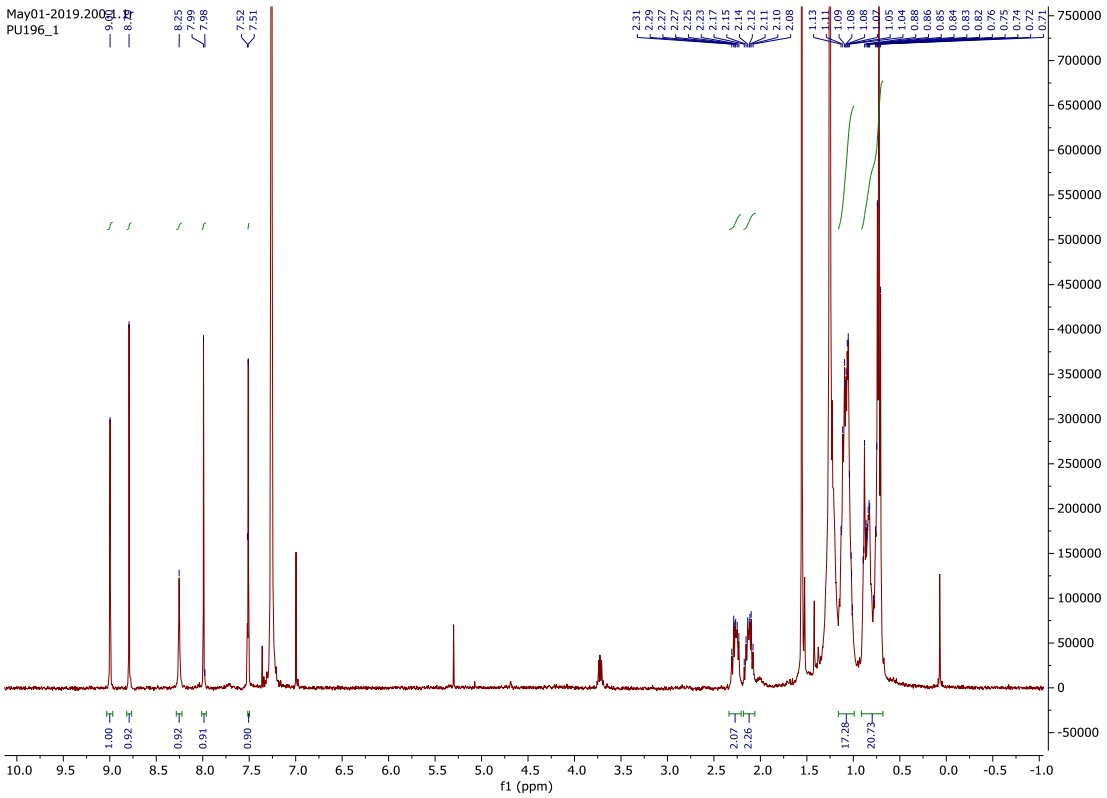


Figure 7.2.26: *^{1}H-NMR (CDCl3) of* ***4Cl-C6-ITIC****.*

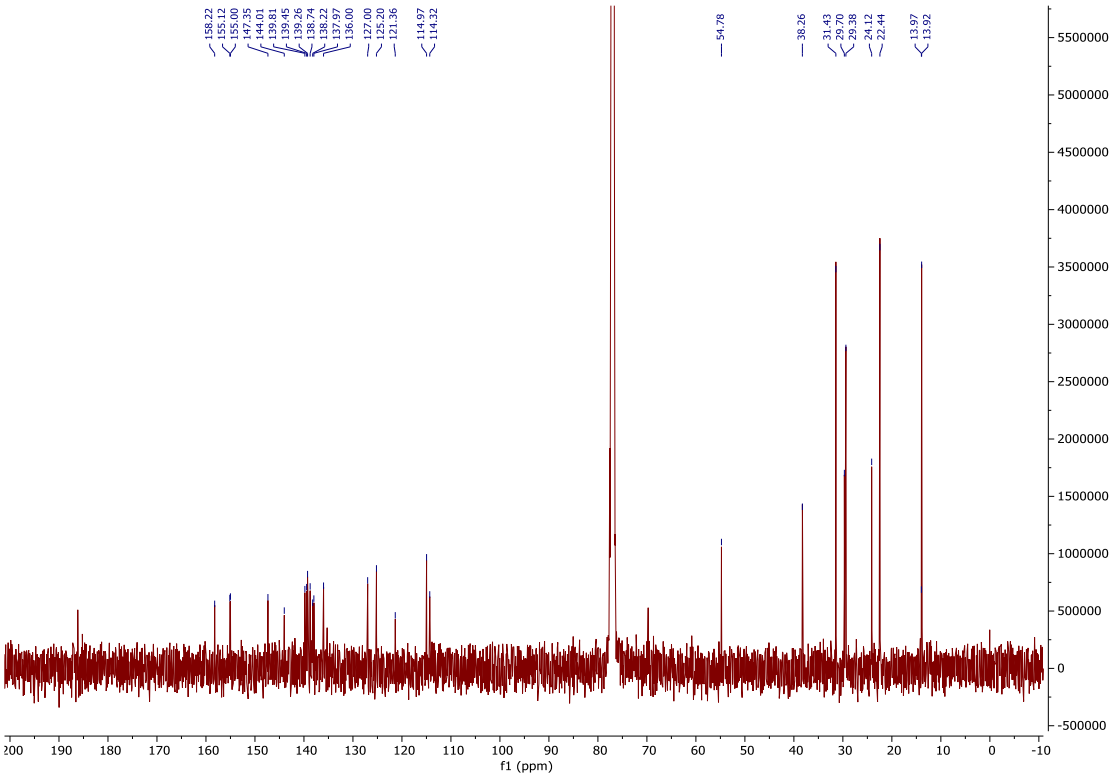


Figure 7.2.27: *^{13}C-NMR (Hot CDCl3) of* ***4Cl-C6-ITIC****.*

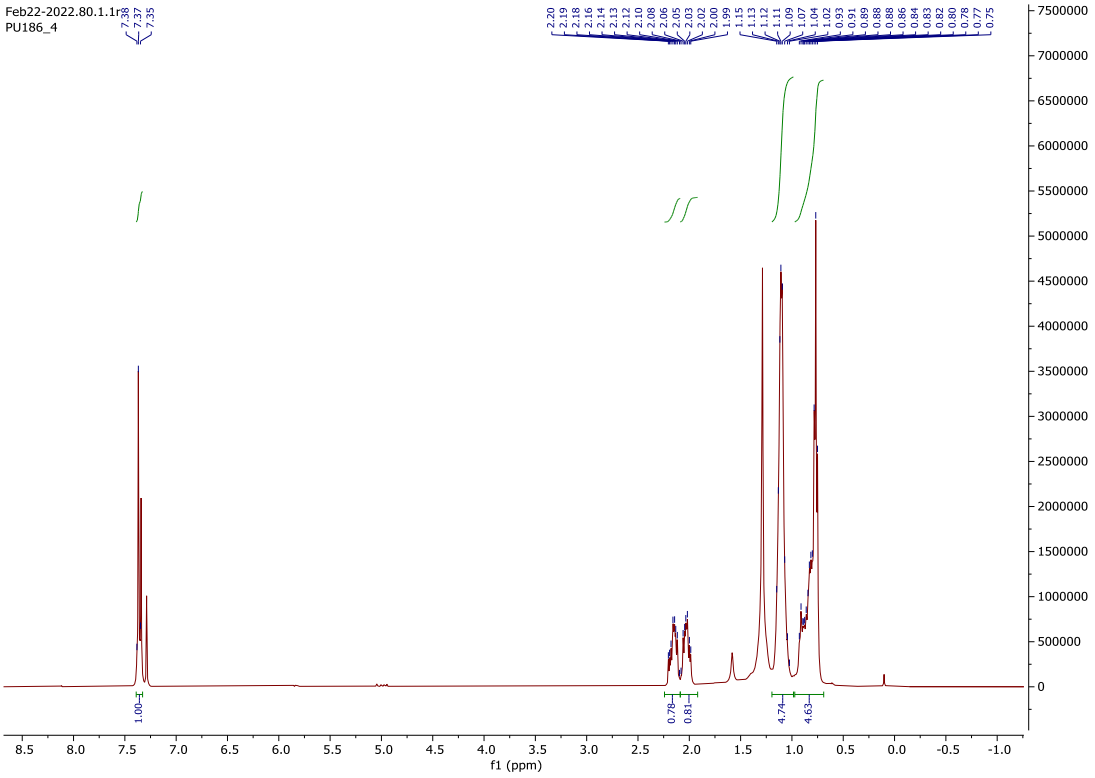


Figure 7.2.28: *^{1}H-NMR (CDCl3) of 6,6,12,12-Tetrahexyl-6,12-dihydrothieno[3,2-b]thieno[2'',3'':4',5']thieno[2',3':5,6]-s-indaceno[2,1-d]thiophene (**3.10**).*

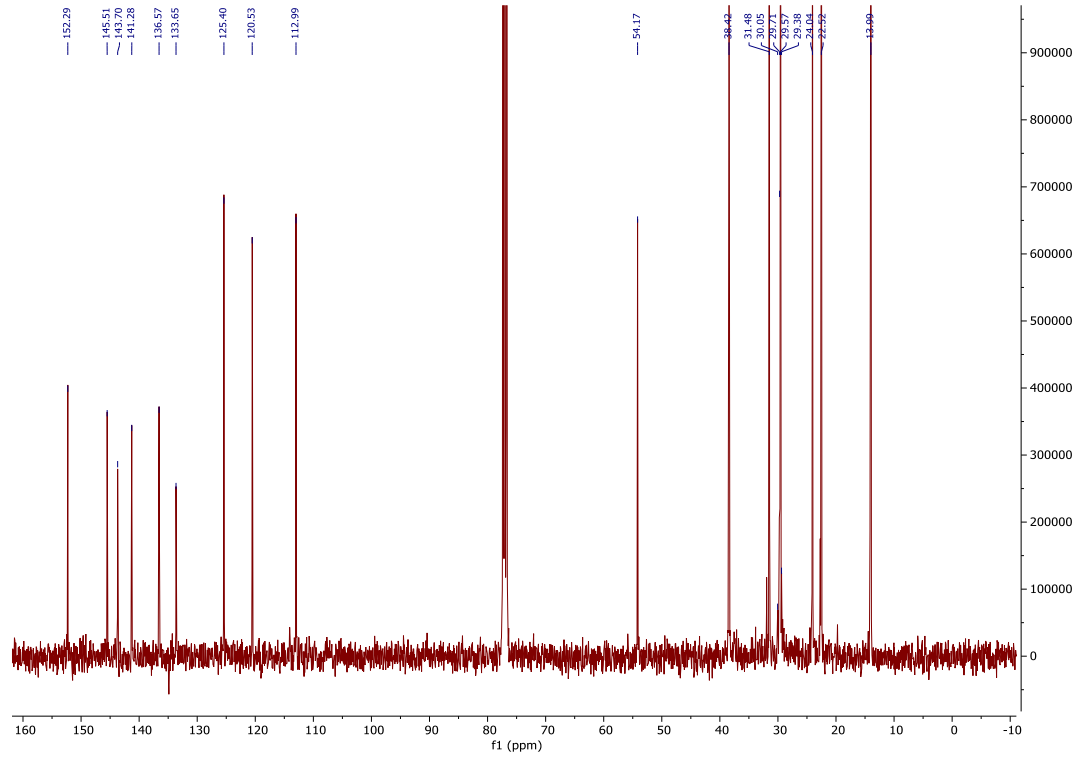


Figure 7.2.29: *^{13}C-NMR (CDCl3) of 6,6,12,12-Tetrahexyl-6,12-dihydrothieno[3,2-b]thieno[2'',3'':4',5']thieno[2',3':5,6]-s-indaceno[2,1-d]thiophene (**3.10**).*

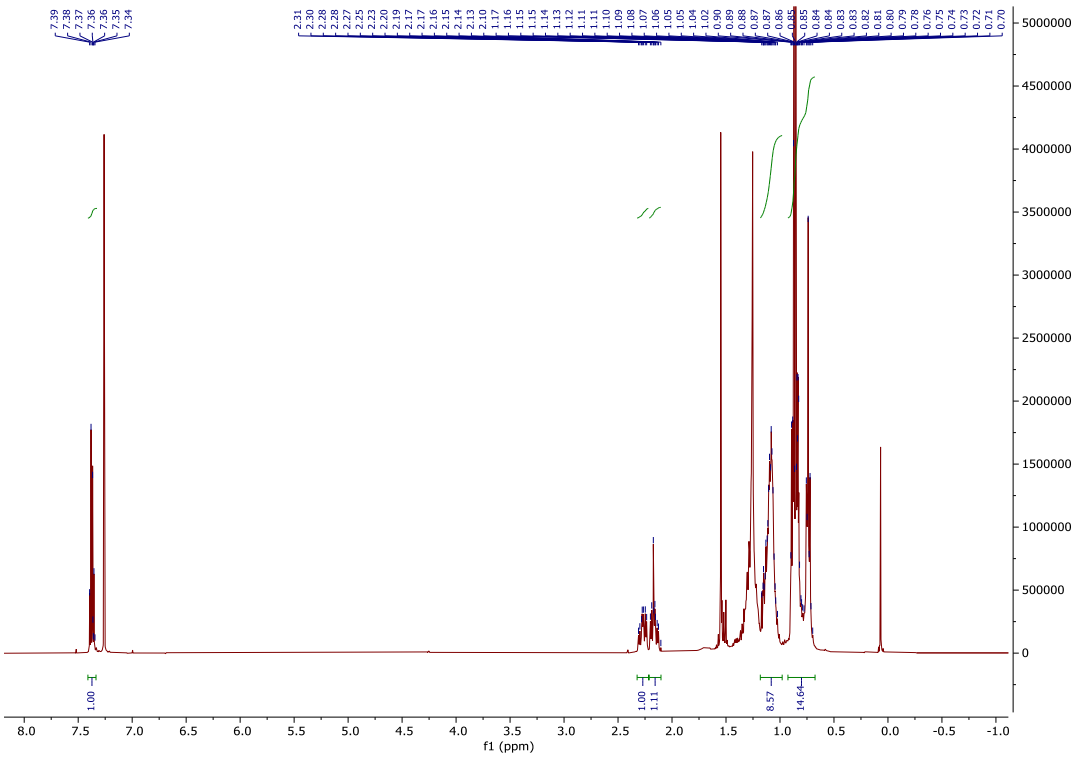


Figure 7.2.30: *^{1}H-NMR (CDCl3) of 5,11-difluoro-6,6,12,12-tetrahexyl-6,12-dihydrothieno[3,2-b]thieno[2'',3'':4',5']thieno[2',3':5,6]-s-indaceno[2,1-d]thiophene (**3.13**).*

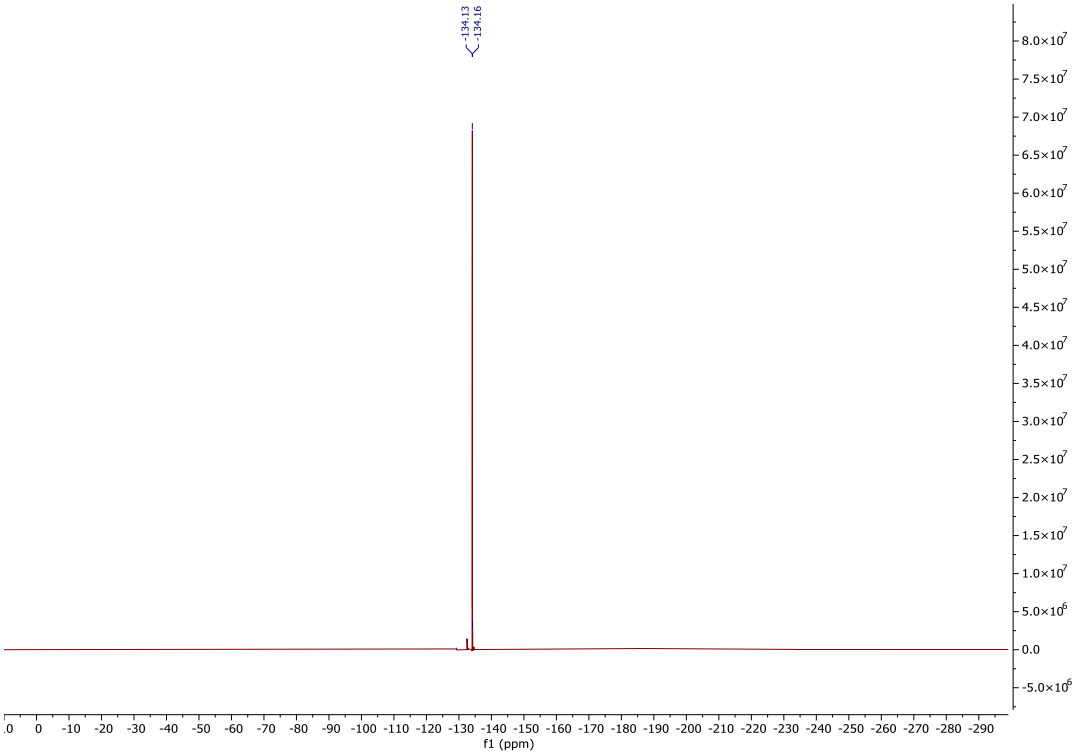


Figure 7.2.31: *^{13}C-NMR (CDCl3) of 5,11-difluoro-6,6,12,12-tetrahexyl-6,12-dihydrothieno[3,2-b]thieno[2'',3'':4',5']thieno[2',3':5,6]-s-indaceno[2,1-d]thiophene (**3.13**).*

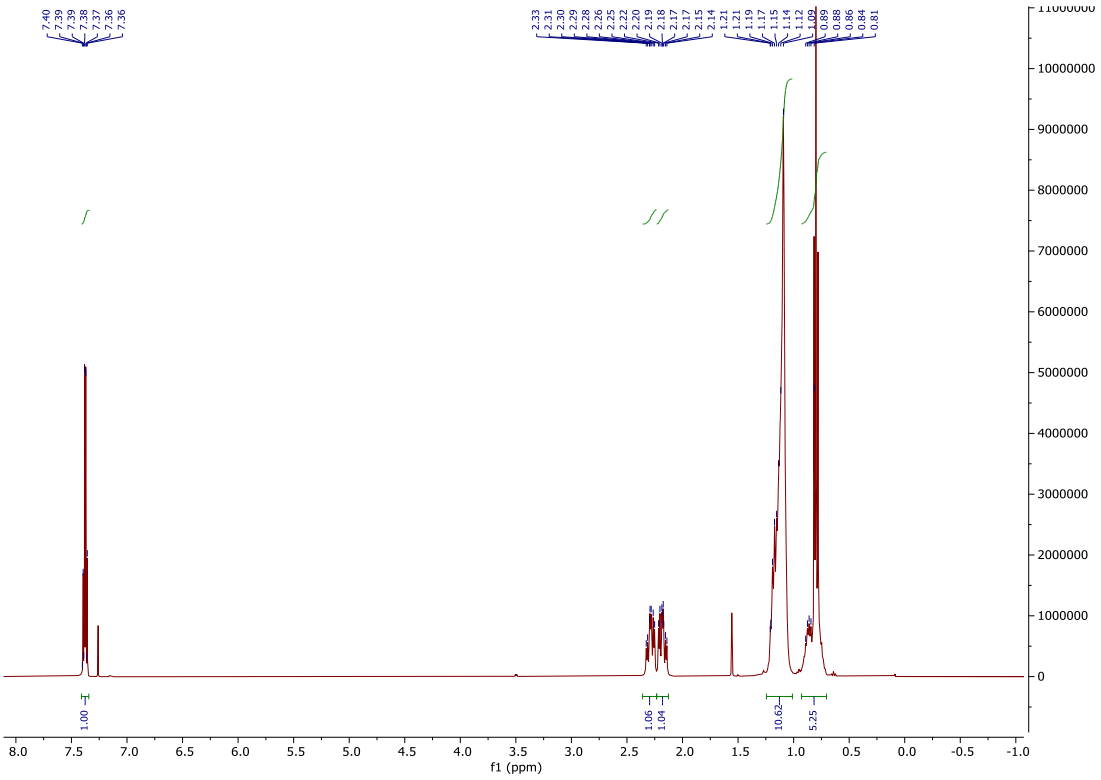


Figure 7.2.32: *^{1}H-NMR (CDCl3) of 5,11-difluoro-6,6,12,12-tetraoctyl-6,12-dihydrothieno[3,2-b]thieno[2'',3'':4',5']thieno[2',3':5,6]-s-indaceno[2,1-d]thiophene (**3.15**).*

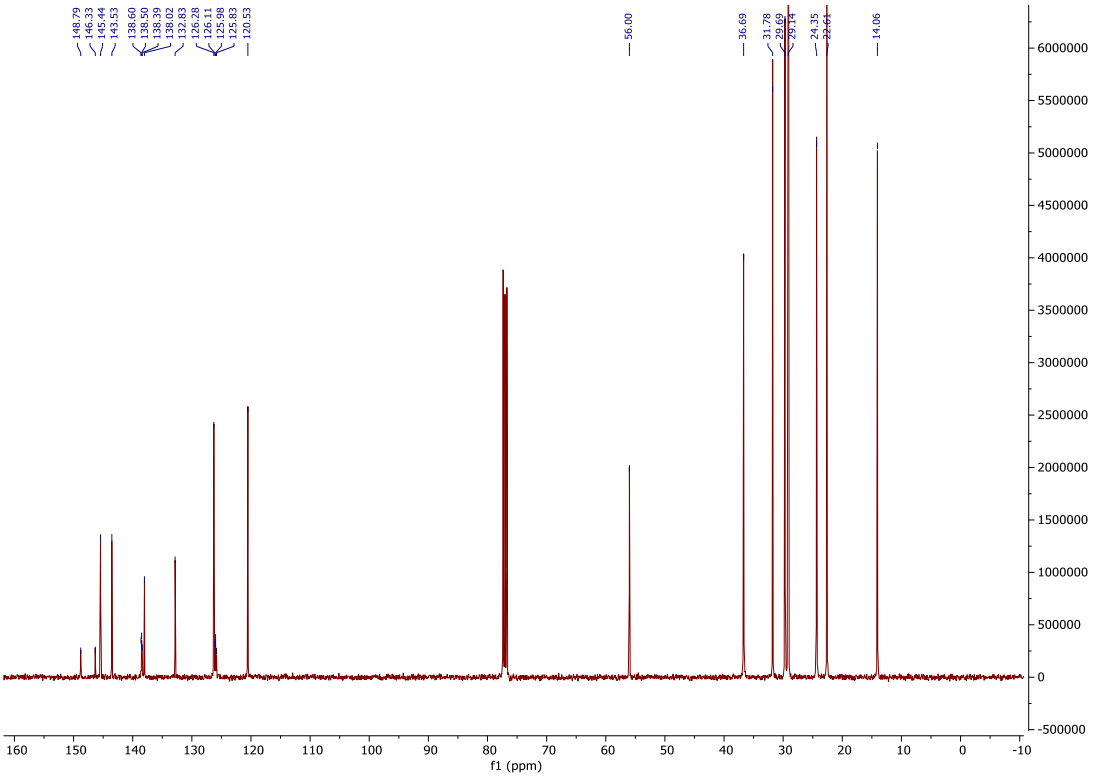


Figure 7.2.33: *^{13}C-NMR (CDCl3) of 5,11-difluoro-6,6,12,12-tetraoctyl-6,12-dihydrothieno[3,2-b]thieno[2'',3'':4',5']thieno[2',3':5,6]-s-indaceno[2,1-d]thiophene (**3.15**).*

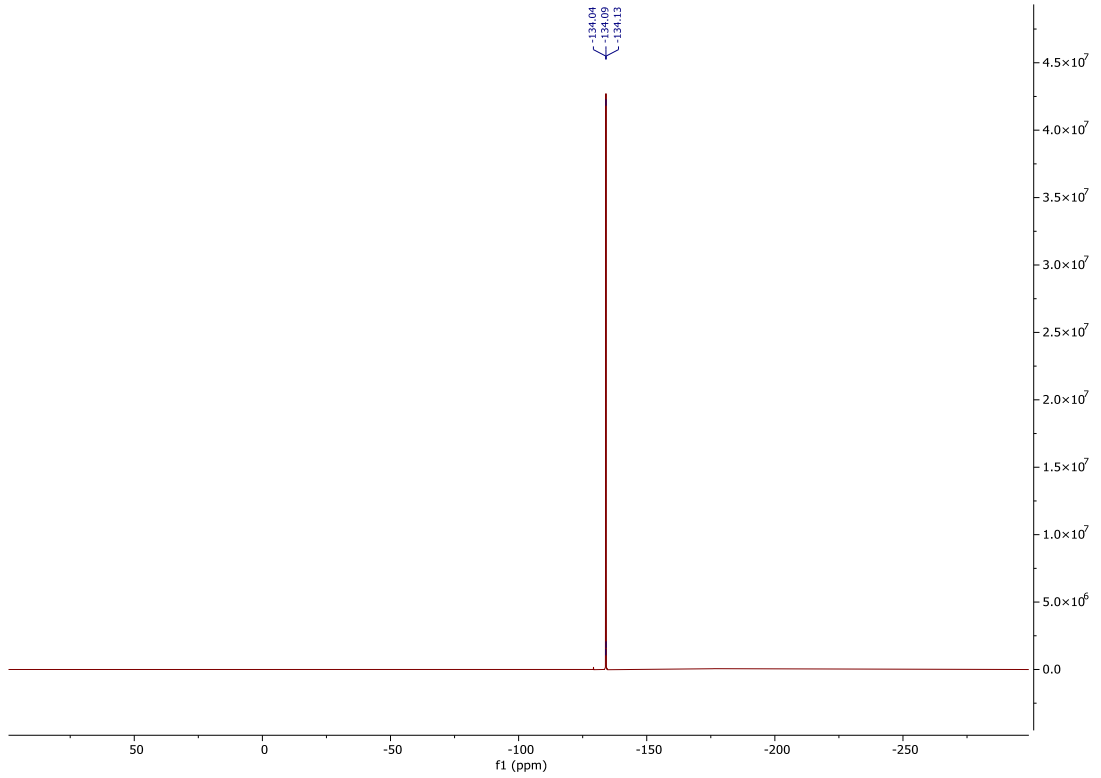


Figure 7.2.34: *[19]F-NMR (CDCl3) of 5,11-difluoro-6,6,12,12-tetraoctyl-6,12-dihydrothieno[3,2-b]thieno[2'',3'':4',5']thieno[2',3':5,6]-s-indaceno[2,1-d]thiophene (**3.15**).*

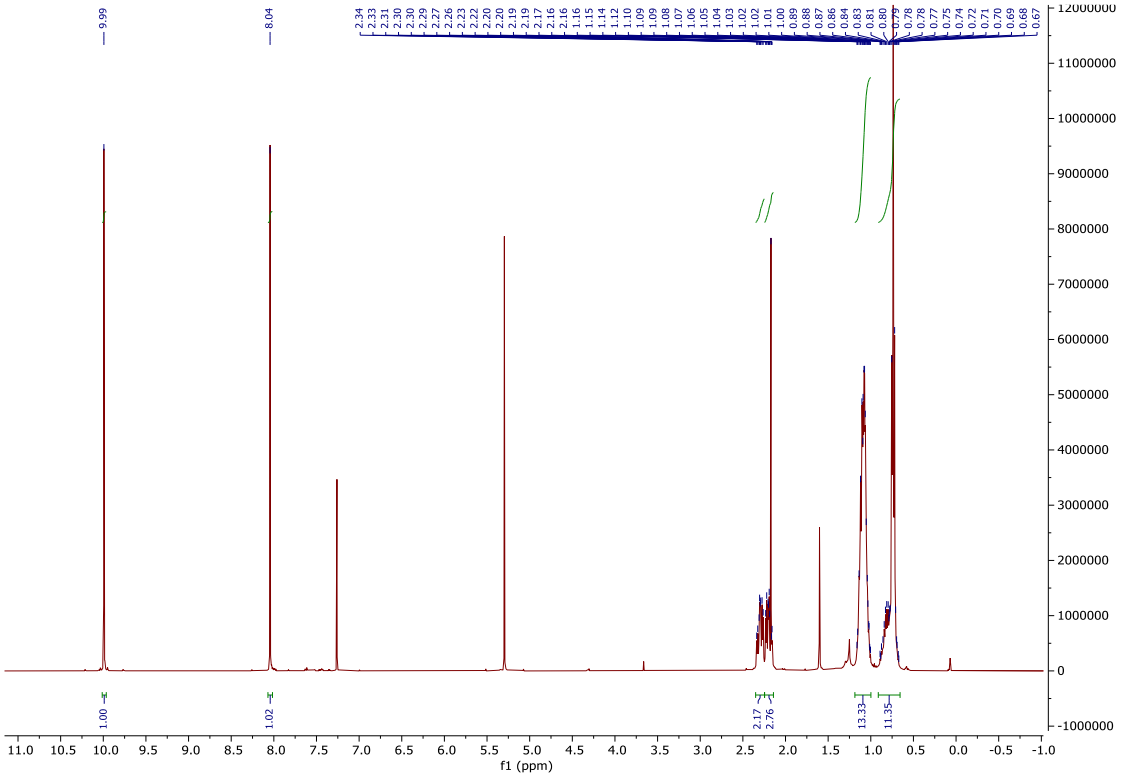


Figure 7.2.35: *[1]H-NMR (CDCl3) of 5,11-difluoro-6,6,12,12-tetrahexyl-6,12-dihydrothieno[3,2-b]thieno[2'',3'':4',5']thieno[2',3':5,6]-s-indaceno[2,1-d]thiophene-2,8-dicarbaldehyde (**3.14**).*

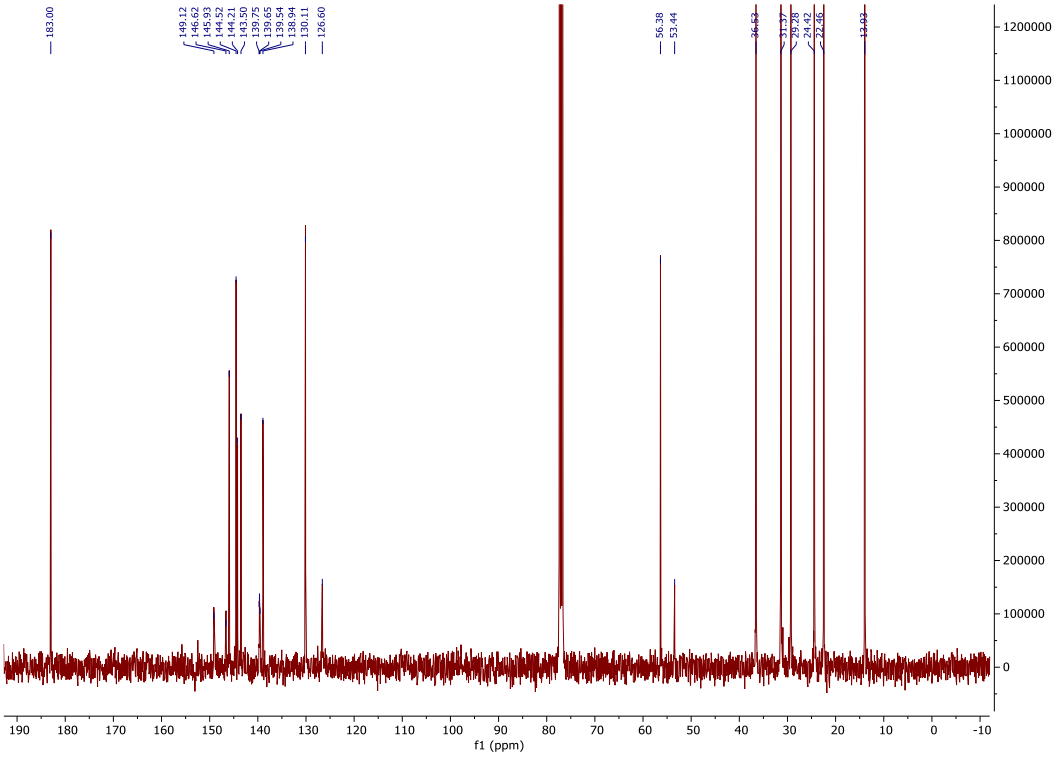


Figure 7.2.36: *^{13}C-NMR (CDCl3) of 5,11-difluoro-6,6,12,12-tetrahexyl-6,12-dihydrothieno[3,2-b]thieno[2'',3'':4',5']thieno[2',3':5,6]-s-indaceno[2,1-d]thiophene-2,8-dicarbaldehyde (**3.14**).*

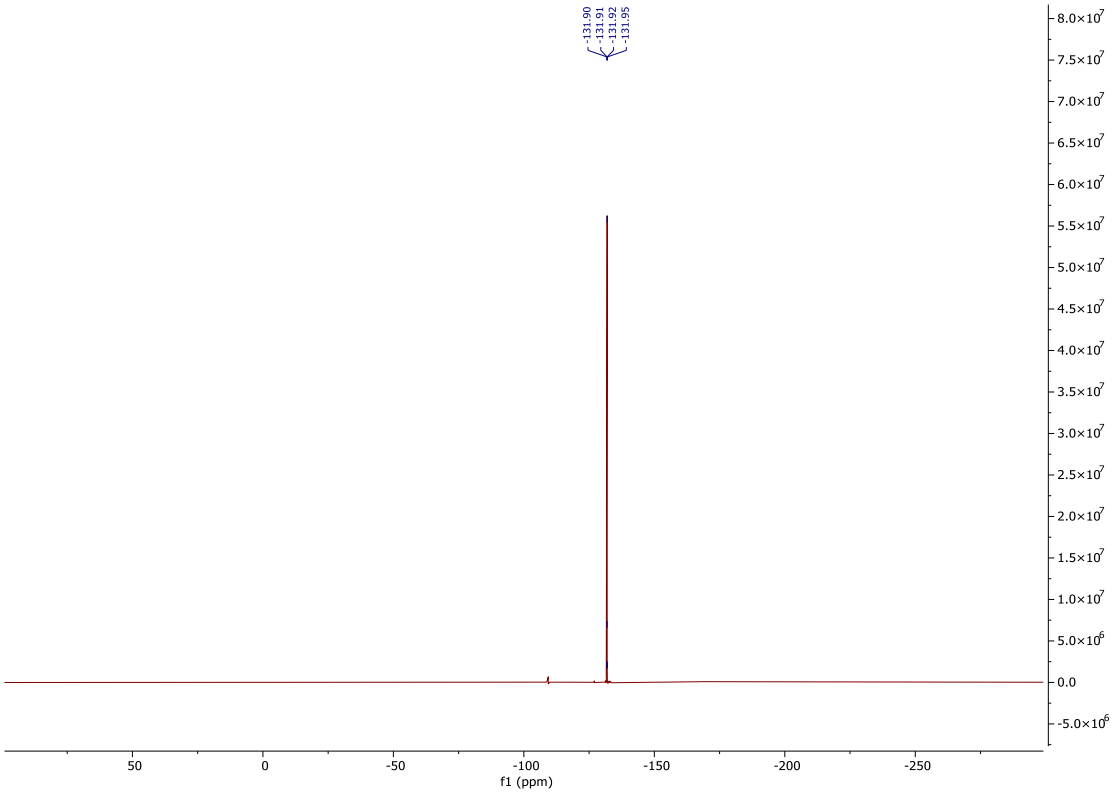


Figure 7.2.37: *^{19}F-NMR (CDCl3) of 5,11-difluoro-6,6,12,12-tetrahexyl-6,12-dihydrothieno[3,2-b]thieno[2'',3'':4',5']thieno[2',3':5,6]-s-indaceno[2,1-d]thiophene-2,8-dicarbaldehyde (**3.14**).*

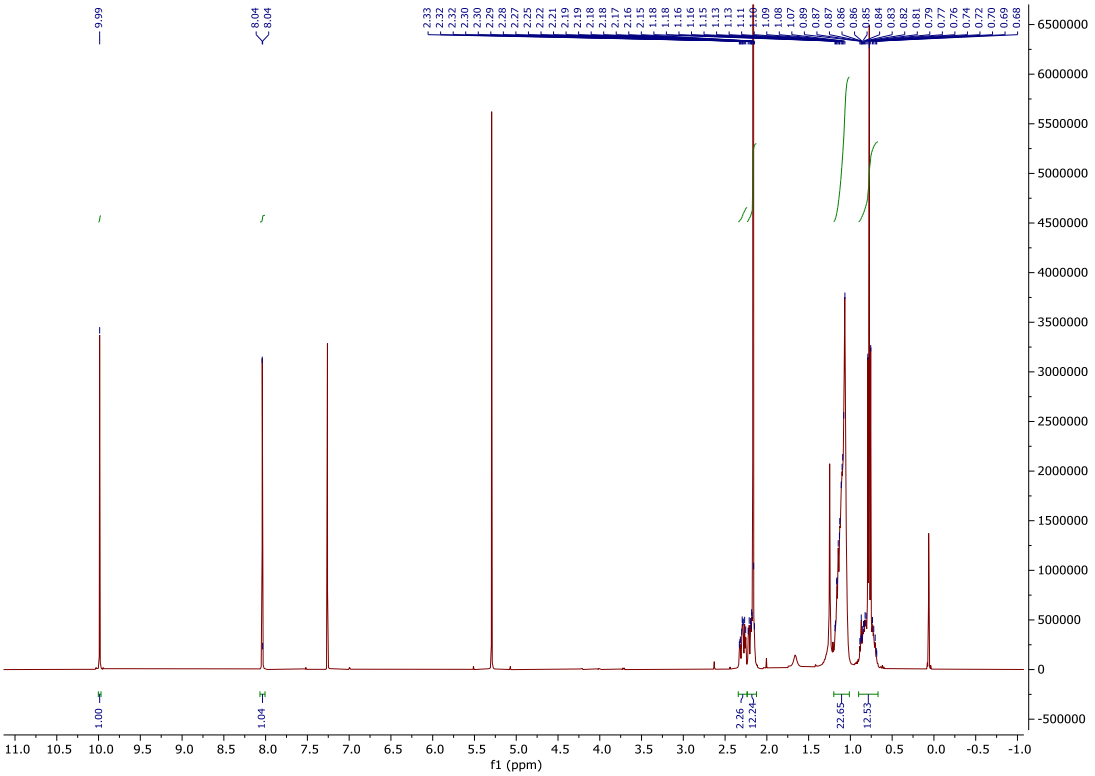


Figure 7.2.38: *^{1}H-NMR (CDCl3) of 5,11-difluoro-6,6,12,12-tetraoctyl-6,12-dihydrothieno[3,2-b]thieno[2'',3'':4',5']thieno[2',3':5,6]-s-indaceno[2,1-d]thiophene-2,8-dicarbaldehyde (**3.16**).*

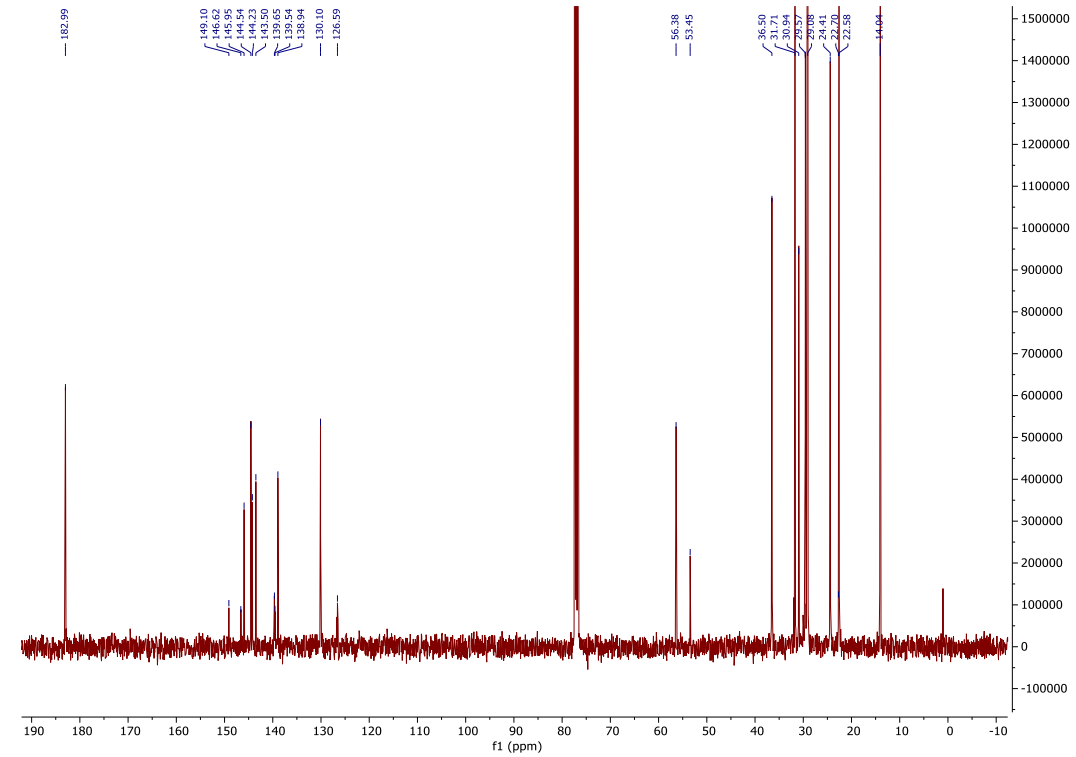


Figure 7.2.39: *^{13}C-NMR (CDCl3) of 5,11-difluoro-6,6,12,12-tetraoctyl-6,12-dihydrothieno[3,2-b]thieno[2'',3'':4',5']thieno[2',3':5,6]-s-indaceno[2,1-d]thiophene-2,8-dicarbaldehyde (**3.16**).*

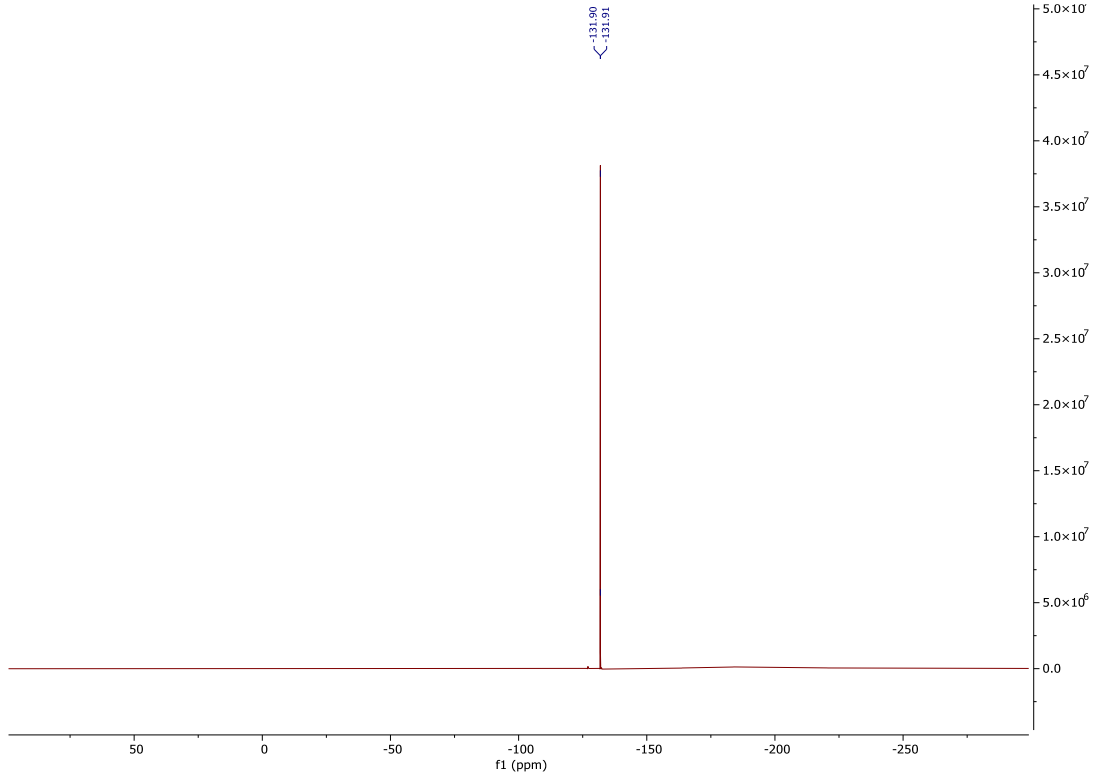


Figure 7.2.40: *^{19}F-NMR (CDCl3) of 5,11-difluoro-6,6,12,12-tetraoctyl-6,12-dihydrothieno[3,2-b]thieno[2'',3'':4',5']thieno[2',3':5,6]-s-indaceno[2,1-d]thiophene-2,8-dicarbaldehyde (**3.16**).*

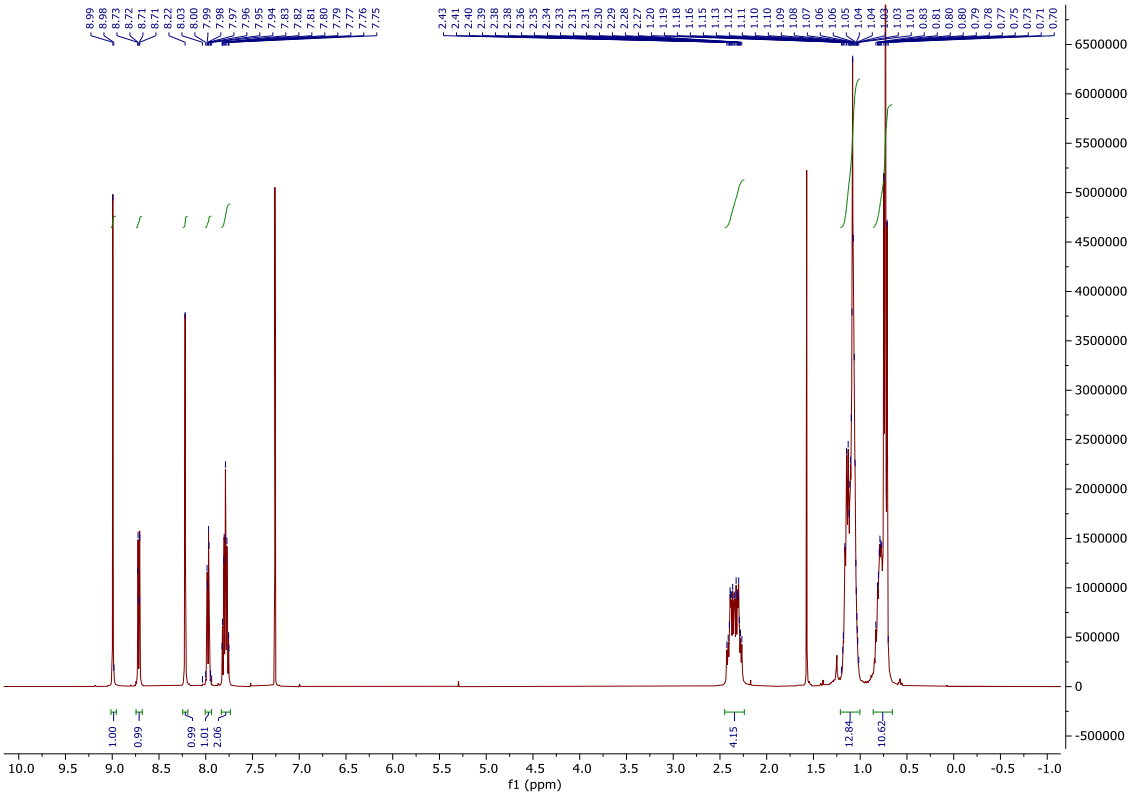


Figure 7.2.41: *^{1}H-NMR (CDCl3) of **C6-2FITIC**.*

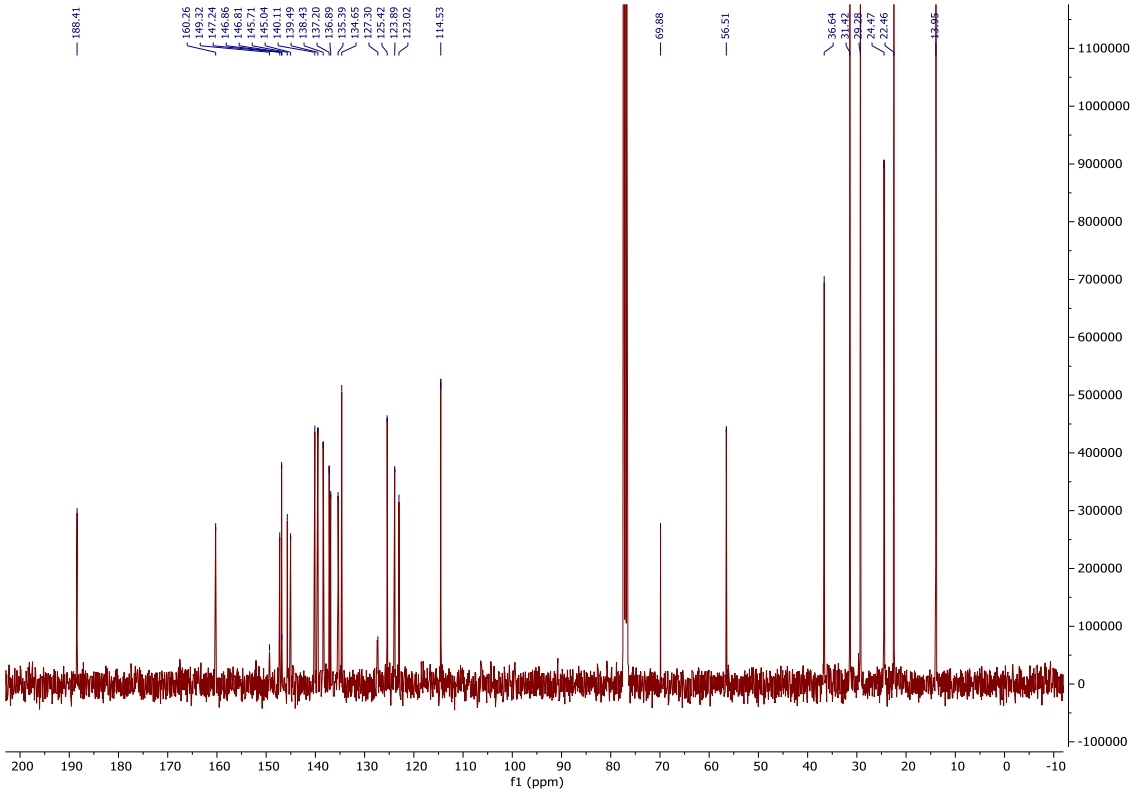


Figure 7.2.42: *^{13}C-NMR (CDCl3) of* ***C6-2FITIC****.*

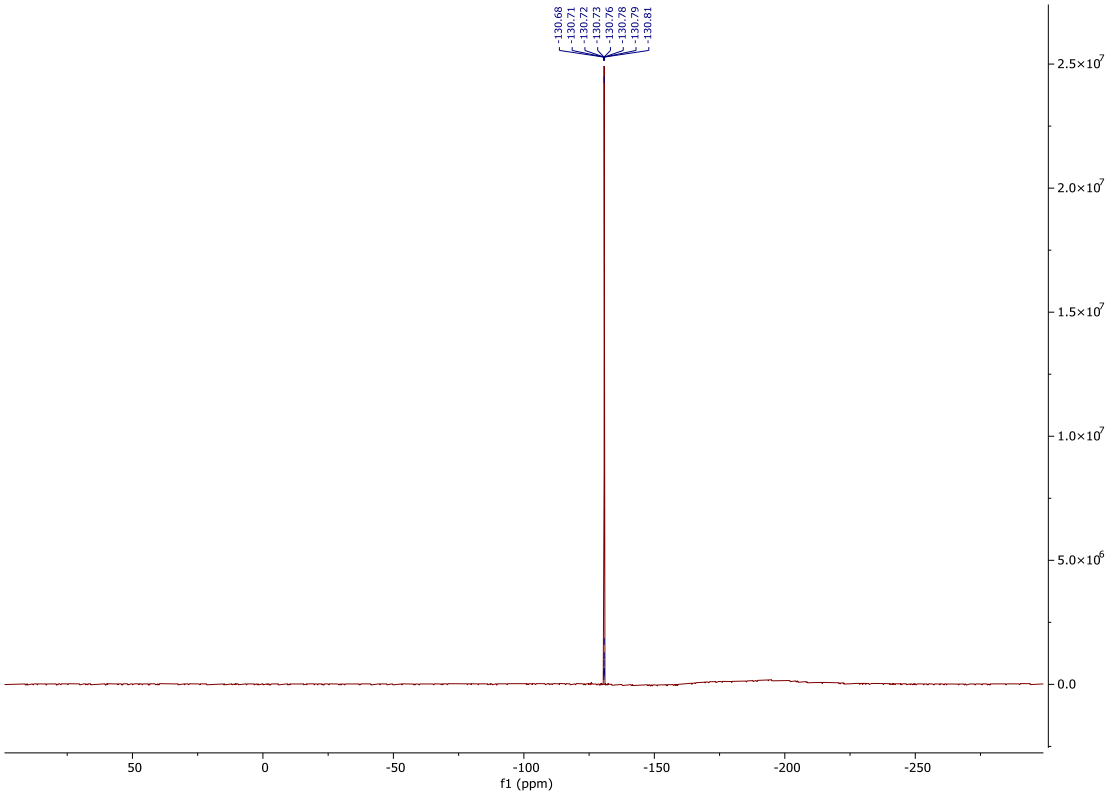


Figure 7.2.43: *^{19}F-NMR (CDCl3) of* ***C6-2FITIC****.*

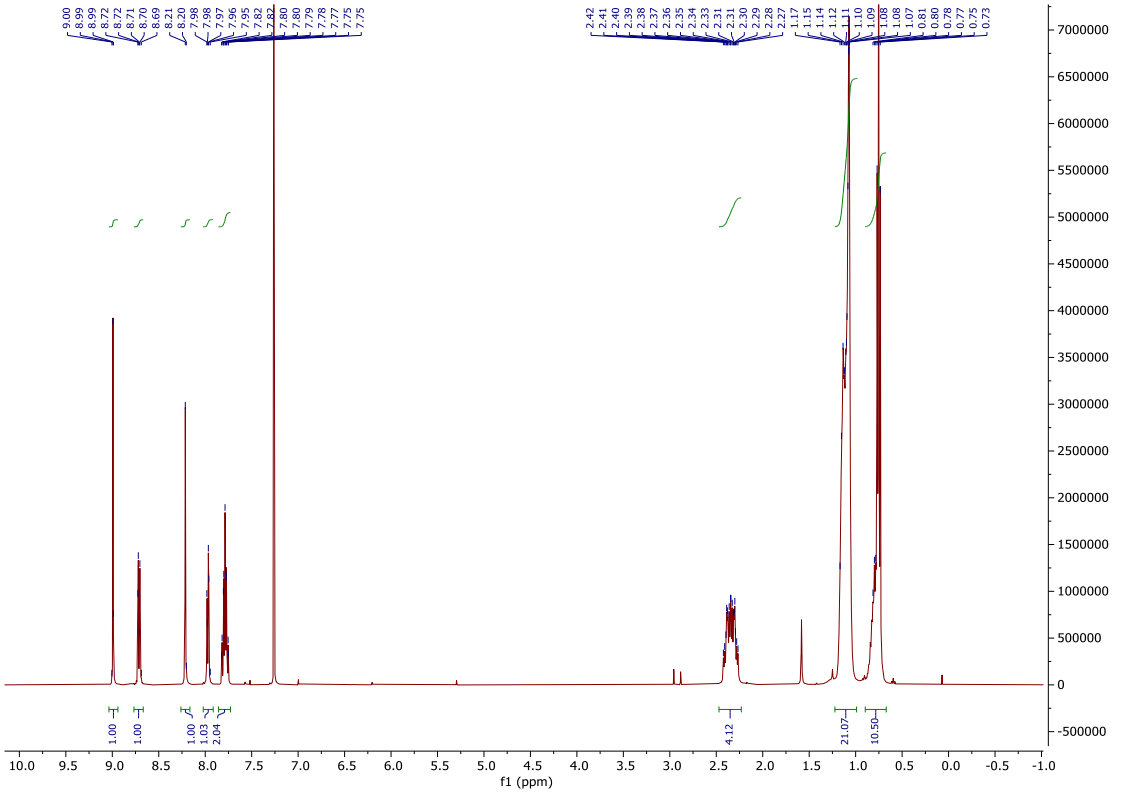


Figure 7.2.44: *^{1}H-NMR (CDCl3) of* ***C8-2FITIC****.*

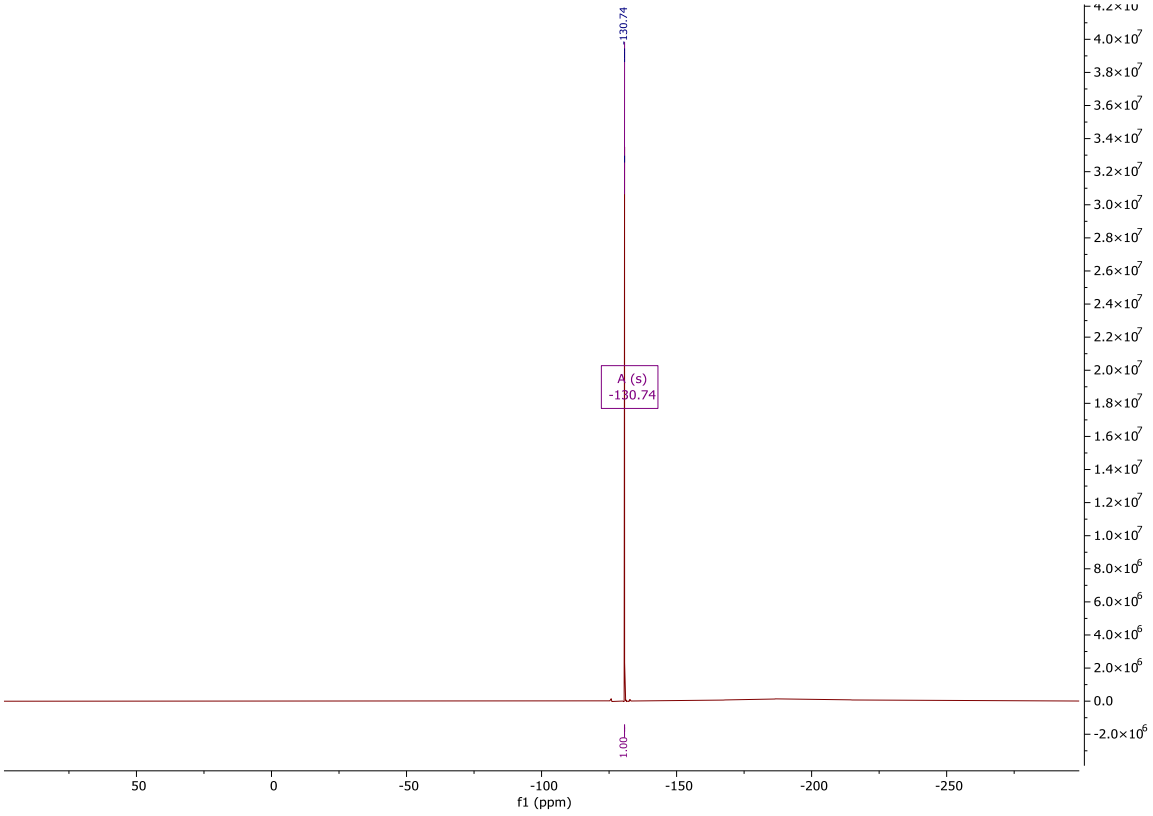


Figure 7.2.45: *^{19}F-NMR (CDCl3) of* ***C8-2FITIC****.*

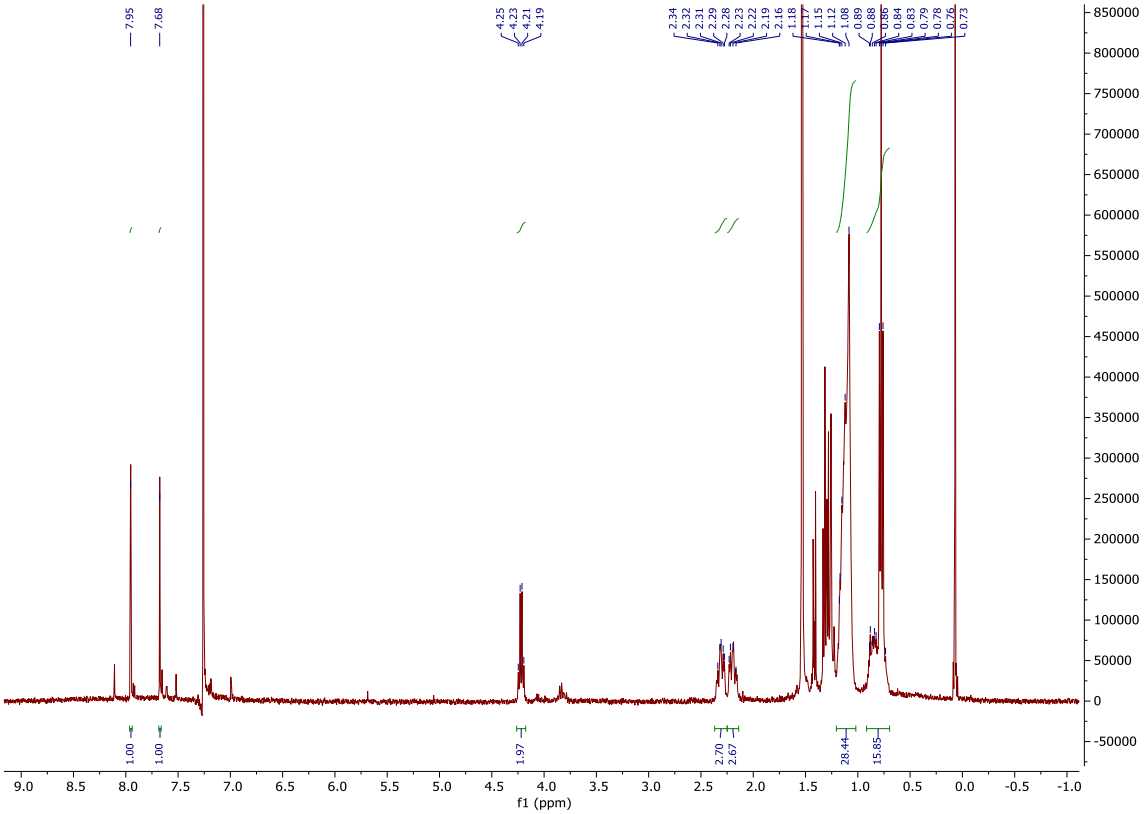


Figure 7.2.46: *^{1}H-NMR (CDCl3) of* ***RH-C8-2FITIC****.*

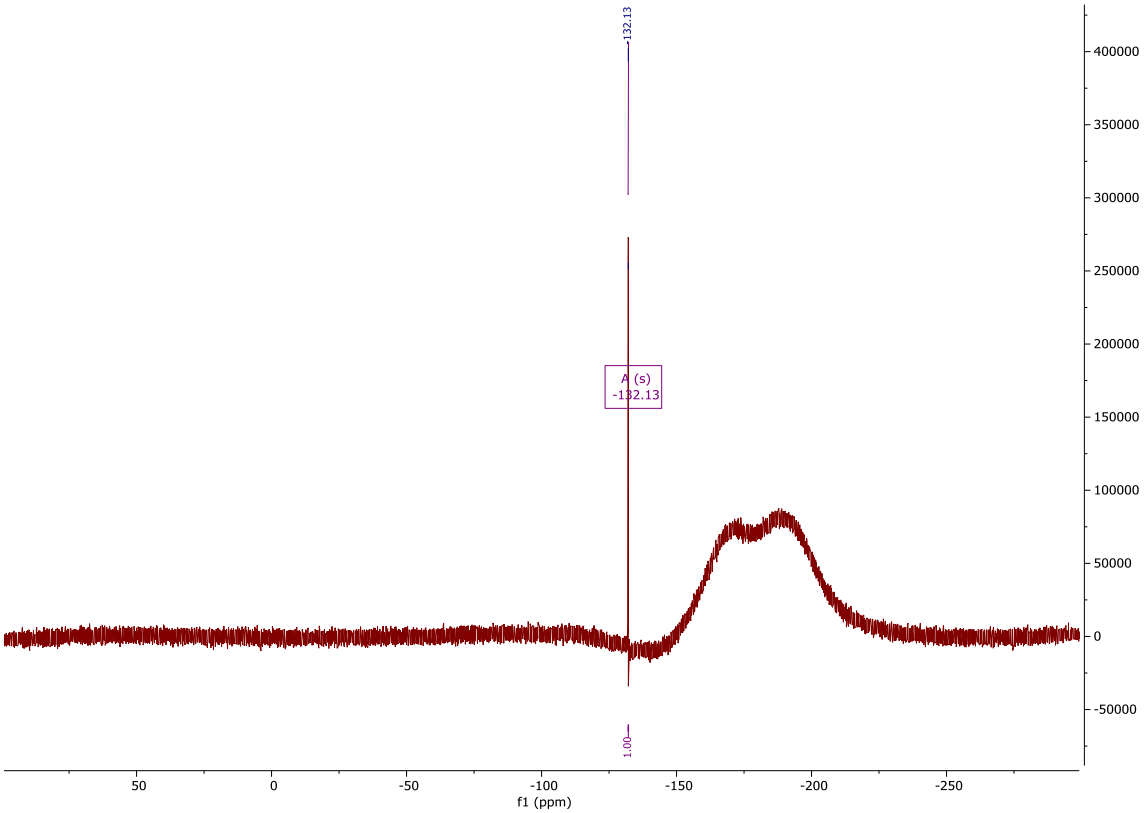
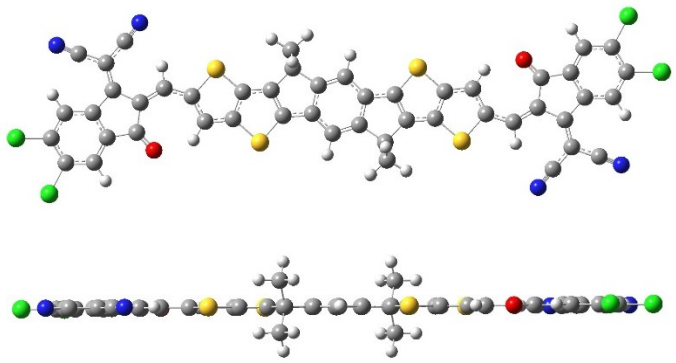


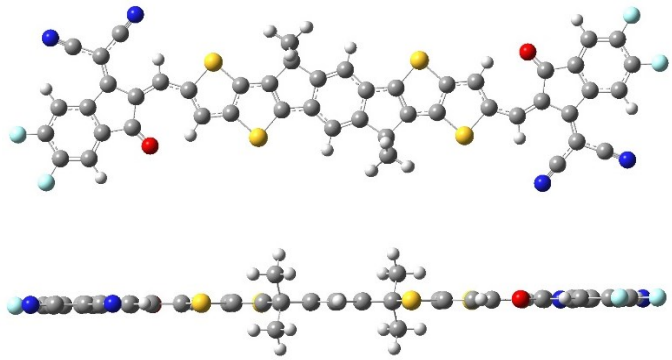
Figure 7.2.47: *^{19}F-NMR (CDCl3) of* ***RH-C8-2FITIC****.*

7.2.3 – DFT results

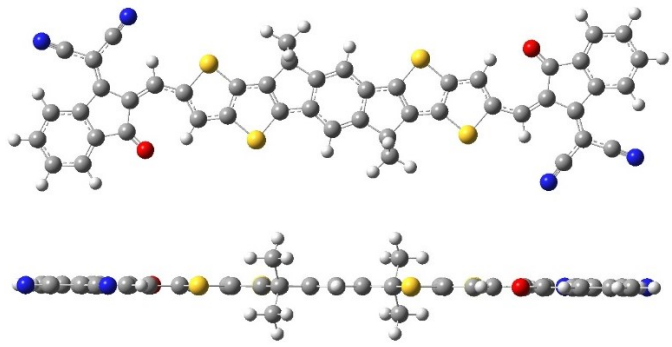
(a)



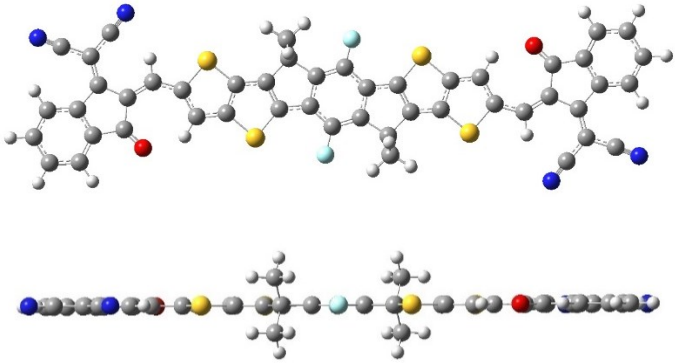
(b)



(c)



(d)



(e)

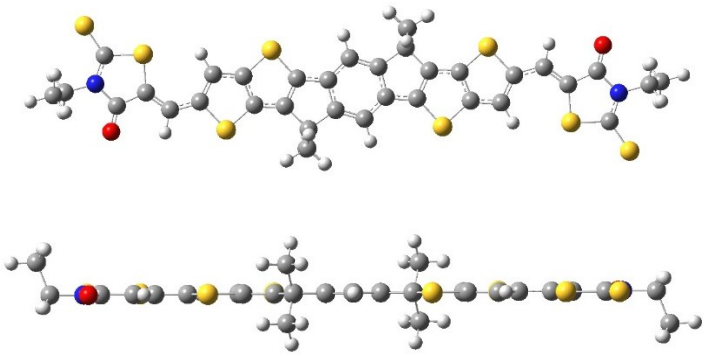


Figure 7.2.48: *NFA structures generated by DFT at the B3LYP level of theory with a 6-31G +G(d,p) basis set showing each acceptor to be planar. Side chains are replaced with methyl groups.* ***(a) 4Cl-C6-ITIC****.* ***(b) 4F-C6-ITIC****.* ***(c) C6-ITIC****.* ***(d) C6-2FITIC****.* ***(e) RH-C6-2FITIC****.*

7.3 - Chapter 4

7.3.1 - CV Traces

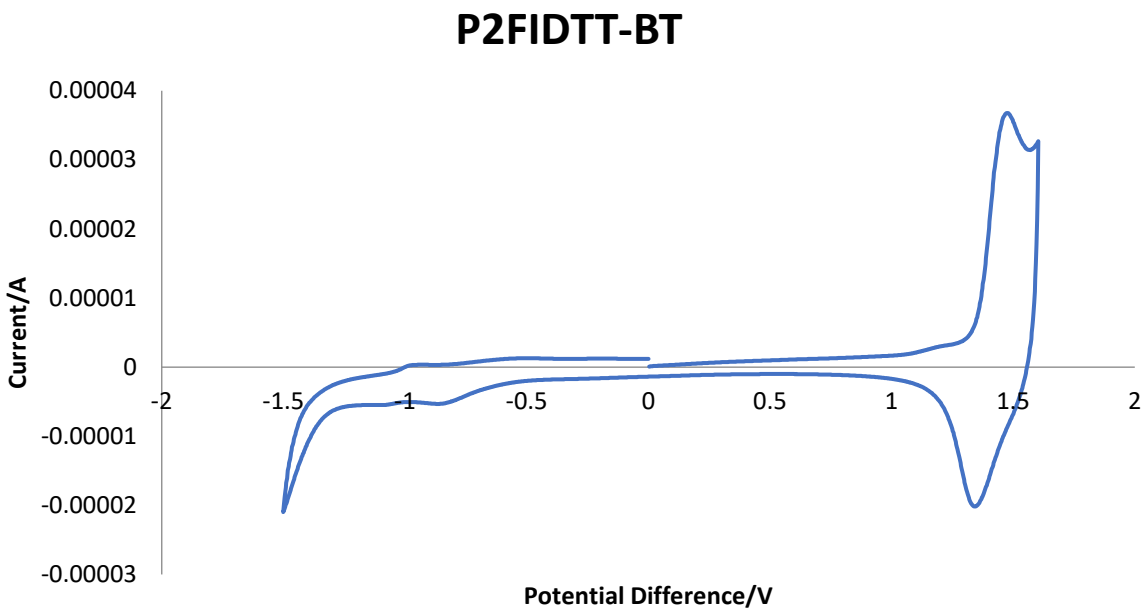


Figure 7.3.1: *CV trace of a drop-cast* ***P2FIDTT-BT*** *film in a 0.1 M solution of* Bu_4NPF_6 *in acetonitrile.*

7.3.2 - NMR Spectra

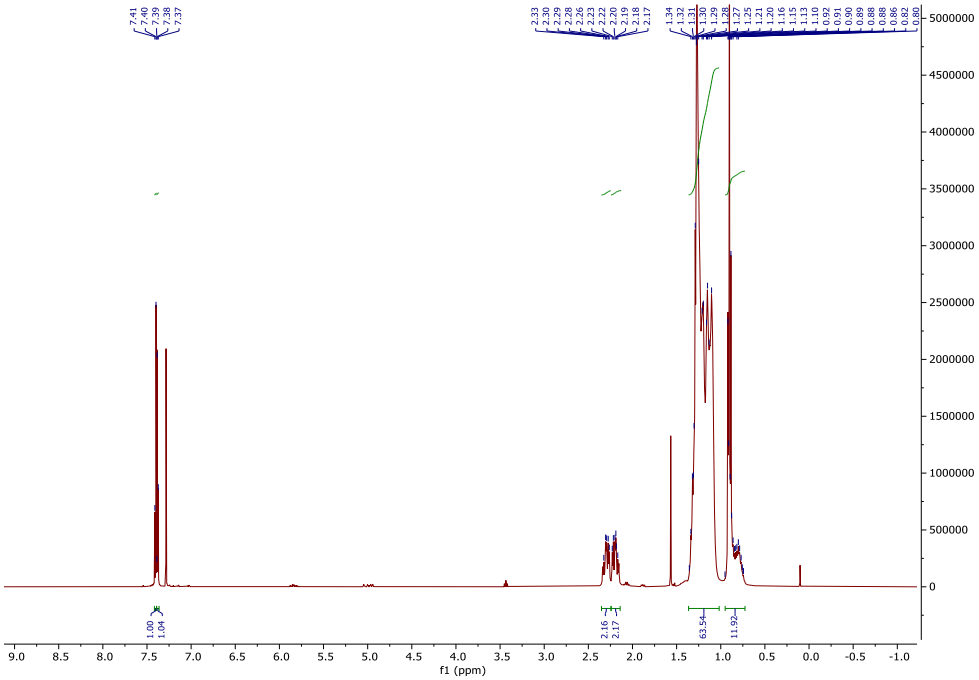


Figure 7.3.2: *^{1}H-NMR (CDCl3) of 5,11-difluoro-6,6,12,12-tetrahexadecyl-6,12-dihydrothieno[3,2-b]thieno[2'',3'':4',5']thieno[2',3':5,6]-s-indaceno[2,1-d]thiophene (**4.1**).*

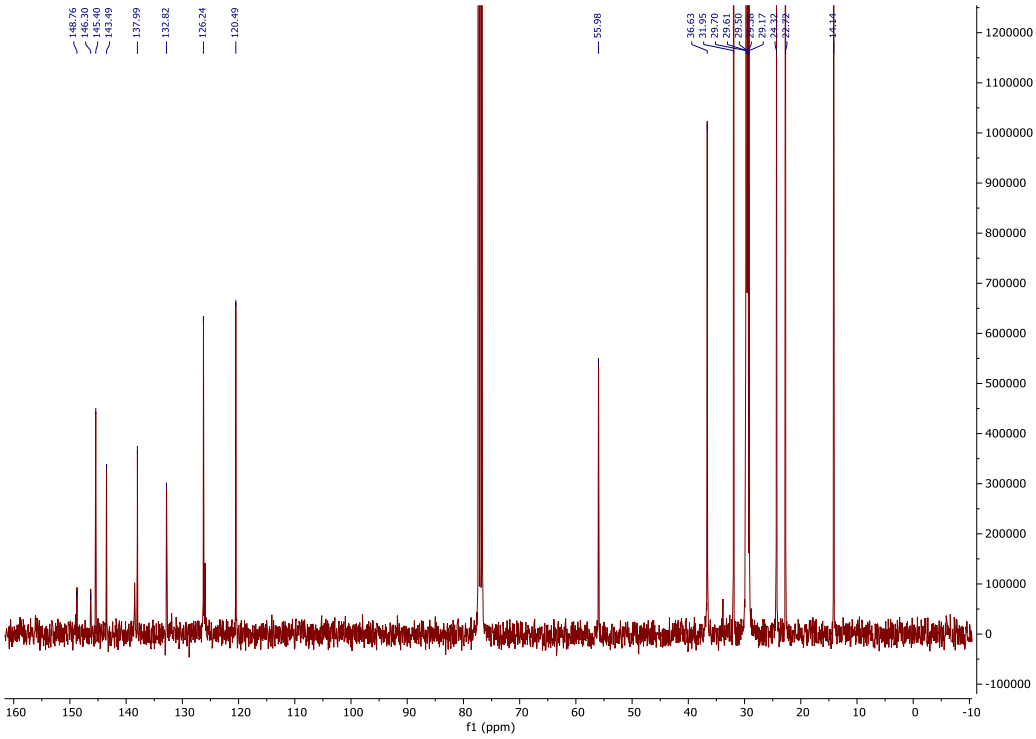


Figure 7.3.3: *^{13}C-NMR (CDCl3) of 5,11-difluoro-6,6,12,12-tetrahexadecyl-6,12-dihydrothieno[3,2-b]thieno[2'',3'':4',5']thieno[2',3':5,6]-s-indaceno[2,1-d]thiophene (**4.1**).*

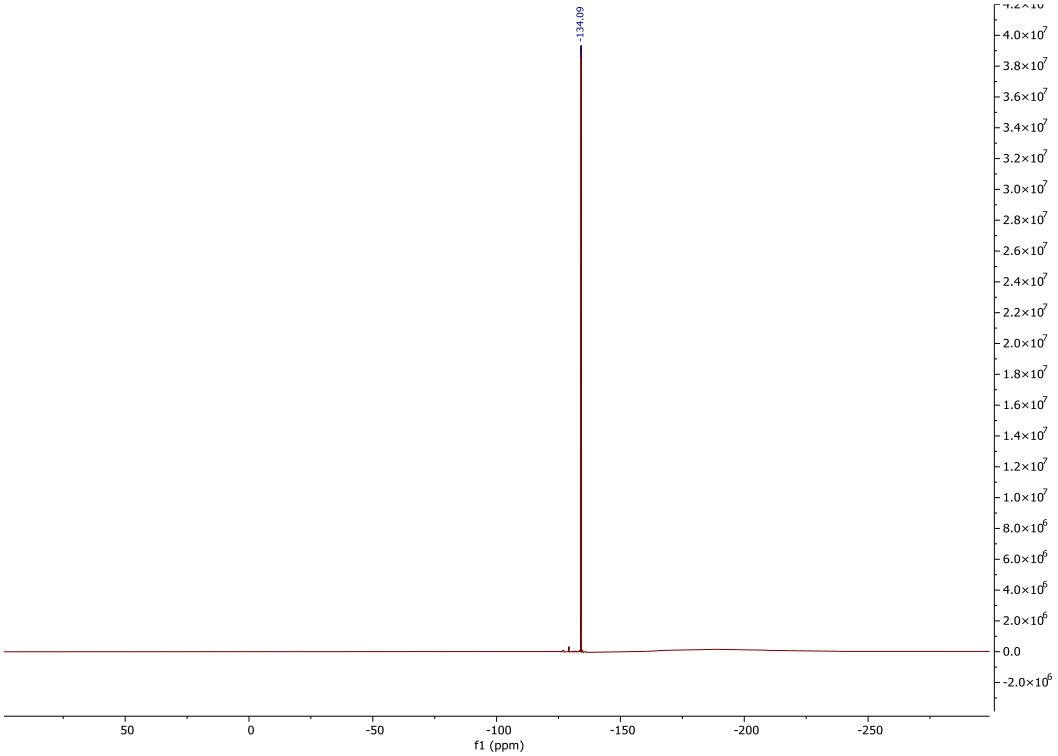


Figure 7.3.4: *^{19}F-NMR (CDCl3) of 5,11-difluoro-6,6,12,12-tetrahexadecyl-6,12-dihydrothieno[3,2-b]thieno[2'',3'':4',5']thieno[2',3':5,6]-s-indaceno[2,1-d]thiophene (**4.1**).*

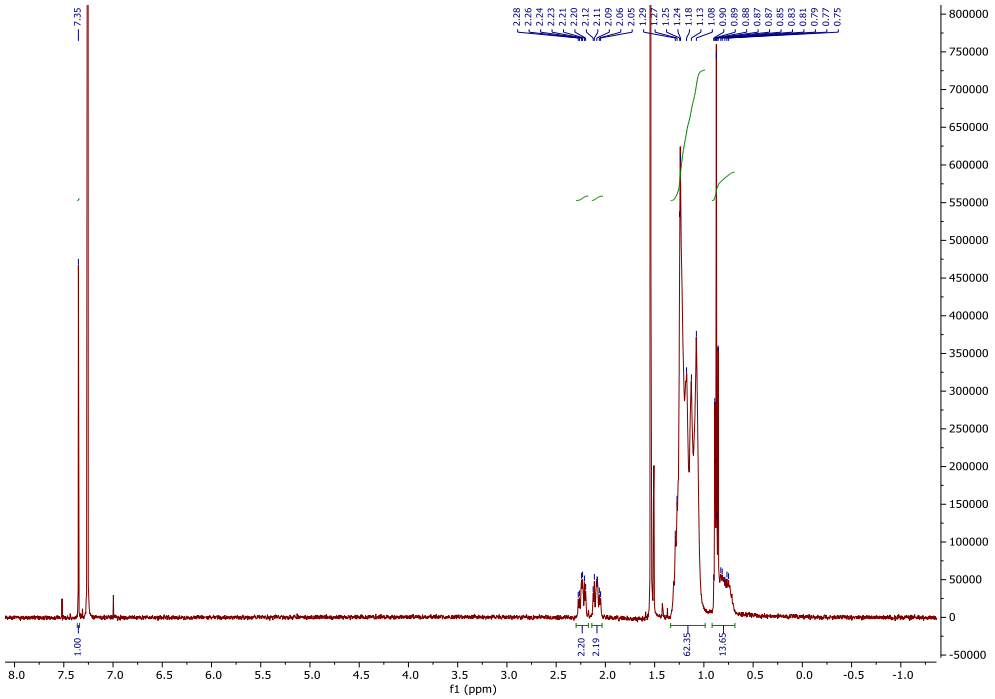


Figure 7.3.5: *^{1}H-NMR (CDCl3) of 2,8-dibromo-5,11-difluoro-6,6,12,12-tetrahexadecyl-6,12-dihydrothieno[3,2-b]thieno[2'',3'':4',5']thieno[2',3':5,6]-s-indaceno[2,1-d]thiophene (**4.2**).*

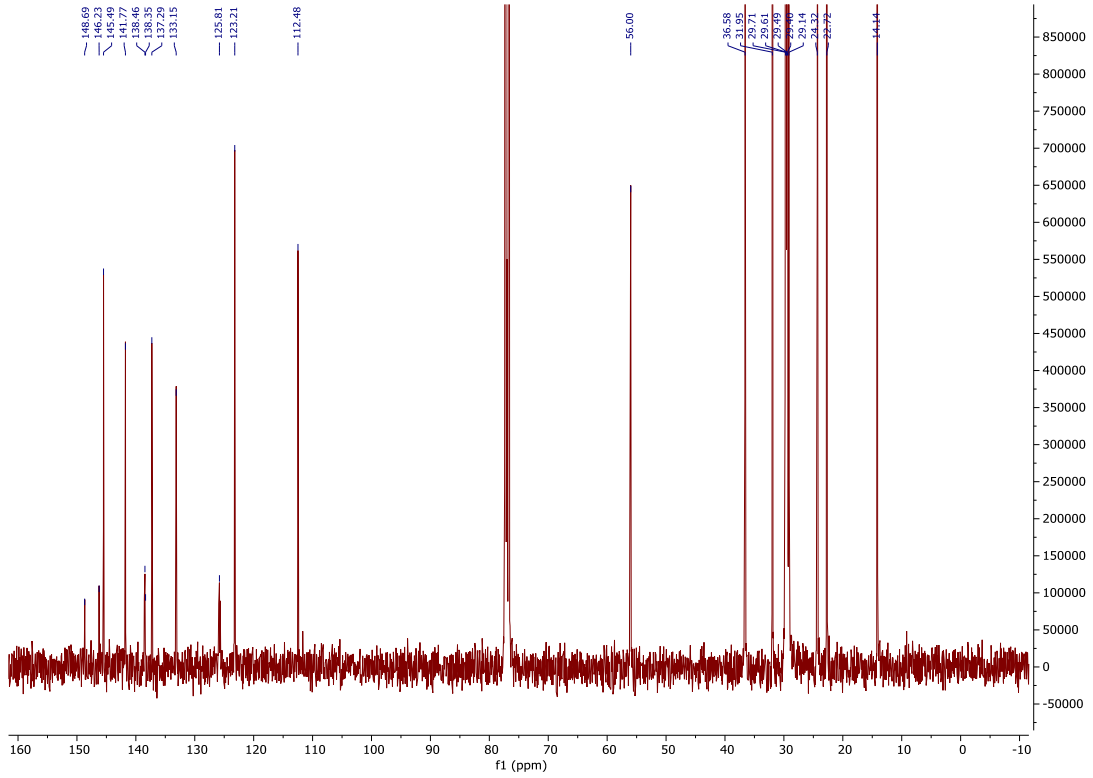


Figure 7.3.6: *^{13}C-NMR (CDCl3) of 2,8-dibromo-5,11-difluoro-6,6,12,12-tetrahexadecyl-6,12-dihydrothieno[3,2-b]thieno[2'',3'':4',5']thieno[2',3':5,6]-s-indaceno[2,1-d]thiophene (**4.2**).*

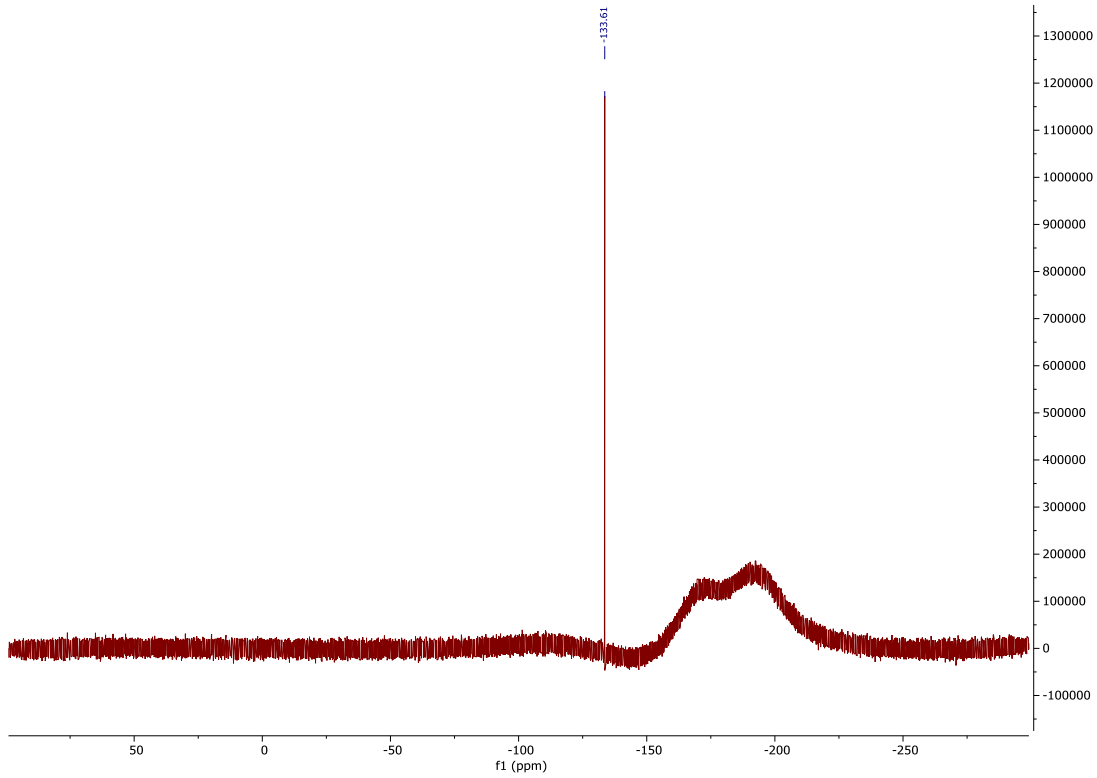


Figure 7.3.7: *^{19}F-NMR (CDCl3) of 2,8-dibromo-5,11-difluoro-6,6,12,12-tetrahexadecyl-6,12-dihydrothieno[3,2-b]thieno[2'',3'':4',5']thieno[2',3':5,6]-s-indaceno[2,1-d]thiophene (**4.2**).*

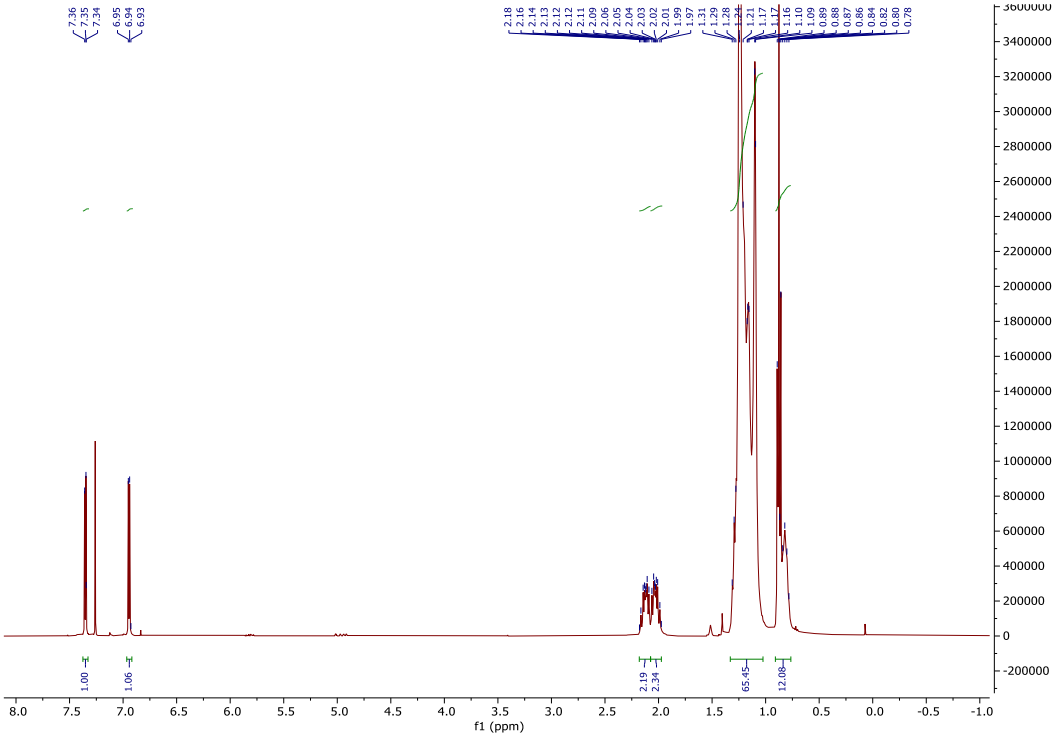


Figure 7.3.8: *^{1}H-NMR (CDCl3) of 5,10-difluoro-4,4,9,9-tetrahexadecyl-4,9-dihydro-s-indaceno[1,2-b:5,6-b']dithiophene (**4.4**).*

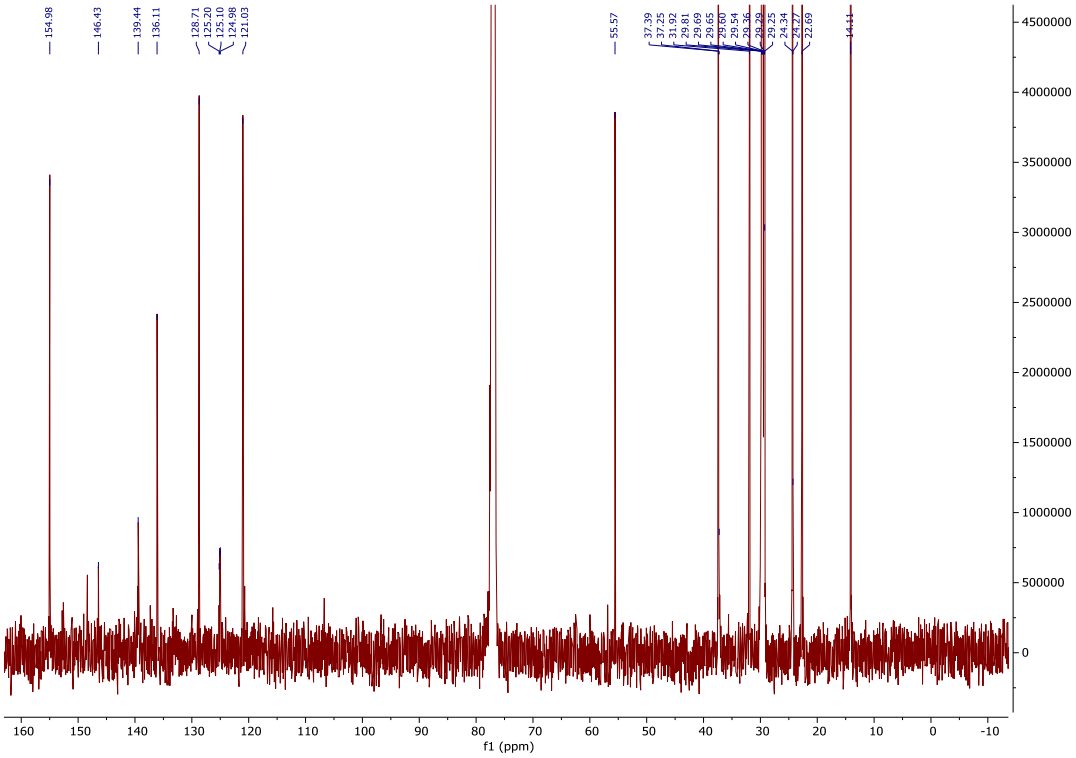


Figure 7.3.9: *^{13}C-NMR (CDCl3) of 5,10-difluoro-4,4,9,9-tetrahexadecyl-4,9-dihydro-s-indaceno[1,2-b:5,6-b']dithiophene (**4.4**). Over 50000 scans were taken.*

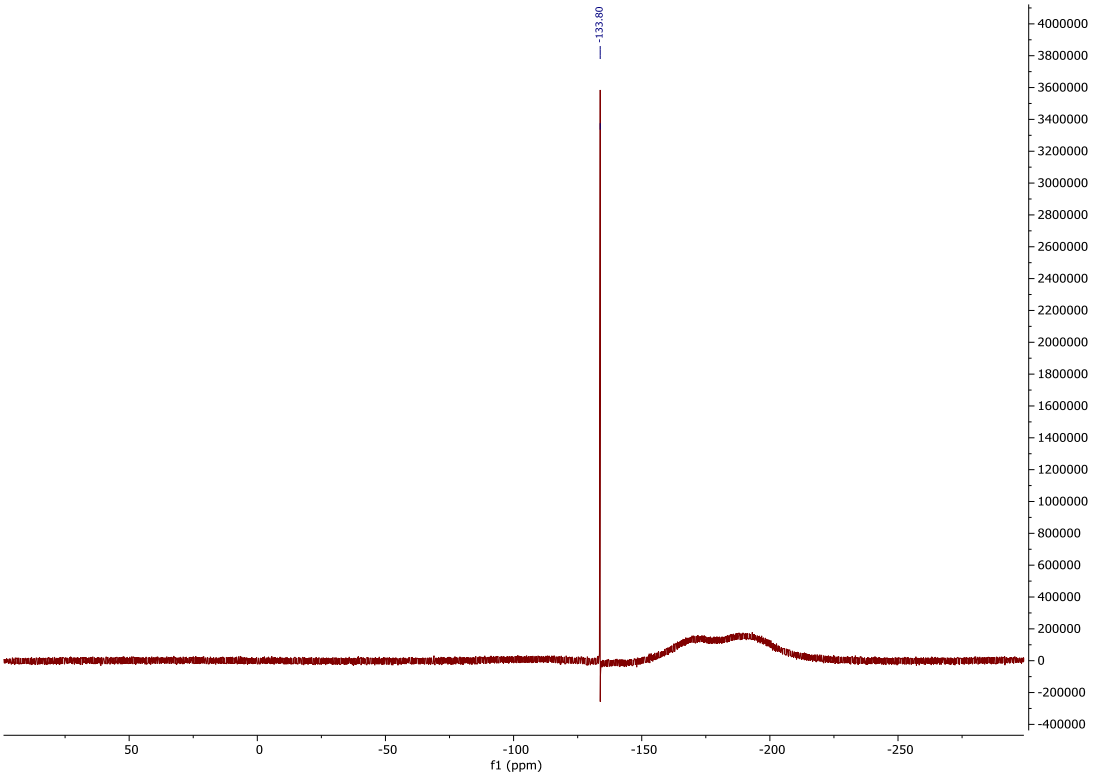


Figure 7.3.10: *^{19}F-NMR (CDCl3) of 5,10-difluoro-4,4,9,9-tetrahexadecyl-4,9-dihydro-s-indaceno[1,2-b:5,6-b']dithiophene (**4.4**).*

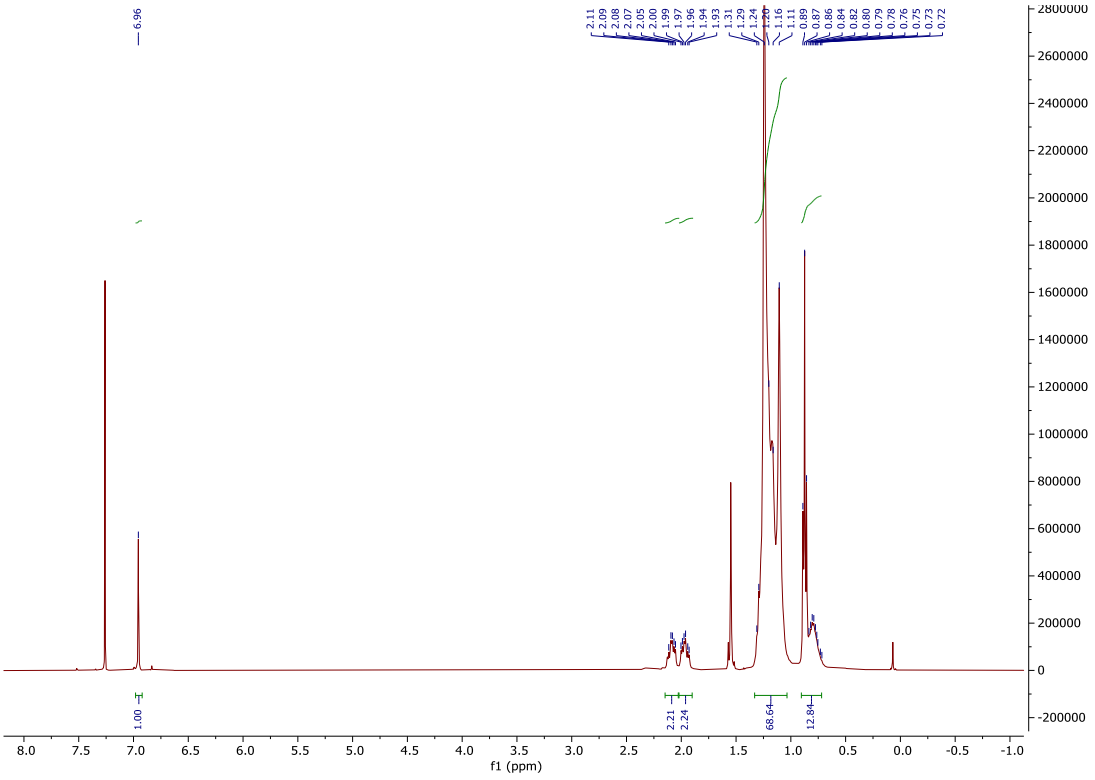


Figure 7.3.11: *^{1}H-NMR (CDCl3) of 2,7-dibromo-5,10-difluoro-4,4,9,9-tetrahexadecyl-4,9-dihydro-s-indaceno[1,2-b:5,6-b']dithiophene (**4.5**).*

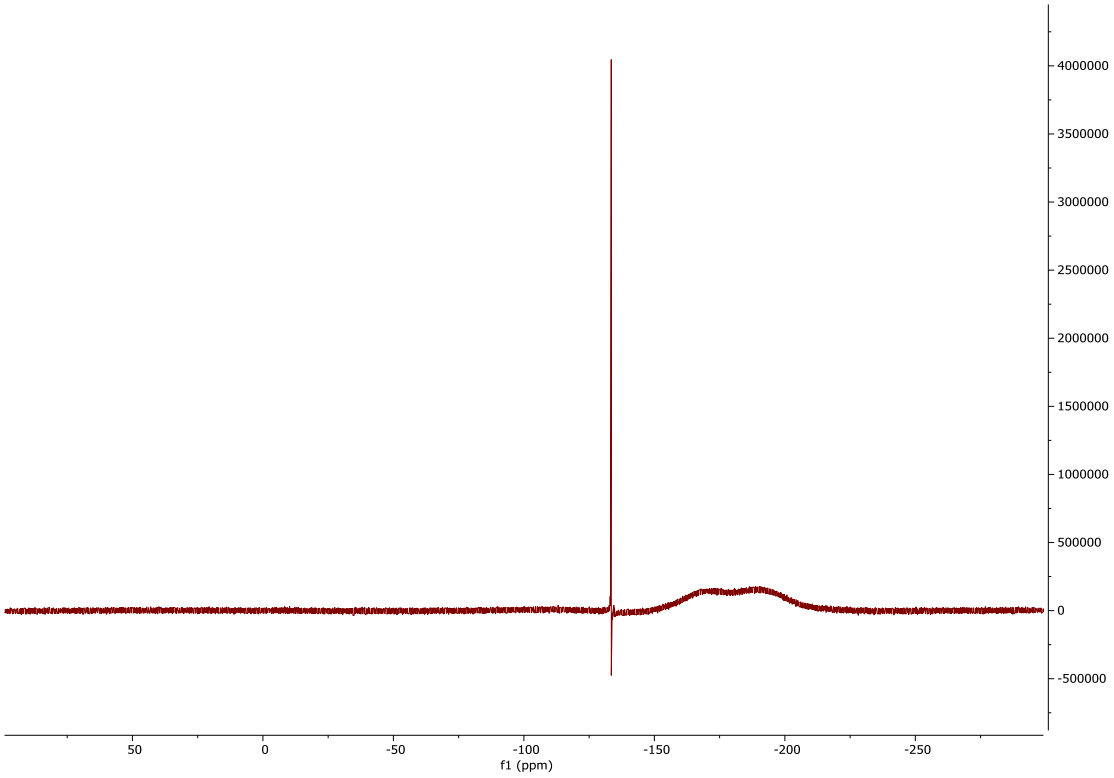


Figure 7.3.12: *^{19}F-NMR (CDCl3) of 2,7-dibromo-5,10-difluoro-4,4,9,9-tetrahexadecyl-4,9-dihydro-s-indaceno[1,2-b:5,6-b']dithiophene (**4.5**).*

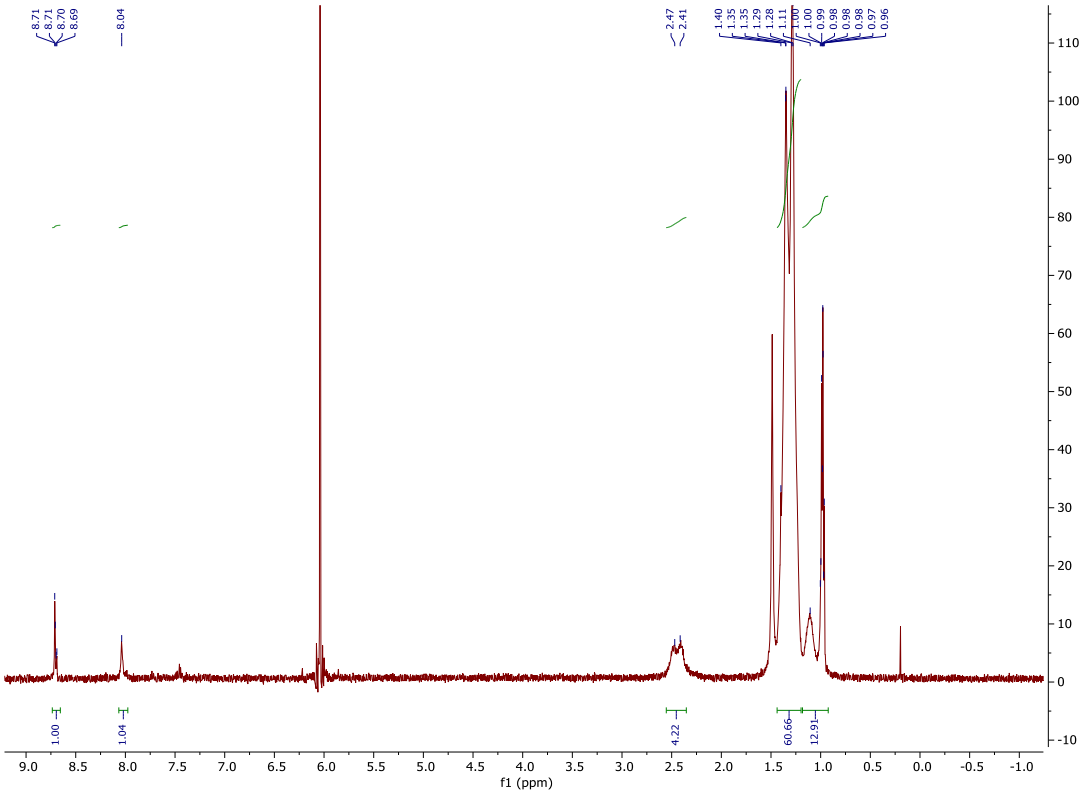


Figure 7.3.13: *^{1}H-NMR (TCE-d2) of **P2FITT-BT**. Spectrum was taken at 393K.*

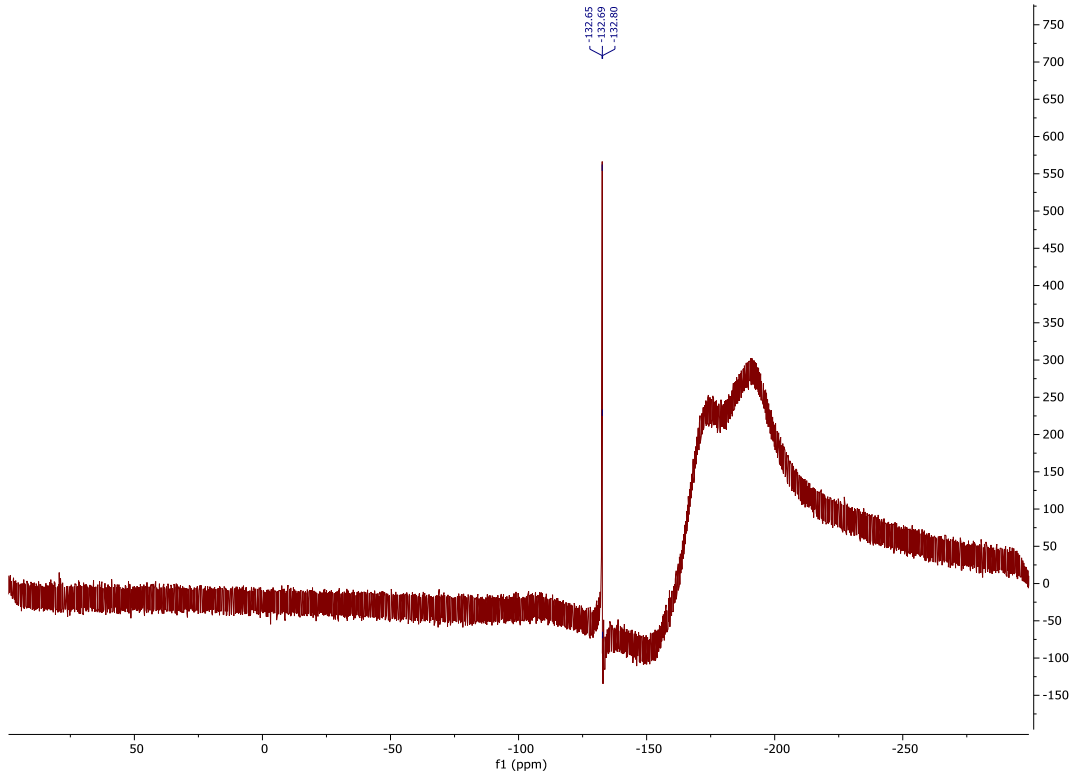
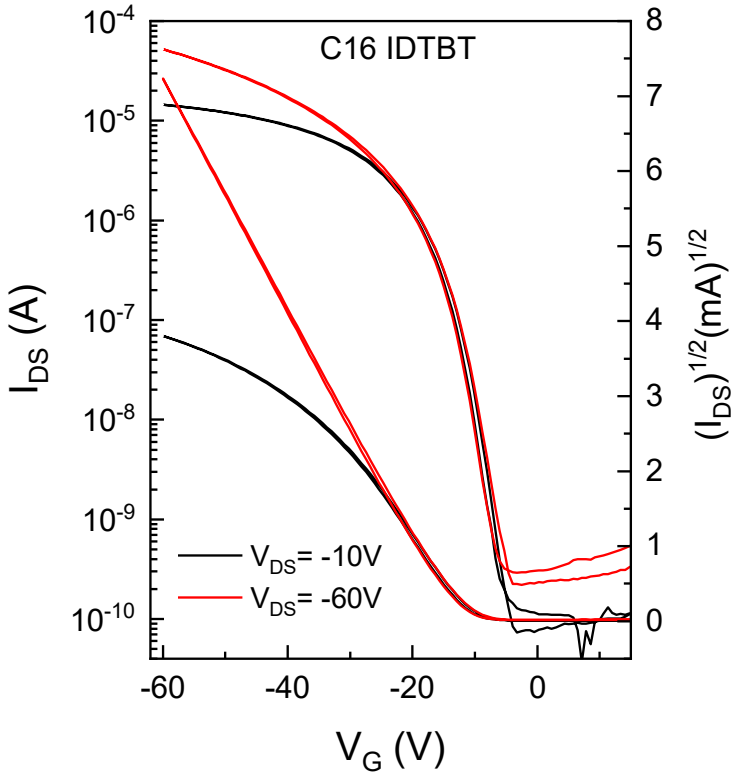
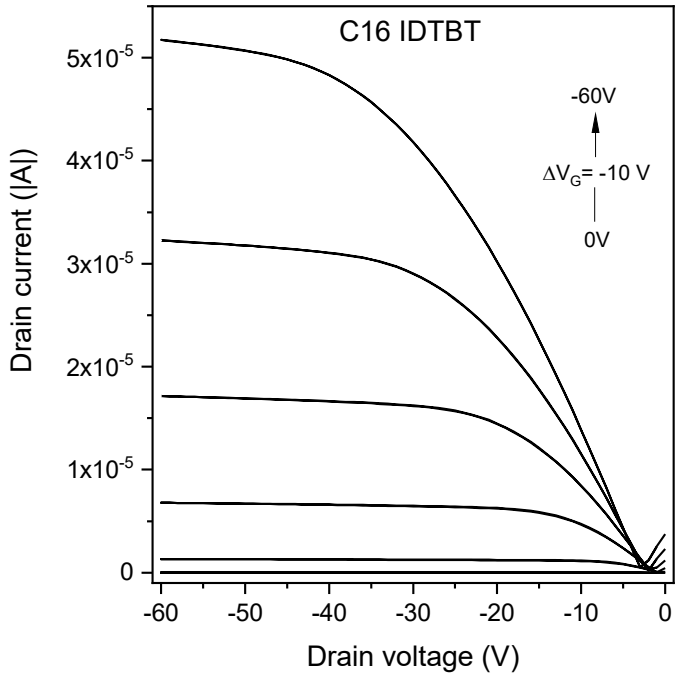


Figure 7.3.14: *^{19}F-NMR (TCE-d2) of* ***P2FITT-BT****. Spectrum was taken at 393K.*

7.3.3 – OFET Data





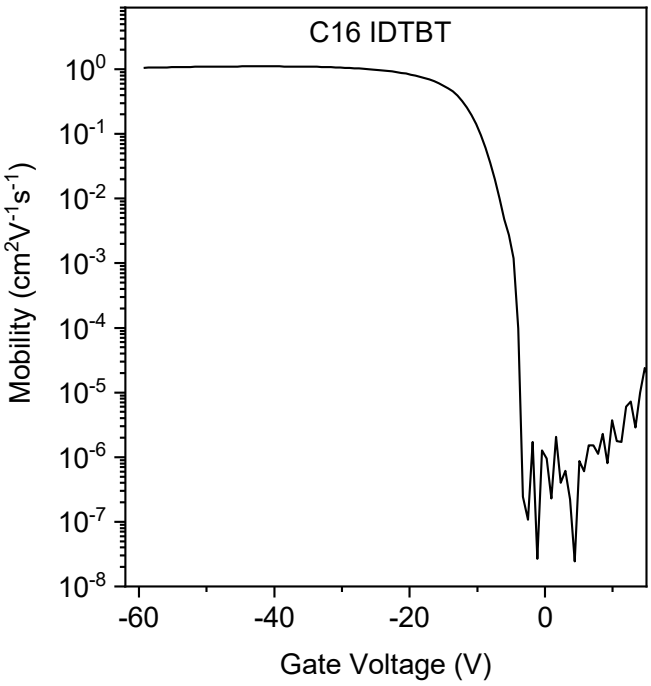
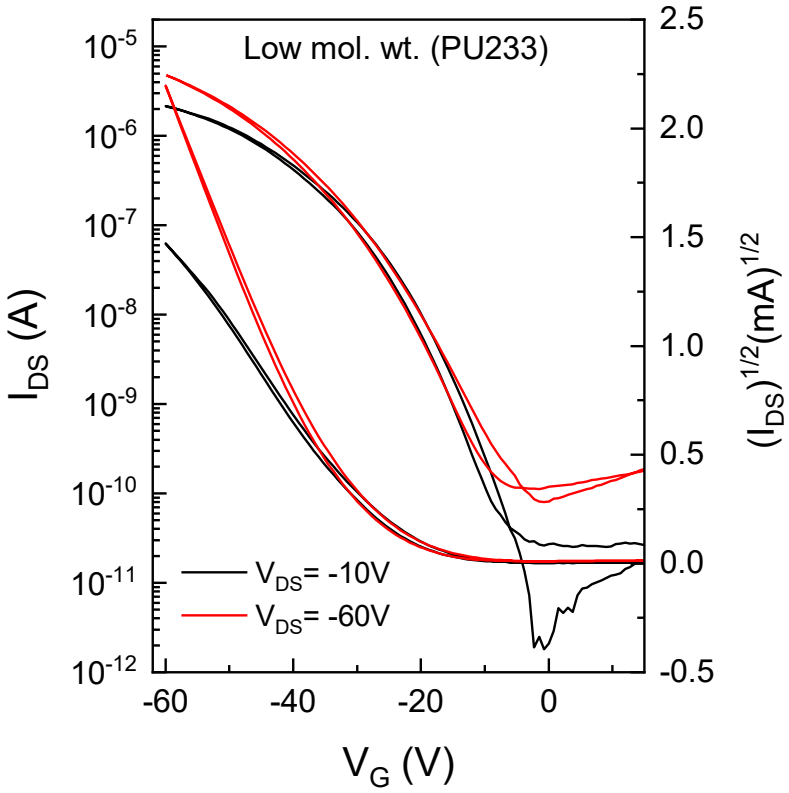


Figure 7.3.15: *Device data for best performing OFET TG-BC spun-cast* ***PIDT-BT*** *device.*



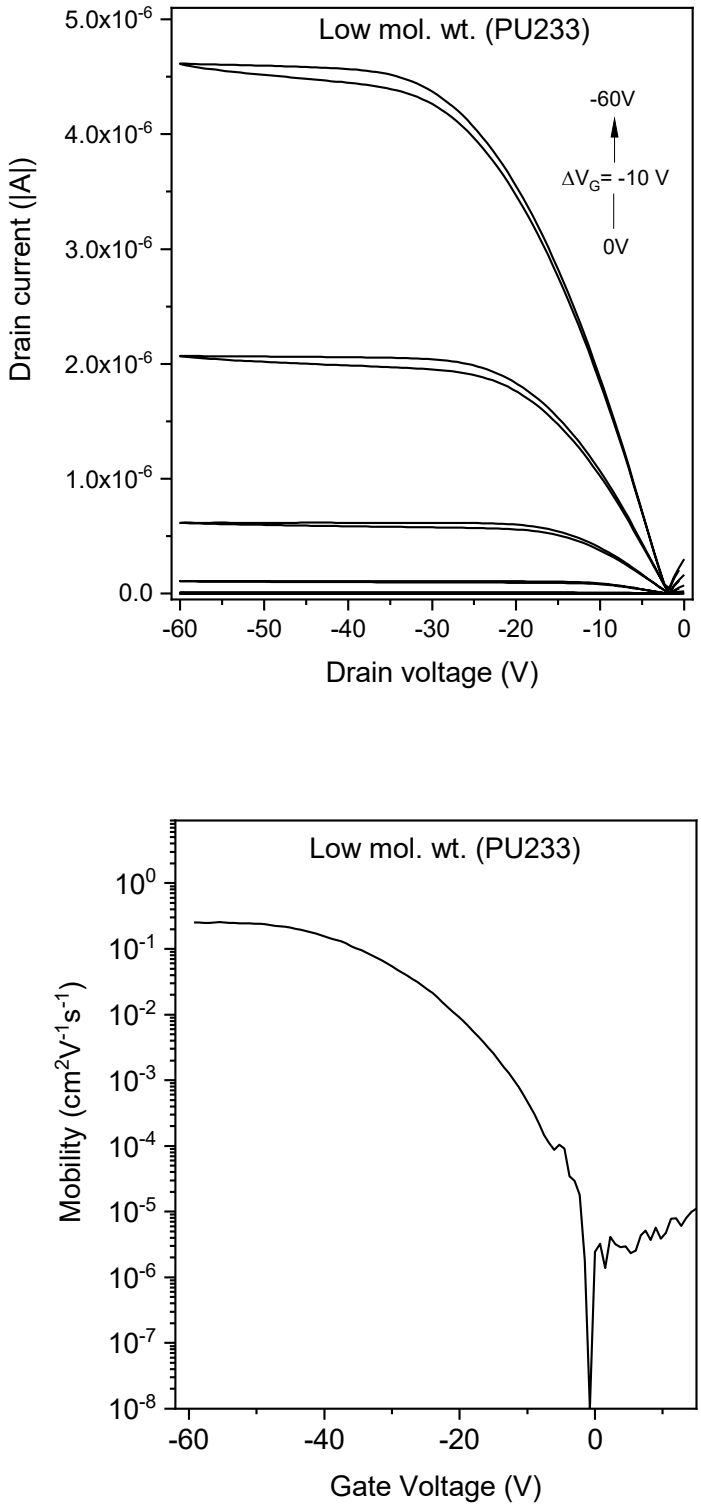
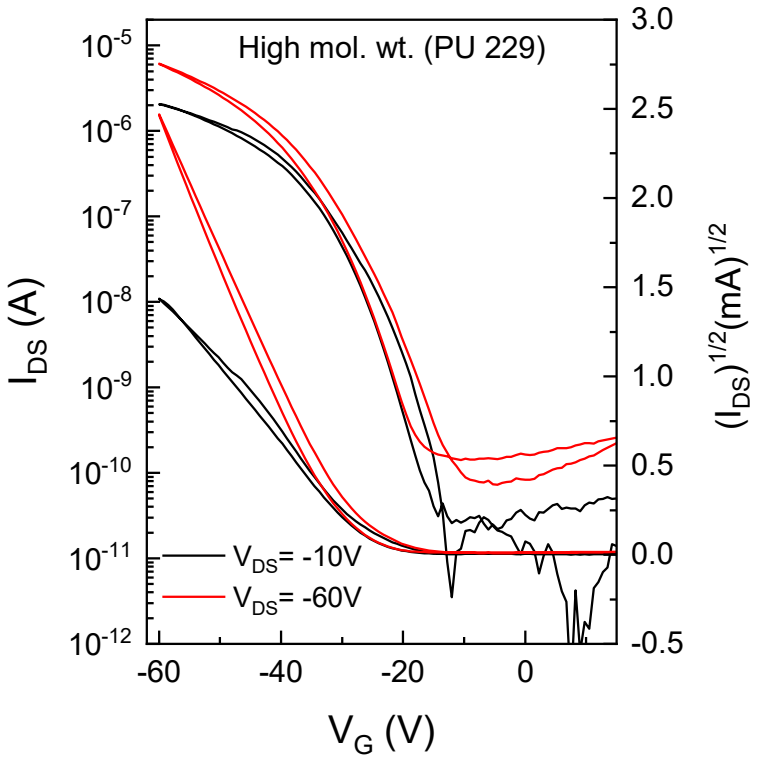
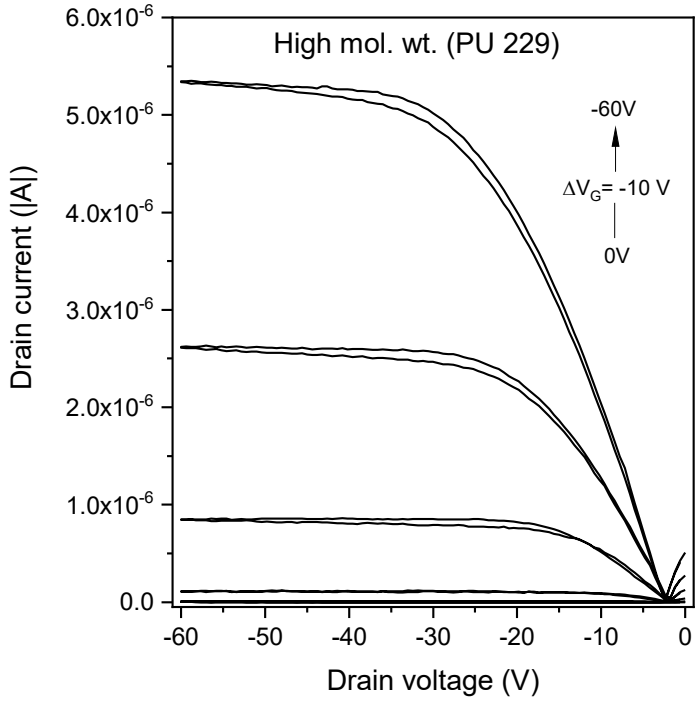


Figure 7.3.16: *Device data for best performing OFET TG-BC spun-cast low molecular weight* ***P2FIDTT-BT*** *device.*


High mol. wt. (PU 229)
I_{DS} (A)
$(I_{DS})^{1/2}(mA)^{1/2}$
V_G (V)
V_{DS}= -10V
V_{DS}= -60V


High mol. wt. (PU 229)
Drain current (|A|)
Drain voltage (V)
-60V
ΔV_G= -10 V
0V

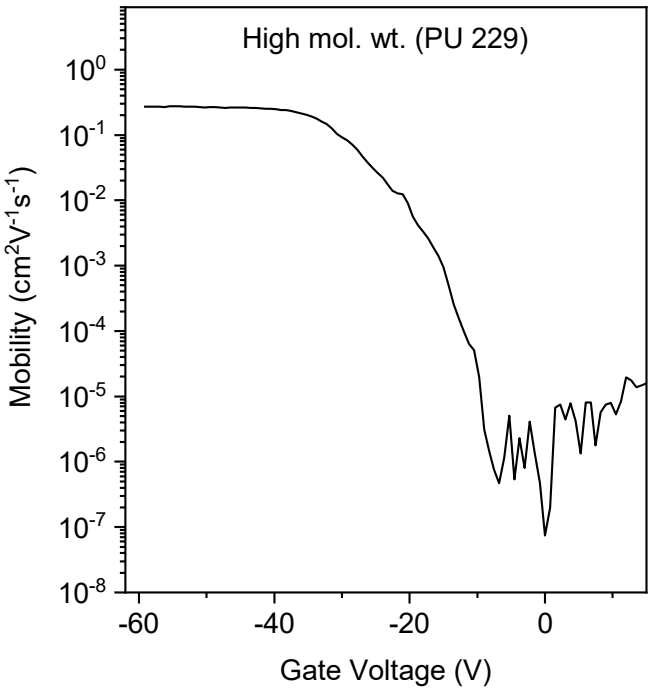


Figure 7.3.16: *Device data for best performing OFET TG-BC spun-cast high molecular weight* ***P2FIDTT-BT*** *device.*

8 – Permissions

Evidence of permission to reproduce **Figure 3** from the publication https://doi.org/10.1021/cm049391x:

